New Routes Towards Nanoporous Carbon Materials for Electrochemical Energy Storage and Gas Adsorption

DISSERTATION

zur Erlangung des akademischen Grades

Doctor rerum naturalium

(Dr. rer. nat.)

vorgelegt der

Fakultät Mathematik und Naturwissenschaften

der Technischen Universität Dresden

von

M. Sc. Martin Oschatz
geboren am 28.05.1987 in Radebeul

Eingereicht am 10.12.2014

Für R, M, O und TT.

Danke!/Thanks!

Table of Contents

1. Motivation

The chemical element carbon plays a key role in the 21st century. It is the ubiquitous element of life and contributes to the balance of our planet by cycles in organisms, ground, water, and atmosphere. However, this element will also become one of the earth's greatest challenges. The term "the new carbon age" is associated with the global warming as a result of increasing carbon dioxide emissions and the depletion of fossil fuels. In simple words, the global carbon circle has sped up. The increasing carbon dioxide concentration in the atmosphere is for the most part caused by the continued combustion of fossil fuels for energy generation and will lead to continuous global warming. The capture of greenhouse gases by adsorption is a promising way to limit the increase of the atmosphere temperature. Furthermore, there is an essential necessity to establish renewable alternatives for energy production and to replace the established technologies based on coal, oil, and gas. In contrast to the latter, alternative sources, such as wind, solar, or hydropower are not independent from time and location. The produced "green energy" has to be stored in rechargeable energy storage devices which then provide it to the consumer "on demand". High power and high energy density are required for such systems to achieve efficient power grid management but often remain unachieved with the established technologies.

In this context, carbon is both a curse and a blessing as it is also one key component to overcome these problems. Especially porous carbon materials are highly attractive in many energy and environmentally relevant applications. These materials provide desirable properties, such as high specific surface area, high pore volume, thermal/chemical stability, beneficial mechanical properties, and high electrical conductivity. In consequence, they are promising candidates for the removal of carbon dioxide or other environmentally relevant gases from exhaust gas mixtures. Furthermore, porous carbons are of outstanding importance in electrochemical energy storage devices, such as batteries or electrochemical capacitors.

As the performance of the materials in these applications is most often depending on their structural parameters, precise control over the pore size and the pore geometry over a wide range is largely desired. Besides a high specific surface area, pore accessibility as well as defined pore sizes are important to achieve because the surface must be completely accessible depending on the targeted application. If the porous carbons exhibit ink-bottle or wormlike pores as it is the case for many activated carbons,

the high surface area is useless because the guest species do not reach the pore interior due to the restricted access or too long diffusion pathways. Hence, carbon materials with hierarchical pore structure are highly attractive. They combine at least two different pore systems of different size which contribute with their individual advantages. While smaller pores provide large surface area, larger pores ensure efficient mass transport.
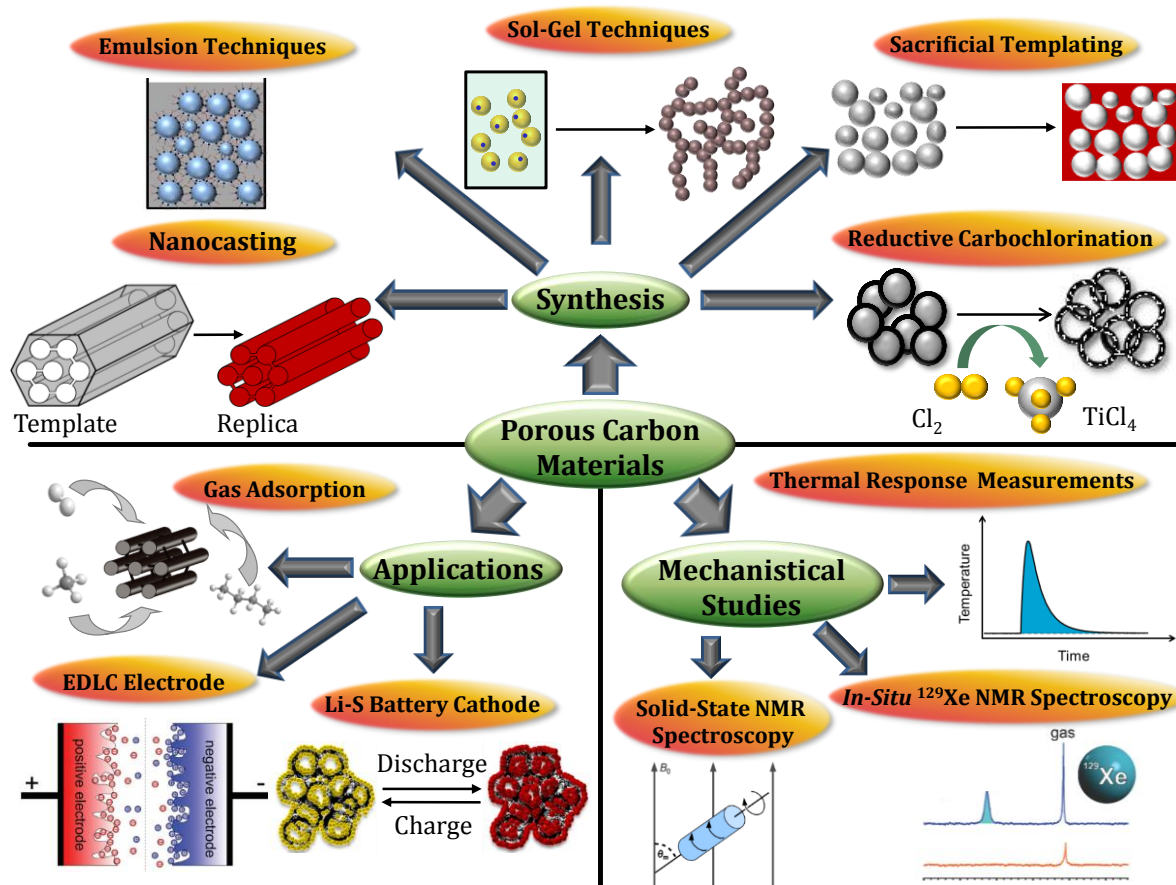
Figure 1. *Porous carbon materials synthesized within this thesis and the investigated applications as well as mechnistical studies.*

In this thesis, novel routes for the synthesis of well-defined carbon materials with tailored and hierarchical pore architectures are presented (Figure 1). One straightforward approach for the synthesis of microporous carbon materials is the extraction of metal- or semi-metal atoms from carbide materials. The resulting materials, known as carbide-derived carbons (CDCs), can reach specific surface areas as high as 3000 m^2/g but they are limited to very narrow cavities with random orientation and adverse materials transport properties. Templating approaches as well as sol-gel methods are used within this thesis to tune these materials with a secondary transport pore structure. The synthesis-structure relationships are evaluated in detail and the

CDCs are characterized by different methods to investigate different structural parameters.

These novel components show outstanding performance in electrochemical energy storage applications. In particular, they are used as electrode materials in electrochemical double-layer capacitors (EDLCs) with different electrolyte systems. EDLCs are among the most promising technologies for electrochemical energy storage because these devices make use of the electrosorption of electrolyte ions on the surface of the electrode material and therefore provide high charge/discharge rates and long cycle life. Furthermore, the CDCs are utilized as host structures for the active material in lithium-sulfur (Li-S) battery cathodes. The Li-S system is a very attractive next-generation battery due to its extremely high energy density. Besides the electrochemical applications, the developed hierarchical CDCs show outstanding performance in the adsorption of environmentally relevant gases, such as carbon dioxide and *n*-butane by combination of high uptakes and rapid adsorption kinetics.

Besides the different approaches towards hierarchical CDCs, a novel scalable and straightforward method for the synthesis of mesoporous carbon materials is presented within this thesis. The so-called Kroll-Carbons (KCs) are produced by the reductive carbochlorination reaction between oxidic nanoparticles and a surrounding carbon matrix. The pore structure of the KCs can be precisely adjusted for optimum performance in different electrochemical energy storage applications.

Most of the discussed energy- and environmentally relevant applications are based on very complex adsorption phenomena. So far, these fundamental principles remain poorly understood. Therefore, some well-defined porous structures are used as model materials to achieve a better understanding of these fundamental adsorption processes on porous carbon surfaces. They are used for the investigation of the physicochemical interaction of electrolyte molecules and gas atoms with the carbon surface based on solid-state NMR spectroscopy experiments and the high-pressure adsorption of ^{129}Xe coupled with an *in-situ* NMR technique, respectively. Finally, the well-defined materials are characterized with a novel method based on their temperature increase during gas adsorption. These experiments allow for new insights into the materials structure and at the same time proof the high potential of this new tool for pore analysis.

2. State of the Art

2.1 Porous Carbon Materials

With ~180 ppm, carbon is only 17th in the list of terrestrial elements` frequency. It ranks after barium, strontium, or sulfur. The second-most frequent element, silicon, is 1300 times as abundant as carbon. Nevertheless, the 6th element in the periodic table of elements is among the most important and froms versatile chemical compounds. Carbon has the highest tendency to form chemical bonds with similar atoms of all chemical elements. Due to its position in the periodic table of elements it forms stable substances with more and less electronegative partners. In consequence, it is (with the exception of hydrogen) the element with the largest number of known chemical compounds. Millions of these compounds are subject of the organic chemistry but only a few element modifications and comparably simple structures are in focus of the inorganic chemistry and materials science. As carbon dioxide it is part of the carbon cycle with huge influence on the global climate and carbonates as well as carbides are among the most interesting classes of minerals.

Carbon allotropes provide a large variety of physical properties. In its transparent, wide band-gap semiconducting diamond modification, it is the hardest material on earth (microhardness > 100 GPa) and as intransparent, highly electrically conductive graphite it is one of the softest (microhardness ~1 GPa). Carbon surfaces can be chemically inert (basal planes of graphite) or active (edge planes of graphite). Due to these completely opposite properties, a large variety of mechanical, electrical, or chemical properties can be combined and this element is one of the most interesting topics in materials science.[1] As one obvious consequence, carbon is the only element that has a major monthly scientific journal named after it. The *Carbon* journal (published by Elsevier Science) exclusively publishes papers dealing with carbon and carbon-based materials. Moreover, a couple of books are dedicated to solely this element, its structure and potential applications.[1-3]

Especially carbon nanomaterials, with their structural units on a nanometer scale, are of outstanding importance for nanotechnology. Nanodiamonds, carbon whiskers, and carbon fibers are not only promising nanostructures for many applications but also display excellent tools for studying one- or two-dimensional phenomena. Graphene is a two-dimensional carbon nanomaterial consisting of a single graphite layer of sp^2 hybridized atoms.[4] The connected benzene rings form a planar honeycomb-type

arrangement of atoms with delocalized double bonds leading to extraordinary electrical conductivity and the highest tensile strength among all materials known so far. Graphene is also the central building block of a large variety of related carbon nanostructures. If a single layer is rolled, carbon nanotubes (CNTs)[5] are formed and if a specific number of the six-rings are replaced by five-rings, the layer is curved to fullerene cages, such as C_{60} (well-known as the "football molecule").[6] Another outstanding feature of graphene is its ultra-high specific surface area (SSA) of 2630 m^2/g, if both sides of the plane are considered. In consequence, it is also the basic building block of intrinsically porous carbon materials. These are, in most cases and from a structural viewpoint, nothing else than highly defective and disordered graphite. In contrast to other carbon nanomaterials with large external surface area, such as carbon nanotubes, fullerenes, or onion-like carbon (multi-shell fullerenes), porous carbons are characterized by a rather defective (amorphous) carbon microstructure and a much higher ratio between internal and external surface area.

Porous carbon materials provide a large SSA and thus a large contact area between carbon and the surrounding phase. These materials are crucial components in various fields, such as electrochemical energy storage, gas adsorption, and biomedicine. Besides a high SSA, these applications require the use of carbon materials with well-defined pore size and pore geometry to achieve optimum performance. Commercial porous carbon materials are relatively low by cost but exhibit wormlike or bottle-neck structured pores.[7, 8] The latter hinder efficient mass transport which limits their applicability in size-selective applications. This justifies the current attempts to tune the pore size of these materials on all levels from micropores (< 2 nm in diameter) to mesopores (2-50 nm) and macropores (> 50 nm).[9, 10]

Macropores and mesopores can be of inter-particular and intra-particular character. For instance, carbon materials with high intra-particular pore volume of more than 5 cm^3/g and SSA as high as 600 m^2/g can be obtained by carbonization of phenol/formaldehyde PolyHIPEs (see section 2.3.3).[11] Macroporous carbon aerogels are another class of open cell foams with high internal porosity (see section 2.3.4). They can be obtained by catalyzed cross-linking of molecular carbon precursors followed by supercritical drying and carbonization.[12] The arrangement and connectivity of the primary particles are influenced by the type of catalyst and the reaction conditions and therefore the final properties of the carbon aerogel can be precisely tuned. Moreover, hard-templating of

silica templates with different diameters is a useful concept to obtain well-defined macroporous carbons.[13] Per definition, a surface curvature is called a pore if its cavity is deeper than wide. However, this definition excludes many carbon nanomaterials with large SSA arising from inter-particular and external porosity, such as carbon nanotubes,[14] carbon onions,[15] or carbon nanoparticles.[16]

Well-defined mesoporous carbon materials can be prepared by the nanocasting procedure (see section 2.3.1) as reported by Ryoo and co-workers. Carbon precursors (e.g. sucrose) are infiltrated into the pore system of ordered mesoporous silica templates followed by carbonization and template removal (Figure 2). The pore structure can be precisely controlled by the infiltration and carbonization conditions or by the choice of the silica template. The resulting carbon materials are widely known as CMKs (Carbons Mesostructured by KAIST) and exhibit narrow mesopore size distributions in combination with SSAs of up to 2000 m^2/g.[17-20] Mesocellular carbon foams with larger disordered mesopores up to 24 nm in size can be obtained by nanocasting of mesocellular SiO_2 foam (MCF) templates with sucrose as the carbon source.[21]
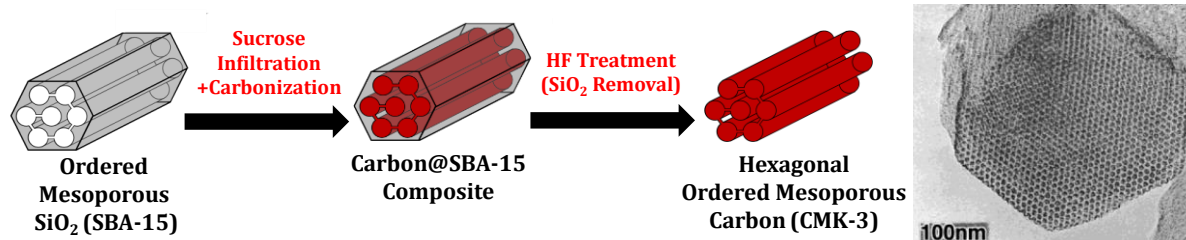
Figure 2. *Synthesis of CMK-3 and TEM micrograph showing the hexagonal ordered pore structure.[17]*

Ordered mesoporous carbon materials can be obtained by soft-templating (see section 2.3.2) as well. The endo-template-based synthesis reported by Zhao and co-workers uses the co-assembly of triblock co-polymers and resin followed by carbonization and *in-situ* template removal. Carbons with various pore geometries from hexagonal to cubic and lamellar structures can be obtained and the *in-situ* template removal during carbonization provides a significant advantage as compared to nanocasting.[22]

The large SSA of porous carbon materials is predominantly provided by micropores. One major class of microporous carbon materials are activated carbons (ACs).[23] Their industrial importance is revealed by the production of about half a million tons per year.[24] The most important feedstocks for these materials are carbon precursors, such

as coal, pitch, wood, and coconut shells. The macromolecular systems are then transferred to carbon products at temperatures > 500°C under inert conditions. These high temperatures cause the evolution of low molecular species due to the decomposition of the precursors. Although this process leads to the partial formation of micropores, the resulting carbon materials are most often characterized by moderate SSA. Additional activation procedures, associated with distinctive weight loss, are usually carried out with regard to introduce further pores, widen already existing pores, or to modify the surface properties. In general, two major processes for the introduction of porosity in ACs are established, denoted as physical and chemical activation.[25] All activation procedures differ in the fraction of pore sizes they create. Physical activation makes use of gaseous oxidation agents, such as carbon dioxide, steam, or air. In principle, carbon atoms are etched from the framework by the formation of carbon monoxide according to Equation 1 (carbon dioxide activation) and Equation 2 (steam activation).

$$(1+x)\ C_{(s)} + CO_{2(g)} \rightleftarrows 2\ CO_{(g)} + x\ C_{(s)} \tag{1}$$

$$(1+x)\ C_{(s)} + H_2O_{(g)} \rightleftarrows H_{2(g)} + CO_{(g)} + x\ C_{(s)} \tag{2}$$
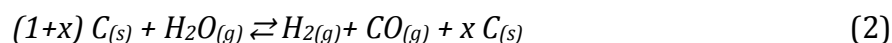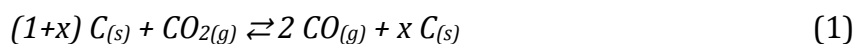
Steam activation is very sensitive towards the formation of narrow pores and has higher conversion rates compared to CO_2 activation because the molecule is smaller and diffuses more rapid into the entire carbon structure. Carbon dioxide oxidation is rather associated with the simultaneous growth of micro- and macropores. Activation with oxygen or air is highly exothermic and does not result in the formation of well-defined products. In contrast to physical methods, chemical activation[26] is based on the use of inorganic dehydration agents that inhibit the formation of carbon-containing by-products, such as methanol. Therefore, they lead to higher carbon yields. The most common activation agents are zinc chloride, potassium hydroxide, and phosphoric acid. The resulting ACs exhibit a relatively well-defined porosity compared to materials obtained from physical activation procedures. At the same time, they contain a larger amount of functional groups and additional synthesis steps (e.g. washing and drying) are necessary.

Besides the use of carbonized precursor materials, activation procedures are well-established for the implementation of micropores into carbon nanomaterials with larger pores and thus the synthesis of hierarchical materials. Carbon aerogels with large meso-

and macropores can be activated with carbon dioxide resulting in significantly increased SSA in excess of 3000 m^2/g.[12] The post-synthesis activation of ordered mesoporous carbon materials increases their porosity and thus also their performance in electrochemical energy storage applications.[27] However, neither chemical nor physical activation procedures form very narrowly distributed pores. For applications where a well-defined microporosity is required, other synthesis strategies, such as templating have to be applied.[28, 29] The use of zeolites as templates is a highly attractive way to produce carbon materials with monomodal and highly ordered micropores coupled with extremely high SSA of up to 4000 m^2/g.[28, 30] Another very useful approach for the generation of micropores apart from classical templating strategies is the carbide-derived carbon (CDC) method.[31]

2.2 Carbides and Microporous Carbide-Derived Carbons (CDCs)

This chapter will focus on the synthesis of CDC materials as well as on their structure and applications. As they are the precursors for CDC carbons, the structure and synthesis of metal or semi-metal carbides will be discussed prior to the carbon materials.

2.2.1 Structure of Metal Carbides

Carbides are chemical compounds that are formed by carbon and more electropositive atoms like metals or the semi-metals boron and silicon.[32, 33] Three classes of carbides can be distinguished. Salt-like carbides (also referred to as ionic carbides) are formed with the electropositive metals and are highly sensitive towards hydrolysis. They are built up by metal cations and the anionic carbon units "C^{4-}", "C_2^{2-}", and "C_3^{4-}". In accordance to their hydrolysis products, the corresponding salt-like carbides are denoted as methanides (e.g. Al_4C_3, Be_2C, or Mg_2C), acetylides (Na_2C_2, CaC_2, or LaC_2), and allylenides (Li_4C_3 or Mg_2C_3).[34] Metallic carbides (also referred to as interstitial carbides) are compounds with transition metals, such as titanium or zirconium. Carbon atoms are inserted into the octahedral interstices in a close packed metal lattice (Figure 3).[32, 35] The radius of the metal atoms must be larger than approximately 135 pm because the ratio $d_{\text{Carbon Atoms}}/d_{\text{Metal Atoms}}$ must not exceed a value of 0.59 to make incorporation of carbon possible. The metallic properties are intact in presence of carbon and therefore metallic carbides are electrically conductive. They are refractory and therefore useful as

metal coatings in cutting tools.[36] If the atom radius is smaller than the critical value, the formation of carbides is still possible but with rather complex structures. The third class are the so-called covalent carbides of silicon (SiC) and boron (B$_4$C). Due to the strong covalent bonds present in these compounds, they stand out by extremely high hardness, good heat conductivity, as well as chemical and thermal stability.[33, 37] Silicon carbide crystallizes in a cubic modification (β-SiC) or rhombohedral/hexagonal polytypes (α-SiC). The structure of the cubic modification is correlated to the diamond structure as every second carbon atom is replaced by a silicon atom resulting in a zinc blende structure (Figure 3).[33] The α-SiC modification is stable above 1800°C and the cubic structure is present at lower temperatures. Silicon carbide is widely applied in abrasive machining and cutting tools, as heating element, in steel production, and in electric devices. Its high natural resistance against oxidation qualifies SiC as an advanced catalyst support for oxidation reactions at high temperatures. Comparable to other non-oxide ceramics which are not in thermodynamic equilibrium in air,[38] silicon carbide forms a SiO$_2$ passivation layer on its surface. Even at temperatures as high as 1600°C this layer stays thin because of the low oxygen diffusion coefficient in the SiO$_2$. Hence, these materials are stable against oxidation even at very high temperatures.[35]
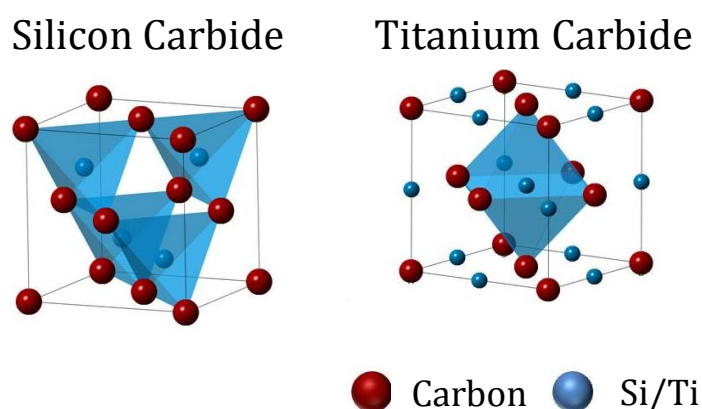
Figure 3. *Crystal structures of titanium carbide and silicon carbide (atom sizes are not true to scale).[35]*

2.2.2 Synthesis of Silicon- and Titanium Carbides

Classical Approaches

Metal carbides can be produced by either chemical (CVD) or physical vapor deposition (PVD) of metal containing precursors according to Equation 3 and Equation 4, respectively.[39]

$$TiCl_{4(g)} + CH_{4(g)} \rightarrow TiC_{(s)} + 4\ HCl_{(g)} \tag{3}$$

$$Ti_{(s)} + CH_{4(g)} \rightarrow TiC_{(s)} + 2\ H_{2(g)} \qquad (4)$$
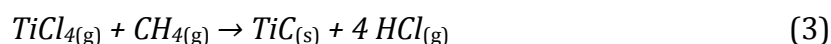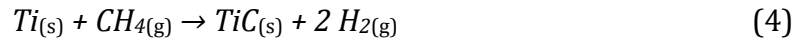
Furthermore, the synthesis of silicon carbide is possible by thermal decomposition of trichlorosilane according to Equation 5.[34]

$$CH_3SiCl_{3(g)} \rightarrow SiC_{(s)} + 3\ HCl_{(g)} \qquad (5)$$
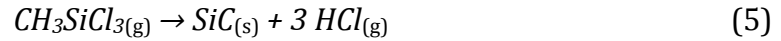
While the direct synthesis from the elements is possible for a number of carbides, carbothermal reduction of the metal oxides is the most established method for the synthesis of these materials on a large scale.[40] Especially for silicon carbide this reaction is highly endothermic and therefore very large temperatures are required for the industrial production of this material by the so-called Acheson-process according to Equation 6.[41]

$$SiO_{2(g)} + 3\ C_{(s)} \rightarrow SiC_{(s)} + 2\ CO_{(g)} \qquad (6)$$
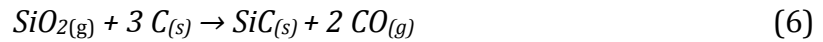
At ambient pressure, the free Gibbs energy of the overall reduction reaction becomes negative at about 1520°C. In consequence, high temperatures are required to achieve reasonable conversion rates.[40] The mechanism of SiC formation is based on the intermediate formation of a gaseous SiO species, i.e. the texture of the resulting carbide follows the distribution of the carbon phase in the raw material.

The carbothermal reduction of TiO_2 to titanium carbide is based on a different mechanism.[42] While the overall reaction is similar, the formation of the gaseous TiO species is too slow. Therefore, the carbothermal reduction is based on the CO/CO_2 system according to Equation 7.

$$TiO_{2(s)} + CO_{(g)} \rightarrow TiO_{(s)} + CO_{2(g)} \qquad (7)$$
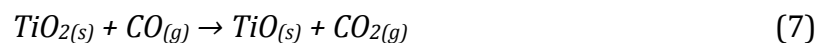
In this way, CO successively exchanges oxygen to carbon in the TiO_2 and the formed CO_2 is regenerated at the carbon domains. In contrast to the carbothermal reduction of SiO_2, the TiC grows into the TiO_2 domains and not into the carbon.[43] Another difference is the lower temperature of approximately 1300°C which is necessary for complete carbothermal reduction of TiO_2.[44]

Precursor-Derived Ceramics

Many of the CDC materials discussed within this thesis are synthesized from carbides which are not obtained by the classical carbothermal reduction approach. These porous

carbides are synthesized from polymeric precursors. Due to the rapid development of the organoelement chemistry in the last years, a large variety of these compounds is available. Ceramics obtained from such polymeric precursors are denoted as precursor-derived ceramics (PDCs).[36, 45] The synthesis of PDCs is a multi-step process which starts with the formation of the non-volatile precursor polymer from organic monomer units. Then, the polymer is formed into the desired shape of the final product which can be one-, two-, or three-dimensional. Afterwards, the network is transformed into the amorphous covalent ceramic, typically by thermal decomposition (pyrolysis) under inert atmosphere. Finally, it is crystallized into the thermodynamically stable phase at high temperatures. The major advantage of this route compared to the carbothermal reduction approach is the fact that the polymeric precursor already contains the chemical information (i.e. metal-carbon bonds) of the desired product in its backbone. In consequence, the temperatures for the formation of a carbide phase are significantly lower. Furthermore, the molecular character of the polymers enables the precise adjustment of the structure and properties of the final ceramic. Hence, more complex shapes can be obtained compared to the carbothermal reduction approach.[35]
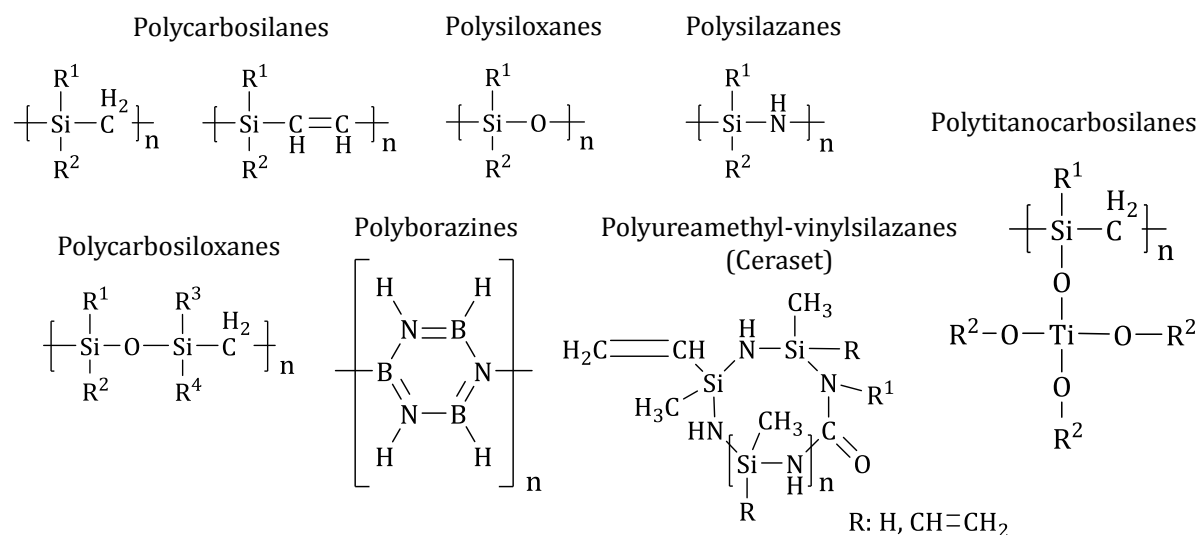
Figure 4. *Structure of selected precursor polymers for the synthesis of PDCs.*

Most of the PDCs described so far are based on silicon-containing polymers, such as polycarbosilanes, polysiloxanes, polysilazines, or polycarbosiloxanes. Other metals can be introduced into the ceramics by using polyborazines, polytitanocarbosilanes, or polyaluminocarbosilanes (Figure 4).[36]

Another significant advantage of the PDC route is the comparably high ceramic yield of 75-85% as the carbon/metal stoichiometry of the polymers is close to the desired product and hydrogen is the primary gas evolved during pyrolysis. The emission of gaseous silicon- or carbon species can be kept at a minimum if proper control is taken over the thermal decomposition process.

Preparation and Chemistry of (Allylhydrido)Polycarbosilanes

The CDC precursor carbides discussed in this thesis are produced from polycarbosilanes. They are a family of polymers characterized by a molecular configuration with carbon and silicon atoms covalently bond to one another in alternating fashion in the primary chain segments.[46] Typically, these methylene-linked silicon segments are highly branched with little cyclization.[47] The direct bonding of silicon and carbon facilitates the formation of near-stoichiometric silicon carbide during pyrolysis.
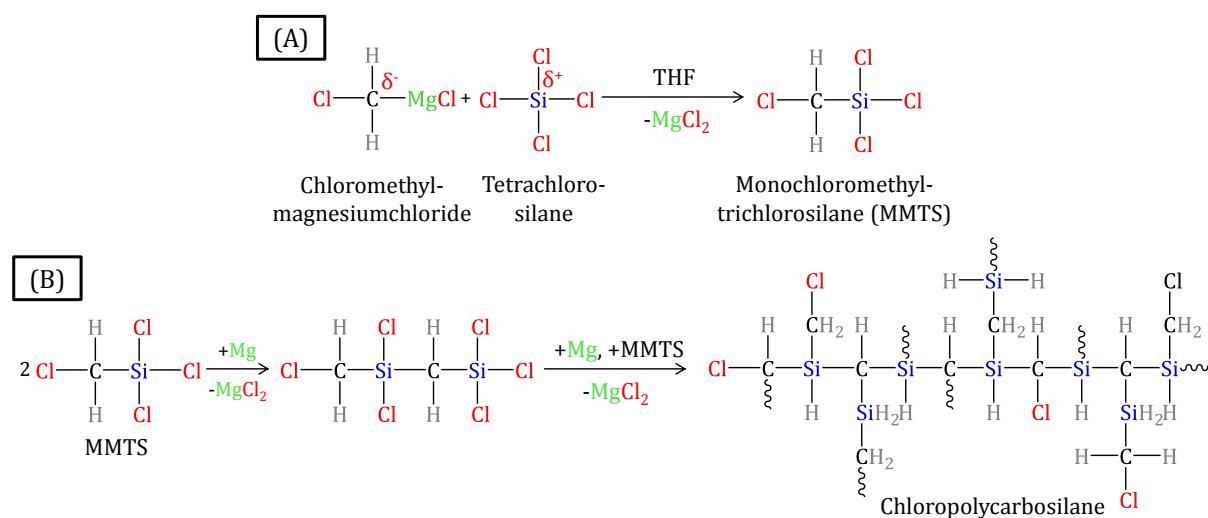
Figure 5. *Synthesis of the monochloromethyltrichlorosilane (MMTS) (A) and chain growth mechanism towards chloropolycarbosilane (B) by the Grignard reaction.*

Grignard synthesis is the most common approach to directly link carbon atoms to silicon.[48] Grignard agents are halogen-organometallic compounds or -segments which couple to other molecules containing halogen in the end-segment. The reaction between the family of magnesium chloromethanes and chlorosilanes is of special interest for the synthesis of polycarbosilanes. The product of the reaction is a monochloro-methyltrichlorosilane (MMTS) and ionically bonded $MgCl_2$ is removed (Figure 5(A)). MMTS is the primary reactive monomer that finally forms polycarbosilanes by

continued Grignard reaction (Figure 5(B)). Di- and tri-chlorinated versions of the methyl- and silyl reactants can also be used in the reaction mixture. This allows control over nature, frequency, content, and length of branching throughout the growing polymer molecule. The resulting chloropolycarbosilane has to undergo a treatment with an appropriate reducing agent (e.g. CaH_2 or $LiAlH_4$) to replace the chlorine atoms against hydrogen.

Within this thesis, one polycarbosilane is used for the synthesis of porous carbides. The allylhydridopolycarbosilane[49] SMP-10 (purchased by Starfire Systems) contains unsaturated allyl side groups, which are probably incorporated into the chloropolycarbosilane prior to the replacement of the chloride groups. Although the actual procedures for the synthesis and the structure of SMP-10 are kept confidential by the manufacturer, it is known that the polymer contains about 15-20% allylic substitution leading to its liquid appearance at ambient conditions. However, the polycarbosilane is not excessively allylated and the carbon/silicon molar ratio is still rather close to one as compared to other polycarbosilanes, e.g. those with large content of methyl side groups.
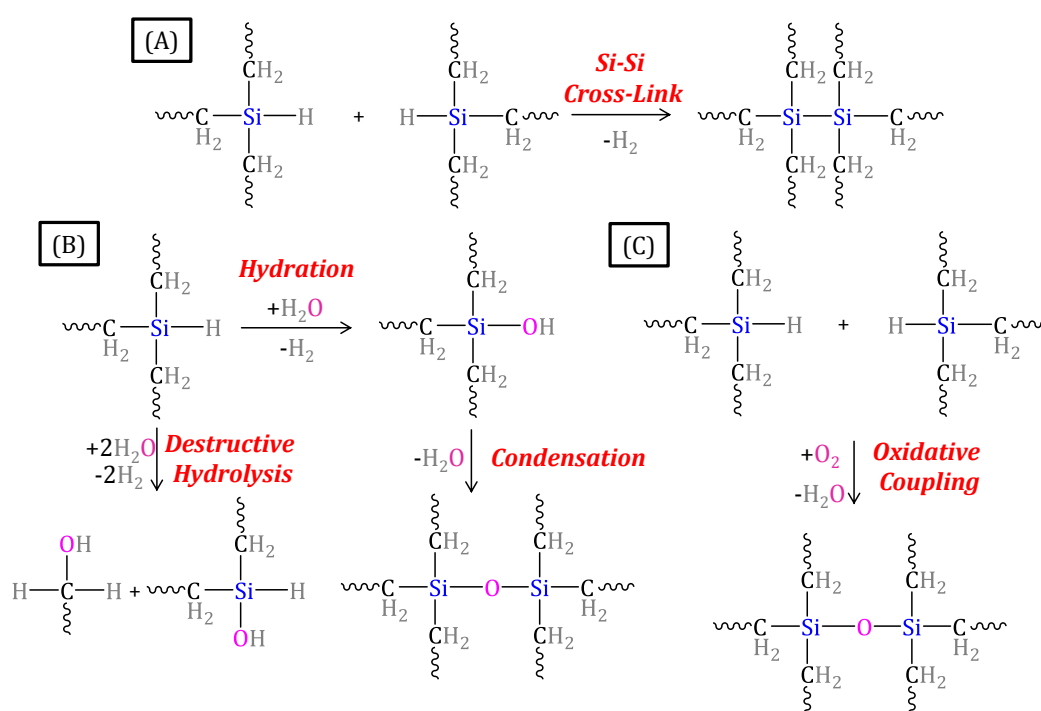
Figure 6. *Potential reactions of SMP-10 with itself (A), water/moisture (B), and air/oxygen (C).*

The liquid state of SMP-10 is accompanied with a couple of advantages for the synthesis of silicon carbide materials as it can be cast on various substrates. Furthermore, it can be

functionalized and cross-linked at the functional groups.[50] Hydrogen atoms attached to silicon are chemically not similar to those bonded to carbon atoms because the Si-H bond is weaker and hence more reactive. All Si-H containing compounds are able to spontaneously generate hydrogen, are hygroscopic, and react with environmental oxygen (Figure 6). Hence, they can potentially undergo undesired sidereactions even before their thermal decomposition to silicon carbide and these could have negative influence on the finally obtained ceramic (e.g. excessive oxygen content).
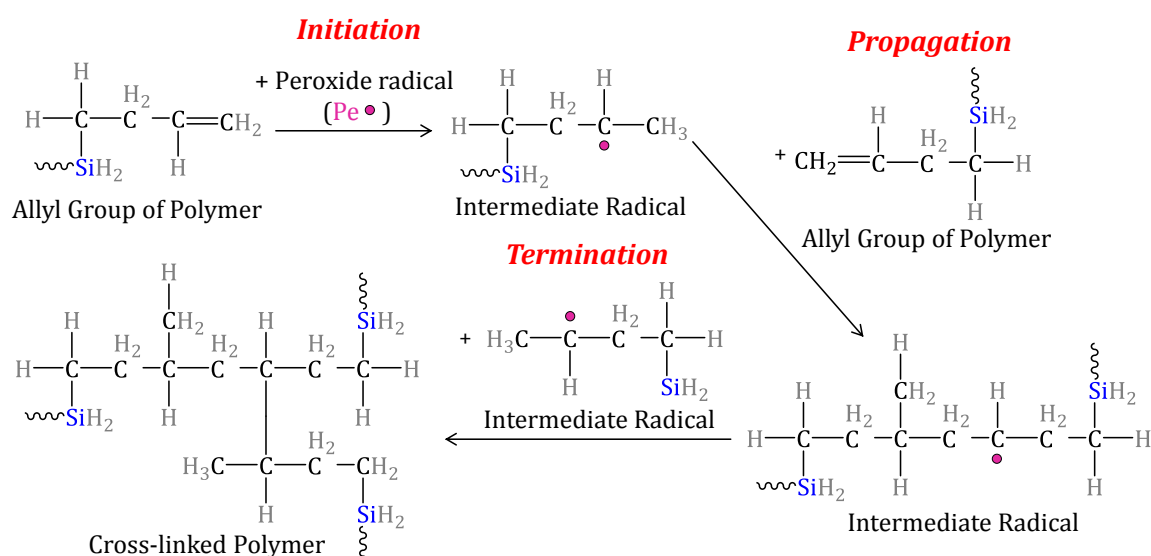
Figure 7. Potential cross-linking mechanism of SMP-10 through the allyl groups initialized by peroxide radicals.

Typically, the conversion of SMP-10 to the SiC ceramic includes the curing/cross-linking of the polymer to a solid "green-body" and pyrolysis into the ceramic.[51] The first step can be performed in different ways. If the polymer is subjected to intermediate temperatures above ~200°C, some of the allyl groups can break down to free radicals. Cross-linking of the polymer takes off spontaneously through the chain reaction of the allyl groups. Alternatively, cross-linking can be initialized by generation of free radicals by a peroxide species at much lower temperatures (Figure 7). The cross-linking can potentially be enhanced by use of allyl- or vinyl-containing organic monomers.[50] Efficient cross-linking can also be achieved by a hydrosilylation mechanism (see section 2.3.4). During pyrolysis, the cured SMP-10 polymer is subjected to higher and higher temperatures leading to the removal of the hydrogen atoms and the formation of an amorphous, glassy form of SiC with a high ceramic yield of 72-78%. At temperatures above 1250°C, crystallization of the cubic β-SiC phase begins.[52]

2.2.3 Synthesis of CDCs

Historical Perspective

High-temperature chlorine treatment of silicon carbide according to Equation 8 was patented in 1918 by Otis Hutchins as a method for the production of $SiCl_4$.[53]

$$SiC_{(s)} + 2\ Cl_{2(g)} \rightarrow SiCl_{4(g)} + C_{(s)} \tag{8}$$
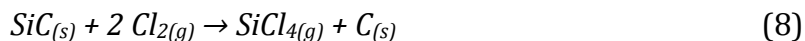
This process was widely used for the production of $SiCl_4$ before pure silicon became abundantly available due to the growth of the semiconductor industry. While the desired product of this conversion ($SiCl_4$ vapor) was collected in a condenser, the remaining carbide-derived carbon was disposed. Initially, CDC was regarded as an undesired by-product, but later it was realized that it was a new class of amorphous carbon. The term "mineral carbon" was introduced according to the absence of hydrocarbon species as commonly present in activated carbons and to distinguish CDCs from carbons based on organic precursors.[54] The observation of carbon nanotube growth[55] and graphene formation[56] during thermal decomposition of silicon carbide were two early milestones in CDC synthesis.

While nowadays the production of $SiCl_4$ is carried out by chlorination of pure silicon, CDCs have received considerable attention because the use of different synthesis conditions and carbide precursors provides the possibility to precisely tailor the pore structure of these carbon materials. CDCs have developed from an undesired by-product of $SiCl_4$ synthesis to a solution in applications where a tailored pore structure is required.[31] Due to the wide variety of available carbide precursors,[35] carbon materials with different shapes and textures (e.g. monoliths,[57, 58] foams,[59, 60] biomorphic structures,[61, 62] powders/nanopowders,[16, 63] fibers,[64, 65] and thin films[66, 67]) can be designed. CDCs show high potential in applications such as catalysis,[59, 68, 69] gas storage/gas separation,[70, 71] batteries,[72, 73] electrochemical double-layer capacitors,[10, 74] linear actuators,[75] the adsorption of biomolecules,[76-78] and the capacitive deionization of water.[79, 80]

CDC Synthesis Procedure

Whenever a carbon material is produced from a metal carbide precursor, it is designated as carbide-derived carbon. These transformations can be achieved by physical (e.g. thermal decomposition)[81] or chemical (e.g. high-temperature halogenation)[82] processes. Electrochemical etching of layered carbides (e.g. Ti_3AlC_2, Ti_2AlC, or Ti_3SiC) is a very

novel method for CDC synthesis at room temperature.[83] However, halogenation of carbides at elevated temperatures is the most important technique for CDC synthesis due to the precisely controllable porosity and carbon microstructure. In recent years, CDC materials have been synthesized from a wide range of binary carbides like B_4C, SiC, TiC, VC, WC, ZrC but also from ternary carbides like Ti_3AlC_2, Ti_3SiC_2 or carbonitrides according to the general Equation 9.[31]

$$x\ MC_{(s)} + y/2\ X_{2(g)} \rightarrow M_xX_{y(g)} + x\ C_{(s)} \tag{9}$$
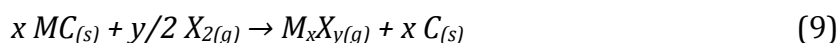
MC is a metal (M) carbide (C) and X is a gaseous halogen (F_2, Cl_2, Br_2, I_2 or mixtures of them) or a halogenated compound (HCl or HF) and M_xX_y a volatile metal halogenide.[84] While fluorination with F_2, CoF_3 or XeF_2 has the drawback to produce mostly highly fluorinated carbons at comparably low temperature,[85, 86] the formation of CDC can also be achieved using Br_2 or I_2 as the halogenation agent.[31] However, high-temperature etching of carbides using chlorine gas is the most common technique for CDC synthesis due to the low price and relatively easy handling compared to other halogens.

CDCs obtained by chlorine treatment of carbides are often generalized as amorphous or highly disordered porous carbon. However, transmission electron microscopy (TEM) studies have identified the presence of a large variety of carbon structures, including nanotubes, fullerene-like structures, carbon onions, nanocrystalline diamond, graphitic ribbons, and even nano-needles in addition to the commonly obtained amorphous carbons and graphite-like structures (Figure 8).[31]
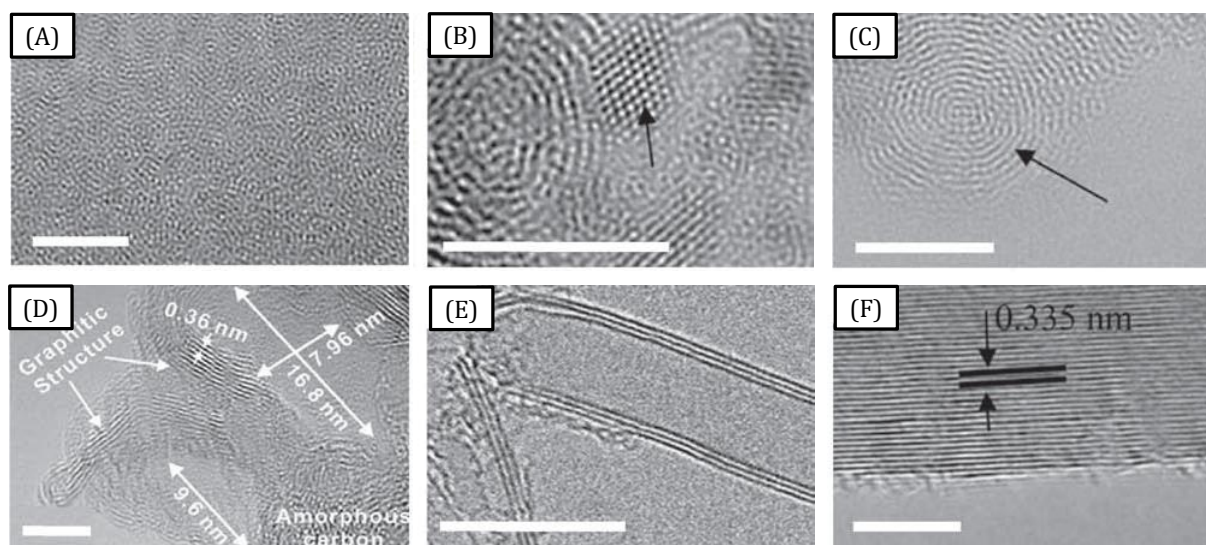
Figure 8. TEM images of various CDC structures (scale bar is 5 nm): disordered porous carbon (A), nano-diamond (B), onion-like carbon (C), mesoporous carbon (D), carbon nanotubes (E), and graphite (F).[31, 84]

From a thermodynamic point of view, the formation of undesired side-products, such as volatile CCl_4 has to be considered. This molecule is particularly favored at low temperatures and may form instead of solid carbon.[87] The optimum temperature range (Range III in Figure 9(A)) for the formation of CDC as the only stable carbon-containing reaction product, the avoidance of by-products, and an optimal yield is strongly dependent on the chlorine-to-carbide ratio (Figure 9(A)).
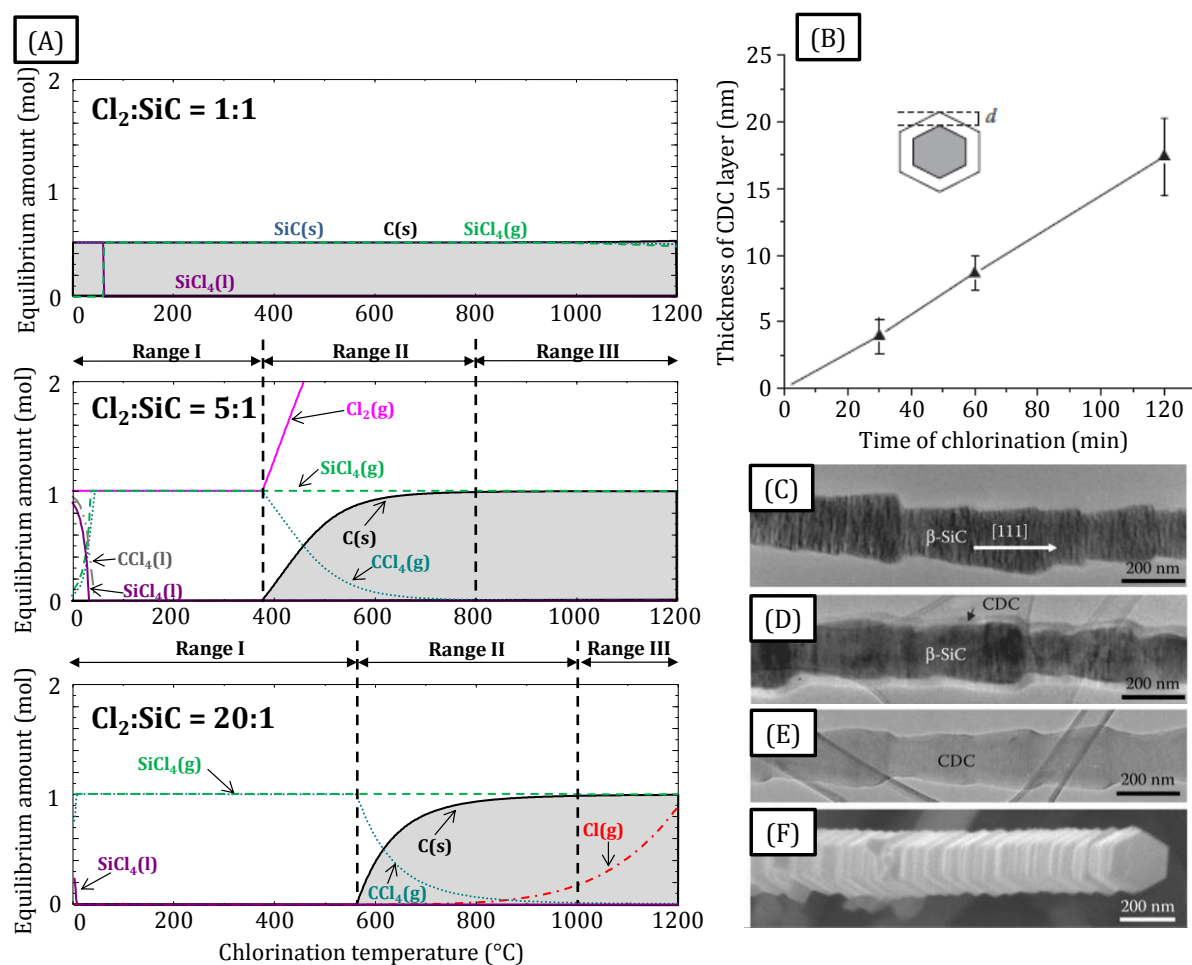
Figure 9. *Thermodynamic calculations for the reaction of Cl_2 with SiC in different molar ratios (A) and thickness over time of the CDC coating of during chlorine treatment of SiC at 700°C (B). TEM micrographs of a β-SiC whisker (C), β-SiC whisker with CDC coating (D), the whisker completely transformed to CDC (E), and SEM micrograph of the chlorinated whisker (F) showing the conformal transformation.*[31, 84]

Regarding the kinetics of carbide halogenation, a linear increase of the porous CDC layer thickness takes place up to a certain width and time. This indicates that the transformation rate is under reaction control (Figure 9(B)).[88] For longer halogenation times and thicker layers, the linear kinetics can be replaced by a linear-parabolic growth behavior indicating the onset of a diffusion-controlled mechanism.[89] At higher temperatures, the area of linear growth of the CDC layer is larger, i.e. the parabolic

growth starts at the presence of thicker CDC layers. Furthermore, the dimension of the carbide precursor significantly influences the reaction rate as densely packed and thick carbide particles require longer etching times compared to thin films or nanoparticles.[31]

It is characteristic for the CDC synthesis that the dimensions, shape and volume of the carbide precursor are maintained along the chemical transformation and it is therefore referred to as a conformal process. One of the most prominent examples of this phenomenon is the transformation of β-SiC whiskers to CDC.[90] After the linear growth of a thin film of CDC on the surface of the ceramic, the whole precursor is finally converted to CDC under full conservation of the original shape of the whisker (Figure 9(C-F)).

A significant difference between CDCs and porous carbons obtained by physical or chemical activation is their comparably low amount of oxygen-containing surface functional groups due to the production in oxygen-free atmosphere. Altough some so-called "dangling bonds" are saturated with oxygen if the material is exposed to air (especially for synthesis temperatures below 1000°C),[91] the CDC surface is of a relatively hydrophobic nature.[92] Significant amounts of chlorine and metal chlorides are captured in the pores of CDCs after synthesis and have to be annealed in order to open blocked pores and to increase the purity.[93] This treatment is carried out at a temperature equal or lower compared to the chlorine treatment because it must not negatively influence the pore structure of the carbons. The most efficient annealing procedures take place under reductive conditions (ammonia or hydrogen flow). In contrast, non-reactive argon shows only limited potential for the removal of residual chlorine.[94]

2.2.4 Pore Structure of CDCs

The general advantage of the CDC route compared to other synthesis methods for carbons is the precise control over the pore size distribution (PSD) by different synthesis parameters. The micropore structure of CDCs depends to a large degree on the elevated synthesis temperature. Higher temperatures favor the mobility of carbon atoms leading to self-organization processes and the preferred formation of larger graphene fringes and multi-walled structures. In contrast, rather narrow pores are obtained at low synthesis temperatures.[87, 95-98] Therefore, the SSAs of many CDCs follow a bell-like temperature dependency with a maximum often in the range of 800-1000°C.[99]

Besides the temperature, the carbon distribution within the carbide precursor strongly dictates the CDC pore size. Carbons derived from carbides with NaCl structure and therefore a uniform first neighbor distribution (e.g. TiC or ZrC) show a rather narrow PSD compared to rhombohedral (e.g. B_4C), orthorhombic (e.g. Mo_2C), or ternary (e.g. Ti_3SiC_2) carbide precursors. If the ternary carbide Ti_3SiC_2 and the binary carbide 3C-SiC are used as precursors, CDCs with different porosities are obtained (Figure 10). The material from the binary carbide shows a narrow pore size distribution. The ternary carbide has a layered distribution of carbon atoms and the corresponding CDC therefore contains a significant amount of mesopores and has higher bulk porosity. Ti_3SiC_2-CDCs also show significant graphitization in contrast to SiC-CDCs.[31]
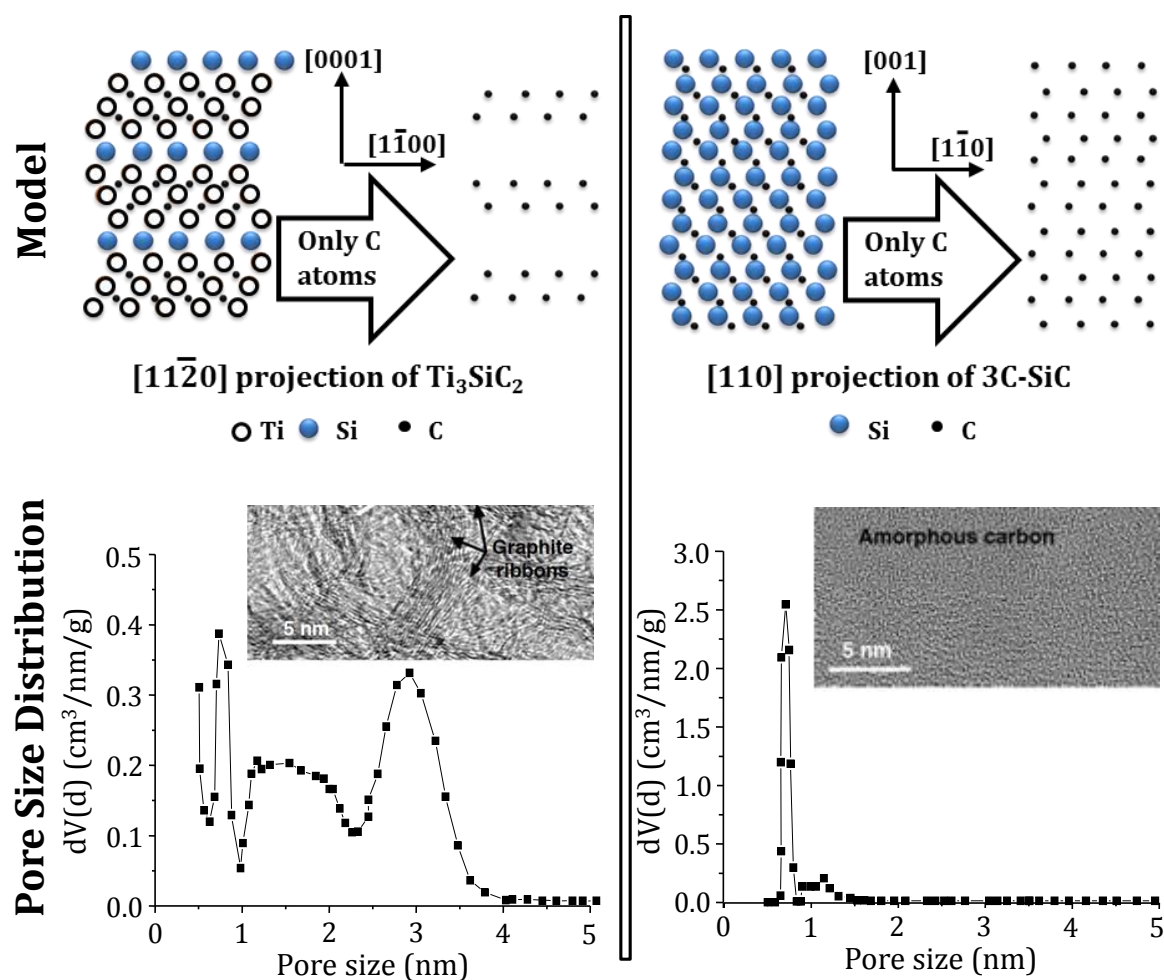
Figure 10. Dependence of the carbide precursor on porosity and nanostructure of the corresponding carbide-derived carbons.[31]

Besides the synthesis temperature and the carbide structure, the PSD of CDCs can be influenced by the presence of additional phases in the precursor which are removable

by the chlorine treatment. For instance, the use of mixtures of TiC and TiO_2 instead of pure TiC increases the pore size from 0.6-0.7 nm for CDC obtained by etching of pure TiC to 0.8 nm for CDC produced from the carbide/oxide mixture due to a partial carbon oxidation.[100] The insertion of μm-sized macropore channels into CDCs can be achieved if a free metal phase is present in a mechanically mixed Si/SiC precursor system.[101]

Chemical (based on KOH, $ZnCl_2$ or H_3PO_4) or physical (based on steam, carbon dioxide or air) post-synthesis activation procedures after the chlorine treatment can be used to further increase the SSA of CDCs.[102-104] Treatments in CO_2 and KOH significantly increase the porosity of the CDCs, while sufficient control over the pore size remains achievable.[105, 106] However, these procedures are associated with a large material burn-off during oxidation and the advantage of the higher porosity should always be critically questioned. In contrast, vacuum annealing of CDCs does not cause sample loss or surface modification and therefore provides a suitable alternative for further enhancing the porosity of CDCs.[92]

2.3 Templated Carbides and CDCs

In recent years, a large variety of templating methods was developed for the implementation of a secondary pore system in addition to the CDC micropores. These efforts are made to achieve enhanced materials transport properties which are crucial in many applications and are often unachieved by purely microporous materials, such as most CDCs.[9] With regard to establish a secondary pore system of meso- or macropores, a porous carbide material needs to be synthesized into which the micropores are inserted during the high-temperature chlorine treatment. Different templating approaches for that purpose along with the resulting carbides and CDCs will be introduced within this chapter.

2.3.1 Hard-Templating Approaches

The hard-templating concept is also referred to as "nanocasting" because it is comparable to a casting process performed on the nanoscale.[107] A solid-state template acts as a space confinement into which a precursor is infiltrated and transferred to the desired product. The structure of the template dictates the structure of the finally obtained material as the latter is an inverse replica of the void space present in the

template. One can distinguish between exo-[108] and endotemplates[109] where the precursor is filled into the internal- and external porosity, respectively (Figure 11).
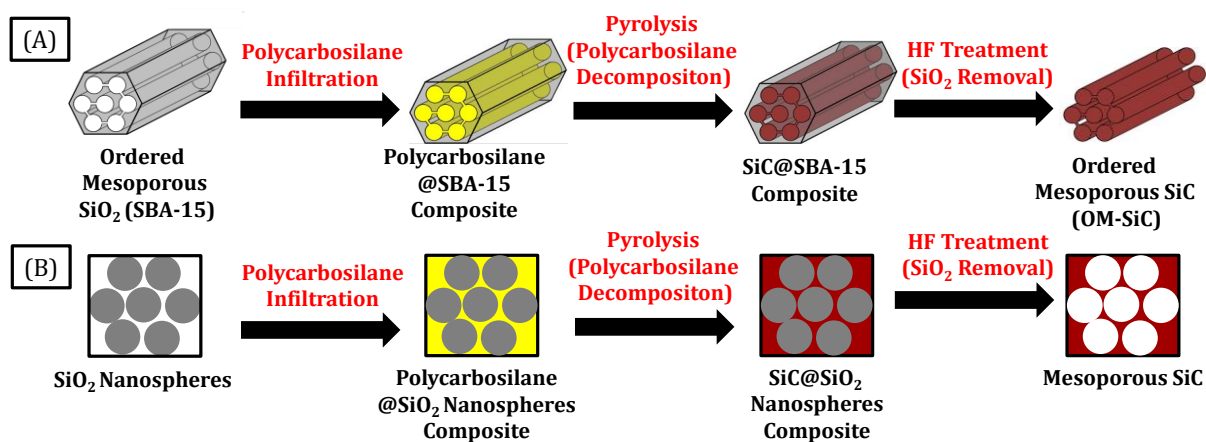
Figure 11. *Synthesis of porous SiC materials by nanocasting of SiO$_2$ exotemplates (A) and endotemplates (B).*

While classical hard-templates (e.g. silica or carbon) are removed after thermal conversion of the precursor,[110, 111] sacrificial templates are decomposed *in-situ* during pyrolysis.[112] In case of silica, the removal of the template is mainly conducted by dissolution in hydrofluoric acid or sodium hydroxide solution. Carbon templates can be removed by oxidation in air or by reduction in ammonia at high temperatures. Thus, materials obtained by the nanocasting route have to withstand relatively harsh conditions.[35] If the template exhibits a periodic regular structure that is conserved during the nanocasting procedure, the corresponding replica materials can be ordered as well. Ordered mesoporous carbons (OMCs) or ordered mesoporous silicas (OMS) are commonly used as the templates but a wide variety of disordered materials, such as activated carbons,[113] silica nanospheres,[109] or silica monoliths[114] are also well established.

In terms of pore geometry, ordered mesoporous materials are subdivided into two-dimensional hexagonal (e.g. CMK-3[17] or SBA-15[115]) and three-dimensional cubic ordering (e.g. KIT-6[116] or CMK-1[18]). The silica templates exhibit micropore connections between the mesopore channels that are filled with precursor and thus stabilize the structure during the replication process. Without these connections, the replica structure would be disordered or at least symmetry degradation could occur.[108]

It can be challenging to precisely replicate the template structure due to the volatility of the precursors or their decomposition products and due to potentially high volume shrinkage during pyrolysis.[35] Therefore, complete and homogeneous infiltration of the

template with precursor is very important for successful nanocasting. As many precursors are solids, they have to be dissolved in appropriate solvents or must be melted to enable their diffusion into the template pores. If the precursor is a liquid, it can be infiltrated directly. Especially when exotemplates are used, the so-called "incipient wetness method" is very efficient. In this technique, the amount of infiltrated precursor liquid is chosen equal to the total pore volume of the template. As volume shrinkage during pyrolysis can largely inhibit the successful replication of the template structure, it is essential for a suitable precursor that it undergoes as little shrinkage as possible during the conversion to the desired product. Furthermore, precursors which are not volatile under the reaction conditions should be used to avoid migration out of the template structure during pyrolysis.[35] These circumstances indicate that the number of potential precursors for the formation of carbide materials is very limited.

Ordered mesoporous silicon carbide materials (OM-SiCs) can be obtained if polycarbosilane polymers are used as the precursors. Hexagonal and cubic ordered structures with SSAs close to 1000 m^2/g can be obtained by using SBA-15 and KIT-6 as the template, respectively. The variation of the infiltration- and pyrolysis conditions further enables to tune the nanoarchitecture of OM-SiCs between tubular and rod-like geometry.[108]
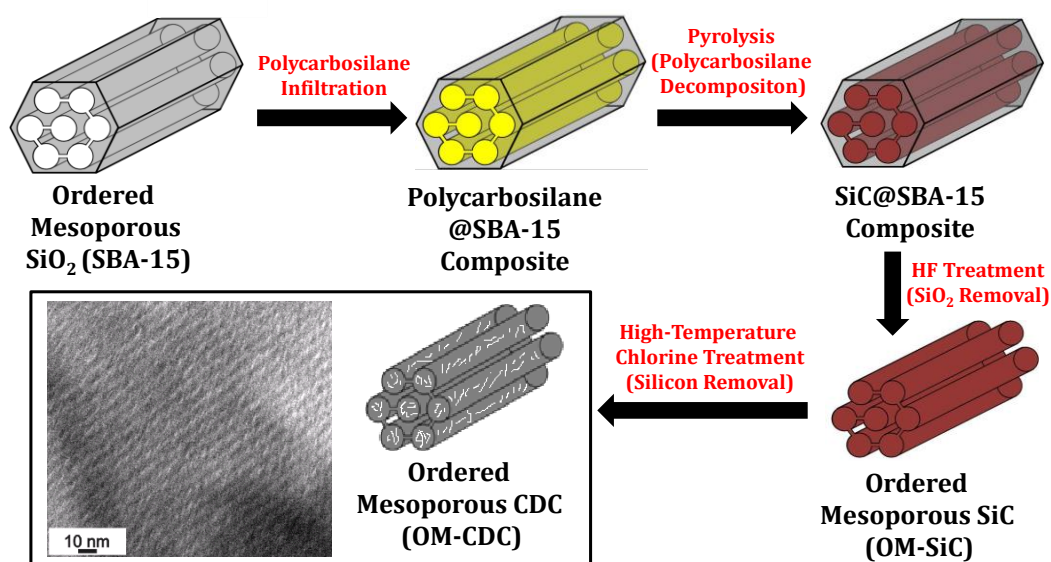
Figure 12. *Preparation OM-SiC-CDC with hexagonal pore structure by nanocasting and high-temperature chlorine treatment as well as TEM micrograph showing the mesoscopic ordering.[117]*

If the OM-SiC material is subjected to high-temperature chlorine treatment, the silicon atoms are removed leading to the formation of micropores within the produced CDC

nanorods. Due to the conformal carbide-to-carbon transformation, the ordered mesopore structure of the precursor is maintained (Figure 12). The resulting OM-SiC-CDCs reach SSAs close to 3000 m^2/g and total micro-mesopore volumes of up to 2 cm^3/g. The mesopore geometry and structure can be adjusted by the symmetry of the SiO$_2$ template, the functionalities of the polycarbosilane, the infiltration/pyrolysis conditions, and the temperature of the chlorine treatment.[70, 117, 118]

OM-SiC-CDCs show outstanding performance in various applications, such as the storage of hydrogen (52.2 mg/g (excess) at -196°C and 40 bar), methane (220 mg/g (excess) at 25°C and 100 bar), and n-butane (870 mg/g (dynamic flow) at 25°C and 80 vol.% n-butane in nitrogen).[118] In the capacitive deionization of water, OM-SiC-CDC shows very high gravimetric capacities of 15.0 mg$_{NaCl}$/g$_{CDC}$ which are significantly beyond those reported for other porous carbon materials.[79] Both, cubic[73] and hexagonal[72] ordered mesoporous SiC-CDCs are highly attractive candidates to host the active material in lithium-sulfur (Li-S) battery cathodes (see section 2.4.2), show good performance as electrode materials in EDLCs (see section 2.4.1), and provide good catalytic activity in the decomposition of methane for hydrogen production.[119]

It is worth to note that OM-SiC-CDCs do not solely show outstanding performances in a large variety of applications but also act as suitable model system for sufficient understanding of fundamental phenomena in porous carbon materials. Their well-defined pore architecture including narrowly distributed and directly connected micro- and mesopores in combination with the high purity allows to deeply investigate adsorptive phenomena and to get information about the structure and influence of the hierarchical pore architecture. In one recent example, preadsorption of n-nonane prior to physisorption of nitrogen at a temperature of -196°C is used to selectively block the micropores and to clearly distinguish their contribution to gas adsorption form the mesopore system.[120]

2.3.2 Soft-Templating Approaches

In contrast to nanocasting, the pore structure of the desired ceramic is dictated by soluble structure-directing agents (SDAs) in soft-templating approaches.[121] This strategy is highly efficient for the introduction of well-defined porosity into ceramics but a more sophisticated adjustment of the template molecular assembly and the precursor chemistry is necessary. The amphiphilic SDA molecules which are most often cationic,

anionic, or non-ionic amphiphilic surfactants self-assemble due to the interplay of mostly weak (e.g. van-der-Waals forces and Coulomb interactions), non-covalent, attractive, and repulsive forces. The resulting structures (e.g. micelles or liquid crystals) are used as templates for the desired ceramics.[35] The latter are obtained by pyrolysis of precursor molecules that self-assemble around the SDAs. As the nanocasting strategy, the soft-templating approach enables the synthesis of ordered mesoporous materials. The first example is the well-known hexagonal ordered silica MCM-41 which was developed in the early 1990s by the researchers of Mobile.[122] Soft-templating approaches require compatibility between the SDA and the ceramic precursor to avoid phase separation that would not lead to the formation of an ordered structure. The formation of the preceramic precursor system can occur by self-assembly of SDA molecules which contain the precursor molecules covalently bonded. Alternatively, the SDA and the organic precursor are used separately a co-assemble if both are compatible with each other (Figure 13).
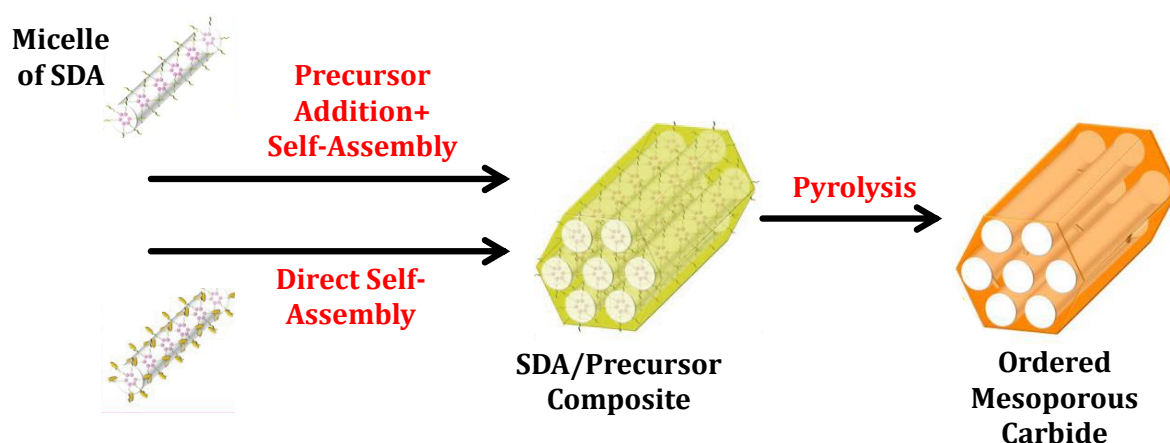
Figure 13. Soft-templating mechanisms for the synthesis of ordered mesoporous carbides.[35]

In both pathways, the precursor molecules are then cross-linked and subsequently transferred to the desired ceramic. Simultaneously, the organic SDA is decomposed and forms an ordered pore network. The latter technique can either be used in aqueous solution, as known for the synthesis of OMS, or as the so-called evaporation-induced self-assembly (EISA) which is most suitable for thin film preparation.[123] In the EISA approach, the solvent evaporates from a sol consisting of the precursor and the SDA. The SDA concentration increases gradually until the critical micelle concentration (CMC) is exceeded and micelles start to form. After complete evaporation, the final mesostructure is established by the formation of the SDA/precursor composite. The formation of this

so-called modulable solid-state period strongly depends on different synthesis parameters (e.g. the relative humidity) and can take seconds to several hours. The major advantage of the EISA technique is the higher number of potentially suitable solvents compared to aqueous sol-gel approaches and therefore a larger variety of accessible porous ceramics.[35]
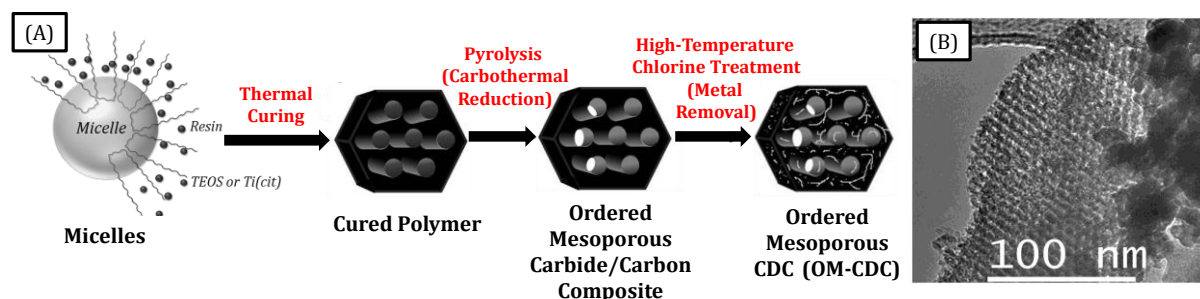
Figure 14. *Preparation of OM-CDC with hexagonal pore structure by soft-templating (A) and TEM micrograph (B) showing the mesoscopic ordering.[124]*

Free-standing films of ordered mesoporous CDCs can be produced by utilizing the amphiphilic triblock copolymer Pluronic F127 as a soft-template for the evaporation-induced self-assembly (EISA) of the carbon precursor polymer resol with metal-containing precursors such as tetraethyl orthosilicate or titanium citrate. Carbon and metal oxide precursors are decomposed under inert atmosphere and the resulting C/SiO_2 or C/TiO_2 composites are converted to ordered mesoporous C/SiC or C/TiC composites by carbothermal reduction. High-temperature chlorine treatment transfers these materials structurally conformal into hierarchical OM-CDCs (Figure 14). The porosity values are strongly dependent on the temperature of carbothermal reduction and the applied ratio of metal precursor/carbon precursor. The temperature of the chlorine treatment significantly influences the micropore size whereas the mesopore diameters remain unaffected.[124, 125]

2.3.3 Emulsion Approaches

In contrast to nanocasting and EISA which are expected to produce carbides with ordered pore structures, a large variety of disordered but well-defined materials can be obtained by emulsion approaches. In particular, water-in-oil microemulsions[50, 126] are appropriate systems and due to their strongly hydrophobic character, polycarbosilanes are highly suitable as the oil phase. Aqueous nanodroplets, which are stabilized by a surfactant, are homogeneously dispersed in the non-polar oil phase and their size is

controllable by the water/surfactant ratio (R_W).[50, 127] The preceramic polymer is then solidified and after pyrolysis of the polymer to the carbide, the resulting pore diameters correspond to the size of the former micelles. CDC materials obtained after high-temperature chlorine treatment offer a hierarchical micro-mesopore structure with SSA of up to 2480 m^2/g and total micro- mesopore volumes as high as 2.0 cm^3/g.[69] Furthermore, the microemulsion technique is useful for the *in-situ* functionalization of CDCs since the nanodroplets can serve as reactors for the growth of well-dispersed nanoparticles (NPs) with defined size.[128]

In a typical microemulsion, the volume of the internal aqueous phase is low in relation to the total volume. However, this value can be increased to more than 74 vol.% and the resulting formulations are designated as high internal phase emulsions (HIPEs). These systems are especially useful to obtain macroporous ceramics. If the continuous oil phase is polymerized or cross-linked, a material known as polymerized high internal phase emulsion (PolyHIPE) is obtained with the structure of the HIPE transferred to the solid state.[129, 130] Silicon carbides with characteristic spherical shells of ~2 µm in size interconnected by windows of ~200 nm in diameter can be obtained if liquid polycarbosilane in combination with cross-linking monomers are used as oil phase (Figure 15(A)). After cross-linking, washing of the PolyHIPE, and subsequent pyrolysis, SiC ceramics with SSAs of up to 167 m^2/g can be produced.[131]
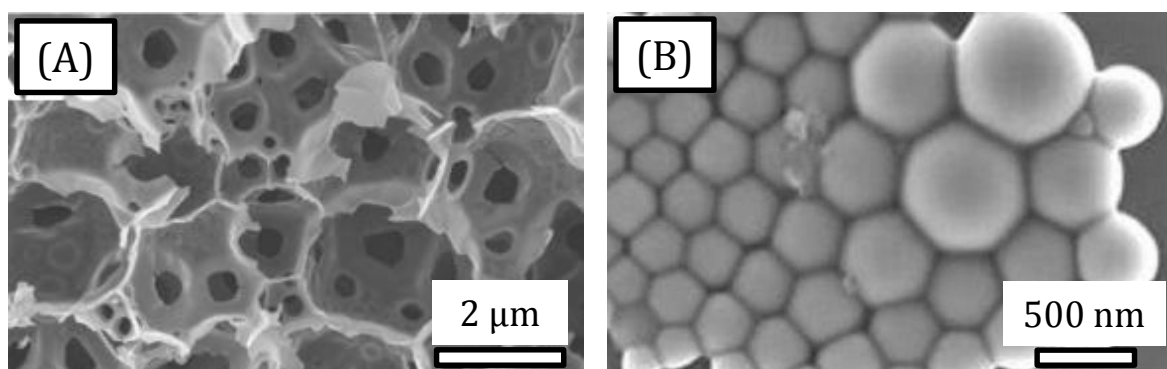
Figure 15. *SEM micrographs of a macroporous silicon carbide obtained from PCS PolyHIPEs (A),[131] and PCS nanospheres from the miniemulsion technique (B).[132]*

One system for the synthesis of polycarbosilane and silicon carbide ceramics with large external SSA are so-called miniemulsions (Figure 15(B)).[133] Miniemulsions consist of larger droplets (50-500 nm) compared to microemulsions and are not thermodynamically, but rather kinetically stable systems. The emulsification is achieved by the introduction of shearing forces using ultrasonic energy. The size of the generated

nanospheres is precisely controllable by the amount of surfactant added to the emulsion and the time and intensity of the ultrasonic treatment.[134] Hydrophobic co-stabilizers are usually added to the oil phase suppressing diffusional degradation (Ostwald ripening) of the droplets, keeping them in their initial size, and stabilizing the emulsion. As one example, miniemulsions are highly useful for the synthesis of SiC/CeO$_2$ core-shell nanostructures with high catalytic activity in the catalytic combustion of methane as reported by Borchardt and co-workers.[132]

2.3.4 Sol-Gel Approaches

In view of sustainable resource management, sol-gel methods are a highly attractive template-free alternative for the synthesis of nanostructured carbides and carbons because they do not employ large amounts of chemicals apart from those forming the final product. Aerogel materials are usually obtained by cross-linking of inorganic or organic gels followed by supercritical extraction of the solvent from the wet gels. Under supercritical conditions, there is no distinction between the liquid and the vapor phase. In consequence, the capillary forces during solvent removal can be kept at a minimum resulting in a highly porous network.[12]
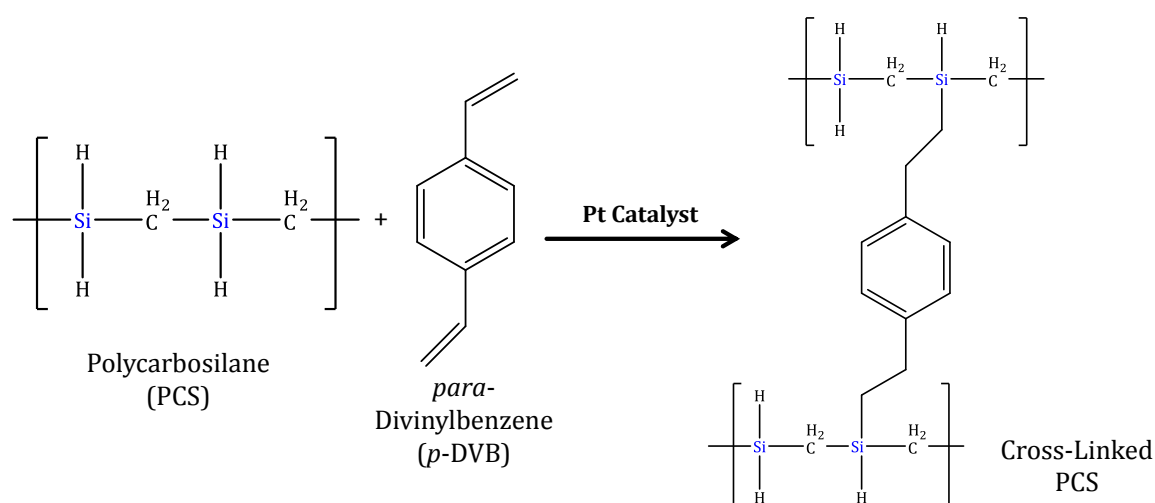
Figure 16. *Platinum-catalyzed hydrosilylation reaction for the synthesis of cross-linked PCS aerogels.[135]*

Especially the direct use of polycarbosilanes is a very promising way to synthesize well-defined ceramics with an aerogel-type pore structure. Polycarbosilane aerogels can be obtained by cross-linking polymers that contain Si-H bonds (e.g. SMP-10, see section 2.1.2) with a cross-linker that exhibits C=C double-bonds (e.g. *para*-divinylbenzene) in highly diluted solution.[135, 136] The cross-linking mechanism is based on the

hydrosilylation reaction catalyzed by a platinum complex (Figure 16). After pyrolysis at maximum temperatures up to 1500°C, carbon-rich monolithic SiC ceramics with high SSA of 444 m²/g are obtained.

2.4 Electrochemical Energy Storage

Due to the rapid technological development, climate change, and population growth, energy production and energy storage play key roles for the sustainable development of economy and society.[137-139] So far, the majority of processes use the conversion of chemical energy stored in coal, oil, or gas sources to produce electricity, heat, or light. On the one hand, it is a major target to replace these fossil fuels with renewable energy sources, such as wind, water or solar power because greenhouse gas emission must be decreased to reduce global warming. On the other hand, advanced storage devices for the "green energy" are in demand as these sources are no longer independent from time and location of energy production. Due to this decoupling of the production from the actual energy demand, various technologies for power grid management or power grid stabilization based on mechanical, physical, thermal, chemical, and electrochemical processes exist or are in development. The latter play a dominating role as they are characterized by comparably high efficiency and ease of operation in terms of pressure and temperature. Especially batteries[138, 140] and EDLCs (also referred to as supercapacitors or ultracapacitors)[141, 142] play a key role to achieve a reliable, sustainable, and safe large-scale use of renewable energy. In general, rechargeable batteries, such as lithium-sulfur (Li-S) batteries are used with regard to their relatively high energy density.[143] In contrast, supercapacitors are applied due to their high power density. Hence, the two devices might fulfill complementary functions when they are hybridized.[137]

2.4.1 Electrochemical Double-Layer Capacitors (EDLCs)

Electrochemical double-layer capacitors are among the most promising technologies for electrochemical energy storage. In contrast to batteries, where the energy storage mechanism is based on time-consuming redox reactions, the charge storage in EDLCs is of purely physical character based on the electrosorption of electrolyte ions on the surface of an electrode material. Porous carbon is widely used EDLCs because it offers a combination of electrical conductivity, high SSA, and electrochemical stability.[10, 144] The

purely electrostatic charge separation mechanism in EDLCs leads to very high power density, rapid charge/discharge, high efficiency, high cyclability, and a broad operating temperature range compared to batteries (Figure 17(A)). At the same time, EDLCs provide considerably higher energy densities than solid-state capacitors.[145] In the last decade, the cost of EDLCs decreased significantly faster than that of batteries and progress in the performance improvements of the EDLCs was noticeably more rapid as well. However, in comparison to batteries, their energy density is still lower.[137]

In contrast to classical EDLCs, so-called pseudocapacitors or redox-supercapacitors use rapid and reversible surface redox reactions (usually on a metal oxide, heteroatom-enriched carbons, or a conductive polymer) for charge storage.[146, 147] Pseudocapacitance can also originate from redox reactions of the electrolyte species on the surface of pristine carbon electrodes. In contrast to classical EDLCs, redox supercapacitors provide significantly higher energy densities but their power performance is lower as they suffer from the use of time-consuming redox reactions.
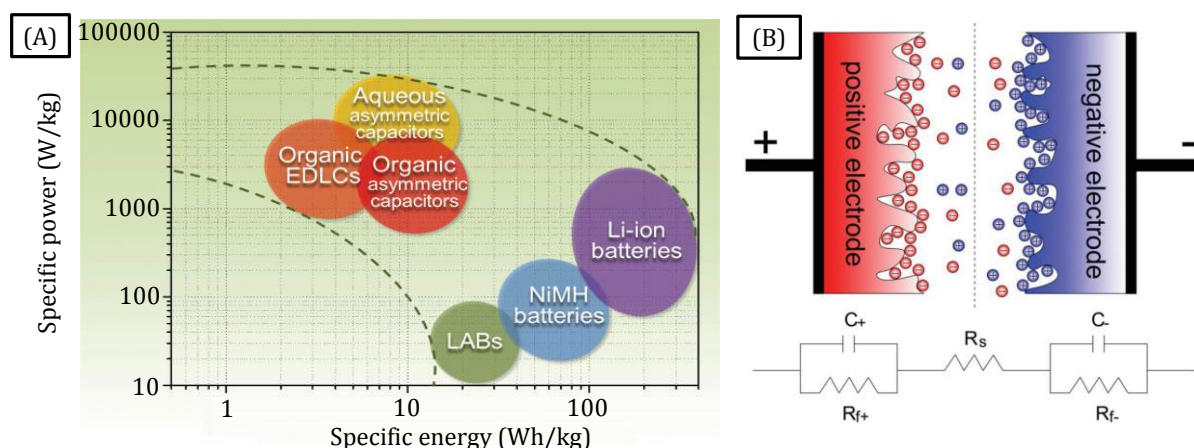
Figure 17. *Ragone plot of specific power vs. specific energy of EDLCs and different battery systems (A) as well as schematic representation of the charged state of an EDLC using porous electrodes ((B) with R: resistor; C: capacitor).[142, 145]*

In their most simple configuration, EDLCs consist of two porous electrodes (contacted by current collectors), which are immersed into electrolyte and separated by an ion-conducting membrane (Figure 17(B)).[142] The electrostatical charge storage in EDLCs takes place by reversible adsorption of electrolyte ions on the active materials leading to charge separation at the electrode-electrolyte interface according to the classical double layer theory of Helmholtz which was later expanded by Gouy, Chapman, and Stern.[142] The specific capacitance (C in F/g) of an EDLC is calculated according to Equation 10.

$$C = \frac{\varepsilon_r \cdot \varepsilon_0 \cdot A}{d} \qquad (10)$$

In Equation 10, ε_r is the dielectric constant of the electrolyte, ε_0 is the dielectric constant of the vacuum, A is the electrode surface area, and d is the charge separation distance. The specific energy (E in Wh/kg) and specific power (W in W/kg) of an EDLC are given by Equations 11 and 12:

$$E = \frac{C \cdot U^2}{2 \cdot 3600 \cdot m} \qquad (11)$$

$$W = \frac{U^2}{4 \cdot ESR \cdot m} \qquad (12)$$

Here, U is the operating voltage, m is the total mass of active material, and ESR is the equivalent series resistance of the system. Most importantly, the specific energy of EDLCs has to be increased to move them closer to batteries (Figure 17(A)). This can be achieved by increasing the cell operating voltage, which is limited by the electrolyte stability, or by enhancing the specific capacitance which is controlled by the carbon-electrolyte interface.[10] Many nanostructured and high-surface area carbon materials with different porous textures including carbon nanotubes (CNTs),[14] carbon fibers,[65] carbon onions,[15] graphene,[148] templated carbons,[27] and activated carbons[149] were tested as electrode materials in EDLCs.

Role of the Electrolyte System in EDLCs

In general, the electrolytes in EDLCs can be subdivided into three classes, namely aqueous, organic, and ionic liquid electrolytes.[145] Aqueous electrolytes based on dissolved salts, acids, or alkali usually provide high ionic conductivity and are comparably low by cost. However, they suffer from the narrow electrochemical stability window of water (1.23 V) limiting the achievable energy density according to Equation 11.[63] Organic electrolytes consist of a salt (e.g. tetraethylammonium tetrafluoroborate, TEABF$_4$) dissolved in an organic media, commonly propylene carbonate (PC) or acetonitrile (AN).[145] These electrolytes usually provide a stability window in the range of 2.2-3.0 V and the achievable specific energy is significantly beyond that of aqueous solutions. In consequence, most of the commercially available systems rely on the use of organic electrolytes.[137] The third class of electrolytes are room temperature ionic liquids (ILs). ILs are molten salts and very promising for the use in EDLCs due to their broad electrochemical stability window (2.6-4.0 V) and non-flammability. The latter is of

particular importance for their use in mobile applications.[150, 151] However, ILs suffer from poor ionic conductivity at room temperature and below leading to limited power performance compared to organic electrolytes.

Due to their very large specific surface area, tunable pore size, and controllable surface chemistry, CDCs are very attractive electrode materials in EDLCs. In aqueous media, they show high gravimetric capacities of up to 196 F/g (TiC-CDC in 1 M H_2SO_4), 217 F/g (TiC/TiO_2-CDC in 1 M H_2SO_4), and 260 F/g (Al_3C_4-CDC in 6 M KOH).[31, 152] In organic electrolytes, TiC-CDC shows the highest capacitance of more than 160 F/g (110 F/cm^3) when $TEABF_4$ in AN is used.[74] This significantly exceeds the values of activated carbons. If post-synthesis activation with KOH is applied, it is possible to significantly increase the gravimetric capacitance to 180 F/g.[153] Recent studies on CDCs in IL electrolytes report specific capacities up to 160 F/g (85 F/cm^3) in ethyl-methylimidazolium-bis(trifluoro-methane-sulfonyl)imide (EMI-TFSI) at 60°C for a TiC-CDC prepared at 500°C because an optimum pore size is achieved at this temperature.[154] N-butyl-N-methylpyrrolidinium bis(trifluoromethanesulfonyl)-imide ionic liquid can be used as the electrolyte even at a temperature of 100°C leading to capacities of 130 F/g.[155] Such studies are of particular importance for high-temperature applications, e.g. EDLCs operating under car hoods. The specific interest in IL electrolytes under these conditions arises from their very low vapor pressure even at high-temperatures and non-flammability providing rather safe operation compared to organic systems.

Role of Pore Accessibility in EDLCs

The very fast charge-/discharge rates of EDLCs can only be accomplished if the electrolyte has fast access to the entire surface area of the electrode material.[10] Therefore, purely microporous carbon materials, including CDCs, often suffer from a distinct capacity drop in the high-power regime. This becomes especially obvious in EDLCs using microporous CDC thin films as the electrode.[66] These electrodes can offer very high volumetric capacities of up to 180 F/cm^3 if their thickness is in the range of several μm. However, if they become thicker, only a small portion of the SSA can be used for ion storage due to diffusion limitations within the microporous electrode and the high volumetric capacity drastically drops.

This drawback can be overcome by the use of electrode materials with nm-sized particles improving the ion transport. Several reports show that the capacitance

increases with decreasing CDC particle size. 30 nm CDC particles show capacitances of up to 150 F/g in aqueous electrolyte (1 M H_2SO_4) and no faradic surface reactions. Compared to CDCs with comparable pore structure but larger particle size they exhibit better electrochemical activity due to their highly accessible micropores.[16] Especially for such powdered materials it is importatnt to note that the packing density of the carbon particles is an important factor. The empty electrode volume that has to be filled with electrolyte must be kept as low as possible to achieve maximum capacities if both components (carbon and electrolyte) are considered.
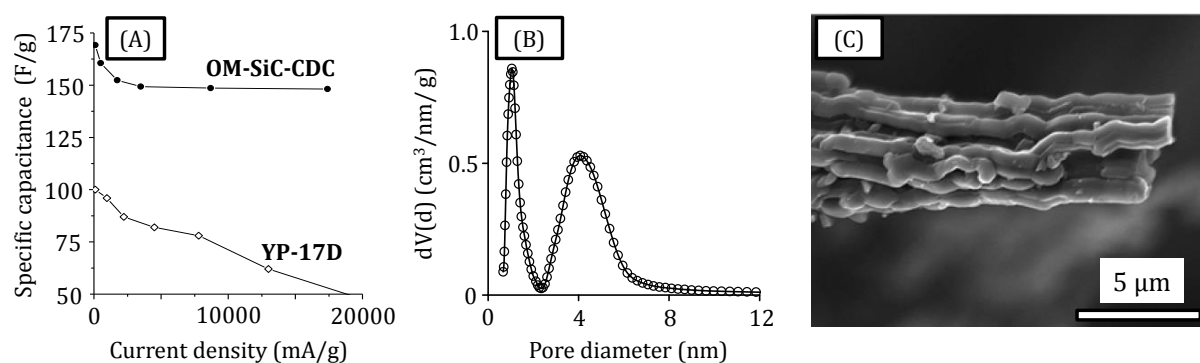
Figure 18. *Capacitance retention versus current density of OM-SiC-CDC in comparison to commercially available activated carbon YP-17D (A), quenched solid density functional theory (QSDFT) pore size distribution of OM-SiC-CDC (B), and SEM micrograph showing the typical particle morphology (C).[156, 157]*

Besides the use of such nanosized CDC electrode materials with large external SSA, the introduction of internal transport pores is a suitable way to overcome diffusion limitations present in purely microporous electrodes. However, strictly mesoporous materials do not store sufficient amounts of ions due to their limited SSA and in consequence, their capacity is limited. The combination of ordered mesopores and a large volume of micropores provided by OM-SiC-CDCs (see secion 3.2.1) is highly suitable for the use in EDLC electrodes. High capacity and rapid charge/discharge are ensured simultaneously by the large SSA and ordered mesopores, respectively.[156-158] OM-SiC-CDCs reach up to 175 F/g in organic electrolyte (1 M TEABF4 in AN), 200 F/g in aqueous electrolyte (1 M H_2SO_4), and 223 F/g in ionic liquid (IL) electrolyte (1-ethyl-3-methylimidazolium-tetrafluoroborate (EMI-BF4)).[156, 157] Especially the high capacity retention at high current densities of OM-SiC-CDC is impressive when compared to activated carbon materials used for commercial devices (Figure 18(A)). This advantage is related to the hierarchical arrangement of well-defined pores in the CDC (Figure 18(B)). While the 1 nm-sized micropores act as reservoirs for ion storage,

mesopores of 4 nm in diameter ensure rapid diffusion of electrolyte ions throughout the μm-sized particles (Figure 18(C)) and therefore ensure sufficient operation at rapid charging/discharging. In a similar way, soft-templated OM-CDCs offer high specific capacities of 146 F/g in organic electrolyte due to the micropores drilled on the walls, while promising rate capability is a result of the mesopore pathways.[125]

Ion Adsorption Mechanisms in EDLCs

From a mechanistic point of view, the capacitance of EDLCs was fully ascribed to the formation of an electrochemical Helmholtz double-layer of electrolyte molecules on the carbon pore wall for a long time. The carbon pores had to fulfill the requirement that the ion with its complete intact solvent shell has to have full access to their interior.[10] More recent studies report on the significant enhancement of the capacitance when the carbon pore size falls below the solvent shell size of the electrolyte ions and the formation of a double-layer would not be possible from a theoretical standpoint.[74, 159, 160]
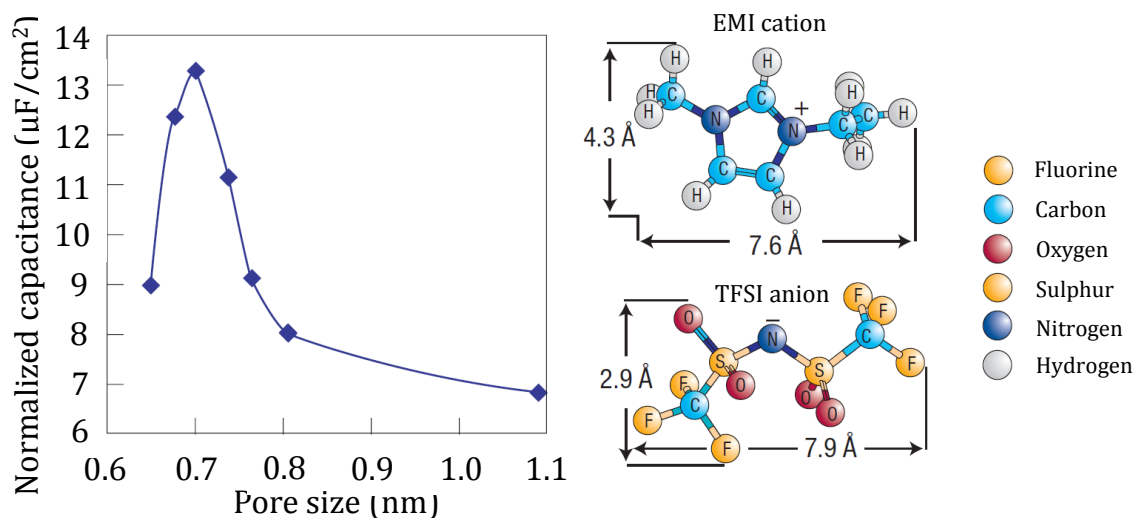
Figure 19. Correlation between the TiC-CDC pore size and capacitance in EMI-TFSI ionic liquid electrolyte.[154]

The first reports on the anomalous increase were based on experimental electrochemical results of TiC-CDC electrodes with the pore size strongly depending on the synthesis temperature. In organic electrolyte (TEABF$_4$ in AN), the highest values are reached for CDCs with a pore size of 0.7-0.8 nm, approximately corresponding to the size of the TEA$^+$ ion (0.67 nm).[74] Similar findings are reported for TiC-CDCs using the pure EMI-TFSI ionic liquid electrolyte at 60°C or dissolved in AN at room temperature.[151] In both cases the highest capacitance is obtained when the size of the

ions matches the CDC pore size resulting in a volcano-type appearance of the plot of the specific capacitance versus the pore size (Figure 19).[154]

Although major progress and improvement of EDLCs has been achieved in recent years, a detailed understanding of the basic mechanisms in these devices is still lacking. Therefore, *in-situ* characterization and modelling techniques are more and more in focus. While the earliest studies are of mainly empirical character (based on electrochemical measurements), dilatomery[161, 162] as well as spectroscopic,[163-166] electrochemical quartz microbalance,[167, 168] and scattering techniques[169] (most often guided and verified by theoretical modelling methods)[170, 171] are widely used today. These studies have improved the understanding of ion storage mechanisms in carbon pores.

2.4.2 Lithium-Sulfur (Li-S) Batteries

Compared to EDLCs, rechargeable batteries stand out due to their considerably higher energy density. In consequence, they are widely applied for electrochemical energy storage in consumer devices (e.g. mobile phones or laptops) and in hybrid electric vehicles (e.g. the Toyota Prius, that uses combustion engine combined with a battery). However, in the last years, significant developments were made in the area of transportation and automotive industry but only very few battery systems achieved commercial use so far. Besides the lead acid- and nickel-metal hydride accumulators, especially lithium-ion batteries (LIBs) are promising devices due to their high energy- and power density.[143] Although major progress has been achieved in the development of advanced electrode materials with higher capacitance and higher operating voltage, LIBs do most often not keep pace with the requirements in terms of capacity, safety, cost, and cycling stability.[172]

One of the most promising battery systems is the lithium-sulfur (Li-S) battery because of the high specific capacity of sulfur of 1672 mAh/g. The theoretical specific energy of such a battery setup is more than five times higher than that of commercial LIBs.[173, 174] A complete Li-S battery could still provide 400-600 Wh/kg. With such a system, a driving distance of up to 500 km would become realistic. As another important advantage, the Li-S battery contains an intrinsic protection mechanism against overcharging, which greatly improves the battery safety.[140] Because sulfur is naturally abundant, inexpensive, non-toxic, and environmentally friendly, the Li-S battery is a very attractive

candidate for the stationary large-scale storage of energy produced by wind-, water-, or solar sources.
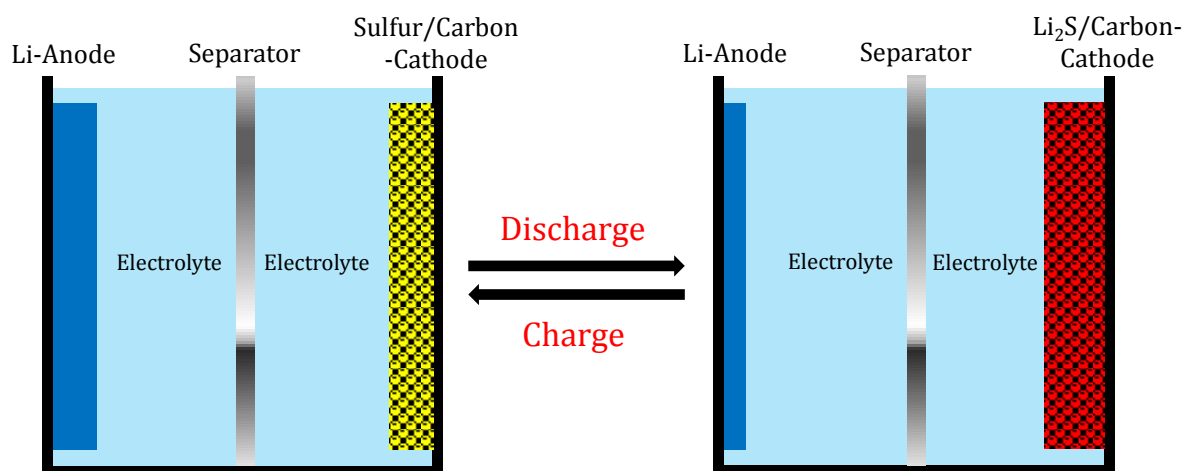
Figure 20. *Principle of the Li-S battery.*

A typical lithium-sulfur battery consists of a lithium anode and sulfur cathode with a separator and the electrolyte salt (most often dissolved in ethers or organic carbonates) in between (Figure 20).[175] In contrast to LIBs, the Li-S system is not based on the classical lithium intercalation but rather on conversion. One sulfur atom accommodates a maximum of two lithium ions according to Equation 13.

$$16\ Li + S_8 \rightleftarrows 8\ Li_2S \tag{13}$$

The operating voltage of 2.1 V versus Li/Li^+ is below the potential of a positive intercalation electrode (e.g. $LiMnO_2$ or $LiCoO_2$). However, this disadvantage is compensated by the high theoretical specific capacitance of 1672 mAh/g which is the highest value known for a solid cathode material. Secondly, the lithium metal anode provides a very high theoretical capacitance of 3860 mAh/g.[173]

In spite of these considerable advantages, the electrochemistry of the Li-S battery is accompanied by significant disadvantages that still hinder the commercialization of this promising energy storage system. One of the major problems is caused by the electrochemical mechanism itself. Under charged conditions, sulfur is present in the standard cyclo-S_8 configuration and during discharge a step-by-step reduction by lithium ions to Li_2S_8, Li_2S_4, Li_2S_2, and Li_2S takes place.[173] During charging, the corresponding oxidation processes occur. The intermediately formed polysulfide species, especially Li_2S_8 and Li_2S_4, can easily react with the organic electrolyte or can

dissolve into it. This leads to detrimental loss of active material from the cathode and decreases the capacity of the battery. Furthermore, polysulfides can migrate to the lithium anode and form an electrochemically inactive layer of Li_2S_2 or Li_2S leading to further decrease of the battery performance. On the other side, these polysulfides can directly react with the anode, form dendrites, and finally cause shortcuts of the battery. Moreover, sulfur and its various discharge products show very low electrical and ionic conductivity and the internal resistance of the battery is therefore very high. This results in high polarization and low energy efficiency. The conductivity of the active material becomes even worse during discharge because an insulating layer is formed on its surface.[173]

These problems force researchers to develop advanced battery components, such as electrolytes, binders, current collectors, or protection layers for the anode with regard to develop rather stable and reliable Li-S batteries.[172] However, the cathode design still seems to be the most challenging assignment since the active material has to have intimate electrical contact to the adsorption sites of an electronic conductor. One option is to coat a conductive carbon- or polymer layer on the sulfur surface but the resulting cathodes suffer from very low cycling stability.[172] Therefore, in most cases, porous carbon materials are used as substrates to host and contact the sulfur due to their high electrical conductivity.[176, 177] The carbon material has to fulfill numerous requirements. There has to be a large contact area between carbon and the active material with regard to achieve a high degree of electric conductivity. Furthermore the particle size of the sulfur should be < 100 nm to keep both the electron transport and diffusion pathways as short as possible. On the other hand the pores in the conductive additive should be as large as possible to obtain high pore volumes with regard to achieve high sulfur loadings and to lower the area of the electrode with respect to the mass of the active compound. Although a high pore-filling degree in the carbon/sulfur composite is desirable it has to exhibit some hollow space to allow access for the liquid electrolyte which acts as both Li-ion transport medium and a secondary conductive agent within the cathode. Void space is also required to balance the volume expansion (~74%) during the conversion of S to Li_2S because the formation of cracks which would lead to the pulverization of the rigid carbon matrix structure has to be avoided. Owing to these numerous requirements, several types of porous carbons show only limited performance in Li-S cell cathodes. For instance, carbon nanotubes (CNTs)[178] or activated carbons[179] suffer from low pore

volume and/or moderate specific surface area limiting the values of electroactive mass that can be accumulated and the contact area between sulfur and carbon, respectively. Macroporous carbon materials are less applicable because the diffusion of soluble polysulfides from the cathode is not effectively restricted compared to materials with smaller pores. One method to avoid this disadvantage of macroporous substrates is the use of high-viscosity electrolytes which decrease the solubility of ions and keeps them at the cathode.[72, 176]

In the most recent studies it was found that especially mesoporous carbon materials can display the conductive additive of choice in Li-S cathodes. According to the work of Nazar and co-workers, the impregnation of ordered mesoporous CMK-3 with a sulfur melt is a method that allows precise control over the ratio of active mass and thus the amount of remaining pore volume in the resulting composite. The obtained Li-S battery cathode exhibits significantly increased cyclability. The sulfur is immobilized between the conductive carbon channels which generate the electric contact resulting in an ordered and interwoven carbon/sulfur composite with exceptional electrochemical properties at moderate cycling rates.[180] A large variety of other mesoporous carbon structures also show promising performance as sulfur host structures in Li-S batteries. Spherical ordered mesoporous carbon nanoparticles of 300 nm in diameter with bimodal mesoporosity exhibit high specific capacity of more than 830 mAh/g after 100 cycles at a current rate of 1 C which is explained with the very high internal pore volume of 2.32 cm^3/g.[181] Porous, hollow carbon/sulfur composites also show very promising electrochemical performance due to large interior void space and mesoporous shells with partially graphitic structure.[182] A systematic study on the optimization of mesoporous carbon (MC) structures for Li-S batteries by Liu and co-workers shows the importance of high mesopore volume of carbon materials for Li-S batteries.[177] As their major advantage, mesoporous carbon materials can be loaded with large amounts of sulfur which is very important for effective operation of the Li-S battery. The amount of carbon substrate within the cathode must be kept as low as possible because it does not actively contribute to the capacitance of the battery.

However, the general problems related to the electrochemistry of the Li-S system cannot be fully prevented and polysulfide dissolution still occurs leading to limited cycling stability. If infiltrated into microporous carbon materials, sulfur exhibits a higher electrochemical activity and cyclability. Even if the pore size of the carbon material falls

below the diameter of the cyclo-S_8 (~0.7 nm), the active material can be incorporated into the host material because it undergoes a structural change into a chain configuration. The spatially limited sulfur species show a large interaction with the carbon pore walls and the critical effect of the formation of soluble polysulfides is effectively suppressed.[183] However, the low pore volume of purely microporous carbon materials limits the amount of sulfur that can be infiltrated into the host material to values below 50 wt.%. This, in turn, limits the capacitance related to the overall cathode. In consequence, hierarchical micro-mesoporous carbon materials are optimum host structures in Li-S cathodes.[176] On the one side, these materials are suitable for the storage of large amounts of sulfur due to their high pore volume and they provide a large electrochemical contact area for the active species. On the other side, formed polysulfides can be adsorbed within the smaller pores and the larger pores provide sufficient space for electrolyte and ion transportation.

2.5 Gas Adsorption

Besides the use in electrochemical energy storage devices (see section 2.4), porous carbon materials play a crucial role in gas storage and gas separation processes.[184] Due to their high SSA and controllable pore volume, they are highly attractive candidates for various applications related to the physical adsorption (physisorption) of gas molecules. One of the most important areas of research concentrates on the storage of hydrogen for energy applications.[185] Furthermore, the adsorption of methane and other hydrocarbons is highly important as they represent important future clean energy sources.[102] Other relevant gases are environmentally harmful or toxic (e.g. CO_2, SO_2, and NO).[186] In terms of energy consumption, physical adsorption of gases into a porous solid adsorbent is highly practicable compared to liquefacation, compression, or storage by reaction with a solid material (e.g. the storage of hydrogen in a metal hydride).

A high gravimetric (cm^3 or mol gas per mass of adsorbent) and volumetric (cm^3 or mol gas per volume of adsorbent) uptake of a porous material is required for efficient gas storage.[58] Furthermore, the pressure at which the highest storage capacity can be achieved is of fundamental importance. However, not only the storage, but also the separation of gases by filtration of components from mixtures (e.g. CO_2/N_2, CO_2/H_2, and CO_2/CH_4) and the removal of harmful volatile organic compounds from air are of great industrial and social importance.[71, 187] In contrast to the storage application, filtration

does not only require a high capacity of the adsorbent but also high selectivity and efficient mass transfer within the porous material because the contact time of the gas mixture and the adsorbent is often limited. Therefore, hierarchically structured materials are of great importance for gas filtration applications. While the micropores lead to high SSAs and therefore high storage capacities, larger meso- or macropores ensure rapid diffusion of gas molecules to the adsorption sites.

Especially ACs are known as adsorbents for many years and are widely applied as filter material in gas masks due to their high specific surface areas and relatively low production cost. Unfortunately, their internal surface area and pore structure is often not well-defined.[7] This can be a great disadvantage because the gravimetric and especially the volumetric storage capacities are limited. Moreover, the broad pore size distribution limits the applicability in size-selective applications. In contrast to ACs, CDCs offer rather narrow pore size distributions combined with high SSA as well as variable surface chemistry and are attractive candidates as adsorbents. TiC-CDCs exhibit outstanding methane storage capacities of up to 14 wt.% at 35 bar and 25°C.[58] This value can be even increased to 18.5 wt.% at 60 bar and 25°C if post-synthesis activation with CO_2 is applied.[102] KOH activated ZrC-CDCs can store as much as 6.2 wt.% hydrogen at -196°C and 20 bar.[106] In contrast to powdered materials, TiC-CDC plate monoliths show enhanced volumetric adsorption capacities up to 35 g/l hydrogen at -196°C and 60 bar as well as 219 cm^3/cm^3 methane at 60 bar and 25°C.[58] Polysilesquioxane-based CDCs also offer high capacities of up to 5.5 wt.% hydrogen at -196°C and 60 bar and 21.5 wt.% methane at 25°C and 60 bar even without post-synthesis activation.[188] As another example of polymer-based materials, OM-SiC-CDCs offer very high storage capacities for hydrogen, methane, and *n*-butane.[118] Due to their hierarchical micro-mesopore architecture, OM-SiC-CDCs combine the high gravimetric capacities with efficient materials transport. This leads to rapid adsorption kinetics making these materials attractive candidates for the efficient filtration of hydrocarbon molecules.

3. Methods

3.1 Nitrogen Physisorption

Physisorption occurs whenever a fluid phase (the adsorptive) gets into contact with the surface of a solid (the adsorbent). The molecules adsorbed on the surface are denoted as the adsorbate. The forces involved are van-der Waals forces (London dispersion forces) and the short-range intermolecular repulsion. While these forces cause non-specific molecular interactions, specific interactions take place when polar molecules adsorb on polar surfaces. However, as long as no chemical bonds are formed (as it is the case in the so-called chemisorption) the process is still regarded as physisorption.[189] A physisorption isotherm is the plot of the adsorbed amount of fluid as a function of the relative pressure p/p_0, where p_0 is the saturation pressure of the adsorptive at a given temperature. Most often, these measurements are performed by volumetric or gravimetric methods. The shape of an adsorption isotherm is influenced by the interplay and the strength of fluid-fluid and fluid-wall interactions. Furthermore, the adsorption isotherm is influenced by the pore size, pore geometry, and surface polarity. In 1985, the IUPAC has published a classification of six types of isotherms and proposed to distinguish pores by their internal width.[190] It has to be noted that this classification is currently under revision. Macropores are pores with a diameter above 50 nm and mesopores are pores of 2-50 nm. Micropores have diameters below 2 nm and are further subdivided into ultramicropores (0-0.7 nm) and supermicropores (0.7-2.0 nm). Pores with diameters below 100 nm are also often referred to as nanopores in accordance to the general definition of nanomaterials. The standard tool for determination of specific surface area and pore size is the physisorption of nitrogen measured at -196°C. This method is highly attractive as it is non-destructive, precise, and allows the calculation of many material properties. Alternative probe techniques are the physisorption of argon at -186°C and carbon dioxide at 0 or 25°C.[191]

3.1.1 Adsorption Mechanisms

The adsorption mechanism of the gas molecules depends on the pore size of the adsorbent. In non- or macroporous solids, the molecules form a monolayer on the surface followed by the occurrence of multilayer adsorption (Figure 21(A)). This phenomenon is caused by the interplay of attractive and repulsive forces between the pore wall and the gas molecules in dependence of their distance. An adsorption isotherm

of type II according to the IPUAC classification is obtained due to the dominant fluid-wall interactions at low relative pressure (monolayer formation) followed by the adsorption caused by fluid-fluid interaction at higher relative pressure (multilayer formation). In microporous materials, the adsorption potentials of the opposite pore walls are overlapping and the adsorption is mostly dominated by the interactions between fluid and pore wall (Figure 21(B)). In consequence, the narrow micropores of 2-3 molecule diameters in width are filled at very low relative pressures ($p/p_0 < 0.01$). Filling of the larger micropores can occur at larger relative pressures ($p/p_0 = 0.01$-0.2) because the enhancement of the adsorbent-adsorbate interaction in the pore center is very small and the increased adsorption is mainly due to asdorbate-adsorbate interactions.[189] After complete micropore filling, the adsorption isotherm reaches a plateau without further uptake of nitrogen.
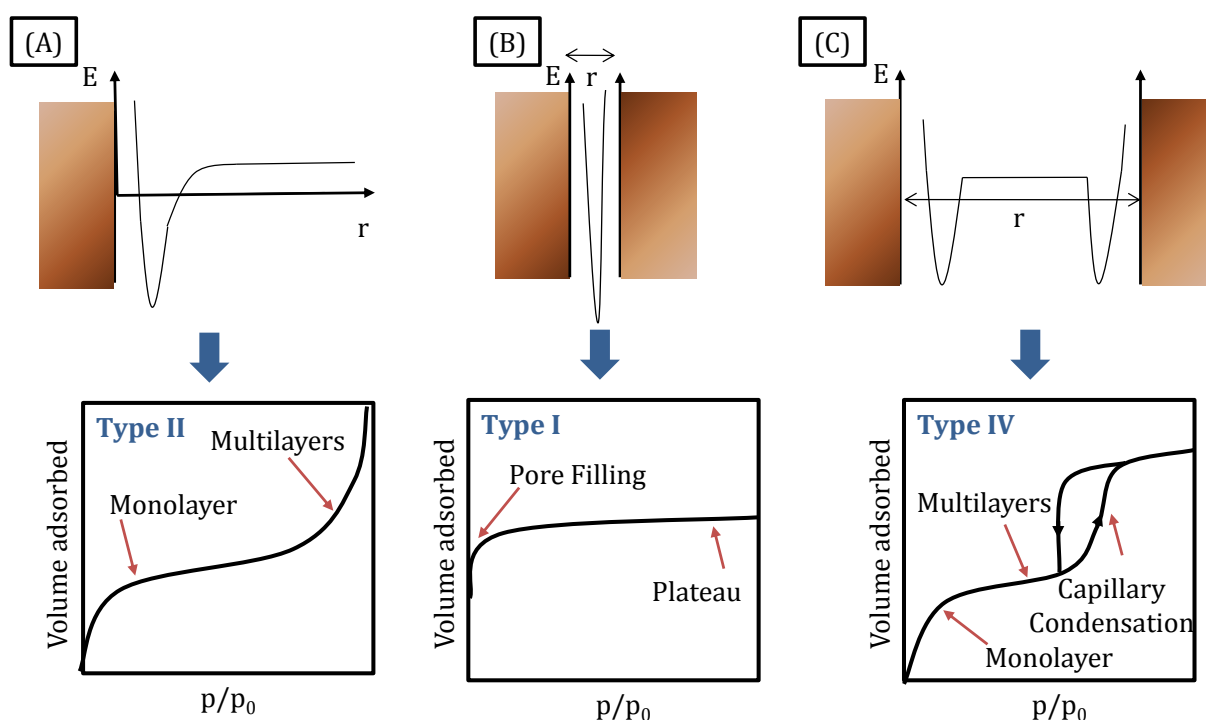
Figure 21. *Lennard-Jones potentials (top) and corresponding adsorption-desorption isotherms (bottom) for macropores (A), micropores (B), and mesopores (C).*

In contrast to micropores, attractive interactions between the fluid molecules strongly influence the adsorption behavior in mesopores and multilayer adsorption occurs. With the adsorption of more and more multilayers of adsorbate, surface tension and curvature effects become more important. At a certain relative pressure of $p/p_0 > 0.2$, the thickness of the multilayer becomes too large. The film cannot be stabilized anymore

and pore condensation (also referred to as capillary condensation) occurs (Figure 21(C)). As the condensation takes place at a pressure below the saturation pressure of the bulk fluid (p_0), this condensation represents an example of a shifted phase transition due to the presence of attractive fluid-wall interactions.[189] Capillary condensation is associated with the formation of a meniscus over which the vapor pressure of the fluid is lowered followed by abrupt condensation and complete filling of the pore. A direct relationship between the relative pressure at which condensation takes place and the pore diameter (or more precisely the radius of the meniscus r_{menisc}) is given be the Kelvin equation (Equation 14), where γ is the surface tension of the bulk fluid, φ is the wetting angle, and V_M is the molar volume of the adsorbate.

$$ln\frac{p}{p_0} = \frac{-2\gamma V_M}{r_{menisc}RT}cos\varphi \qquad (14)$$

3.1.2 Hysteresis Loops

Types of Hysteresis Loops

Capillary condensation is most often accompanied by the occurrence of hysteresis loops, i.e. desorption of the condensed liquid occurs at a relative pressure different from the adsorption. The adsorption hysteresis is considered to be an intrinsic property of the vapor-liquid phase transition because it is delayed by the existence of metastable adsorption states and hindered nucleation of liquid bridges. During adsorption, the condensation occurs delayed due to the metastabilities which are associated with the nucleation of liquid bridges. In contrast, during desorption, the liquid-vapor interface is already present and evaporation takes place in thermodynamic equilibrium without nucleation. Four different types of hysteresis loops are distinguished according to the IUPAC classification (Figure 22).[190] Ordered mesoporous silica materials, such as SBA-15 or KIT-6 reveal a narrow distribution of uniform, cylindrically-shaped pores which cause a type H1 hysteresis.[115, 116] Materials with a rather complex pore structure in which networks effects (e.g. percolation or pore blocking) are present, give rise to a type H2 hysteresis. H3 and H4 hystereses contain a characteristic step-down in the desorption branch associated with the hysteresis loop closure. Isotherms with H3 hysteresis loops are generally attributed to the presence of non-rigid aggregates of plate-like particles or assemblies of slit-shaped pores. Such isotherms are usually not expected to provide a reliable assessment of the pore size distribution or the total pore

volume as they do not exhibit limited adsorption at high relative pressures. Type H4 hysteresis loops are characteristic for materials which contain a complex network of combined micro- and mesopores.
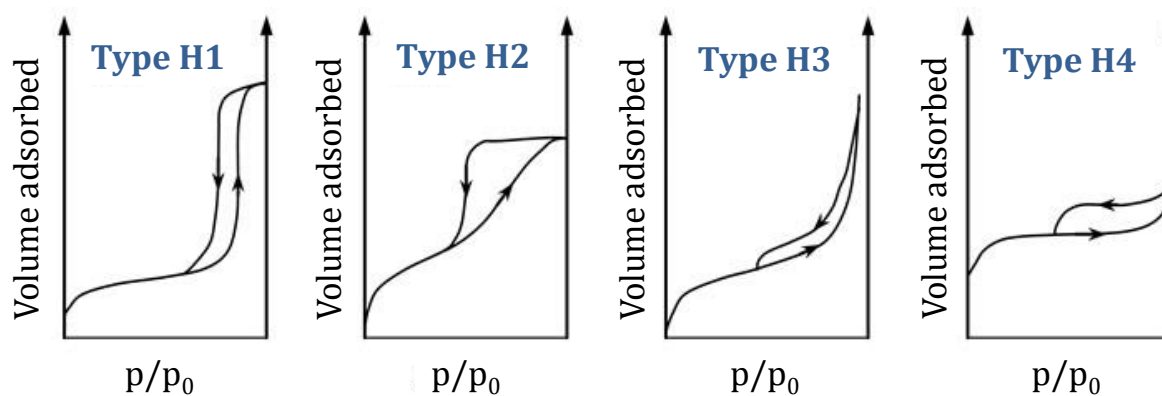
Figure 22. *IUPAC classification of hysteresis loops.*[190]

As described above, the desorption branch is usually the one which is in thermodynamic equilibrium. Therefore, the use of this branch is recommended by IUPAC for pore size analysis.[190] However, this assumption is only valid for materials which do not exhibit pore blocking or percolation effects. Hysteresis phenomena in pore networks with ink-bottle pores are quite complex and the evaluation of the desorption branch for the pore size determination will lead to incorrect interpretation of material properties. In spite of this disadvantage, the different mechanisms of desorption from ink-bottle pores can give important information about pore connectivity in these materials. In principle, two different mechanisms can be distinguished: pore blocking and cavitation.

Pore Blocking and Cavitation
It is widely known that evaporation of the pore condensate from a network of ink-bottle pores is obstructed by the pore constrictions, i.e. the emptying of their interior can only occur through the neck.[192] In other words, the pore stays filled until the neck empties and the relative pressure at which an ink-bottle pore empties depends on the size of its neck. The desorption branch is therefore very steep and an H2 hysteresis loop results. Conventional H2 hysteresis will also occur if the size distribution of the pores is relatively broad but the neck size distribution is narrow (Figure 23(A)). A different type of H2 hysteresis, the so-called "inverse H2 hysteresis", takes place if the pore size distribution is narrower compared to the size distribution of the necks. In consequence,

the desorption branch is less steep then the adsorption branch in such a case (Figure 23(B)).[189]
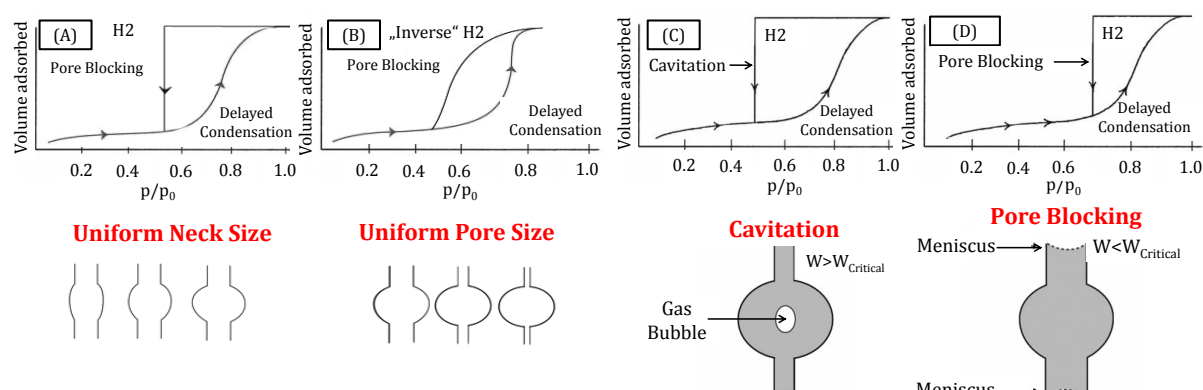
Figure 23. *Hysteresis phenomena in ink-bottle pores: Pore blocking with conventional H2 hysteresis in pores with uniform neck size (A) and uniform pore size (B) as well as H2 hysteresis caused by cavitation in pores with the neck size (W) larger than the critical neck size (C) and pore blocking (D) in pores with W<W$_{Critical}$.*[189]

If the neck diameter falls below a certain temperature-depending value (estimated to be ~6 nm for nitrogen at -196°C), the mechanism of desorption from the pore body involves cavitation which is the spontaneous nucleation and growth of gas bubbles in the metastable condensed fluid (Figure 23(C)). The pore neck remains filled while the pore body empties. It is assumed that the tensile stress limit of the condensed fluid, i.e. the pressure at which cavitation induced evaporation occurs, does not depend on the pore structure of the adsorbent but is rather a universal feature of the adsorptive. However, recent work also reveals that the onset of cavitation can also depend on the size and geometry of the cavity if its diameter falls below a certain value.[193]

3.1.3 Pore Size Distribution

As the physisorption of gases (especially nitrogen at -196°C) is a widely applied technique for the characterization of porous materials, many different methods are known for the determination of the materials parameters (e.g. SSA, pore volume, or pore size distribution). The PSD can be calculated using classical macroscopic thermodynamic methods, such as the Barett-Joyner-Halenda (BJH) method,[194] which is based on the Kelvin equation (Equation 14). As the BJH method makes use of the capillary condensation effect, there are also classical methods for the determination of the micropore volume, such as the Horvath-Kawazoe approach.[195] However, all of them make the assumption that the adsorbed liquid has the same thermophysical properties

(e.g. triple point, critical point, freezing point) as the bulk fluid. This leads to inaccuracies in the pore size and pore volume determination. For instance, it is known that the BJH method underestimates the pore size of OMS materials with pore sizes below 10 nm by 20-30% because it assumes a flat, nonporous surface and does not differentiate between the thermo-physical properties of the adsorbed molecules and the bulk fluid.[196]

Due to these serious disadvantages, microscopic methods based on the density functional theory (DFT) have been developed providing a more realistic description of the thermo-physical properties of the adsorbed fluid. Therefore, pore size analysis based on non-local density functional theory (NLDFT) methods is more accurate as it takes fluid-fluid as well as fluid-wall interactions into account. These approaches are based on theoretical model isotherms which are calculated by methods of statistical mechanics.[197] Such isotherms (denoted as "local isotherms") are calculated by integration of the equilibrium density profiles of the fluid in the model pores in dependence of the relative pressure. An array of local isotherms calculated for a set of pore sizes with certain geometry in a given range for a given adsorbate is called a "kernel". A kernel can be regarded as theoretical reference for a given adsorption system. The calculation of the PSD is based on the correlation of these theoretical physisorption isotherms with the experimental data by solving the so-called integral adsorption equation (IAE).[189] It is important to note that the numerical values of a given kernel depend on various parameters, such as the gas-gas- and gas-solid interactions as well as the pore geometry. The validity of the applied model can be checked by comparison of the calculated NLDFT (fitting) isotherm with the experimental data. As the NLDFT methods take the nano-confinement of the fluid correctly into account, the pore size analysis is much more accurate compared to the BJH method as e.g. shown for OMS materials.[189] Furthermore, this method offers the advantage that the adsorption behavior of the fluid can be described over the entire range from micro- to mesopores.

In-spite of the fact that NLDFT is a suitable method for the calculation of the PSD of a variety of ordered and hierarchically structured materials, it does not sufficiently take the chemical and geometrical heterogeneities of the pore walls of carbon nanomaterials into account. The non-local DFT method assumes a structureless and smooth graphitic surface but in porous carbon materials the electron density of the surface is very heterogenic with curved pore walls and often many functional groups. In consequence,

the theoretical isotherm exhibits multiple adsorption steps related to the formation of a monolayer, second layer, and so on. However, these are experimentally not observed. This mismatch causes artificial gaps in the pore size distributions because the computational scheme fitting the experimental isotherm as a linear combination of the theoretical isotherms in individual pores attributes a layering step to a filling step within a pore of certain size. This problem can be overcome by the use of the so-called quenched solid density functional theory (QSDFT) method.[198] This method takes the surface heterogeneity of carbon materials correctly into account. The PSDs calculated by the QSDFT method do not contain anymore the artificial gaps typical for NLDFT. Although QSDFT methods are able to describe the PSDs of porous carbons much more accurately, pore blocking and cavitation effects can still cause artifacts if the PSD is calculated from the desorption branch of the isotherms. In consequence, advanced QSDFT methods have been developed. They calculate the pore size distribution from the adsorption branch taking correctly into account the delay in condensation due to metastable adsorption states.[199] The PSDs calculated from these advanced kernels do not reveal the artificial PSD peak. Although it is widely known that the QSDFT method is useful for the precise calculation of the PSD of carbon materials with even very complex pore structure, the method only leads to accurate results if the pore structure of the adsorbent is compatible with the chosen kernel.

3.1.4 Specific Surface Area

One way to access the specific surface area of a material from the nitrogen physisorption measurements is the use of the Langmuir equation.[200] This method has the drawback that it is not applicable for mesoporous materials because it assumes a monolayer of adsorbed molecules. However, this is not the actual situation in a mesopore. For substances containing such pores, the calculation of the SSA by the Brunauer-Emmett-Teller (BET) equation is the more accurate method because it assumes multilayer adsorption of a fluid on the pore surface with a different adsorption enthalpy between the first and the following layers.[201] From the BET equation (Equation 15), where V_{ads} is the total adsorbed volume, V_{Mono} is the volume of a monolayer, and C is the adsorption constant, $\frac{p}{(p_0-p)V_{ads}}$ is plotted against the relative pressure and the volume of the monolayer can be calculated by extrapolation of the line to its intersection with the y-axis $\frac{1}{C \cdot V_{Mono}}$ or from the slope $\frac{C-1}{C \cdot V_{Mono}}$.

$$\frac{p}{(p_0-p)V_{ads}} = \frac{1}{C \cdot V_{Mono}} + \frac{C-1}{C \cdot V_{Mono}} \frac{p}{p_0} \tag{15}$$

If the V_{Mono} is known, the SSA can be calculated according to Equation 16 where S_g is the SSA in m²/g, N_A is the Avogadro constant ($6.022 \cdot 10^{23}$ mol⁻¹), σ is the required surface area of a single N₂ molecule in dense package (0.162 nm²), V_{Mol} is the ideal gas volume ($2.241 \cdot 10^{-2}$ m³/mol), and m_{Ads} is the mass of the adsorbent.

$$S_g = \frac{N_A \cdot V_{Mono} \cdot \sigma_{N_2}}{V_{Mol} \cdot m_{Ads}} \tag{16}$$

3.1.5 Pore Volume

Total Pore Volume

Although many nanoporous materials can be well characterized by nitrogen physisorption it has to be noticed that the applicability of this molecule for the determination of the pore volume is limited. The accessibility of the smallest pores by nitrogen (kinetic diameter: 0.364 nm) is limited. Therefore, alternative adsorptive molecules, such as hydrogen, will lead to higher pore volumes. At upper pore sizes, the applicability of nitrogen is limited as well. According to the IUPAC standard, the total pore volume has to be calculated by the total amount of adsorbed nitrogen at high relative pressure (p/p_0 = 0.95). This volume is then converted into its liquid volume with the assumption that the nitrogen density of the adsorbed phase is equal to its bulk density (Gurvich rule).[190] As long as solely micro- and mesoporous materials are analyzed and the adsorption isotherm shows a plateau at high relative pressures, this method can be used. If larger pores are present, the isotherm does not reach saturation. In such a case, the total pore volume must be calculated for pores smaller than a certain size.

Micropore Volume

As for the calculation of the pore size distribution, classical macroscopic methods also exist for the calculation of the microprobe volume, such as the statistical thickness method (t-plot)[202] or the use of the Gurvich rule at p/p_0 = 0.2. However, in this thesis the pore size distributions of the discussed materials were calculated by QSDFT methods. Therefore, the micropore volume is mostly calculated according to the cumulative QSDFT pore volumes at a diameter of 2 nm.

3.2 Thermal Response Measurements (InfraSORP Technology)

As described in section 3.1, the use of volumetric gas physisorption, especially the adsorption of nitrogen at -196°C, is a widely used tool for the characterization of porous materials. Important structural parameters can be directly evaluated from the isotherm. A major drawback of these methods is the long time that is needed for one experiment.

Thermal response measurements are an attractive alternative for the rapid characterization of porous materials. The so-called InfraSORP technology is based on the optical adsorption calorimetry and measures the time-resolved temperature change (thermal response) of the porous adsorbent during adsorption of a test gas due to the release of the heat of adsorption (Figure 24).[203, 204] Once the maximum temperature is achieved, the sample cools down to equilibrium conditions due to the continuous supply of test gas (dynamic flow conditions).
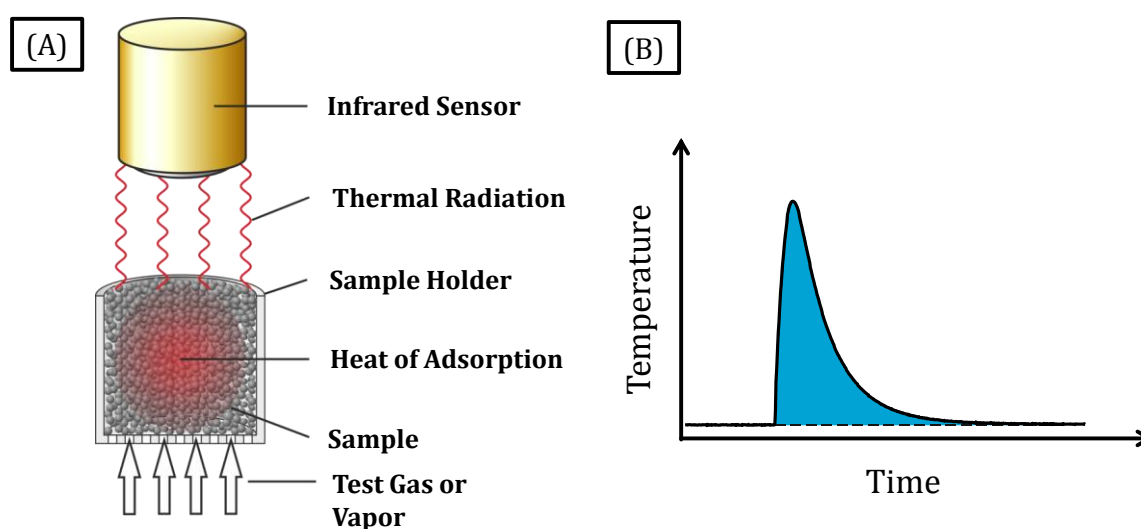
Figure 24. Setup of the thermal response measurement (A) and time-dependent thermal response curve with the integrated area marked in blue (B).

The magnitude of temperature change depends on the heat capacity of the material, the number of adsorbed molecules, the amount of heat released by each molecule, the speed of adsorption, and the heat transfer properties (convection, conduction, radiation) of sample and calorimeter. Thus, the thermal response curve of a porous material contains important information about the adsorption capacity which is assumed to be proportional to the heat released.[205] Furthermore, adsorption kinetics can be directly evaluated as the time constant of the optical calorimeter is negligible. Among different potential adsorptives, especially *n*-butane seems to be a very suitable probe molecule

due to its high heat of adsorption, low price, and non-toxic character. The saturation pressure of *n*-butane at RT is 2.4 bar and therefore the relative pressure is p/p$_0$ ~0.4 at 1 bar. Hence, this molecule fills micropores and potentially forms multilayers in mesopores at ambient conditions.

3.3 Mercury Intrusion Porosimetry

As described in section 3.1, nitrogen physisorption cannot be evaluated in terms of the total pore volume if the material contains pores which remain unfilled by the adsorptive at high relative pressures. In such a case, porosimetry can be applied to get more information about the pore structure (e.g. size, volume, and size distribution) as well as the bulk- and skeleton density. Porosimetry in general involves the intrusion of a non-wetting fluid into the pores of a material at high pressure by the use of a porosimeter. Mercury is highly attractive for probing pore space by porosimetry because it does not wet most substances and does therefore not penetrate pores by capillary action, unless it is forced to do so.[206] Furthermore, it has a high surface tension and a large contact angle. If mercury is forced into the pores, the required pressure is inversely proportional to the pore size, i.e. only slight pressure is required to force the liquid into large pores but high pressure is required to force it into small pores. The pore size can be determined based on the external pressure needed to force the liquid into a pore against the opposing force of the surface tension of the liquid. A quantitative relation between the pore diameter (d_{Pore}) and the applied pressure (P) is given by the Washburn equation (Equation 17), where θ is the contact angle of the intrusion liquid and σ is the surface tension of the intrusion liquid.

$$d_{Pore} = \frac{-4\sigma cos\theta}{P}$$
(17)

By measuring the volume of mercury that intrudes into the material by a certain pressure change, the volume of pores in the corresponding diameter range can be calculated.

4. Experimental Section

4.1 List of Used Chemicals

Table 1. *List of used chemicals.*

Chemical	Formula	Purity	Supplier
1,3,5 Trimethylbenzene (Mesitylene)	C_9H_{12}	98%	Sigma Aldrich
Aluminum Oxide Aeroxide Alu 130	Al_2O_3	> 99.8%	Evonik
Allylhydridopolycarbosilane (SMP-10)	not specified	n. s.	Starfire Systems
Azobisisobutyronitrile (AIBN)	$C_8H_{12}N_4$	98%	Sigma Aldrich
Cyclohexane	C_6H_{12}	99.7%	Merck
Ethanol	C_2H_5OH	99%	VWR
Hexadecane	$C_{16}H_{34}$	98%	Fluka
Hydrochloric Acid Solution	HCl	37%	BASF
Hydrofluoric Acid Solution	HF	35-40%	VWR
Methanol	CH_3OH	99.8%	VWR
Methylmethacrylate (MMA)	$C_5H_8O_2$	99%	Merck
para-Divinylbenzene (*p*-DVB)	$C_{10}H_{10}$	80%	Sigma Aldrich
Platinumdivinyltetramethyl-disiloxane in Xylene	$C_8H_{18}OPtSi_2$	2% Pt	Sigma Aldrich
Pluronic P123	$EO_{20}PO_{70}EO_{20}$	~100%	Sigma Aldrich
Polytetrafluoroethylene (PTFE)	$(C_2F_4)_n$	60% in H_2O	Sigma Aldrich
Potassiumperoxodisulfate	$K_2S_2O_8$	99%	Fluka
Silicon Dioxide Aerosol 90 and Aerosol 380	SiO_2	> 99.8%	Evonik
Sodiumhydroxide	NaOH	Technical	VWR
Sodiumdodecylsulfate (SDS)	$NaC_{12}H_{25}SO_4$	99%	Fluka
Sucrose	$C_{12}H_{22}O_{11}$	99%	Roth
Sulfur	S_8	> 99.5%	Sigma Aldrich
Sulfuric Acid	H_2SO_4	96%	Sigma Aldrich
Tetraethylorthosilicate (TEOS)	$Si(C_2H_5O)_4$	98%	Sigma Aldrich
Titanium Carbide	TiC	99%	Sigma Aldrich
Titanium Dioxide P25 and P90	TiO_2	99.5%	Evonik

4.2 List of Used Gases

Table 2. *List of used gases.*

Gas	Formula	Purity	Supplier
Argon 4.6	Ar	99.996%	Air Liquide
Chlorine 2.8	Cl_2	99.8%	Air Liquide
Hydrogen 3.0	H_2	99.9%	Air Liquide
Carbon Dioxide 4.5	CO_2	99.995%	Air Liquide
Nitrogen 5.0	N_2	99.999%	Air Liquide
Helium 5.0	He	99.999%	Air Liquide
Methane 5.5	CH_4	99.9995%	Air Liquide
n-Butane 3.5	*n*-C_4H_{10}	99.95%	Air Liquide

4.3 Materials Synthesis

4.3.1 Silica and Polymer Templates

Ordered Mesoporous SiO_2 (SBA-15)

The hexagonal ordered silica SBA-15 was synthesized by dissolving 66.8 g of the triblock copolymer Pluronic P123 ($EO_{20}PO_{70}EO_{20}$, Sigma Aldrich) in 1212 g deionized water and 38.6 g concentrated aqueous hydrochloric acid solution over night at 35°C in a 2000 ml polypropylene bottle under intense stirring. Then, 143.6 g of tetraethyl orthosilicate (TEOS, 98%, Sigma Aldrich) were added to the solution and the mixture was stirred at 35°C for another 24 h. The white suspension was then transferred to a teflon-lined autoclave and hydrothermally treated at 130°C for 24 h followed by filtration and washing with ~2000 ml deionized water/ethanol (1:1 by volume). For complete removal of the structure-directing agent, the SBA-15 was calcinated at 550°C for 5 h in a muffle furnace (60 K/h heating rate). The SiO_2 yield is 95-98%.

Mesocellular SiO_2 Foam (MCF)

28 g of Pluronic P123 were dissolved in 946 g deionized water and 165.5 g concentrated aqueous hydrochloric acid solution over night at 35°C in a 2000 ml polypropylene bottle under intense stirring. Then, 28 g 1,3,5 trimethylbenzene (Mesitylene, 98%, Sigma Aldrich) were slowly dropped into the mixture under continued stirring. After 2 h, 61.6 g TEOS were added to the solution followed by stirring for another 24 h. The white

suspension was then transferred to a teflon-lined autoclave and hydrothermally treated at 110°C for 24 h followed by filtration, washing and calcination in analogy to SBA-15.

Polymethylmethacrylate (PMMA) Template Spheres by the Miniemulsion Technique

In a slim 50 ml beaker, 0.25 g hexadecane (98%, Fluka) and 0.15 g azobisisobutyronitrile (AIBN, 98%, Sigma Aldrich) were dissolved in 6.2 g methylmethacrylate (MMA, 99%, Merck). To this mixture was added a solution of 0.072 g soduimdedecylsulfate (SDS, 99%, Fluka) in 24 g of deionized water and stirred for 10 min. Then, the miniemulsion was prepared by ultrasonicating the mixture for 2 min using an ultrasound finger Labsonic P (Sartorius) with 0.5 cycles at 90% amplitude under cooling with an ice bath. For polymerization, the miniemulsion was filtered over glass wool and treated over night at 80°C in a polypropylene bottle. The mixture was placed in a petri dish and water was evaporated at 80°C until the polymer became completely dry.

4.3.2 Hard-Templated CDCs

Ordered Mesoporous Silicon Carbide-Derived Carbon (OM-SiC-CDC)

Hexagonal ordered OM-SiC-CDCs were synthesized by the infiltration of 2 g of the SBA-15 powder (see section 4.3.1) with a mixture of SMP-10/*para*-divinylbenzene (4:1 by weight) by the incipient wetness method using a spatula and high pressure. The volume of the liquid mixture was chosen according to the pore volume of the silica (100 vol.% pore filling). The resulting yellow powder was then placed in an alumina boat in a horizontal tubular furnace equipped with an alumina tube and purged under flowing argon. The temperature was increased to 800°C and maintained there for 2 h (60 K/h heating rate). Silica removal was achieved by placing the pyrolyzed material in a mixture (150 ml) of deionized water/ethanol/concentrated aqueous hydrofluoric acid (HF) solution (1:1:1 by volume) for at least 3 h. After filtration and 3 times of washing with large amounts of ethanol, the obtained brown powder (ordered mesoporous silicon carbide, OM-SiC) was dried over night at room temperature (RT). For the high-temperature chlorine treatment, approximately 2 g of the OM-SiC were placed in a quartz boat in a quartz tube (inner diameter: 25 mm) in a horizontal tubular furnace and purged with 150 ml/min argon for approximately 1 h. Then, the temperature of the furnace was raised to 800°C while the argon flow was maintained at the same level

(450 K/h heating rate). At 800°C, the gas flow was subsequently changed to a mixture of 80 ml/min chlorine and 70 ml/min argon. After 3 h at 800°C, chlorine was switched off and the CDC was cooled to 600°C under an argon flow of 150 ml/min. Then, the gas flow was changed to 80 ml/min hydrogen and the temperature maintained for 1 h. After the post-reductive treatment, the samples were cooled to RT under moderate argon flow.

Carbide-Derived Carbon Mesofoams (CDC-MFs)

2 g of the mesocellular SiO_2 foam (see section 4.3.1) was infiltrated with 4.66 g SMP-10 by the incipient wetness method according to a theoretical pore filling of 100 vol.%. Pyrolysis was performed as described above for the OM-SiC-CDCs at different maximum temperatures ranging from 700-1300°C. The high-temperature chlorine treatments at maximum temperatures of 700 or 1000°C as well as post-reductive treatments under flowing hydrogen were also performed similar to the above-described samples.

Carbide-Derived Carbon Monoliths (CDC-Ms)

The used silica monoliths were provided by Prof. Dr. Bernd Smarsly and Martin von der Lehr (Justus-Liebig University Giessen, Institute of Physical Chemistry). 0.93 g of defined monoliths were placed into a 25 ml Schlenk tube together with a mixture of SMP-10/*para*-divinylbenzene (3:1 by weight) completely covering the pieces. The mixture was evacuated for 24 h at room temperature. The PCS loaded monoliths were then dried at 80°C for 12 h under air. Pyrolysis of the infiltrated monoliths was performed at a maximum temperature of 800°C for 2 h (30 K/h heating rate). Template removal was achieved by placing the pyrolyzed material in a mixture (150 ml) of deionized water/ethanol/concentrated aqueous hydrofluoric acid (HF) solution (1:1:1 by volume) for at least 24 h, washing with ethanol for several times and drying at 80°C over night. The high-temperature chlorine treatment at a maximum temperature of 800°C as well as the post-reductive treatment under flowing hydrogen were performed similar to the above-described samples.

4.3.3 CDCs from Emulsion Approaches

PolyHIPE-CDCs

In a 60 ml polypropylene bottle, 4.37 g SMP-10 and 1.71 g *para*-divinylbenzene were mixed under mild stirring to form the oil phase of the high internal phase emulsion

(HIPE) with a volume of 6.25 ml including 30 vol.% of the cross-linker. This was mixed with 2.13 g Span-80 (Fluka) as surfactant. After 1 min, a solution of 0.346 g $K_2S_2O_8$ in 18.75 ml distilled water was added drop-wise to the oil phase by continuously raising the stirring rate in order to ensure a homogeneous commingling. The resulting creamy emulsion was then held at 80°C for 24 h. The removal of surfactant was achieved by soxhlet extraction with a mixture of methanol/water (30:70 by volume) for 24 h. After drying at 80°C, the monolithic pieces of the PolyHIPEs were heated in a horizontal alumina furnace under flowing Argon to 700, 800, or 1000°C as described above (60 K/h heating rate). Finally, they were converted to CDCs by high-temperature chlorination at the maximum pyrolysis temperature as described above, followed by the conventional hydrogen annealing procedure at 600°C.

CO$_2$ Activation of PolyHIPE-CDCs

A large amount of PolyHIPE-CDCs was produced at a pyrolysis-chlorination temperature of 700°C without the post-reductive treatment under hydrogen. As a reference, 400 mg of this material was annealed under the above-described conditions. The CO$_2$ activations were performed using 400 mg of the large-batch chlorinated material for each experiment. The raw material was placed into a quartz boat inside a quartz tube (inner diameter: 25 mm) and purged with flowing argon. The sample was then heated to the elevated temperature of activation (450 K/h heating rate) followed by subsequently changing the gas flow to 50 ml/min carbon dioxide and annealed. As it is well-known that the activation is very sensitive to the temperature of the material, it has to be noticed that the given values are those of the furnace. The temperatures of the samples can be ~40 K lower. The activated samples were cooled down under flowing argon.

CDC Nanospheres (CDC-NS)

In a slim 50 ml beaker, 3 g SMP-10 and 2.74 g *para*-divinylbenzene or 4.2 g SMP-10 and 1.8 ml *para*-divinylbenzene were mixed according to volume ratios of 50:50 or 70:30, respectively. Then, 250 mg of hexadecane (98%, Fluka) were added. To this was added a solution of 0.072 g sodiumdodecylsulfate (SDS, 99%, Fluka) in 24 g of deionized water and stirred for 10 min. The miniemulsion was prepared by ultrasonicating the emulsion for 2 min using an ultrasound finger Labsonic P (Sartorius) with 0.5 cycles at 90% amplitude under cooling with an ice bath. For polymerization, the miniemulsion was

filtered over glass wool and 0.1 g of a solution of H_2PtCl_6 in water (1:1000 by weight) was added followed by a treatment at 80°C in a polypropylene bottle over night for cross-linking. The miniemulsion with the cross-linked organic phase was then transferred to a petri dish and the water phase was evaporated at 80°C. Pyrolysis of the dry cross-linked polycarbosilane spheres to silicon carbide materials, high-temperature chlorine treatment for the transformation to CDCs (both at a maximum temperature of 700°C), and the post-synthesis treatment under flowing hydrogen were performed as described above.

4.3.4 CDC Aerogels

Synthesis of CDC Aerogels

Polycarbosilane aerogels were prepared according to a slightly modified procedure previously reported by Sorarù and co-workers.[135] A mixture of 1.74 g SMP-10 and 1.62 g *para*-Divinylbenzene was dissolved in 24.9 g cyclohexane and stirred for 10 min at RT. 40 µl of the hydrosilylation-catalyzing complex platinumdivinyltetramethyldisiloxane (~2% Pt in xylene, Sigma Aldrich) were added and the mixture was stirred for another 5 min at RT followed by hydrothermal treatment in a teflon-lined autoclave at 200°C for 1 h. After cooling to RT, the bright yellow gel was transferred to a supercritical drying autoclave and the solvent was exchanged with liquid CO_2 at least twice a day for 5 days. The drying was achieved by raising the temperature of the autoclave to 37°C and the pressure up to 100-110 bar followed by decreasing the pressure to 1 bar over a period of approximately 2 h. The obtained PCS aerogels were pyrolyzed at 700 or 1000°C and the high-temperature chlorine treatments were performed at the maximum pyrolysis temperature followed by subsequent hydrogen annealing.

CO_2 Activation of CDC Aerogels

CO_2 activation of the CDC Aerogels was performed according to the procedure described for the PolyHIPE-CDCs (see section 4.3.3) at a maximum temperature of 950°C for 4 h.

4.3.5 CDCs from Sacrificial Templates

PMMA-templated CDC materials were synthesized by intense mixing of 4.5 g of the PMMA template spheres (see section 4.3.1) with 1.5 g SMP-10 in a mortar. The resulting yellow powder was subsequently pyrolyzed at a maximum temperature of 800°C for 2 h

(30 K/h heating rate). The high-temperature chlorine treatment at a maximum temperature of 800°C as well as the post-reductive treatment under flowing hydrogen was performed similar to the above-described samples.

4.3.6 Kroll-Carbons

Kroll-Carbons from TiO$_2$ Templates

P25 and P90 fumed titanium dioxide nanoparticles (P25 with SSA = 50 ± 15 m^2/g and P90 with SSA = 90 ± 20 m^2/g) were purchased from Evonik (Germany). In-house made TiO$_2$ nanoparticles were produced by M. Sc. Tim Biemelt by a flame spray pyrolysis process at the Institute of Inorganic Chemistry at the Technical University (TU) Dresden according to a procedure described by Madler and co-workers.[207] 2 g of titania nanoparticles were mixed in a petri dish with a 10 ml aqueous solution of 2.5 g of sucrose (99%, Roth Chemicals) to which was added 0.03 g 96% sulfuric acid. The resulting white dispersion was then left at 100°C for 3 h and at 160°C for another 3 h to achieve complete polymerization of the disaccharide. Approximately 2 g of the black hydrocarbon/titanium dioxide composite was then placed in a quartz boat inside a quartz tube (inner tube diameter 25 mm) in a horizontal tubular furnace and flushed with argon. The furnace was heated up to 900°C (300 K/h heating rate) and annealed for 1 h under constant argon flow. Subsequently, the gas flow was changed to a mixture of 80 ml/min chlorine and 70 ml/min argon for 2 h while keeping the temperature at the same level. The furnace was cooled down to room temperature under argon flow. A post-reductive treatment was performed in the same tube with 80 ml/min hydrogen at 600°C for 2 h.

Kroll-Carbons from Al$_2$O$_3$ Templates

For the synthesis of Kroll-Carbons based on Al$_2$O$_3$ templates, 2.54 g of Al$_2$O$_3$ nanoparticles (Aeroxide Alu 130 with SSA = 130 ± 20 m^2/g), purchased from Evonik (Germany), were dispersed in a solution of 5.0 g sucrose in 80 ml deionized water followed by the addition of 8 droplets (~160 mg) of concentrated sulfuric acid. The mixture was transferred to a Petri dish and treated for 3 h at 100°C and for another 3 h at 160°C. Carbonization and high-temperature chlorine treatment were performed similar to the Kroll-Carbons from TiO$_2$ Templates. A post-reductive treatment with 80 ml/min hydrogen at 600°C for 2 h was also carried out under similar conditions.

Kroll-Carbons from SiO$_2$ Templates

For the synthesis of Kroll-Carbons based on SiO$_2$ templates, 2.0 g of SiO$_2$ nanoparticles (Aerosil 380 with SSA = 380 ± 30 m^2/g and Aerosil 90 with SSA = 90 ± 15 m^2/g) were dispersed in a solution of 4.75 g sucrose in 10 ml deionized water followed by the addition of 2 droplets (40 mg) of concentrated sulfuric acid. The following synthesis steps are performed according to Kroll-Carbons based on TiO$_2$ and Al$_2$O$_3$ templates.

4.3.7 Miscellaneous Carbon Materials

Synthesis of Microporous CDCs from Polymer Precursors

The synthesis of microporous CDC materials from polymer precursors was performed starting from pristine SMP-10 polymer. Liquid SMP-10 was placed into an alumina boat into an alumina tube in a horizontal tubular furnace and purged under flowing argon. The temperature was increased to 700 or 1000°C and maintained there for 2 h (60 K/h heating rate). High-temperature chlorine treatment at a maximum temperature of 700 or 1000°C and the hydrogen treatment were performed similar to the CDC materials described above.

Synthesis of Microporous CDCs from Titanium Carbide Powder

Crystalline TiC powder (99%, Sigma Aldrich) with a particle size < 4 μm was used as CDC precursor. High-temperature chlorine treatments at different maximum temperatures and post-synthesis hydrogen treatments at 600°C were performed as for the OM-SiC-CDCs described above (see section 4.3.2).

Synthesis of CMK-3

In a Petri dish, 2 g of the SBA-15 template (see section 4.3.1) were mixed with a 10 ml aqueous solution of 2.5 g sucrose to which was added 0.28 g 96% sulfuric acid. Polymerization of the hydrocarbon was achieved by heating the mixture to 100°C for 6 h followed by subsequent heating to 160°C for another 6 h. Complete infiltration of template pores was achieved by repeating the procedure described above with a 10 ml aqueous solution of 1.6 g of sucrose to which was added 0.18 g of 96% sulfuric acid, again followed by heating to 100°C and 160°C. Carbonization was carried out under flowing argon atmosphere in a horizontal tubular furnace. The material was heated to 900°C (heating rate: 150 K/h) and annealed for 2 h. Silica removal was achieved by

placing the carbonized composite material in a mixture (150 ml) of deionized water/ethanol/concentrated aqueous hydrofluoric acid solution (1:1:1 by volume) for at least 3 h. After filtration and washing with large amounts of ethanol, the CMK-3 material was dried at RT.

4.4 Characterization Methods

4.4.1 Structural Characterization

Nitrogen Physisorption

Prior to all measurements the carbide and carbon samples were degassed under vacuum at 150°C over night. Polymeric materials were degassed under vacuum at 50°C to avoid structural deformation. Nitrogen physisorption experiments at -196°C were performed on a Quadrasorb apparatus (Quantachrome Instruments, USA). Low-pressure isotherms were measured on an Autosorb 1C (Quantachrome). The specific surface areas of the materials were calculated using the multi-point BET method. The corresponding relative pressure range is given at the appropriate position for each material. The total pore volume was calculated by the Gurvich rule. The corresponding relative pressure for the calculation is given at the appropriate position for each material. The pore size distributions were calculated using quenched solid density functional theory (QSDFT) method integrated into the ASiQwin 3.00 analysis software (Quantachrome). The specific kernel is given at the appropriate position for all PSDs. Micropore volumes were calculated from the cumulative pore volumes at a diameter of 2 nm.

Carbon Dioxide and Water Physisorption

Carbon dioxide physisorption measurements were performed at 0°C on the Autosorb 1C apparatus (Quantachrome). Pore size distributions were calculated by applying the non-local density functional theory (NLDFT, carbon dioxide on carbon) to the carbon dioxide physisorption isotherms.

Water vapor physisorption isotherms were measured at 25°C on a Hydrosorb 1000 apparatus (Quantachrome).

Raman Spectroscopy

Raman spectroscopic investigations of the CDC mesofoams (see section 5.2.1), PMMA-CDCs (see section 5.4), and the Kroll-Carbons from SiO_2 and Al_2O_3 templates (see section

5.6.2) were performed by Dr. Christoph Ziegler and M. Sc. Stefan Klosz (Institute of Physical Chemistry, Technical University Dresden). The spectra were obtained on a RM-2000 Raman microscope (Renishaw, United Kingdom) using a Gem532 (532 nm wavelength) laser (Laser Quantum, Germany) as the excitation source.

Raman spectra of the CDC aerogels (see section 5.3) and the carbon materials for the fundamental adsorption studies (see section 5.5.1) were performed by B. Sc. Jana Schaber (Institute of Bioanalytical Chemistry, Technical University Dresden). The spectra were recorded on a Holospec f/1.8 spectrograph (Kaiser Optical Systems, USA) at 785 nm excitation wavelength. The spectra were fitted with a 4-band fit (mixed Gaus-Lorentzian peak fitting).

Fourier Transform Infrared Spectroscopy (FTIR)

FTIR spectra of the materials pressed with dry KBr (1:300 by weight) were recorded by Dipl. Chem. Florian Wisser (Institute of Inorganic Chemistry, Technical University Dresden) by using a Bruker Vertex 70 (Bruker, USA) instrument in transmission mode at a resolution of 2 cm^{-1} with 32 scans.

Scanning Electron Microscopy (SEM) and Electron Dispersive X-ray Spectroscopy (EDX)

SEM investigations were performed on a Zeiss DSM982 (Carl Zeiss, Germany) at a beam voltage of 4 kV. The samples were sputtered with gold prior to analysis. Elemental analyses using EDX were obtained as a mean value of 3-5 measurements in a magnification of 3000-5000. SEM investigations of the PMMA-CDCs (see section 5.4) were performed at the Georgia Institute of Technology (GeorgiaTech, Atlanta, USA) Zeiss Ultra60 FE-SEM (Carl Zeiss, Germany) at a beam voltage of 5 kV.

Transmission Electron Microscopy (TEM)

The samples were prepared by shortly crushing the synthesized powders in a ball mill and suspending in ethanol or isopropanol under sonification. The resulting suspension was dropped onto a copper grid coated with holey carbon and dried under infrared light. The TEM investigations were carried out by Dr. Martin Lohe and M. Sc Giovanni Mondin (Institute of Inorganic Chemistry, Technical University Dresden) on a Cs-corrected JEOL JEM-2010F microscope (JEOL, USA) at an accelerating voltage of 200-300 kV. The TEM studies of the PMMA-CDC (see section 5.4) were performed at GeorgiaTech on a Tecnai G^2 F30 (FEI, Netherlands) at an accelerating voltage of 300 kV.

Dynamic Light Scattering (DLS)

DLS measurements of the highly diluted aqueous dispersions were performed at 25°C using the Zetasizer Nano-ZS (Malvern Instruments, United Kingdom).

Small-Angle X-ray Scattering (SAXS)

SAXS measurements were carried out on a Bruker Nanostar (Bruker) with $CuK_{\alpha 1}$ radiation ($\lambda = 0.154$ nm) and a position-sensitive Histar 2D detector.

Wide-Angle X-ray Diffraction (WAXD)

The measurements were performed in Bragg-Brentano geometry on a PANalytical X'Pert Pro (PANalytical, Netherlands) with $CuK_{\alpha 1}$ radiation.

Thermogravimetric Analysis (TGA)

TGA measurements were performed on a STA 409CD (Netzsch, Germany) in air or argon atmosphere with a heating ramp of 5-10 K/min.

Mercury Porosimetry

Mercury porosimetry of the PolyHIPE-CDCs (see section 5.1.1) and the CDC aerogels (see section 5.3) were performed by Dr. Matthias Thommes and Dr. Katie A. Cychosz (Quantachrome) on a PoreMaster-60 GT (Quantachrome). The mercury intrusion measurement of the CDC monoliths (see section 5.2.2) was performed by Dipl. Chem. Martin von der Lehr (Institute of Physical Chemistry, Justus-Liebig-University Gießen,) on a Pascal 140/440 porosimeter (Thermo Fisher Scientific, Italy). The PSDs were calculated from the mercury intrusion data by applying the Washburn equation. A contact angle of 140° was used for the calculation as well as a surface tension of 480 ergs.

4.4.2 Further Adsorption Measurements

Gravimetric n-Butane Adsorption

The measurements were performed with a micro-balance B111 (Setaram, France) in combination with a micro-calorimeter TG-DSC 111 (Setaram) at 25°C and atmospheric pressure under dynamic conditions (*n*-butane in nitrogen flow). Prior to all measurements, the samples were degassed at 150°C for 16 h in nitrogen flow.

Volumetric n-Butane Adsorption

The volumetric n-butane adsorption measurements were carried out at 5°C on a BELSORP-MAX apparatus (BEL, Japan).

n-Butane Breakthrough Measurements

n-Butane breakthrough measurements were performed at a total gas flow of 20 ml/min (*n*-butane diluted in nitrogen flow). The relative amount of the organic gas was varied by mass flow controllers. A cylindrical stainless steel cell (3 cm in length, 1 cm in diameter) was used as the adsorption column. Prior to the measurements, all samples were flushed with nitrogen for 1 h. Breakthrough curves were recorded by exhaust gas detection using a thermal conductivity detector.

High-Pressure Methane and Hydrogen Adsorption Measurements

High-pressure methane physisorption experiments were carried out at 25°C using a magnetic suspension balance (Rubotherm, Germany). The buoyancy corrections were performed as described elsewhere.[208] The helium measurement prior to the gravimetric methane adsorption was used for the determination of the skeleton density. Hydrogen adsorption measurements at -196°C were performed on a volumetric BELSORP-HP apparatus (BEL).

Thermal Response Measurements (InfraSORP)

The thermal response of the samples was measured using the previously described single-cell optical calorimeter setup (InfraSORP Technology by Fraunhofer/Rubotherm).[205] Small amounts of powdered sample (5-25 mg) were placed in the sample cell and purged with nitrogen until a constant sample temperature was observed. When the sample was at constant temperature, it was exposed to a flow of 70 ml/min of the test gas (carbon dioxide or *n*-butane) using a mass flow controller. The thermal response function was fitted to the measured data using Origin 7.5 software.

For *n*-butane adsorption/desorption cycling of the samples (see sections 5.2.2 and section 5.5.3), the samples were exposed to the test gas for a certain time. Then, nitrogen was passed by the sample cell to remove *n*-butane from the lines for 90 s. Subsequently, the nitrogen flow was subjected to the sample cell for a certain duration initializing desorption of *n*-butane from the samples leading to a decrease of the temperature. In the

subsequent cycles, *n*-butane was adsorbed again on the partially desorbed samples for the same time as in the first cycle, lines were flushed with nitrogen for 90 s, and the hydrocarbon was desorbed under nitrogen flow for a longer time compared to the prior cycles, followed by the repeated adsorption of *n*-butane, the further increased desorption, and so on.

4.4.3 Nuclear Magnetic Resonance (NMR) Spectroscopy Measurements

Solid-State Magic Angle-Spinning (MAS) NMR

The solid-state NMR spectroscopy investigations (see section 5.5.1) were performed by Dr. Silivia Paasch and Prof. Dr. Eike Brunner (Institute of Bioanalytical Chemistry, Technical University Dresden). The carbon samples were loaded with 1 M $TEABF_4$ in AN by the incipient wetness method, i.e. the amount of solution was exactly adjusted to the available pore volume in order to avoid an excess of solution in the interparticle space surrounding the particles of the material. Solid-state ^1H, ^{11}B and ^{13}C NMR spectra were recorded on a Bruker AVANCE 300 spectrometer using a commercial 2.5 mm double-resonance (^1H, X) MAS NMR probe. During signal acquisition, SPINAL ^1H-decoupling was applied.[209] The MAS frequency was 16 kHz. The spectra were recorded with a recycle delay of 3 s for ^1H and ^{11}B and 180 s for ^{13}C. Ramped-amplitude cross-polarization (CP)[210] was applied for the acquisition of $^{13}C\{^1H\}$ CP MAS NMR spectra.

^{129}Xe NMR

The ^{129}Xe NMR investigations (see section 5.5.1) were performed by M. Sc. Julia Pallmann and Prof. Dr. Eike Brunner (Institute of Bioanalytical Chemistry, Technical University Dresden). The experiments were carried out by using a homemade *in-situ* high-pressure apparatus.[211] Samples were transferred into the single crystal sapphire tube under argon atmosphere. The samples were activated over night using high vacuum (10^{-8}-10^{-7} bar) to prevent artifacts due to surface adsorption of atmospheric molecules. The application of relative pressures $p/p_0 = 1$ would require an absolute pressure of ~60 bar within the tube at RT. Although the sapphire tube withstands such pressures, the tubing connecting the tube inside the magnet with the outside pump rack and xenon reservoir does not allow this pressure. However, at the chosen lower temperature (237 ± 3 K), a relative pressure of $p/p_0 = 1$ corresponds to ~19 bar. This is accessible for the apparatus. After pressurizing the samples, a subsequent equilibration

phase of at least 15 min has been deferred. In the case of cooled samples, a further phase of minimum 1 h was incorporated for thermal equilibration. All experiments were performed using an Avance 300 (Bruker, Karlsruhe, Germany) NMR spectrometer coupled with a BIOSPIN SA BCU-Xtreme unit (Bruker). The ^{129}Xe NMR spectra were recorded at a resonance frequency of 83.02 MHz using a 10 mm HR probe, a pulse length of 6 µs, and relaxation delays of 5 s. Temperature calibration and referencing of the ^{129}Xe NMR chemical shift have been performed as previously described.[211]

4.4.4 Electrochemical Characterization

Electrode Materials in EDLCs

The characterization of the CDC nanospheres (see section 5.1.2) and the CDC mesofoams (see section 5.2.1) was performed by Dipl. Chem. Katja Pinkert (Institute for Complex Materials, Leibniz Institute for Solid State and Materials Research Dresden). The carbon materials were suspended in acetone and mixed with a polyvinylidene-difluoride (PVDF)-acetone solution, resulting in a carbon:PVDF mixture (95:5 by weight) without conductive agent. The slurry was uniformly dropped on a platinum coin current collector with a diameter of 12 mm and dried at 80°C for 12 h. Each electrode comprised about 5 mg of active material. Two electrodes were assembled in a symmetrical electrode configuration, separated by a Whatman GF/D glass microfiber filter (GE Healthcare Life Sciences, USA), and soaked with the aqueous electrolyte (1 M H_2SO_4). The sandwich was placed in a Swagelok-type test cell. Electrochemical measurements were carried out at 25°C using a multichannel VMP3 potentiostat–galvanostat (Bio-Logic, France). The capacitance determination of the symmetrical two-electrode cells was accomplished by cyclic voltammetry (CV) experiments at different scan rates. Five cycles were measured at each potential scan rate and the capacitance was calculated from the 5th cycle. The differential specific capacitance for CV plots at different scan rates is calculated according to Equation 18, where C_{spec} is the differential specific capacitance in F/g (based on the mass of electroactive material in a single electrode), I_{spec} is the specific response current density at the applied potential step in A/g (based on the mass of electroactive material in a single electrode), and ν is the potential scan rate in mV/s.

$$C_{spec} = \frac{I_{spec}}{\nu} \tag{18}$$

The integral specific capacitance is calculated according to Equation 19, where I_{spec} is the specific response current density in A/g (based on the mass of electroactive material in a single electrode) integrated over the applied potential window V_2-V_1.

$$C_{spec} = \frac{1}{\nu \, (V_2 - V_1)} \int_{V_1}^{V_2} I_{spec} dV \qquad (19)$$

Galvanostatic charge-discharge (C-D) measurements up to 0.9 V were performed at current densities from 1-20 A/g (based on the mass of electroactive material in a single electrode). The specific capacitance was calculated according to Equation 20, where dV/dt is the slope of the discharge curve in V/s.

$$C_{spec} = \frac{2 I_{spec}}{\left(\frac{dV}{dt}\right)} \qquad (20)$$

Potentiostatic impedance spectroscopy was carried out in the frequency range from 1 mHz-100 kHz with a 10 mV alternating current (AC) amplitude. The specific capacitance was calculated according to Equation 21 where f is the operating frequency in Hz, $Im(Z)$ is the imaginary part of the total device resistance in Ω, and m is the mass of electroactive material in a single electrode.

$$C_{spec} = \left(\frac{2}{2 \, \pi \, f \, Im(Z) \, m}\right) \qquad (21)$$

The characterization of the CDC aerogels (see section 5.3.2) and the Kroll-Carbons based on silica or alumina templates (see section 5.6.2) was performed at GeorgiaTech. The materials were ground into powders in a mortar and were suspended in ethanol under mild sonication. A suspension of polytetrafluoroethylene binder (PTFE, 60 wt% in water, Sigma Aldrich) was added and the resulting slurry of 5 wt% PTFE and 95 wt% of carbon was concentrated by slow evaporation of ethanol at 80°C under constant stirring. The highly viscous mixture was then dried on a glass plate and mixed with razor blades. When the mass became dry with a rubberlike (clay) consistency, it was rolled to a thickness of ~150 μm between aluminum foil sheets using a roll mill. The resulting composites were dried over night at 80°C under vacuum.

For the measurements in the aqueous electrolytes, electrodes of ~1 cm^2 (2-3 mg active material) were cut out and the device assembly took place under air atmosphere. A high-purity gold foil (Sigma Aldrich, USA) was used as the current collector and a commercially available Dreamweaver Silver separator (Dreamweaver International,

USA) was placed between the electrodes. The sandwich was assembled in a beaker-type cell configuration and held together using Teflon slabs and screws. Sufficient wetting of the porous carbon electrodes with sulfuric acid was ensured by adding an excess of electrolyte solution to the beaker followed by a treatment under vacuum at RT for 1 h. For the measurements in the ionic liquid electrolyte EMIBF$_4$, (> 98%, IoLiTec Ionic Liquids Technologies GmbH, Germany) and the organic electrolyte 1 M TEABF$_4$ in AN, the devices were assembled in a stainless steel coin cell configuration in an argon filled glovebox. Carbon coated aluminum foil was used as the current collector and the above mentioned Dreamweaver product as the separator. In case of the organic electrolyte, a GORE membrane (W.L. Gore and Associates, USA) of 25 μm in thickness and with 60% porosity was used (4-5 droplets of the electrolyte were used for the wetting of the electrodes and the separator and the excess amount was removed during compression of the coin cell).

For electrochemical measurements, aluminum contacts were fixed to the coin cells. CV measurements were performed on a Solartron 1480A (AMETEK Advanced Measurement Technology, USA) from -0.6-0.6 V (aqueous electrolyte), 0-2.0 V (organic electrolyte), or -2.0-2.0 V (ionic liquid electrolyte) at scan rates of 1-1000 mV/s. The gravimetric capacitance of each electrode at different scan rates was calculated from the CV data according to Equation 22 where dU/dt is the scan rate, m is the mass of active material in a single electrode, and $I(U)$ is the total current.

$$C_{electrode} = 2C_{cell} = \left(\frac{2}{(dU/dt)m}\right)\left\{\int_{-0.6V}^{0.6V} I(U)dU - \int_{-0.6V}^{0.6V} I(U)dU\right\}\frac{1}{2}\frac{1}{1.2V} \qquad (22)$$

C-D experiments at charge/discharge current densities of 0.1-20 A/g (based on the mass of a single electrode) were carried out with an Arbin SCTS supercapacitor testing system (Arbin Instruments, USA). The specific capacitance was calculated according to Equation 23 where I is the total current, dU/dt is the slope of the discharge curve, and m is the mass of active material in a single electrode.

$$C_{electrode} = 2C_{cell} = \left(\frac{2I}{(dU/dt)m}\right) \qquad (23)$$

EIS measurements were performed on a Gamry Potentiostat (Gamry Instruments, USA) from 100 kHz-1 mHz with a 10 mV alternating current (AC) amplitude.

Electrode Materials in Li-S Batteries

Electrochemical characterization of the CDC mesofoams (see section 5.2.1) and the KCs from titania templates (see section 5.6.1) were performed by M. Sc. Sören Thieme (Fraunhofer Institute for Material and Beam Technology (IWS) Dresden). The carbon/S nanocomposites were prepared by combining pristine sulfur (Sigma Aldrich, ≥ 99.5%) with finely ground carbon material in a defined C:S weight ratio. After homogenization in a mortar, the mixture was transferred into a ceramic crucible and heated to 155°C for 12 h under air to perform the melt infiltration of sulfur. The cathodes were prepared by homogeneously mixing multiwalled carbon nanotubes (MWCNT, NanocylNC 7000 series) as the conducting agent and poly(tetrafluorethylene) (PTFE, ABCR) binder with the carbon/S nanocomposites in a defined weight ratio followed by intensive grinding at elevated temperature. The as-prepared self-supporting cathode foil was laminated onto a carbon-coated, expanded aluminum current collector (Benmetal, 99.5% with 20% Electrodag EB-012). Circular electrode discs (diameter 12 mm, area 1.131 cm^2) were punched out for electrochemical characterization.

For electrochemical characterization, the carbon/S composite cathode (working electrode), one layer of Celgard 2500 separator (Celgard, USA), and a lithium metal chip (Pi-Kem, 99.0%, diameter 15.6 mm, thickness 250 μm) were stacked and subsequently sealed airtight in 2016 coin cells. Prior to stacking, the cathode was thoroughly wetted with 8 μl liquid electrolyte per mg of sulfur consisting of 1 M lithium-bis(trifluoromethylsulfonyl)imide (LiTFSI, Sigma Aldrich, 99.95%) and 0.25 M lithium nitrate additive (LiNO$_3$, Alfa Aesar, 99.98%, anhydrous) dissolved in a mixture (1:1 by volume) of 1,2-dimethoxyethane (DME, Aldrich, 99.5%, anhydrous) and 1,3-dioxolane (DOL, Aldrich, 99.8%, anhydrous). The whole cell assembly took place in an argon-filled glove box. The long-term stability of the carbon/S composite cathode was investigated by galvanostatic cycling at room temperature at different current rates with a Cell Test System (BASYTEC, Germany) in a voltage range of 1.8-2.6 V vs. Li/Li$^+$.

The electrochemical testing of the PMMA-CDCs as Li-S cathode components was performed at GeorgiaTech. The S/PMMA-CDC composites and polyacrylic acid (PAA, Polysciences) as a binder were mixed in water:ethanol (1:3 by weight) to prepare a slurry for casting an electrode. The ratio of S/PMMA-CDC to PAA binder was 85:15 by weight. No conductive additives were used. The slurry was stirred at room temperature for 1 h and cast on an aluminum foil. After drying overnight at RT under vacuum, coin

cells were assembled with 1 M, 3 M, and 5 M LiTFSI in dimethoxyethane (DME):1,3-dioxolane (DIOX) (1:1 by volume) as electrolyte, a celgard2400 (Celgard) separator and a pure Li foil (Alfa Aesar, 99.9%) as anode. 0.2 M $LiNO_3$ (Alfa Aesar, 99.99%) was added to the electrolyte as an additive. The cells were equilibrated for 24 h before operation. The average sulfur surface loading was ~0.5 mg/cm². The coin-cells were assembled inside an argon-filled glovebox and cycled with different C-rates in the range 3.0-1.2 V vs. Li/Li⁺ in galvanostatic mode using an Arbin battery test system (Arbin Instruments). The durability test was carried out at 0.2 C with separate cells.

5. Results and Discussion

The major aim of this PhD thesis was the controlled design of carbon nanomaterials with hierarchical pore structures for applications related to gas adsorption and electrochemical energy storage. For the synthesis of these materials, several templating approaches were applied and a wide range of pore sizes and pore geometries as well as different textures on the nanoscale are approachable. In chapters 5.1-5.4, novel carbide-derived carbon materials with tuned secondary pore sizes in addition to the typical CDC microporosity are presented (Figure 25). Their synthesis-structure relationships and their potential applications in gas adsorption and electrochemical energy storage are discussed. Furthermore, particular interest was pointed on the use of CDCs as model materials for a rather detailed understanding of the fundamentals of adsorption processes on porous carbon surfaces. The results of these investigations are presented in section 5.5. A new class of primarily mesoporous carbon materials (designated as Kroll-Carbons, KCs) is described in section 5.6. These materials were produced by the reductive carbochlorination reaction between oxidic nanoparticles (fumed titania, fumed silica, and fumed alumina) and a surrounding carbon matrix.
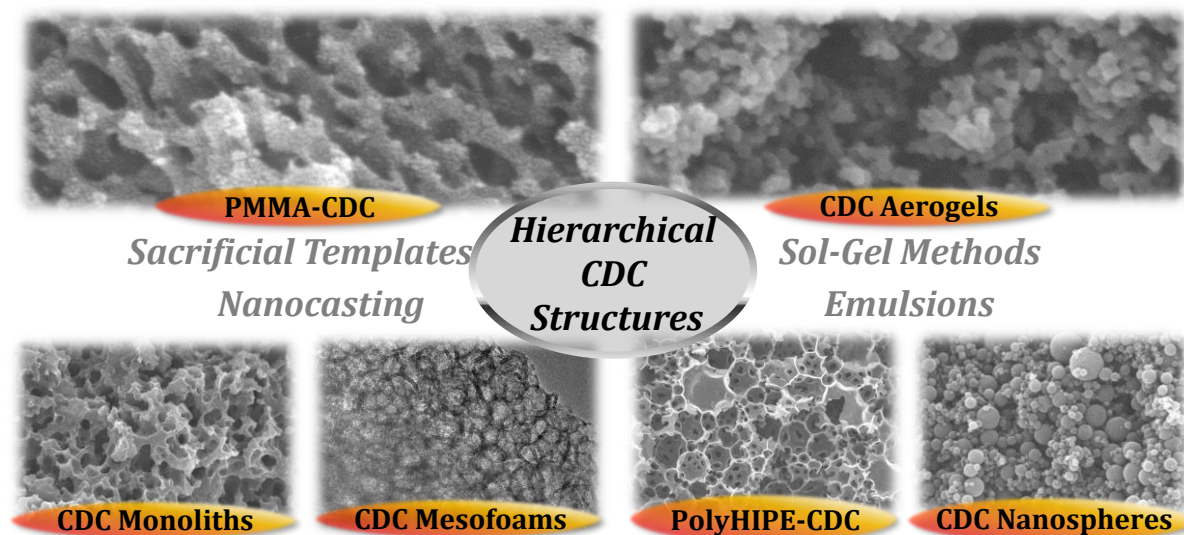
Figure 25. SEM or TEM micrographs of the CDC structures synthesized within this thesis.

5.1 CDCs from Emulsion Approaches

Emulsion approaches (see section 2.3.3) are widely used for the synthesis and functionalization of nanostructured solids. Within this thesis, two different types of emulsions are used for the synthesis of nanoporous carbide-derived carbon materials.

High Internal Phase Emulsions (HIPEs) are applied for the synthesis of macroporous CDC materials with micro- and mesoporous walls. These carbons offer a combination of large capacities with high accessibility of the nanopores and are therefore very attractive for the use in hydrocarbon adsorption.[212] A post-synthetic activation procedure can be applied to further increase their specific surface areas and micropore volumes leading to even higher uptakes.[213]

Furthermore, miniemulsions were used for the synthesis of uniformly-sized CDC nanospheres with diameters of 20-400 nm. These materials are spherically shaped and their pore structure can be influenced by the amount of organic cross-linker in the miniemulsion. In symmetrical EDLCs in aqueous electrolyte, CDC nanospheres offer high gravimetric capacities.

5.1.1 PolyHIPE-CDCs

Synthesis and Structure

The PolyHIPEs are produced by cross-linking of the preceramic allylhydrido-polycarbosilane SMP-10 with the cross-linker *para*-divinylbenzene in the oil phase of high internal phase emulsions (HIPEs). An aqueous solution of the radical initiator $K_2S_2O_8$ acts as the internal phase and the droplets are stabilized with the surfactant Span-80 (Figure 26).
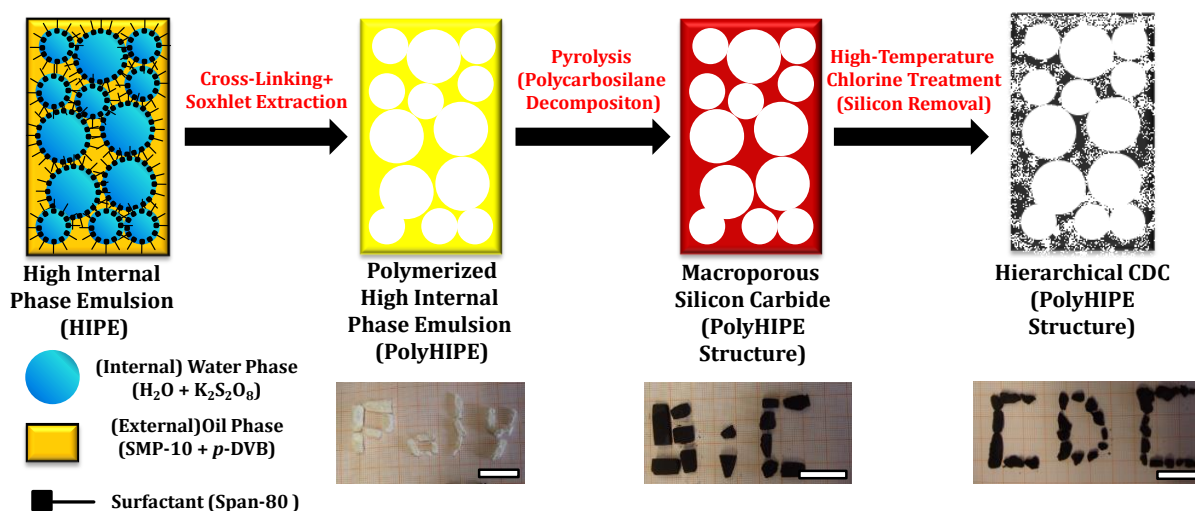
Figure 26. *Procedure for the preparation PolyHIPE-CDC and photographs of the materials in different synthesis stages (scale bar: 1 cm).*

After cross-linking of the polymer chains and surfactant removal by a soxhlet extraction procedure, the resulting PolyHIPEs are pyrolyzed to silicon carbides (PolyHIPE-SiC) at

maximum temperatures of 700, 800, or 1000°C and subsequently converted to PolyHIPE-CDCs by high-temperature chlorine treatment at the maximum pyrolysis temperature. The monolithic morphology of the PolyHIPEs can be fully maintained over the entire synthesis pathway (Figure 26). This allows the production of these CDCs in complex shapes without the use of additional binding agents which is most often a highly desired property for porous carbon materials. A post-reductive treatment under flowing hydrogen is performed to ensure the removal of residual chlorine and metal chlorides adsorbed in the pores of the PolyHIPE-CDCs after silicon extraction. In consequence, the finally obtained materials show carbon contents of 99.9 wt.% at all applied synthesis temperatures. Potential impurities of chlorine, silicon and oxygen are below the detection limit (Table 3).

Table 3. *EDX analyses of PolyHIPE-SiCs and PolyHIPE-CDCs prepared at different temperatures.*

Material	Carbon (wt.%)	Silicon (wt.%)	Oxygen (wt.%)	Chlorine (wt.%)
PolyHIPE-SiC-700°C	63.3	28.9	7.8	-
PolyHIPE-SiC-800°C	56.7	35.8	7.5	-
PolyHIPE-SiC-1000°C	59.6	29.9	10.5	-
PolyHIPE-CDC-700°C	> 99.9	< 0.1	< 0.1	< 0.1
PolyHIPE-CDC-800°C	> 99.9	< 0.1	< 0.1	< 0.1
PolyHIPE-CDC-1000°C	> 99.9	< 0.1	< 0.1	< 0.1
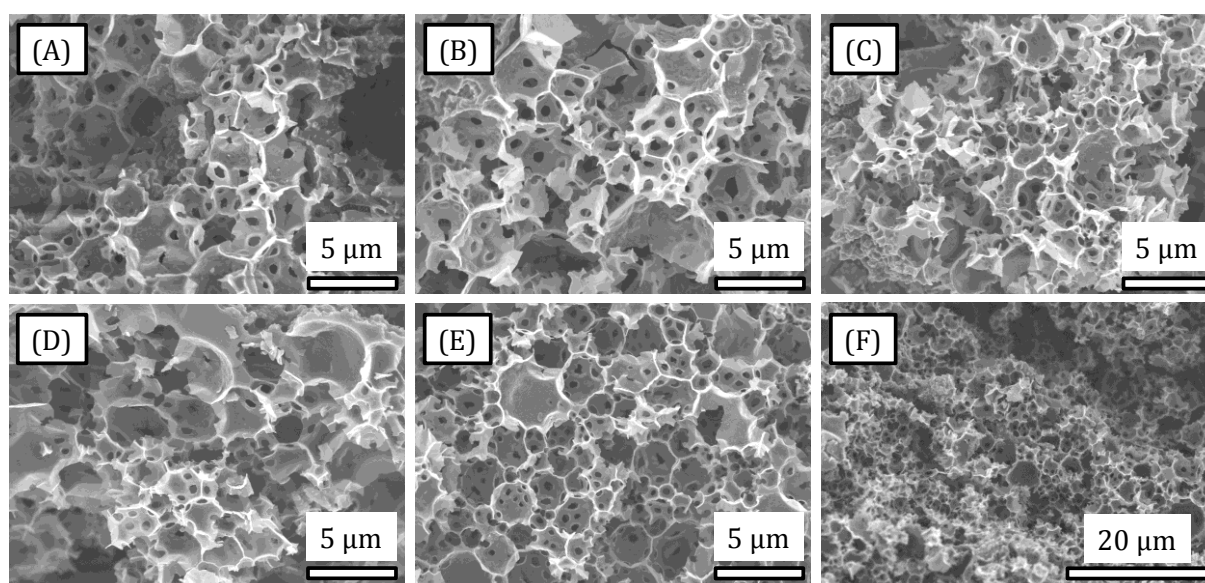
Figure 27. *SEM micrographs of the PolyHIPE-SiCs (A-C) and PolyHIPE-CDCs (D-F) prepared at 700°C (A and D), 800°C (B and E), and 1000°C (C and F).*

SEM images of the silicon carbide intermediates before the high-temperature chlorine treatment (Figure 27) show the presence of a macroporous network that is typical for PolyHIPEs.[131] It consists of large pores (voids) in the μm-range. They are interconnected by smaller gates (windows) of several 100 nm in diameter. This leads to advanced accessibility of the surface area throughout the entire particle and the absence of closed pores. Due to the highly conformal character of the high-temperature chlorine treatment (i.e. the absence of volume shrinkage or sintering processes), this morphology does not change during silicon removal. The carbide-derived carbon materials exhibit a similar macroporous structure independent of the elevated synthesis temperature (Figure 27).
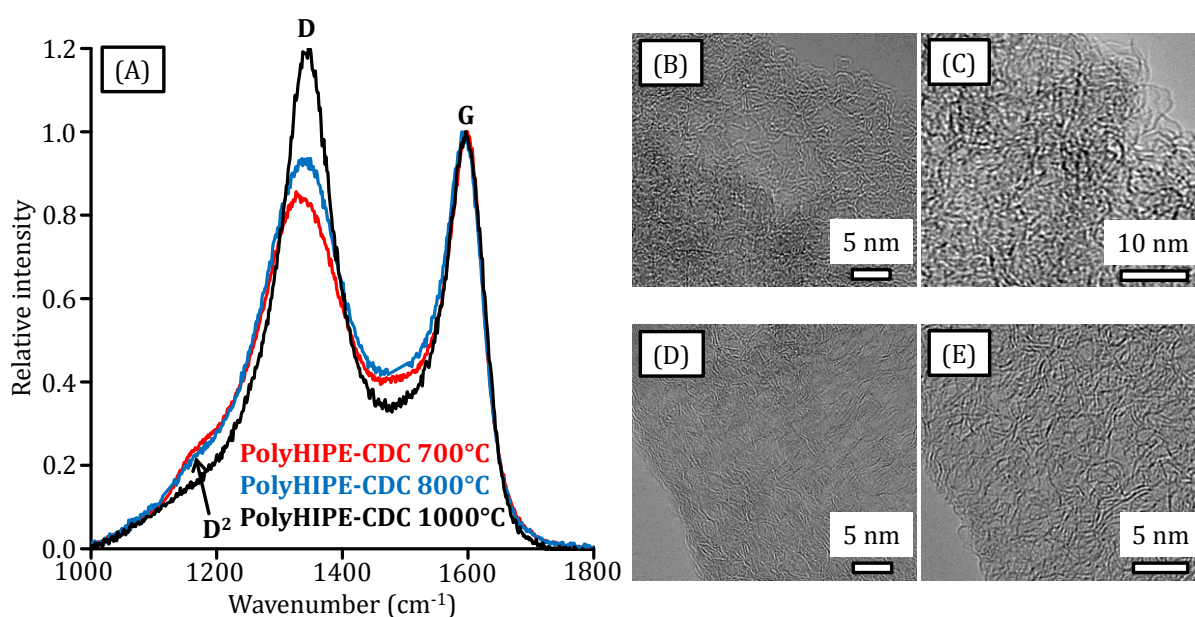
Figure 28. *Raman spectra (A) of PolyHIPE-CDCs prepared at 700°C (red), 800°C (blue), and 1000°C (black) and TEM micrographs of PolyHIPE-CDCs prepared at 700°C (B and C) and 1000°C (D and E).*

Raman spectra of Poly-HIPE-CDCs (Figure 28(A)) are comparable with those originally reported for microporous carbide-derived carbons.[82] They are typical for highly amorphous carbon materials built-up by mostly disordered carbon fringes. The area and intensity of the D-band (associated with the presence of defective graphite domains) and therefore the I_D/I_G ratio increases when the synthesis temperature rises from 700°C to 1000°C owing to the preferred formation and organization of sp^2 hybridized carbon. The decreasing full-width at half maximum (FWHM) of the D-band (Table 4) as well as the disappearance of the shoulder D^2-band also indicate increased structural ordering in the CDCs prepared at higher temperatures.
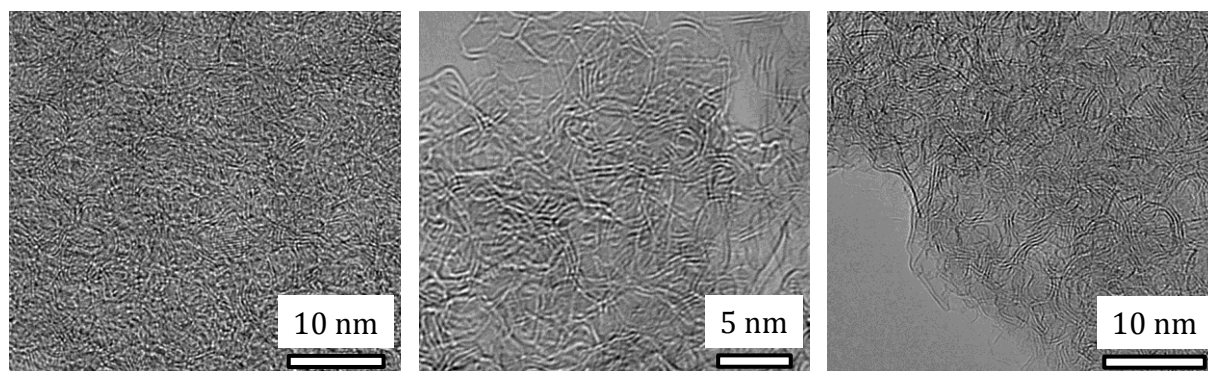
Figure 29. *TEM micrographs of PolyHIPE-CDCs pyrolyzed at 1500°C and chlorinated at 1000°C.*

Table 4. *Porosity and Raman data summary of PolyHIPE-CDCs prepared at different temperatures.*

Material	SSA_{BET} (m^2/g)[a]	V_{Micro} (cm^3/g)[b]	$V_{Micro+Meso}$ (cm^3/g)[c]	V_{Macro} (cm^3/g)[d]	FWHM D-band (cm^{-1})	I_D/I_G
PolyHIPE-CDC-700°C	2345	0.73	1.10	7.45	171	1.26
PolyHIPE-CDC-800°C	2201	0.69	1.03	6.99	162	1.31
PolyHIPE-CDC-1000°C	1649	0.58	0.74	5.58	106	1.45

[a] Specific surface area calculated using the BET equation (p/p_0 = 0.01-0.1).

[b] Micropore volume calculated from the cumulative pore volume up to a diameter of 2 nm (QSDFT method for nitrogen on carbon with slit/cylindrical pores at -196°C, adsorption branch kernel).

[c] Micro- and mesopore volume calculated at p/p_0 = 0.95.

[d] Macropore volume calculated from mercury intrusion porosimetry (pores > 50 nm).

TEM investigations of the carbon microstructure visualize the highly amorphous structure of PolyHIPE-CDC prepared at 700°C (Figure 28(B,C)). When the temperature is increased to 1000°C, some parallel arranged fringes can be observed in the carbon microstructure indicating the onset of graphitization which is responsible for the higher intensity of the D-band. However, because these ribbons are still curved and only 2-4 layers are stacked. Hence, the presence of a purely graphitic nanostructure can be ruled out (Figure 28(D,E)). This difference in the carbon structure is related to the rather amorphous character of the silicon carbide precursor at lower pyrolysis temperature with longer inter-atomic distances which hinder the formation of graphitic carbon crystallites. Moreover, the mobility of the carbon atoms in the reorganization during chlorination at 700°C is significantly lower compared to higher temperatures and

therefore the preferred formation of amorphous carbon can be observed. In accordance, TEM images of a macroporous CDC obtained from PolyHIPE-SiC pyrolyzed at a maximum temperature of 1500°C and chlorinated at 1000°C show the presence of planar and parallel arranged graphitic carbon domains which are significantly larger in stacking number and length compared to the CDCs obtained from the PolyHIPE-SiC prepared at 1000°C despite the equal conditions of the chlorine treatment (Figure 29).[214]

Nitrogen physisorption measurements (Figure 30(A,B)) further underline the differences of the carbon microstructures present at different synthesis temperatures which significantly influence the micro- and mesoporosity of PolyHIPE-CDCs. Large uptakes of nitrogen at low relative pressures are observed for all samples independent of the elevated temperature due to the filling of the narrow micropores present in the materials. BET SSAs of 2345, 2201, and 1649 m^2/g and total micro-mesopore volumes of 1.1, 1.03, and 0.74 cm^3/g are achieved at synthesis temperatures of 700, 800, and 1000°C, respectively (Table 4). The decreasing micropore volumes and surface areas are related to the preferred formation of graphitic carbon and rather narrow micropores at higher temperatures.
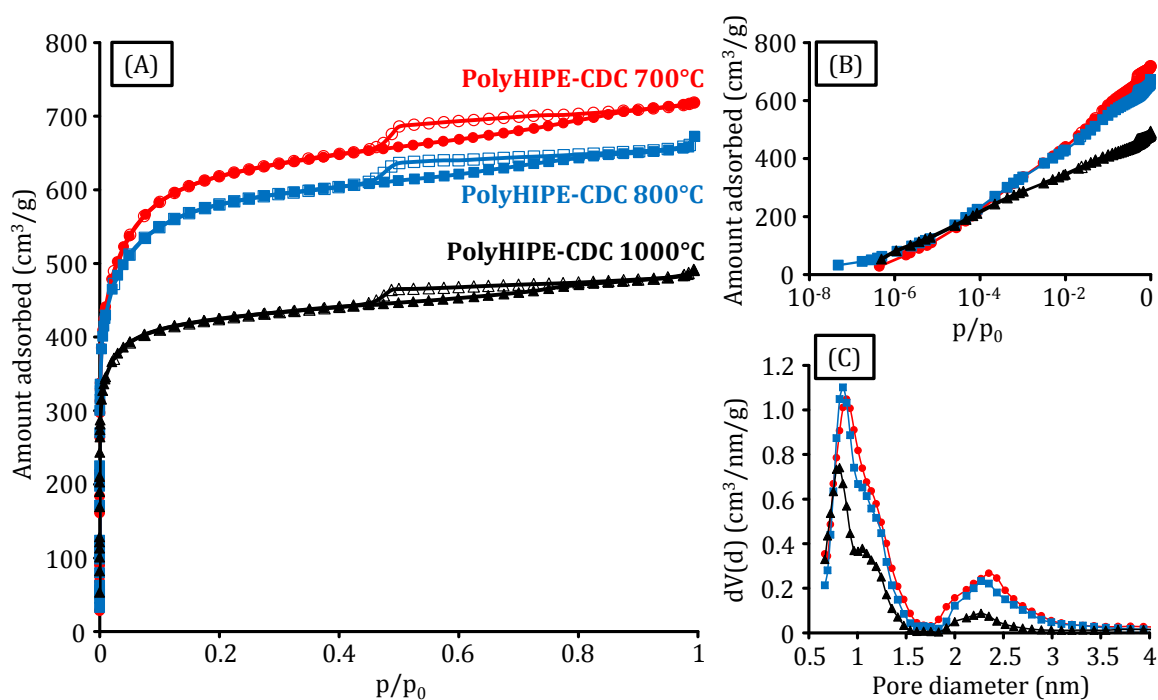
Figure 30. *Linear (A) and semi-logarithmic (B) plots of nitrogen physisorption isotherms (-196°C) and corresponding QSDFT (nitrogen on carbon with slit/cylindrical pores at -196°C, adsorption branch kernel) pore size distributions (C) of PolyHIPE-CDCs prepared at 700°C (red circles), 800°C (blue squares), and 1000°C (black triangles).*

Although the walls of PolyHIPE-CDCs predominantly contain micropores, the nitrogen adsorption isotherms show hysteresis loops of type H4 indicating the presence of a certain amount of mesopores. The step in the desorption branches at a relative pressure p/p_0 = 0.4-0.5 is caused by the presence of cavitation effects within the pore structure of the CDCs because some mesopores are accessible only through the micropores (see section 3.1.2). Hence, the condensed nitrogen in these pores does not desorb under equilibrium conditions but rather by the formation of vapor bubbles which diffuse out. Due to this, the pore size distributions have to be calculated from the adsorption braches of the isotherms (see section 3.1.3). As already suggested from the shape of the isotherms, the QSDFT-PSDs (Figure 30(C)) show the presence of both micro- and mesopores with maxima in the diameter ranges of 0.8-0.9 nm and 2.2-2.3 nm, respectively. The meso- as well as the micropores of the PolyHIPE-CDC prepared at 1000°C are slightly narrower compared to the materials prepared at lower temperatures.
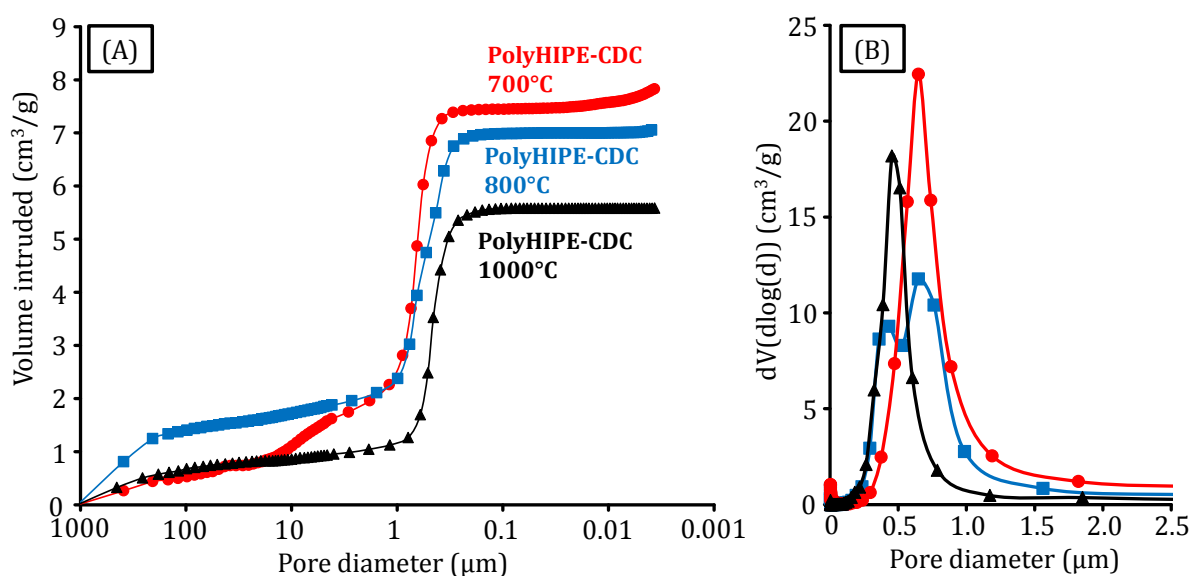
Figure 31. *Mercury intrusion curves (A) and corresponding macropore size distributions (B) of PolyHIPE-CDCs prepared at 700°C (red circles), 800°C (blue squares), and 1000°C (black triangles).*

Due to the interconnected void-window-type pore system, PolyHIPE-CDCs offer extremely high pore volumes on the macroscopic scale. This is shown by the large amounts of intruded liquid in mercury porosimetry measurements (Figure 31(A)). If only the pores above 50 nm are taken into consideration, the materials offer pore volumes as high as 7.45, 6.99, and 5.58 cm³/g for synthesis at 700, 800, and 1000°C, respectively (Table 4). In combination with the micro- and mesopores, PolyHIPE-CDC

prepared at 700°C contains an intrinsic pore volume of more than 8.5 cm^3/g. The decreasing macropore volumes at higher temperatures are related to more distinctive volume shrinkage of the voids and windows during pyrolysis from polymeric PolyHIPEs to macroporous SiC materials. The calculated macropore size distributions (Figure 31(B)) correspond to the average size of the windows interconnecting the larger voids and shows maxima centered at 0.65 and 0.45 µm for synthesis at 700 and 1000°C, respectively being in good accordance to the SEM investigations (Figure 27).

Gas Storage Properties
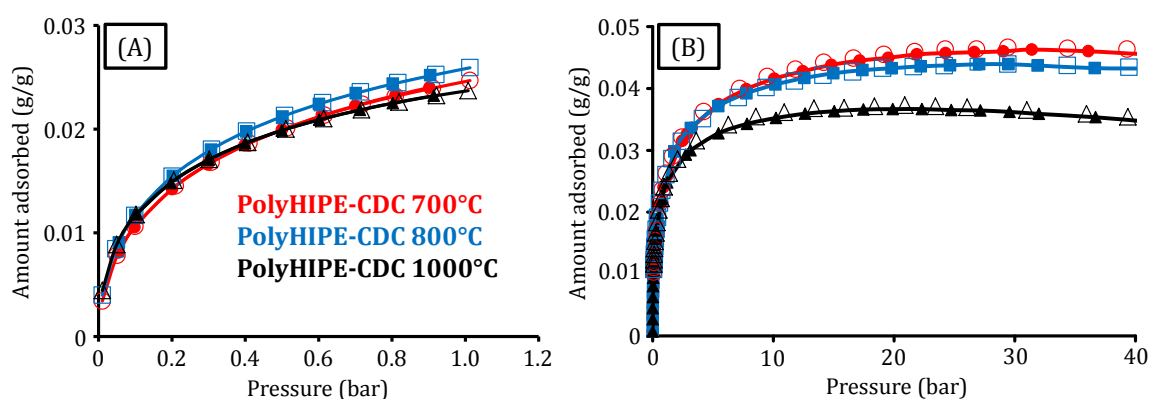
Figure 32. *Hydrogen physisorption isotherms (-196°C) and ambient pressure (A) and under Gibbs excess conditions (B) of PolyHIPE-CDCs prepared at 700°C (red circles), 800°C (blue squares), and 1000°C (black triangles).*
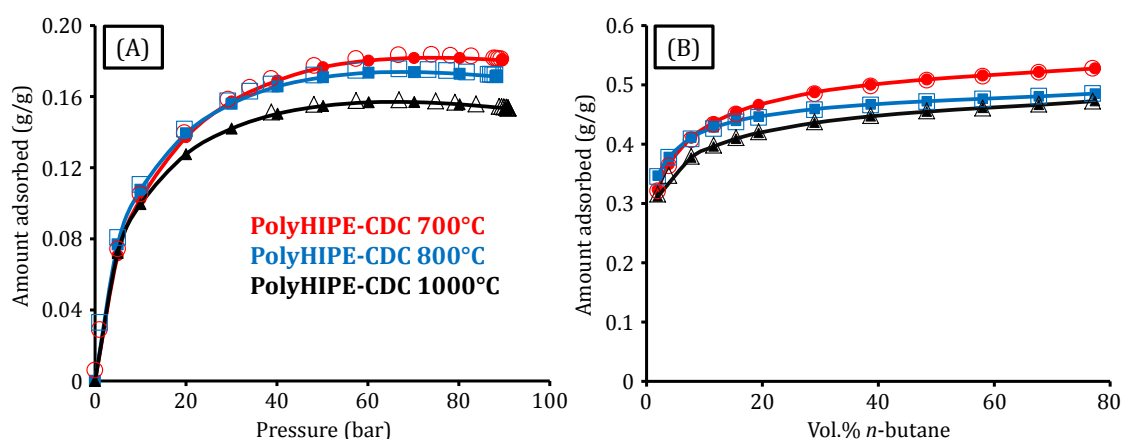
Figure 33. *Methane physisorption isotherms (25°C) under Gibbs excess conditions (A) and gravimetric n-butane physisorption isotherms (25°C) under dynamic conditions (B) of PolyHIPE-CDCs prepared at 700°C (red circles), 800°C (blue squares), and 1000°C (black triangles).*

Due to the presence of high micro- and mesopore volumes within the walls of the macroporous structure of PolyHIPE-CDCs and their high SSA, these materials are very

promising for the storage of hydrogen and hydrocarbons. At -196°C, they store 0.026 g/g and 0.046 g/g hydrogen at 1 and 30 bar (Gibbs excess conditions), respectively (Figure 32 and Table 5). In hydrocarbon storage, the capacities are 0.18 g/g methane at 25°C/70 bar (Gibbs excess conditions) and 0.53 g/g *n*-butane at 25°C/1 bar/80 vol.% *n*-butane in nitrogen (Figure 33 and Table 5). These values are higher than those reported for the metal-organic framework Cu_3Btc_2 (HKUST-1) and close to the capacities achieved by OM-SiC-CDC and other polymer-based CDCs under similar conditions.[70, 208] The amounts of gas adsorbed in the pores of PolyHIPE-CDCs decrease with increasing synthesis temperature due to the lower micropore volume and SSA (Table 4).

Table 5. Gas adsorption capacities of PolyHIPE-CDCs prepared at different temperatures.

Material	CH_4 (25°C, 70 bar) (g/g, excess)	H_2 (-196°C, 30 bar) (g/g, excess)	n-C_4H_{10} (25°C, 80 vol.%) (g/g, 1 bar)
PolyHIPE-CDC-700°C	0.182	0.046	0.53
PolyHIPE-CDC-800°C	0.174	0.044	0.49
PolyHIPE-CDC-1000°C	0.157	0.036	0.47

At this point it should be mentioned that the distinctive macropore system of the PolyHIPE-CDCs causes relatively low material density. This limits its applicability in gas storage where high volumetric uptakes are desired (see section 2.5). Due to the fact that these materials combine a high gravimetric capacity with a well-defined transport pore arrangement and a monolithic shape, they rather display excellent materials for the adsorptive removal of hydrophobic compounds from gas mixtures. However, as the SSA and micropore volume of the PolyHIPE-CDCs are still below those of tuned activated carbons and CDCs, enhancement of these parameters is still needed. In the following, post-synthetic activation of these materials with CO_2 as the oxidation agent will be described.

CO_2 Activation and n-Butane Breakthrough

Post-synthetic activation of CDCs is a suitable way to further increase their nanoporosity. For instance, chemical activation of ZrC-CDC with KOH increases the specific surface area of the starting material by 50%.[106] Osswald and co-workers

presented vacuum annealing as a suitable method to further tune the pore structure and potentially the surface functionality of CDCs for a given application.[92]

Table 6. *Porosity data summary and burn off ratios of the PolyHIPE-CDCs after CO_2 activation for different times at different temperatures.*

Material[a]	SSA_{BET} (m^2/g)[b]	V_{Micro} (cm^3/g)[c]	$V_{Micro+Meso}$ (cm^3/g)[d]	Activation burn off (%)[e]
PH-CDC-after HT-Cl	1579	0.65	0.80	-
PH-CDC-PR-HT	2223	1.01	1.24	0
PH-CDC-A-850-2	2215	0.91	1.11	16.5
PH-CDC-A-850-4	2459	1.01	1.23	25.3
PH-CDC-A-850-6	2635	1.04	1.36	43.5
PH-CDC-A-875-2	2655	1.07	1.32	28.8
PH-CDC-A-875-4	2723	1.07	1.41	46.9
PH-CDC-A-875-6	2516	0.98	1.32	53.7
PH-CDC-A-900-2	2543	1.01	1.30	34.6
PH-CDC-A-900-4	2925	1.13	1.51	54.7
PH-CDC-A-900-6	2971	1.05	1.56	70.6
PH-CDC-A-925-2	2984	1.14	1.59	56.3
PH-CDC-A-925-4	3080	1.14	1.70	74.1
PH-CDC-A-925-6	3045	1.09	1.77	72.0
PH-CDC-A-950-2	2968	1.16	1.60	55.0
PH-CDC-A-950-4	3104	1.09	1.81	79.0
PH-CDC-A-950-6	2927	1.02	1.83	88.2
PH-CDC-A-975-2	3033	1.12	1.71	72.2
PH-CDC-A-975-4	3021	1.08	1.77	76.7
PH-CDC-A-975-6	3032	0.97	1.96	82.2

[a] PH: PolyHIPE; HT-Cl: High-temperature chlorine treatment; PR-HT: Post-reductive hydrogen treatment; A-X-Y: CO_2 activated at X: temperature in °C and Y: time in h.

[b] Specific surface area calculated using the BET equation (p/p_0 = 0.05-0.2).

[c] Micropore volume calculated from the cumulative pore volume up to a diameter of 2 nm (QSDFT method for nitrogen on carbon with slit pores at -196°C, equilibrium branch kernel).

[d] Micro- and mesopore volume calculated at p/p_0 = 0.97.

[e] Burn off values related to the mass of material after hydrogen treatment.

For the post-synthetic enhancement of the porosity of PolyHIPE-CDCs, physical activation with CO_2 seems to be most attractive because of the inexpensive and non-

corrosive gaseous reactant, comparably simple processing, and the absence of an additional washing step which would be crucial in a chemical activation procedure.[25] CO_2 acts as a relatively mild oxidizer and allows a rather precise control over the development of micropores compared to activation with steam or air. Moreover, it is known that heating of CDCs in carbon dioxide after the high-temperature chlorine treatment is a suitable method for the removal of adsorbed chlorine species.[94]

Chlorine-containing PolyHIPE-CDCs (i.e. the materials obtained after high-temperature chlorine treatment at 700°C without a post-reductive purification under flowing hydrogen) are CO_2 activated in the temperature range from 850-975°C and for durations from 2-6 h (Table 6). The chlorinated starting material has a SSA of 1579 m^2/g and a micro- mesopore volume of 0.8 cm^3/g (Figure 34(A) and Table 6). EDX measurements reveal the presence of more than 11 wt.% chlorine after silicon etching (Table 7). The standard post-reductive treatment under flowing hydrogen at 600°C leads to the quantitative removal of the halogen species (Table 7) and therefore increases the SSA and the micro- mesopore volume to 2223 m^2/g and 1.24 cm^3/g, respectively (Figure 34(A) and Table 6).

400 mg of chlorine-containing PolyHIPE-CDCs are used for each single batch of activation with a constant CO_2 flow of 50 ml/min. Due to the partial oxidation of carbon, the pore volumes and SSAs of the materials can be significantly increased compared to the conventional hydrogen treatment (Figure 34(A) and Table 6). At activation temperatures above 900°C, the porosity values increase more than at lower temperatures. Compared to the hydrogen-treated sample, a 40% higher specific surface area and a 37% higher micro-mesopore volume can be achieved during activation at 950°C for 4 h and 975°C for 6 h, respectively. This increase in porosity is associated with a distinctive weight loss (Table 6). The burn offs are slightly higher compared to previous works on physical activation of μm-sized microporous SiC-CDC and TiC-CDC particles.[25, 104] In contrast, the weight loss observed during activation of the PolyHIPE-CDCs is nearly equal compared to a previous report on CO_2 activation of biomorphic CDC structures that exhibit a fibrous macrostructure.[105] This higher burn off can be explained by the distinctive macropore arrangement present in the PolyHIPE-CDCs and the biomorphic materials. These pores allow the oxidation agent to access many possible reaction sites in the walls of the CDCs leading to higher reaction rates compared to materials that do not have a secondary pore arrangement.
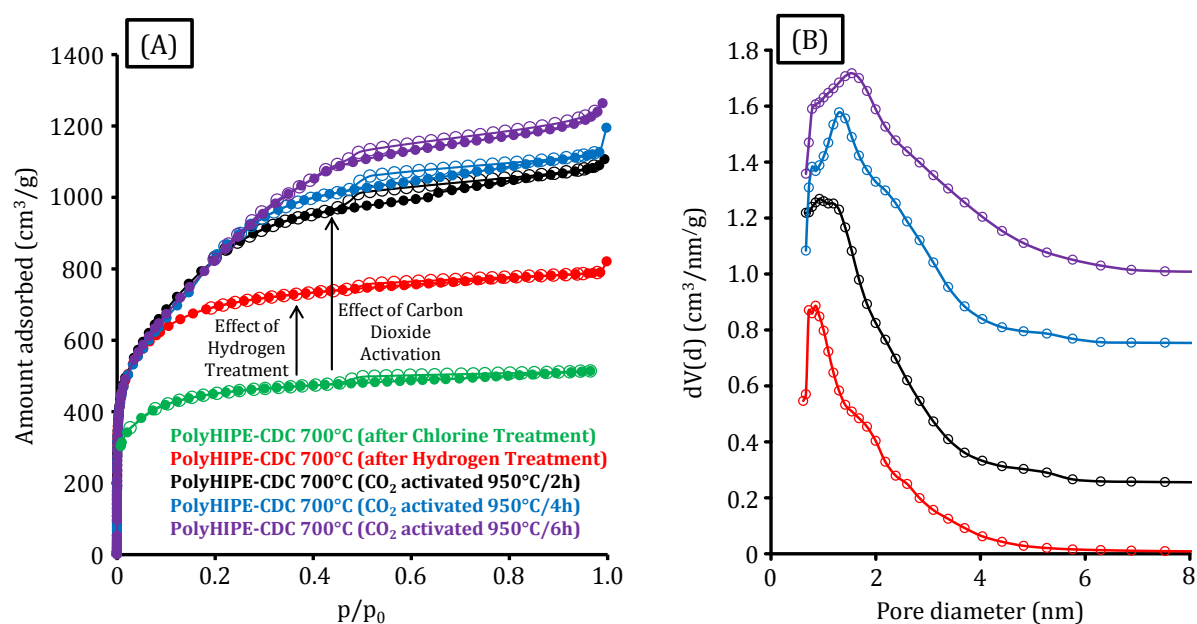
Figure 34. *Nitrogen physisorption (-196°C) isotherms (A), corresponding QSDFT (nitrogen on carbon with slit pores at -196°C, equilibrium branch kernel) pore size distributions (vertical offset) (B) of the PolyHIPE-CDCs after chlorine treatment, hydrogen treatment, and CO_2 activation at 950°C for different durations.*

Table 7. *EDX analyses of PolyHIPE-CDCs after chlorine treatment, hydrogen treatment and CO_2 activation at 925 and 950°C for 2-6 h.*

Material[a]	Carbon (wt.%)	Silicon (wt.%)	Oxygen (wt.%)	Chlorine (wt.%)
PH-CDC-after HT-Cl	86.4	11.3	1.1	1.2
PH-CDC-PR-HT	> 99.7	< 0.1	< 0.1	< 0.1
PH-CDC-A-925-2	95.2	4.5	< 0.1	0.2
PH-CDC-A-925-4	95.8	3.9	< 0.1	0.2
PH-CDC-A-925-6	99.8	< 0.1	< 0.1	0.1
PH-CDC-A-950-2	99.9	< 0.1	< 0.1	< 0.1
PH-CDC-A-950-4	99.9	< 0.1	< 0.1	< 0.1
PH-CDC-A-950-6	99.9	< 0.1	< 0.1	< 0.1

a) PH: PolyHIPE; HT-Cl: High-temperature chlorine treatment; PR-HT: Post-reductive hydrogen treatment; A-X-Y: CO_2 activated at X: temperature in °C and Y: time in h

At activation temperatures above 900°C, the obtained materials exhibit the largest micropores volumes for CO_2 treatments of 2 h. At longer activation times, the micropore volumes decrease while the total micro- and mesopore volumes rise continuously indicating a pore growth towards small mesopores. This observation is reconfirmed by the PSDs of the CDCs activated at 950°C for different times (Figure 34(B)). A broadening of the PSD as well as a shift to lower relative volume of micropores (< 61%) can be

observed for activation for 4 or 6 h. In contrast, the PolyHIPE-CDCs that underwent a carbon dioxide treatment for 2 h and the CDC after post-reductive hydrogen treatment both exhibit higher relative micropore volumes of 73% and 81%, respectively (Table 6). This growth of mesopores can be explained by the higher oxidation rates at higher activation temperatures which are also responsible for the increased burn off values.

It is well-known that the major contribution of gas adsorption capacity in nanoporous carbon materials is set by narrow micropores.[106] However, the pore widening observed is not necessarily a disadvantage because other reports on CDC activation show higher gas uptakes due to enhanced specific surface areas even at decreased micropore volumes after the oxidation process.[25] EDX analyses of the PolyHIPE-CDCs activated at 925 and 950°C (Table 7) show the possibility to remove chlorine species adsorbed in the carbons after high-temperature chlorine treatment. At activation times of 2 h, the CO_2 treatments are not suitable for quantitative removal of the halogen residuals from the carbons but the detected amounts are significantly below the material before activation. If longer activation times are applied, the purity of the carbons can be increased to > 99 wt.% rendering the carbon dioxide treatment as a suitable method for the removal of chlorine species. No additional oxygen can be detected and therefore the appearance of surface oxidation processes during activation can be ruled out.

The absence of large oxygen contents indicates a very hydrophobic surface chemistry of the activated PolyHIPE-CDCs without the presence of large numbers of oxygen-containing functionalities such as hydroxyl- or carboxyl groups. In accordance, the water adsorption isotherm of the PolyHIPE-CDC activated at 950°C for 4 h shows a very weak adsorbent-adsorbate interaction as the adsorption uptake increases at relative pressures $p/p_0 > 0.8$ (Figure 35(A)). This feature is highly desired for the adsorption of non-polar gases because it enhances the interaction between the solid and gas phase by decreasing the preferential adsorption of water, which decreases the adsorption capacity for hydrogen and hydrocarbon molecules. Adsorption of the latter is effectively suppressed at low and medium humidity.

The monolithic morphology of the PolyHIPE-CDCs is converted during the majority of the performed activation procedures (Figure 35(B-D)). Materials treated at 950°C (for 2 or 4 h) or below show only marginal volume shrinkage compared to the parent material after high-temperature chlorine treatment. This is related to the fact that the macropore

system of this hierarchical CDC ensures rapid diffusion of the activation agent through the entire particle. This leads to a very homogeneous oxidation procedure without a gradient between the particles peripheries and the centers of the monoliths. In contrast, activation of 950°C (for 6 h) or 975°C causes significant volume shrinkage or even damage of the monolithic shape as a result of the drastically decreased mechanical stability. The PolyHIPE-typical macropore structure of nearly spherical, µm-sized voids interconnected by smaller windows of several 100 nm in size is also still intact after the CO_2 activation procedures, even under relatively harsh conditions (Figure 35(E-G)). In consequence, these materials now combine a distinctive macropore arrangement leading to rapid mass transfer and a high accessibility of the micro- and mesopores with significantly advanced nanopore volume and SSA and monolithic morphology.
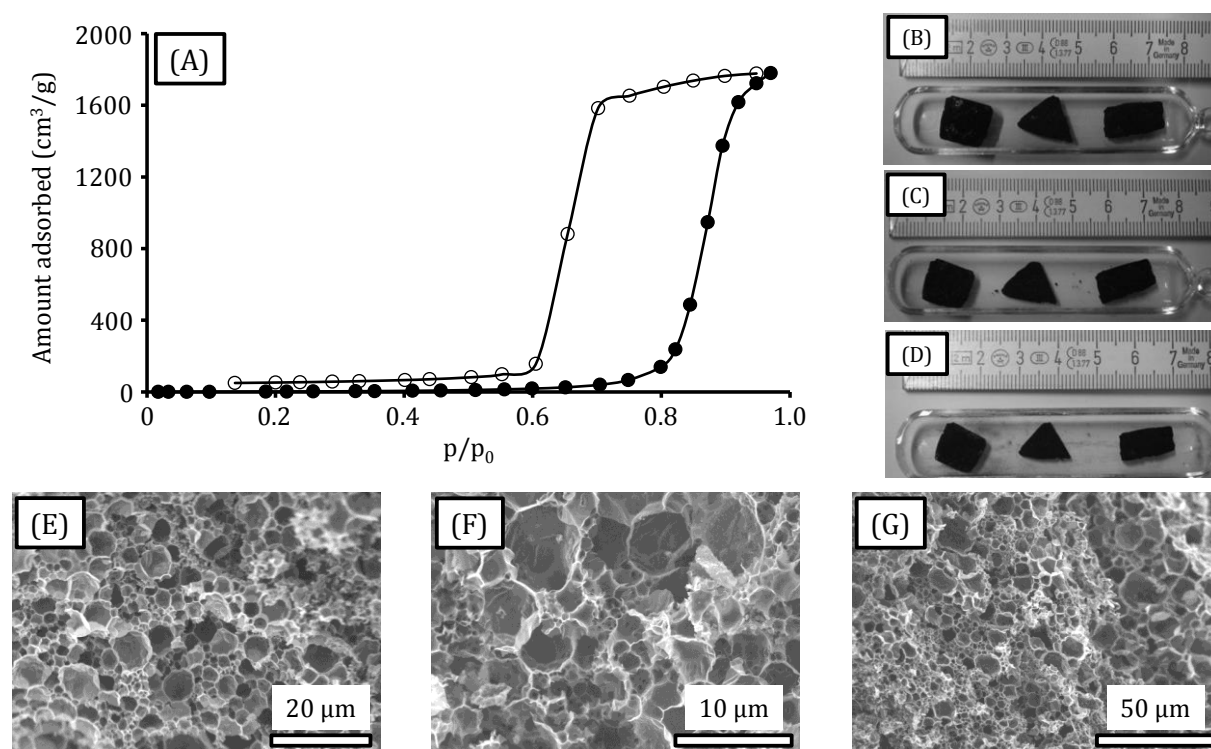
Figure 35. *Water vapor physisorption isotherm (25°C) of the PolyHIPE-CDC activated at 950°C for 4 h (A), digital photographs of the silicon carbide precursor (B), the PolyHIPE-CDC prepared at 700°C after hydrogen treatment (C), and after CO_2 activation for 4 h at 950°C (D) as well as SEM micrographs of the PolyHIPE-CDC prepared at 700°C after chlorination (E) and after CO_2 activation for 4 h at 950°C (F and G).*

The significantly higher SSA and nanopore volumes of the CO_2 activated PolyHIPE-CDCs lead to increased gravimetric capacities in hydrogen and hydrocarbon storage compared to the material that underwent a conventional post-reductive treatment under hydrogen atmosphere (Figure 36). The sample activated at 950°C for 4 h displays a good example because it shows a very high SSA above 3100 m^2/g (Table 6). Moreover, it does not

contain chlorine impurities (Table 7) and shows highly hydrophobic surface characteristics (Figure 35(A)). The activated material shows a maximum methane uptake of 0.214 g/g at 85 bar and 25°C (Gibbs excess). This is a 20% higher value compared to the hydrogen treated material. Hydrogen adsorption experiments under Gibbs excess conditions show a 19% increase of the maximum storage capacity to 0.056 g/g at 45 bar and -196°C. These are among the highest gravimetric uptakes for CDC materials reported so far. Only KOH activated ZrC-CDCs and CDCs obtained by high-temperature chlorine treatment of polymer-derived silicon oxycarbide show marginally higher uptakes.[106, 188] The methane storage capacities of the activated PolyHIPE-CDCs are comparable to those reported for CO_2 activated TiC-CDCs and OM-SiC-CDCs.[70, 102]
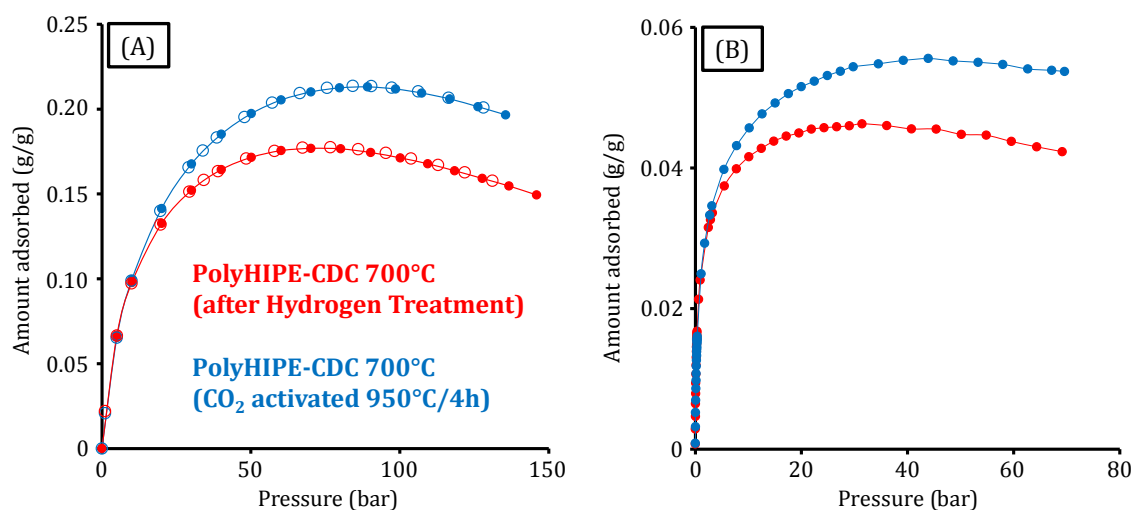
Figure 36. *High-pressure Gibbs excess methane (25°C) (A) and hydrogen (-196°C) (B) physisorption isotherms of the PolyHIPE-CDC prepared at 700°C after hydrogen treatment (red) and after CO_2 activation for 4 h at 950°C (blue).*

Like the CDCs after chlorination, the CO_2 activated materials are characterized by an extremely low material density. At a skeleton density of 2.88 g/cm³, the material density (including pores) is as low as 0.058 cm³/g. However, due to the higher SSA and nanopore volume compared to the parent material, CO_2 activated PolyHIPE-CDCs are an even more interesting material for the adsorptive filtration of volatile, non-polar organic compounds from gas mixtures as they now provide outstanding gravimetric uptakes with a distinctive transport pore system. The activated CDCs and the parent material after hydrogen treatment are compared in *n*-butane adsorption under different conditions. Gravimetric adsorption isotherms of the organic compound at 25°C under constant flow by applying different concentrations of *n*-butane in nitrogen show a

higher adsorption capacity in the activated material independent of the elevated concentration (Figure 37(A)). At 77 vol.% n-butane, a 62% higher uptake (0.86 g/g) is determined in comparison to the non-activated material (0.53 g/g) due to the enlarged specific surface area and higher volume of micro- and narrow mesopores. The gravimetric adsorption capacity of the Poly-HIPE-CDCs after activation is comparable to those reported for OM-SiC-CDCs[70] and one of the highest ever-reported values for porous materials. It is about four times higher compared to the metal-organic framework $Cu_3(btc)_2$ (HKUST-1) and even outperforms the highly porous MIL-101 as well as the commercially available activated carbon Sorbonorit 3 under the same conditions.[187]
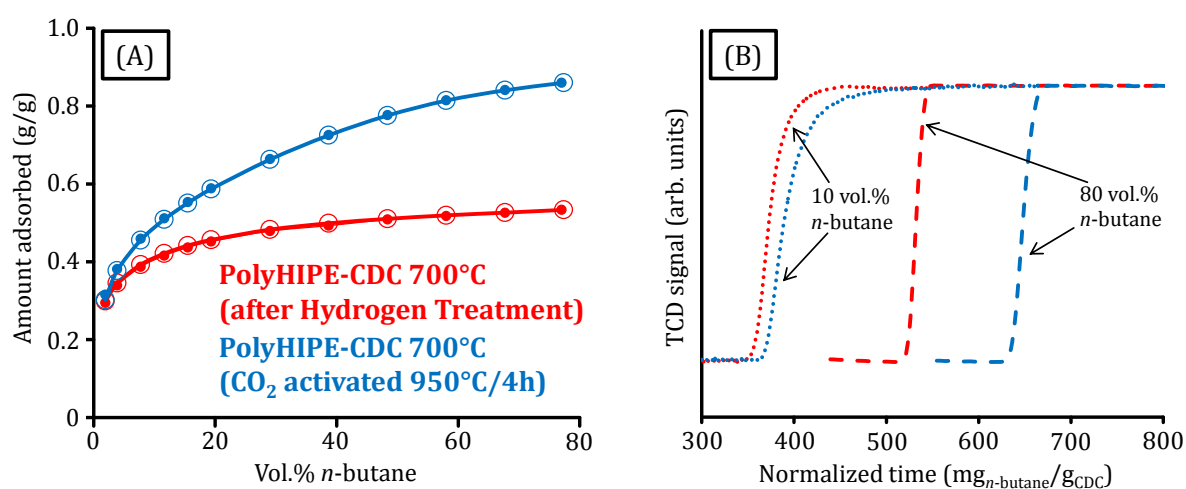
Figure 37. *N-butane physisorption isotherms (25°C) (A) and n-butane breakthrough curves at different concentrations (25°C, 1 bar, n-butane diluted with nitrogen) (B) of the PolyHIPE-CDC prepared at 700°C after hydrogen treatment (red) and after CO_2 activation for 4 h at 950°C (blue).*

The advanced adsorption capacity of the activated material is also obvious under breakthrough conditions (Figure 37(B)). In such a measurement the adsorbent is placed in a column and the adsorptive is flowing through this bed. The exhaust gas composition is measured over the time. From the step of the breakthrough, the adsorption kinetics can be determined and from the time of the breakthrough, the adsorption capacity can be determined. These measurement conditions are rather close to actual practice when the materials are applied in filter systems. The activated PolyHIPE-CDC shows higher capacities independent of the n-butane concentration. The normalized time of breakthrough increases especially at high concentrations due to the rather high gas uptake. Comparable and high steepnesses of slopes in the curves at the same amount of

n-butane in the gas mixture indicate high adsorption rates. Thus, the CO_2 activated PolyHIPE-CDCs combine a high accessibility of the micropores with significantly enhanced gravimetric uptakes in hydrocarbon adsorption.

5.1.2 CDC Nanospheres (CDC-NS)

Synthesis and Structure

CDC nanospheres are produced by cross-linking of miniemulsions which consist of SMP-10 and *p*-DVB. Hexadecane is used as co-surfactant in the oil phase. It cannot form micellar aggregates itself but displays a surface-active agent that acts in addition to the surfactant by further lowering the interfacial energy.[133, 134] The surfactant sodiumdodecylsulfate (SDS) is dissolved in the water phase. Then the phases are mixed and ultrasound is used as the source of shearing force to obtain a stable miniemulsion (Figure 38). Cross-linking and solidification of the organic nanodroplets is achieved by the addition of a platinum species and heat treatment. After removal of the aqueous phase by evaporation, the obtained cross-linked PCS nanospheres are pyrolyzed to silicon carbide materials and subsequently transformed to CDCs by high-temperature chlorine treatment. The pore structure of the CDC-NS is controllable by the ratio of SMP-10 and *p*-DVB cross-linker in the oil phase of the emulsion. In this study, the SMP-10/*p*-DVB volume ratio is adjusted to 70:30 (CDC-NS-70:30) and 50:50 (CDC-NS-50:50).
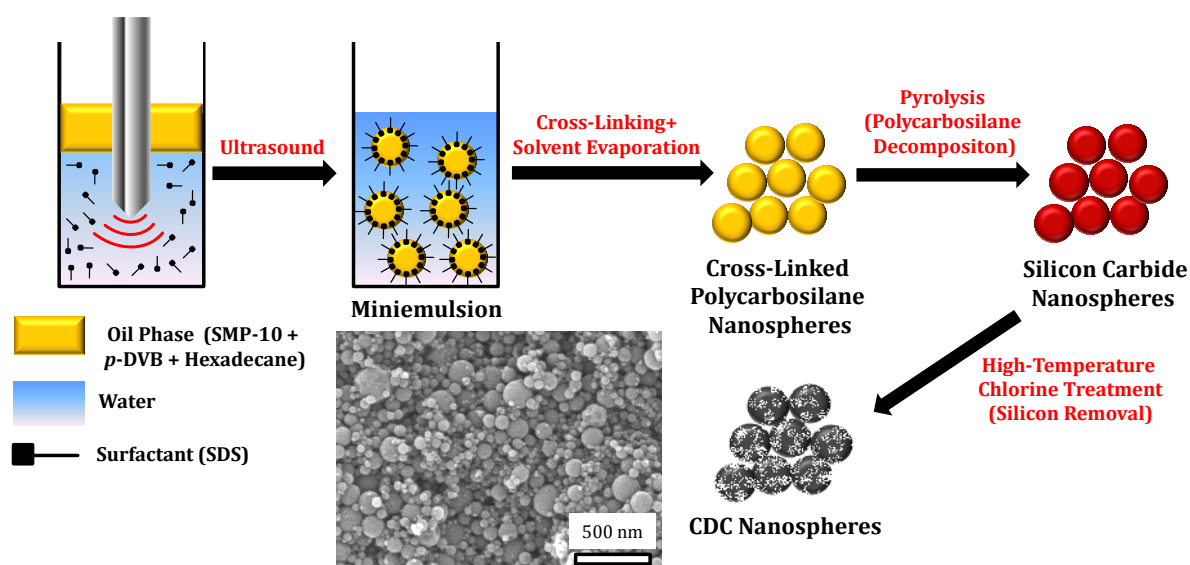
Figure 38. *Preparation and SEM micrograph of CDC nanospheres from miniemulsions.*

Thermogravimetric analysis of the cross-linked polycarbosilane nanospheres (Figure 39(A)) under air atmosphere show a larger residual mass for the material with

the higher SMP-10 content due to the formation of a larger amount of SiO_2 instead of volatile carbon oxide species. The higher mass gain at 200-400°C is associated with the formation of silicon oxide species from the polycarbosilane. In contrast to the polymers, the finally obtained CDC-NS show no residual mass as a result of the quantitative carbon combustion. However, despite similar heating rates, the CDC-NS-70:30 require larger temperatures for complete oxidation compared to the CDC nanospheres with higher content of cross-linker.
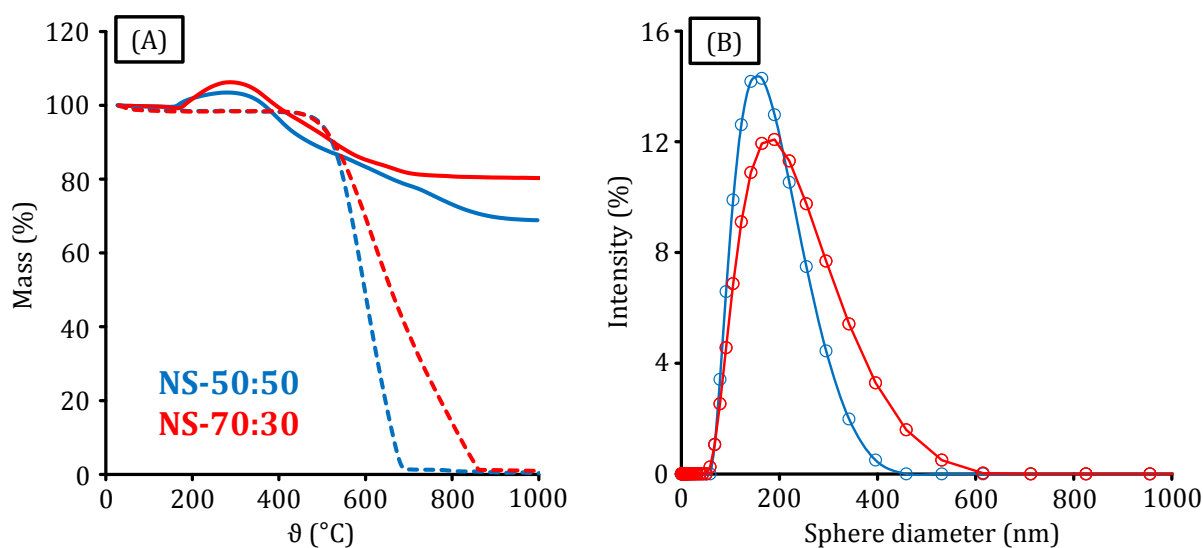
Figure 39. *Thermal analysis under air atmosphere with a heating rate of 5 K/min (A) of the polycarbosilane nanospheres (straight lines) and the CDC nanospheres (dotted lines) as well as dynamic light scattering analysis (B) of the PCS nanospheres synthesized with a SMP-10/p-DVB ratio of 50:50 (blue) and 70:30 (red).*

Dynamic light scattering experiments of the cross-linked polycarbosilane nanospheres (Figure 39(B)) in aqueous dispersion show that the hydrodynamic diameter of the particles is 20-400 nm (polydispersity index: 0.117) and 20-600 nm (polydispersity index: 0.197) for SMP-10/p-DVB ratios of 50:50 and 70:30, respectively. The respective z-average sizes are 147.0 nm (50:50) and 171.5 nm (70:30). The absence of larger particles indicates that the spheres are highly separated and that agglomeration or Ostwald ripening does not take place in the kinetically stable miniemulsion system.

SEM micrographs of the SiC- and CDC nanospheres show the nearly perfect spherical shape of the particles (Figure 40) even after the removal of the silicon atoms. The diameters of approximately 20-200 nm are slightly below those determined by DLS measurements due to the absence of the hydration shell and potential shrinkage during evaporation of the water phase or during pyrolysis. The spheres form a relatively dense package with a large inter-particular porosity. Furthermore, the CDC-NS-50:50

(Figure 40(C)) contain a higher number of defects and partially hollow structures compared to the CDC-NS-70:30. The latter show no holes and a rather smooth surface (Figure 40(D)).
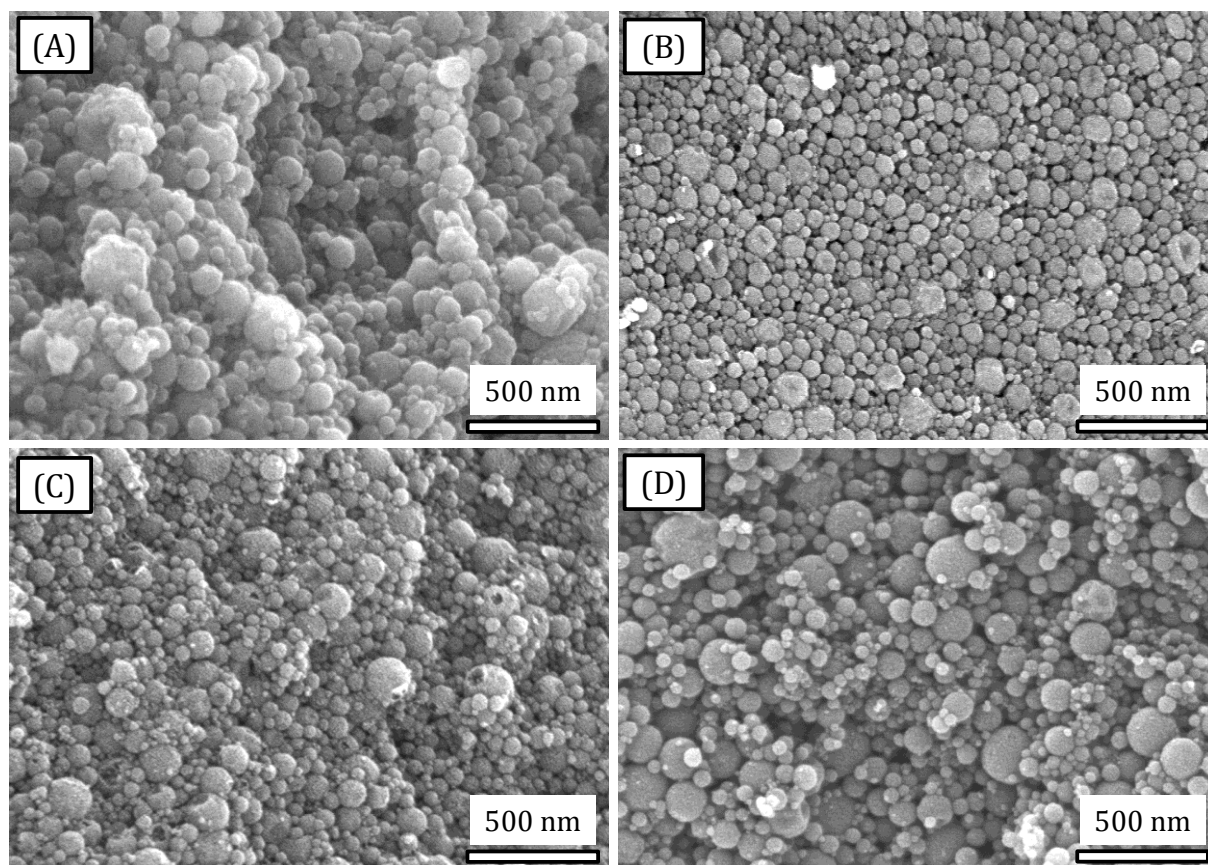
Figure 40. *SEM micrographs of the SiC nanospheres (A and B) and CDC nanospheres (C and D) obtained from miniemulsions with SMP-10/p-DVB ratios of 50:50 (A and C) or 70:30 (B and D).*

In the nitrogen physisorption isotherms of the PCS nanospheres (Figure 41(A)), a large uptake and a hysteresis at relative pressure $p/p_0 > 0.9$ can be observed due to the adsorption of nitrogen on the outer surface of the nanospheres and the condensation in the inter-particular pore system. The SSAs are below $50\,m^2/g$ because no pores are present within the particles (Table 8). After pyrolysis, the SSA of the SiC nanospheres obtained from the microemulsion with the SMP-10/*p*-DVB ratio of 50:50 is significantly higher compared to the material prepared with lower amount of cross-linker (Table 8). This can be explained with the evolution of gaseous products during cross-linking which is more pronounced if the content of *p*-DVB in the oil phase is higher. A comparably broad hysteresis loop is present in the isotherm of the *p*-DVB-rich material due to the presence of higher internal mesopore volume in these rather defective silicon carbide

spheres (Figure 41(B)). At the same time, the total pore volumes (including the inter-particular pores) are comparable (Table 8).
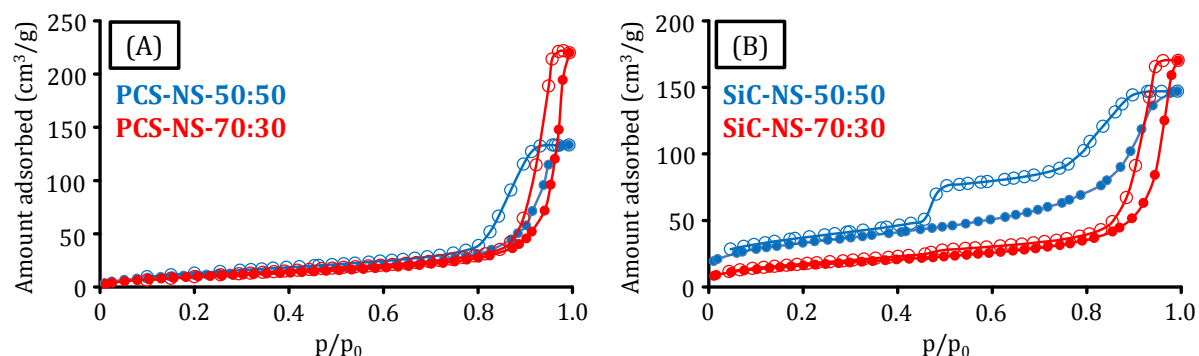
Figure 41. *Nitrogen physisorption isotherms (-196°C) of the polycarbosilane nanospheres (A) and the silicon carbide nanospheres (B) obtained from miniemulsions with SMP-10/p-DVB ratios of 50:50 (blue) or 70:30 (red).*

Table 8. *Porosity data summary of PCS-, SiC-, and CDC nanospheres obtained from miniemulsions with different SMP-10/p-DVB ratios.*

Material	SSA_{BET} (m^2/g)[a]	V_{Micro} (cm^3/g)[b]	$V_{Micro+Meso}$ (cm^3/g)[c]
PCS nanospheres-50:50	44	n. d.	0.21
PCS nanospheres-70:30	39	n. d.	0.34
SiC nanospheres-50:50	120	n. d.	0.23
SiC nanospheres-70:30	60	n. d.	0.26
CDC nanospheres-50:50	2347	0.69	1.53
CDC nanospheres-70:30	2298	0.64	1.67

[a]   Specific surface area calculated using the BET equation (p/p_0 = 0.05-0.2).
[b]   Micropore volume calculated from the cumulative pore volume up to a diameter of 2 nm (QSDFT method for nitrogen on carbon with slit/cylindrical pores at -196°C, adsorption branch kernel).
[c]   Micro- and mesopore volume calculated at p/p_0 = 0.99.

After the high-temperature chlorine treatment, the SSA and total pore volume significantly increase to maximum values of 2347 m^2/g and 1.67 cm^3/g, respectively (Table 8). Due to the conformal carbide-to-carbon transformation, the isotherms exhibit the same shape as for the silicon carbide nanospheres (Figure 42(A)). Both CDC samples contain micropores centered at 0.9-1.0 nm with a minor contribution of pores of 0.6 nm in size and contain narrow mesopores (Figure 42(B)). As already suggested from the nearly equal SSA values, the micropore volumes are comparable as well (Table 8). Due to the rather porous and defective structure within the nanospheres, CDC-NS-50:50

additionally contain a minor volume of mesopores of 6-10 nm in size. The step in the desorption branch of this material suggests that these pores are located inside the nanospheres because they are surrounded by micropores which are responsible for the desorption by cavitation.
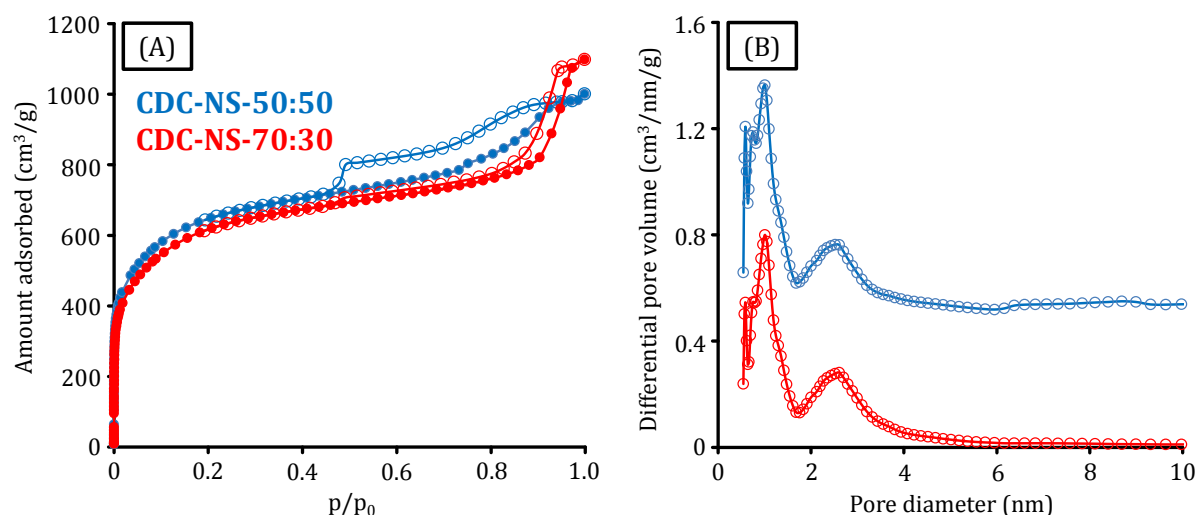
Figure 42. *Nitrogen physisorption isotherms (-196°C) (A) and corresponding QSDFT (nitrogen on carbon with slit/cylindrical pores at -196°C, adsorption branch kernel) pore size distributions (B) of the CDC-NS-50:50 (blue) and CDC-NS-70:30 (red). The PSD of the CDC-NS-50:50 is vertical offset by 0.5 cm³/nm/g.*

CDC-NS as Electrode Material in Aqueous EDLCs

CDC-NS are promising candidates for the use as ion storage media in EDLCs, especially so-called electrochemical flow capacitors (EFCs). In EFCs, mostly spherical carbon materials with high SSA are utilized for charge storage.[215] As in classical EDLCs, the charge storage takes place in the electric double-layer of charged carbon particles but a fluidized carbon-electrolyte slurry is employed as the active material. For charging and discharging through the formation of the electrochemical double-layer it is pumped into a polarized electrochemical cell and for charge storage it is pumped into reservoirs. In spite of the fact that the EFC design seems to be limited to stationary energy storage devices, it combines the general advantages of EDLCs and redox flow batteries, namely the rapid charging/discharging and the decoupling of energy- and power ratings. As the mass of the current collectors, separator and other materials is relatively small compared to the mass of the slurry, EFCs offer much higher overall energy density compared to EDLCs.

The characterization in a classical symmetrical 2-electrode EDLC device based on 1 M H_2SO_4 aqueous electrolyte reflects the influence of the pore structure of the nanospheres

on their electrochemical performance. Due to their higher SSA and micropore volume, CDC-NS-50:50 show higher specific capacitance in cyclic voltammetry at all elevated scan rates as compared to the material prepared from the miniemulsion with lower *p*-DVB concentration (Figure 43(A-C)). At the lowest scan rate of 2 mV/s, CDC-NS-50:50 show a capacitance of 174 F/g. 52% of this value can still be utilized at a high scan rate of 500 mV/s. In contrast, the CDC-NS-70:30 reach only 32% of its initial specific capacitance at this scan rate. This difference is likely related to the additional mesopores and defects in the material prepared with a high amount of cross-linker. These structural features enhance the ion diffusion within the electrode and lead to higher capacitance retentions at high current densities.
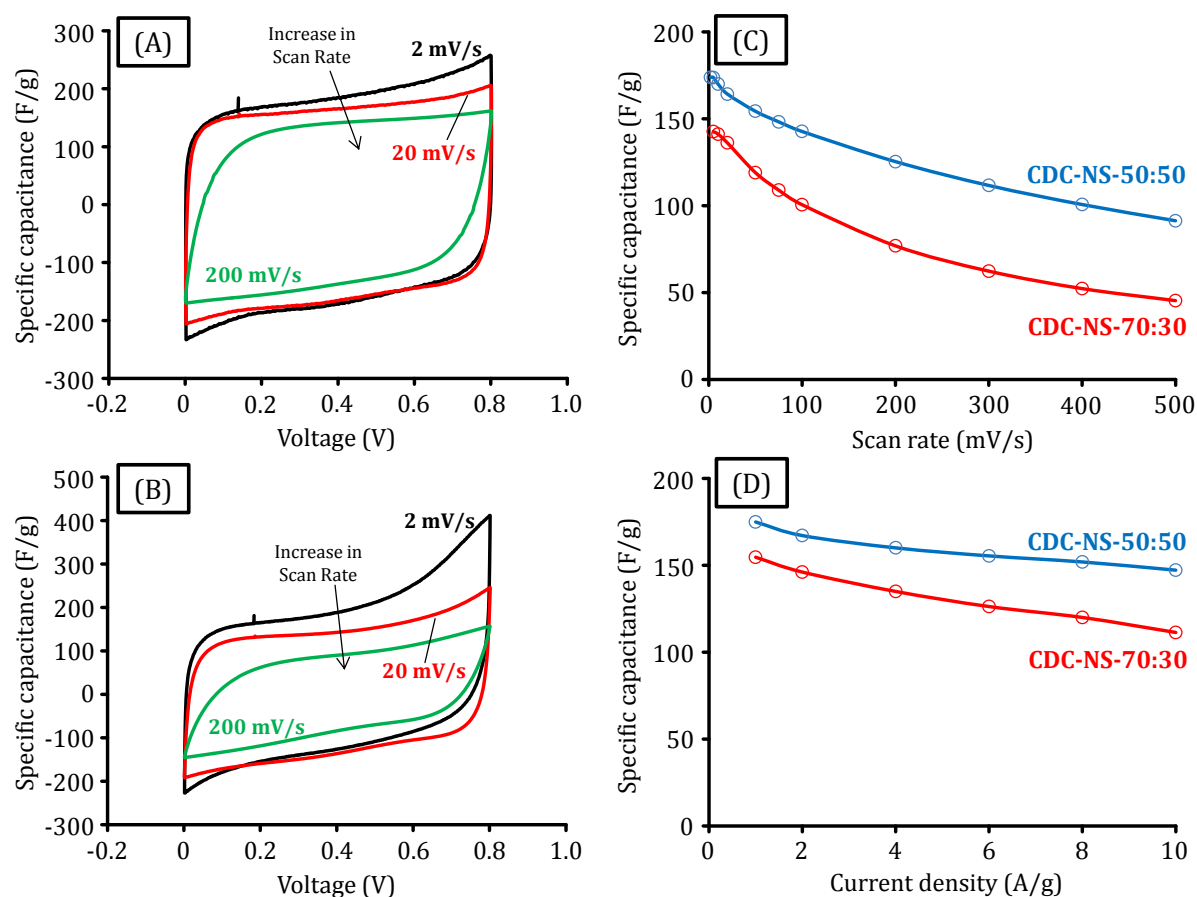
Figure 43. *Cyclic voltammograms at different scan rates of CDC-NS-50:50 (A) and CDC-NS-70:30 (B) as well as specific capacities obtained from the CV measurements (C) and galvanostatic charge-discharge tests (D) in 1 M H₂SO₄ electrolyte.*

The specific capacitances obtained from CV measurements are in accordance with those calculated from galvanostatic charge-discharge tests (Figure 43(D)). At a current density of 1 A/g, CDC-NS-50:50 and CDC-NS-70:30 provide 175 F/g and 155 F/g, respectively. In

accordance to cyclic voltammetry, the capacitance drop at higher current densities is larger for the material prepared with less cross-linker.

The relative frequency-dependent performance of the materials during electrochemical impedance spectroscopy (EIS) measurements (Figure 44) also indicates the favorable EDLC characteristics for the CDC-NS-50:50 in the low- and mid-frequency area. The drop of the capacitance of the CDC-NS-70:30 starts at higher frequency due to insufficient ion diffusion properties in the pore system of this material. In contrast, the CDC-NS-50:50 can operate with higher specific capacities at similar frequencies as a result of the enhanced electrolyte mobility in the pore system of this material.
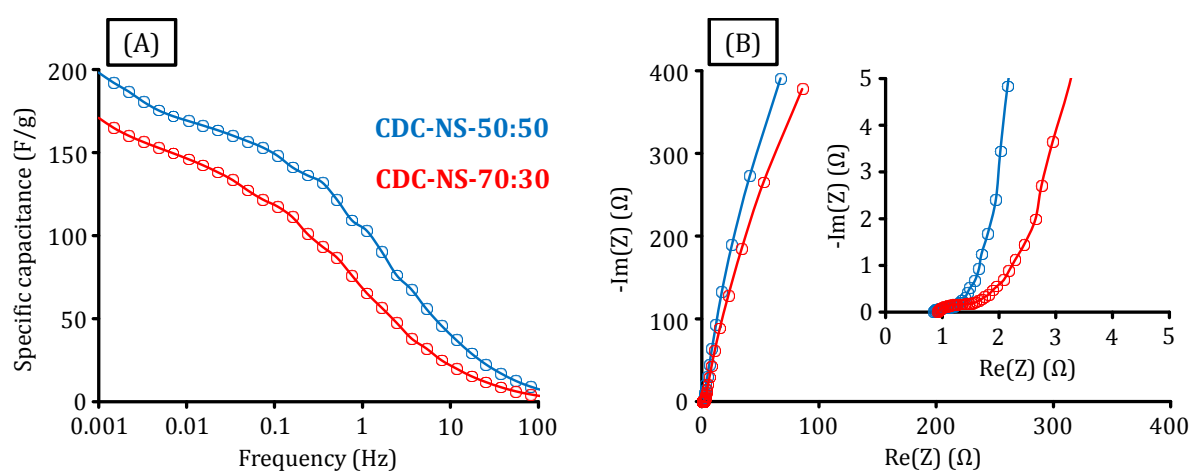
Figure 44. *Frequency response (A) and Nyquist plots (B) of CDC-NS-50:50 (blue) and CDC-NS-70:30 (red).*

In summary, CDC nanospheres provide sufficient electrochemical performance in classical EDLC devices. They are promising candidates for the use in electrochemical flow capacitors due to their spherical morphology and controllable pore structure.

5.2 Hard-Templated CDCs

Hard-templating ("nanocasting") approaches make use of solid-state templates acting as space confinement into which a precursor is infiltrated followed by subsequent transformation into the desired product and removal of the template (see section 2.3.1). In this chapter, the use of the nanocasting approach is described for the synthesis of CDC materials with different pore architecture and morphological appearance. On the one hand, hierarchical micro-mesoporous CDC mesofoams (CDC-MFs) are produced from mesocellular SiO_2 foam templates as described in section 5.2.1. The nanostructure and porosity of these materials is precisely controllable by the elevated synthesis

temperature. CDC-MFs are highly attractive electrode components in electrochemical energy storage devices. Their synthesis-structure relationships along with the use in electrochemical double-layer capacitors and as host structure for the active material in lithium-sulfur battery cathodes will be discussed.[52]

On the other hand, micro-meso-macroporous CDCs with monolithic appearance (CDC-Ms) are prepared by direct nanocasting of silica monoliths using vacuum-assisted infiltration of liquid polycarbosilane. The structure of these CDC-Ms along with their *n*-butane adsorption properties are described in section 5.2.2.[216]

5.2.1 CDC Mesofoams (CDC-MFs)

Synthesis and Structure

When the nanocasting strategy is applied for the synthesis of nanostructured solids, resulting pore sizes are highly uniform and precisely controllable because they are dictated by the thickness of the template pore walls. In case of hexagonal structured OM-SiC-CDC (see section 2.3.1), the resulting mesopore diameter of ~4 nm is in good accordance to the size of the walls within the SBA-15 template.[117] Despite the highly uniform pore structure present in OM-SiC-CDCs, its synthesis is accompanied by the disadvantage that the diameter and volume of mesopores is limited when using such ordered mesoporous exotemplates with limited pore wall thickness. Moreover, the carbon yield per template mass is limited due to the relatively low total pore volume of SBA-15. This limits the amount of polycarbosilane that can be infiltrated into the porous silica.
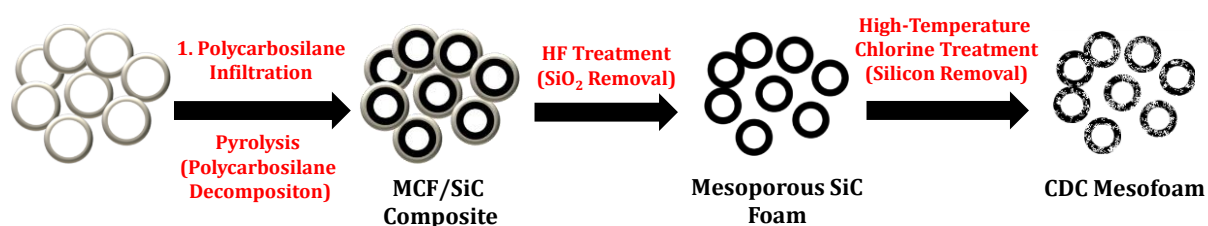
Figure 45. Preparation of CDC mesofoams.

The use of large-pore silica templates with relatively thick pore walls as the exotemplate for the production of hierarchically structured CDCs provides a promising alternative to overcome these limitations. CDC mesofoams can be produced by nanocasting of large-pore mesocellular SiO_2 foams (MCFs)[217] (Appendix 1) with polycarbosilane precursors. MCFs provide higher accessibility for the highly viscous polymeric precursor as

compared to ordered mesoporous materials (e.g. KIT-6 or SBA-15) and no co-monomers like *p*-DBV are necessary to achieve homogeneous filling as it is the case for templates with smaller pores.[118] Moreover, the high pore volume of the template significantly increases the carbon yield related to the mass of silica. After infiltration, the polycarbosilane is converted to silicon carbide by pyrolysis followed by subsequent template removal in HF solution. The obtained mesoporous SiC foams are finally converted to CDC-MFs by high-temperature chlorine treatment (Figure 45).
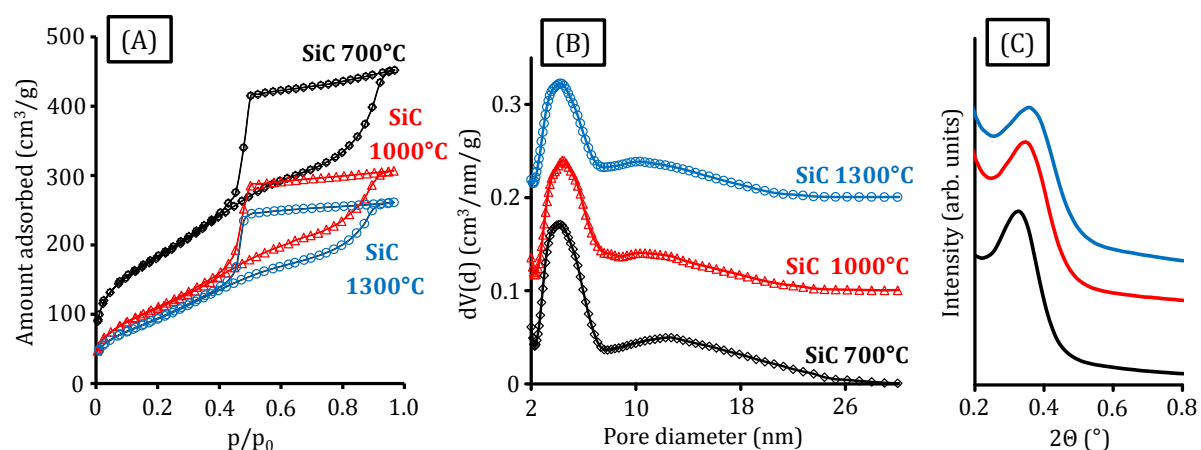
Figure 46. *Nitrogen physisorption (-196°C) isotherms (A), corresponding QSDFT (nitrogen on carbon with slit/cylindrical pores at -196°C, adsorption branch kernel) pore size distributions (B), and small-angle XRD patterns (C) of mesoporous SiC foams prepared at 700°C (black), 1000°C (red), and 1300°C (blue). The PSDs in (B) are vertical offset by 0.1 cm³/nm/g for SiC 1000°C and 0.2 cm³/nm/g for SiC 1300°C.*

As the properties of CDC materials are known to strongly depend on the structure of the elevated carbide precursor (see section 2.2.4), a detailed analysis of the latter is crucial for a profound understanding of the synthesis-structure relationships. The nitrogen physisorption isotherms of the mesoporous SiC foams (Figure 46(A)) show that their nanostructure is significantly influenced by the pyrolysis temperature. All isotherms are of type IV due to the presence of a distinctive mesopore system independent of the synthesis temperature. Adsorption of nitrogen takes place up to high relative pressures of $p/p_0 = 0.95$ and is associated with the filling of large mesopores. The PSDs calculated from the isotherms show the presence of 4.2 nm and 10.2-12.6 nm-sized pores (Figure 46(B)). According to Hyeon and co-workers, the smaller pores correspond to the replication of the MCF template pore walls, whereas the larger pores represent the spherical pores within the replica structure.[21] The SSA and total pore volume of the silicon carbide significantly decreases when the pyrolysis temperature is increased from 700 to 1300°C (Table 9). This is caused by rather distinct shrinkage at higher synthesis

temperatures as indicated by the shift of the maxima in the mesopore size distributions from 12.6 (700°C) to 10.2 nm (1300°C). At all elevated synthesis temperatures, the samples are almost exclusively mesoporous and micropores only contribute slightly to the total pore volume (Table 9).

Table 9. *Porosity and EDX data summary of the mesoporous SiC foams prepared at different temperatures.*

$T_{Pyrolysis}$ (°C)	SSA_{BET} (m^2/g)[a]	$V_{Micro+Meso}$ (cm^3/g)[b]	V_{Micro} (cm^3/g)[c]	*d* Spacing (nm)[d]	C/Si/O $(wt.\%)$[e]
700	658	0.70	0.11	26.7	58.5/36.3/5.2
1000	402	0.48	0.03	25.2	45.9/47.9/6.2
1300	343	0.40	0.02	24.5	45.5/49.3/5.2

[a]   Specific surface area calculated using the BET equation (p/p_0 = 0.05-0.2).
[b]   Micro- and mesopore volume calculated at p/p_0 = 0.95.
[c]   Micropore volume calculated from the cumulative pore volume up to a diameter of 2 nm (QSDFT method for nitrogen on carbon with slit/cylindrical pores at -196°C, adsorption branch kernel).
[d]   Calculated from the first peak in small-angle XRD patterns.
[e]   Calculated from EDX data.

The peaks in the small-angle X-ray scattering (SAXS) patterns of the mesocellular SiO_2 foams (Appendix 1(B)) and the silicon carbide structures (Figure 46(C)) are not associated with the presence of a long-range ordered pore system including any plane or space group.[217] The constructive scattering is rather caused by the presence of uniformly-sized spherical pores ("voids" or "cells") and spheres present in the template and the replica, respectively. According to Kim and co-workers, calculation of the *d* spacing of the lowest order peak allows to estimate the cell diameter by applying the Bragg equation.[218] In a first approximation, the distance of the centers of two interconnected pores can be directly correlated to the *d* spacing because the X-ray scattering occurs due to an electron density contrast between the spherical pores and the spherical silicon carbide pore wall structures. The first peaks of the MCF as well as the silicon carbide synthesized at 700°C are located at 2θ = 0.33° which corresponds to a *d* spacing of 26.7 nm for both materials and represents the size of the voids. The equal positions of the peaks indicate that the replica material prepared at the lowest temperature is an ideal copy of the MCF template. The first SAXS peaks of the silicon carbides synthesized at 1000 and 1300°C shift to higher 2θ values as a result of the decreased cell sizes of 25.2 and 24.5 nm, respectively (Table 9).
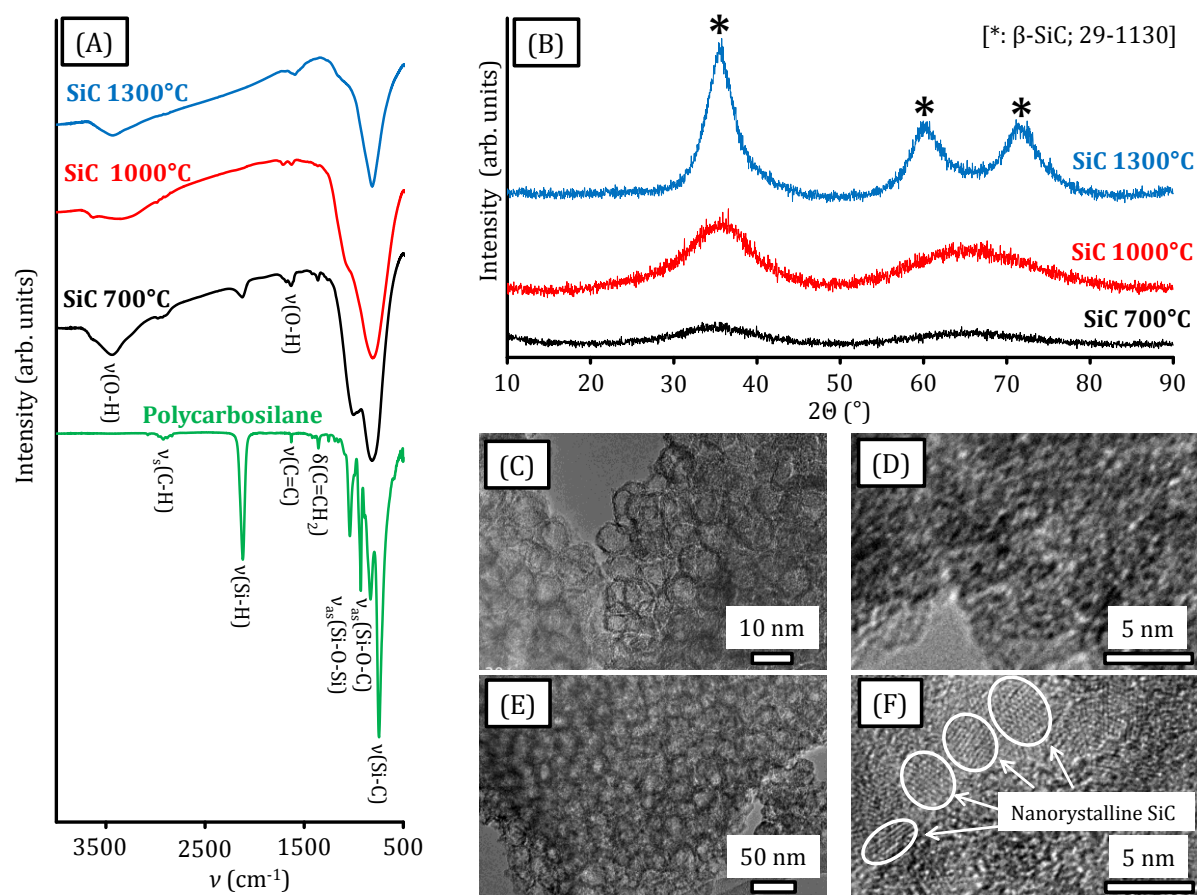
Figure 47. *FTIR spectra (A), wide-angle XRD patterns (B), and TEM micrographs (C-F) of mesoporous SiC foams prepared at 700°C (black), 1000°C (red), and 1300°C (blue). The FTIR spectrum of the polycarbosilane (green) is shown for comparison in (A). The TEM micrographs correspond to materials obtained at 700°C (C and D) and 1300°C (E and F).*

Fourier transform infrared (FTIR) spectra and wide-angle X-ray powder diffraction patterns (Figure 47(A,B)) further indicate the strong influence of the pyrolysis temperature on the structural properties of the mesoporous SiC foams due to different decomposition stages of the polymeric precursor and crystallization degrees of the resulting materials. The carbide thermally treated at the lowest temperature of 700°C shows aliphatic C-H ($2920 \; cm^{-1}$), Si-H stretching ($2139 \; cm^{-1}$), C=C ($1630 \; cm^{-1}$), and $C=CH_2$ ($1417 \; cm^{-1}$) vibration signals which are characteristic for the polymeric polycarbosilane precursor. Their presence is related to the incomplete fracturing of the polymeric structure at the lowest synthesis temperature. The atoms in this low-temperature material only exhibit a short-range order and Bragg reflections corresponding to crystalline silicon carbide are extremely broad and of low intensity (Figure 47(B)). At higher pyrolysis temperatures, the hydrocarbon and Si-H vibrations completely disappear and the resulting materials are ceramics rather than partially

decomposed polymers. In consequence, the FTIR spectra show the characteristic ν_s (Si-C) symmetric stretching vibration signals at high intensity and the Bragg reflections corresponding to crystalline β-SiC are observed. Due to the presence of larger nanocrystalline carbide domains, the reflections of the sample synthesized at the highest pyrolysis temperature of 1300°C show a smaller FWHM and are better resolved than for the material obtained at 1000°C. Although all samples exhibit a short-range order due to Si-C bonds, pyrolysis at 700°C does not form crystalline areas and interatomic distances in this material are hence larger as already indicated by the lower degree of shrinkage during thermal conversion of the precursor.

The incomplete decomposition of the polycarbosilane is further confirmed by EDX measurements (Table 9). The carbon/silicon weight ratio decreases at higher temperatures owing to a rather complete decomposition of the polymer precursor to volatile hydrocarbon species. As porous SiC is known to rapidly form a SiO_2 layer on the surface, EDX analyses reveal the presence of 5-7 wt.-% oxygen in the mesoporous silicon carbides independent of the pyrolysis temperature.

TEM analyses (Figure 47(C-F)) of the mesoporous SiC materials show the presence of a cellular mesopore structure due to the precise replication of the MCF template. The void sizes appear to be smaller compared to those of the template (Appendix 1(C,D)) as a result of the partial filling of the interior space with precursor. At higher magnification, silicon carbide nanocrystals, surrounded by amorphous structures, are observed in the material prepared at 1300°C. In contrast, the low-temperature analogue shows no long-range order or ordered lattice fringes. This confirms the amorphous character of this material.
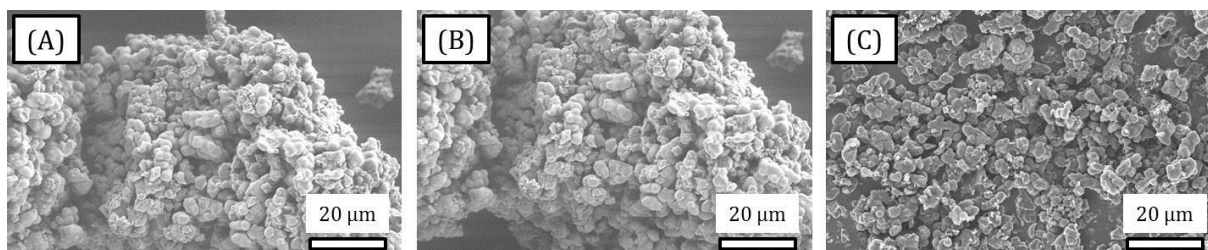

Figure 48. SEM micrographs of MCF (A), mesoporous SiC foam (B), and CDC-MF (C) particles.

Nanocasting is a technique for the precise replication of a template structure and hence the particle size and -shape of the mesoporous SiC materials is close to the MCFs. The selective extraction of the silicon atoms from the carbide materials does also not change

the particle texture due to the highly conformal character of the CDC process (Figure 48). EDX measurements of the CDC-MFs show complete silicon removal independent of the temperature of the chlorine treatment. The carbon contents are higher than 99.8 wt.-%. Silicon and oxygen are below the detection limit.

Table 10. *Porosity and Raman data summary of CDC-MFs prepared at different pyrolysis-chlorination temperatures.*

$T_{Pyro-Chlorinat.}$ [°C]	SSA_{BET} $(m^2/g)^{[a]}$	$V_{Micro+Meso}$ $(cm^3/g)^{[b]}$	V_{Micro} $(cm^3/g)^{[c]}$	$V_{<1nm}$ $(cm^3/g)^{[d]}$	FWHM D-band (cm^{-1})	$I_D/I_G^{[e]}$
700-700	2772	2.61	0.53	0.25	173	1.86
1000-1000	2542	2.33	0.55	0.36	91	2.14
1300-1000	2384	2.31	0.49	0.34	69	2.20

[a] Specific surface area calculated using the BET equation (p/p_0 = 0.05-0.2).
[b] Micro- and mesopore volume calculated at p/p_0 = 0.95.
[c] Micropore volume calculated from the cumulative pore volume up to a diameter of 2 nm (QSDFT method for nitrogen on carbon with slit/cylindrical pores at -196°C, adsorption branch kernel).
[d] Volume of pores > 1 nm calculated from the cumulative pore volume up to a diameter of 1 nm (QSDFT method for nitrogen on carbon with slit/cylindrical pores at -196°C, adsorption branch kernel).
[e] Calculated from the integrated intensities of the D-band and the G-band.

High-temperature chlorine treatment of the silicon carbide precursors is associated with the formation of large micropore volumes within the walls of the mesoporous precursors and leads to the formation of highly porous CDC mesofoams with SSAs higher than 2700 m^2/g and total pore volumes of more than 2.6 cm^3/g (Table 10). The nitrogen physisorption isotherms (Figure 49(A,B)) show high uptake of nitrogen at low relative pressures and a distinct hysteresis loop because the mesopore system of the former silicon carbide is still intact. Accordingly, the PSDs (obtained from low-pressure nitrogen physisorption isotherms) show the presence of a hierarchical micro-mesopore system in the CDC-MFs (Figure 49(C,D)). Mesopores even larger than 10 nm in diameter are present and the total micro- and mesopore volume of CDC-MFs is significantly beyond the values reported for OM-SiC-CDCs.[120] The SSAs decrease with increasing pyrolysis-chlorination temperature as it is typical for polymer-based CDCs (see section 5.1.1). This can be explained by the rather crystalline characteristics of the precursors prepared at higher temperatures which lead to CDCs with smaller micropore volumes compared to low-temperature precursors (Table 10). The nanocrystalline carbide

domains present in these materials are transformed into CDC structures with micropores of 0.6 nm in size. In contrast, the surrounding amorphous SiC yields 1.0 nm-sized micropores. This leads to a bimodal PSD in the micropore range (Figure 49(D)) and to higher volumes of pores smaller than 1 nm compared to the CDC-MFs prepared at 700°C (Table 10). The latter exclusively contains micropores of 1.1 nm in diameter explaining the higher total- and micropore volume as well as the higher SSA compared to the CDC-MFs prepared at higher temperatures.
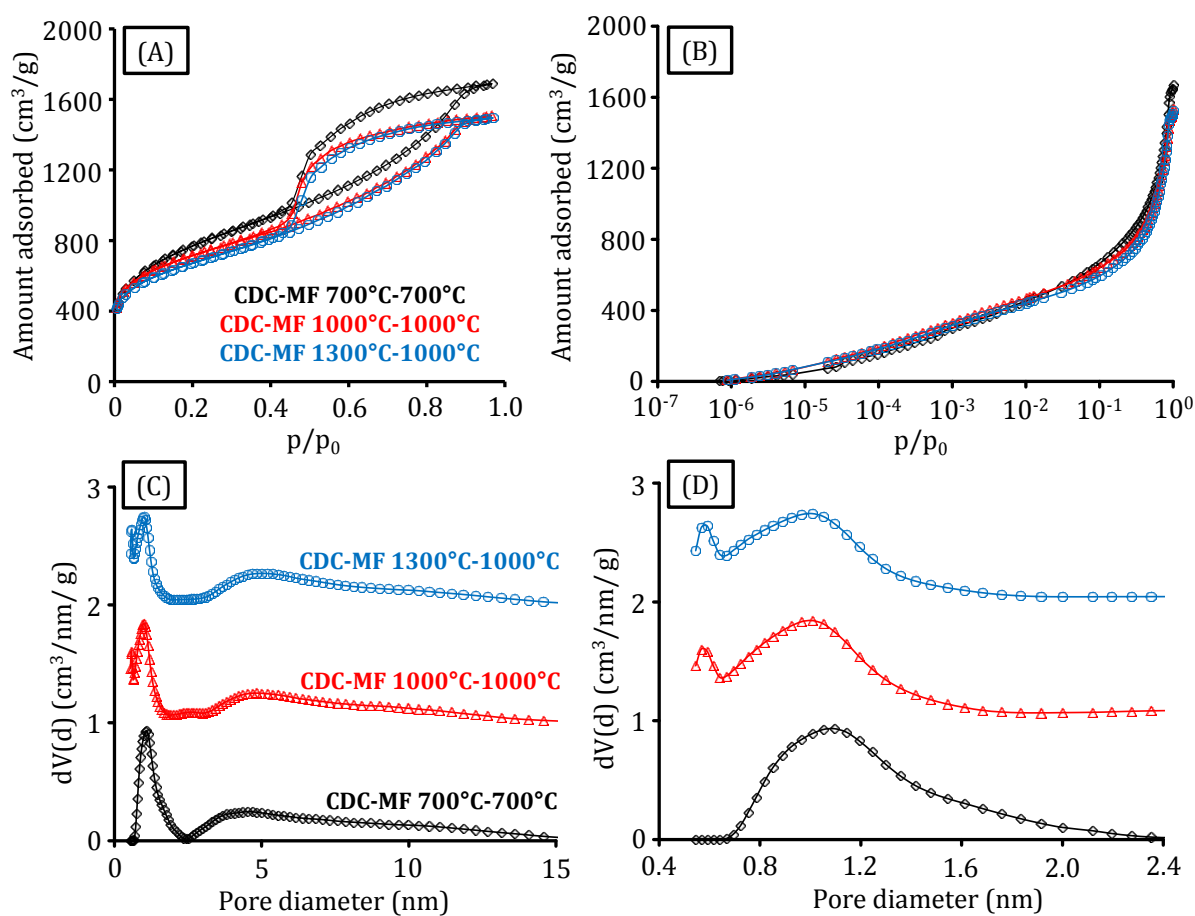
Figure 49. *Linear (A) and semi-logarithmic (low pressure measurements) (B) plots of nitrogen physisorption isotherms (-196°C) and corresponding QSDFT (nitrogen on carbon with slit/cylindrical pores at -196°C, adsorption branch kernel) pore size distributions (C and D) of the CDC-MFs prepared at pyrolysis-chlorination temperatures of 700°C-700°C (black diamonds), 1000°C-1000°C (red triangles), or 1300°C-1000°C (blue spheres).*

At all elevated temperatures, the peaks in SAXS curves (Figure 50(A)) of CDC-MFs are still present after the high-temperature chlorine treatment. However, the uniformly-sized cages in the CDCs are slightly smaller compared to those of the SiC mesofoams resulting in lower *d* spacings in the range of 21.0-22.6 nm. TEM micrographs of the CDC-

MFs further proof the presence of the uniform arrangement of near-spherical mesopores (Figure 50(B,C)).
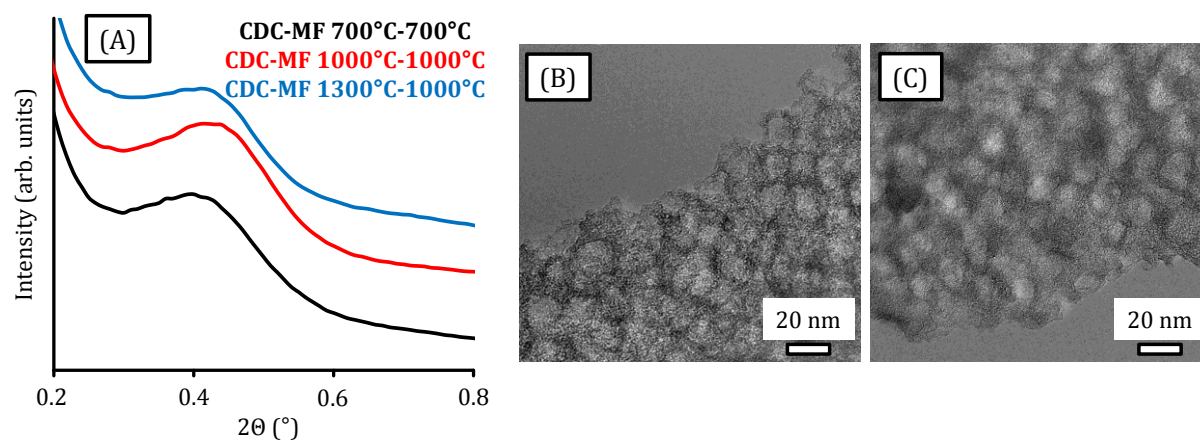
Figure 50. *Small-angle XRD patterns (A) of CDC-MFs prepared at pyrolysis-chlorination temperatures of 700°C-700°C (black), 1000°C-1000°C (red), or 1300°C-1000°C (blue), and TEM micrographs of CDC-MFs prepared at 700°C-700°C (B) and 1300°C-1000°C (C).*
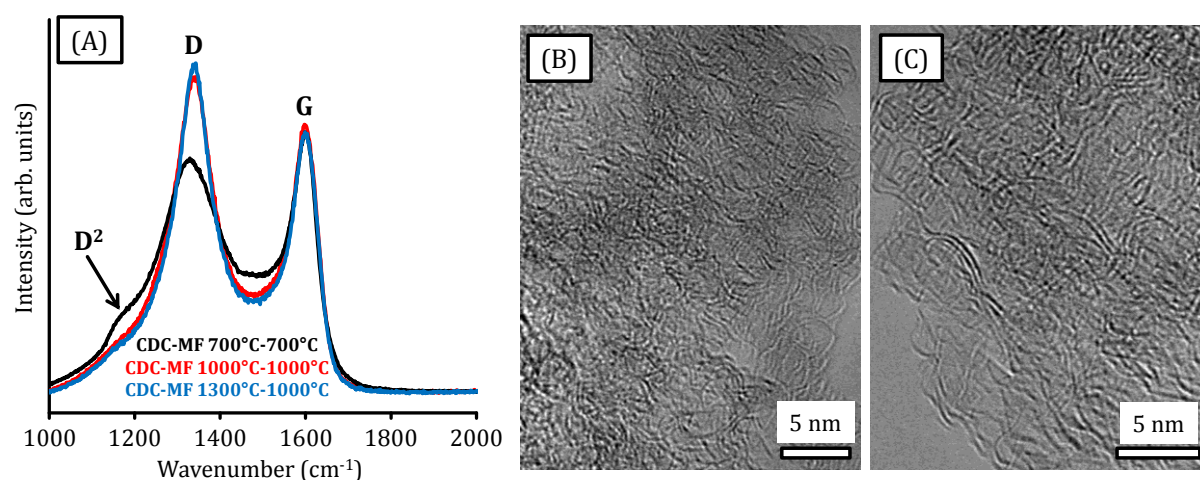
Figure 51. *Raman spectra (A) of CDC-MFs prepared at pyrolysis-chlorination temperatures of 700°C-700°C (black), 1000°C-1000°C (red), or 1300°C-1000°C (blue), and TEM micrographs of CDC-MFs prepared at 700°C-700°C (B) and 1300°C-1000°C (C).*

Raman spectroscopy measurements of CDC-MFs (Figure 51(A)) show a strong dependence of the carbon ordering on the elevated synthesis conditions. A sharp increase of the I_D/I_G ratio at higher synthesis temperatures indicates the preferred formation of graphitic carbon and increased structural ordering (Table 10). The decreasing FWHM of the D-band (Table 10) as well as the disappearance of the shoulder D^2-band at 1140-1220 cm^{-1} (Figure 51(A)) further indicate increased graphitization in the mesopore walls of the CDC-MFs prepared at higher temperatures. TEM micrographs of the CDCs at higher magnification (Figure 51(B,C)) further reveal that the materials

prepared at low temperatures consist of mostly disordered sp² carbon fringes. In contrast, the high-temperature analogue forms more graphite stacks during chlorine treatment. This represents an additional explanation for the lower micropore volume.

In summary, CDC-MFs exhibit very high specific surface areas and large micro- and mesopore volumes in combination with precise control over the carbon microstructure by varying the synthesis temperature. The porosity values of CDC-MFs even surpass those of previously reported OM-SiC-CDCs, which show outstanding performance in various applications (see section 2.3.1). The advanced infiltration behavior of the MCF template particles allows the formation of a distinct mesopore system in the final CDC with no directed orientation but a high degree of uniformity throughout the whole particle. Its hierarchical pore structure makes this material highly suitable for electrochemical energy storage devices, such as EDLCs or Li-S batteries.

CDC-MFs as Electrode Materials in Aqueous EDLCs

The characterization of CDC-MFs as an electrode material in EDLCs focuses on the materials obtained at pyrolysis-chlorination temperatures of 700°C-700°C and 1000°C-1000°C. The activated carbon YP-50F (Kuraray Chemical, USA), used in commercial EDLCs, is evaluated as benchmark material (Appendix 2).

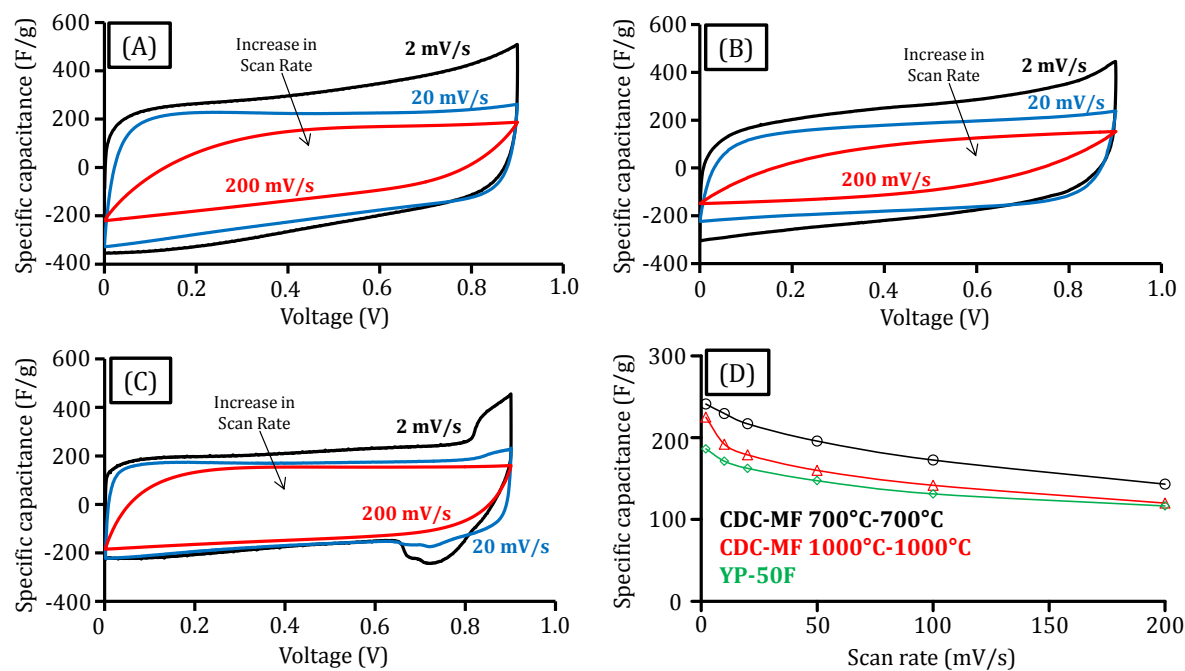***Figure 52.*** *Cyclic voltammograms at different scan rates of CDC-MFs prepared at pyrolysis-chlorination temperatures of 700°C-700°C (A), 1000°C-1000°C (B), and YP-50F (C) as well as specific capacities obtained from the CV measurements (D) in 1 M H_2SO_4 electrolyte.*

Cyclic voltammograms of the CDC-MFs in 1 M aqueous H_2SO_4 electrolyte solution (Figure 52(A,B)) are rectangular within the whole potential range of 0-0.9 V independent of the synthesis temperature and the applied scan rate. The CDCs do not contain large amounts of surface functional groups and are highly uniform. Therefore, they show an ideal EDLC behavior. In contrast, side reactions occur for YP-50F as evidenced by redox peaks in the potential range of 0.6-0.9 V caused by pseudocapacitive interaction between the electrolyte and surface functional groups or impurities present in the commercial material (Figure 52(C)). At higher scan rates, these faradic side-processes are too slow to contribute to the capacitance and the CVs exhibit a rectangular shape. CDC-MFs prepared at 700°C show a maximum specific capacitance as high as 241 F/g at a scan rate of 2 mv/s (Figure 52(D)). This is the highest value ever achieved by polymer-based CDCs and surpasses the capacities previously reported for ordered mesoporous SiC-CDCs[157] by ~20% due to the higher micro-mesopore volume available for ion adsorption. Both CDC-MF samples exhibit higher capacities compared to the commercially available YP-50F with a maximum of 186 F/g. Due to the significantly higher SSA and micropore volume, the capacitance of the low-temperature CDC-MF surpasses the values achieved by the material prepared at 1000°C over the entire range of scan rates (Figure 52(D)).

The specific capacities of the materials obtained by galvanostatic charge-discharge measurements (Figure 53(A)) are in good accordance to the values determined from cyclic voltammetry. The hierarchical CDC synthesized at 700°C provides 241 F/g at a low current density of 0.1 A/g. The high capacitance retention of 175 F/g at a current density as high as 20 A/g considerably exceeds the capacities of the CDC-MF prepared at 1000°C (117 F/g) and YP-50F (140 F/g). This remarkable capacitance retention of the low-temperature material is related to the presence of larger micropores compared to the high-temperature sample in combination with the cellular mesostructure. Both of these structural features provide sufficient pathways for ion transportation and hence ensure rapid charge-discharge.

The relative frequency-dependent performance of the materials during electrochemical impedance spectroscopy (EIS) measurements (Figure 53(B,C)) also indicates the favorable EDLC characteristics of the CDC-MFs prepared at 700°C in the low- and mid-frequency area. The drop of the capacitance starts at two orders of magnitude higher frequencies compared to the high-temperature material (Figure 53(C)). This difference

is related to the different micropore sizes in both materials. Micropores present in the CDC-MFs prepared at 1000°C are smaller in diameter (0.6-1.0 nm) than in the material prepared at 700°C (1.1 nm). These narrow micropores lead to insufficient ion diffusion at high frequencies. In contrast, ions still reach the adsorption sites if larger micropores are present as it is the case in the CDC-MF prepared at 700°C. This effect is further confirmed by the frequency response of the reference material, which contains micropores comparable in size to the low-temperature CDC (Appendix 2(B)). In consequence, the drop in capacitance occurs at a frequency close to the CDC-MF prepared at 700°C.
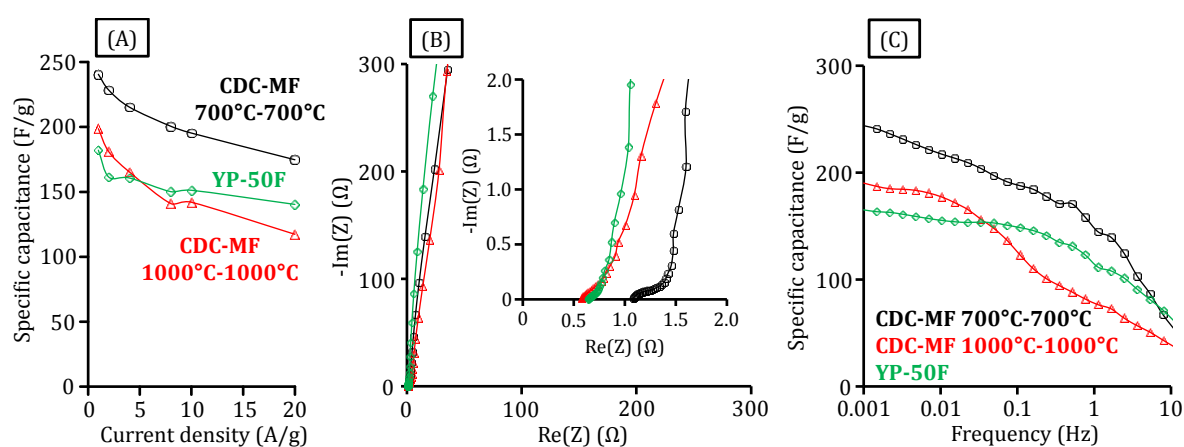
Figure 53. *Capacitance retention with current density increase from galvanostatic charge-discharge tests (A), Nyquist plots (B), and frequency response (C) of CDC-MFs prepared at pyrolysis-chlorination temperatures of 700°C-700°C (black spheres), 1000°C-1000°C (red triangles), and YP-50F (green diamonds).*

In summary, CDC-MFs display outstanding electrode materials for aqueous EDLCs with high gravimetric capacities and promising high-power performance due to their combination of high SSA and the distinctive cellular mesostructure providing sufficient ion transport pathways. CDC mesofoams show the highest ever-reported capacities among polymer-based CDCs and are redox stable over a wide potential range up to 0.9 V due to their high purity and low concentration of surface functional groups.

CDC-MFs in Li-S Battery Cathodes

Due to the high micro- and mesopore volume, CDC-MFs, particularly when prepared at 700°C, are highly attractive candidates as sulfur host materials in Li-S battery cathodes. They can be infiltrated with large amounts of the active material. Here, a CDC-MF/S composite with a C:S ratio of 1:3 (by weight) is discussed. This loading corresponds to a theoretical pore filling degree of 56% in the charged- and 100% in the discharged state.

After the addition of 10 wt.% binding- and 10 wt.% conducting agent, a cathode with 60 wt.% total sulfur content and an active material surface loading of 3.61 mg/cm² is obtained.
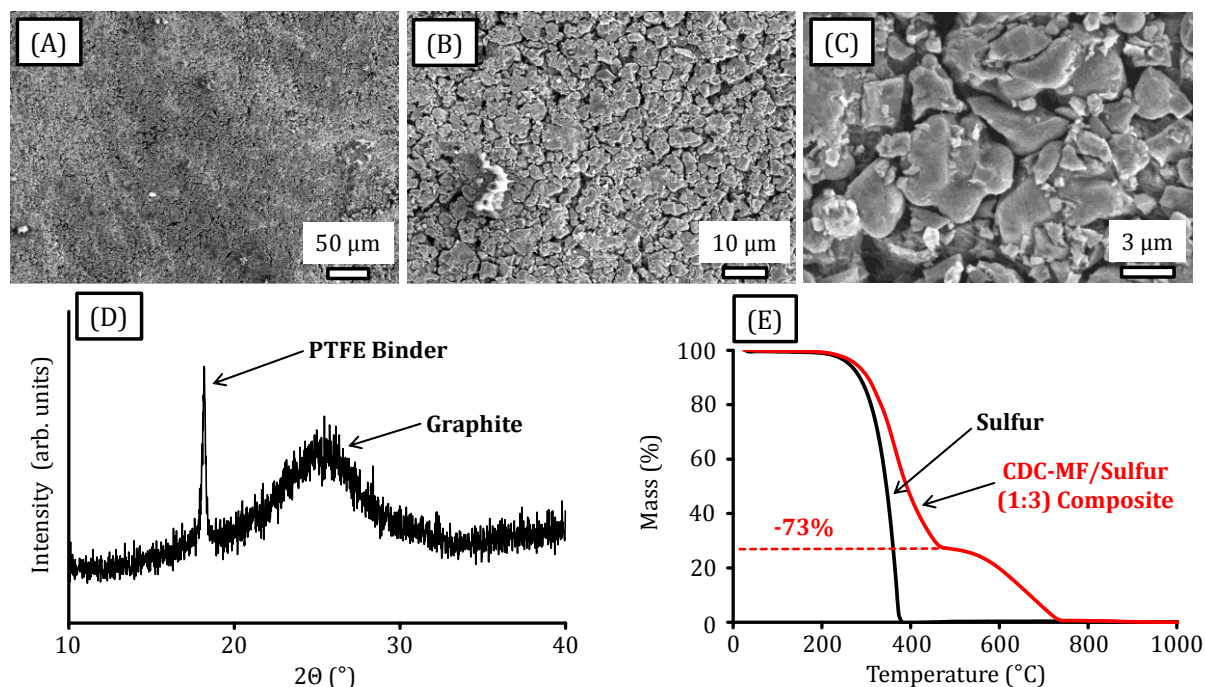
Figure 54. SEM micrographs (A-C) and wide-angle XRD pattern (D) of the CDC-MF/S cathode as well as thermogravimetric analysis under air atmosphere of the CDC-MF/S (1:3) composite and pristine sulfur (E).

The smooth cathode surface contains high inter-particular porosity (Figure 54(A-C)). Hence, sufficient electrolyte penetration throughout the active material layer is ensured. The wide-angle X-ray powder diffraction pattern (Figure 54(D)) of the cathode shows the characteristic broad peak of graphitic carbon due to the use of carbon nanotubes as conductive additive. A sharp reflection is caused by the polytetrafluorethylene (PTFE) binder. Sulfur is completely infiltrated into the CDC-MF host structure and homogeneously distributed on the nanoscale. Hence, no reflections corresponding to crystalline sulfur are observed. The sulfur content of 73 wt.% in the CDC-MF/S composite is in good accordance to the theoretical value of 75 wt.% as shown by thermogravimetric analysis under oxidative conditions (air atmosphere). Complete combustion of the active material appears at 500°C which is a much higher temperature compared to the pristine sulfur reference (Figure 54(E)). This indicates the strong confinement of sulfur within the carbon pore system. The weight loss above 500°C is associated with the combustion of the CDC-MF host structure.
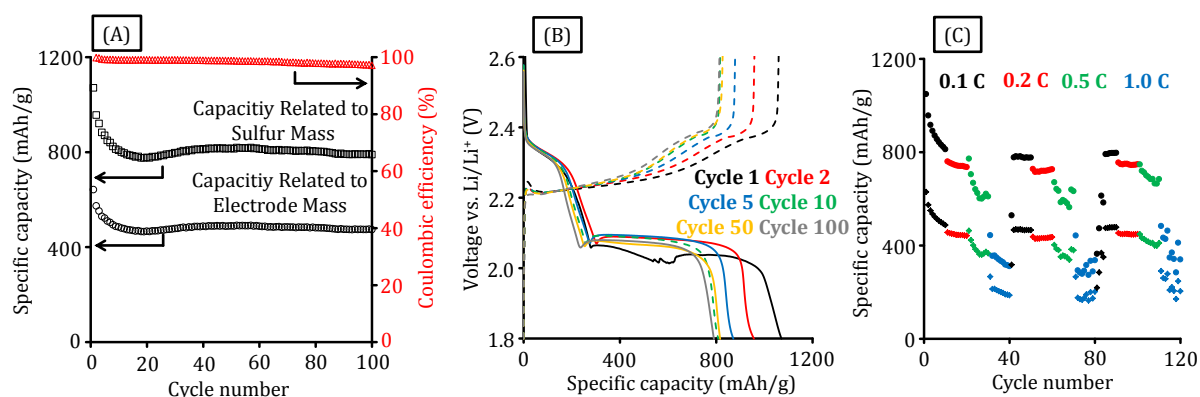
Figure 55. *Discharge capacities of the CDC-MF/S cathode during galvanostatic cycling at 0.1 C (A), corresponding voltage profiles of different cycles (B), and cycling stability at various C-rates (C). Higher values in (C) correspond to the mass of active material and lower values to the mass of the total electrode.*

Galvanostatic cycling of the CDC-MF/S cathode at a constant current rate of 167 mAh/g (0.1 C) shows a remarkable initial discharge capacity of 1070 mAh/g$_{Sulfur}$ and high cycling stability (Figure 55(A)). A capacity of 790 mAh/g$_{Sulfur}$ can be utilized after 100 cycles, i.e. 74% of the initial capacity is reversibly exploited. The sulfur utilization of 64% is slightly lower than the feasible utilization limit of 75% (1256 mAh/g$_{Sulfur}$) as predicted by Akridge and co-workers.[219] This is related to the high S/C ratio and the high sulfur surface loading caused by the high active layer thickness of 80 μm. The latter restrains the initial electrolyte penetration as indicated by the suppressed second plateau observed for the first cycle discharge profile (Figure 55(B)). However, after this initial activation, a discharge profile with a well-pronounced voltage plateau at 2.05-2.09 V vs. Li/Li$^+$ is observed over the subsequent cycles. Within the first ten cycles, the length of the charge and discharge profiles decreases, followed by the stabilization of the sulfur utilization at a stable value of 47%. This result is remarkable as the combination of high sulfur loadings and low current rates is known to favor lithium polysulfide shuttling and leads to significant loss of active a material and thus decreases the capacity during cycling.[220] The outstanding performance of the CDC-MFs as sulfur host material can be attributed to intimate, long-lasting contact between insulating sulfur and the conductive porous carbon structure which provides ideal pore geometry for the use in sulfur-containing cathodes. The spherical mesopores can be considered as individual reaction compartments and are well suited for the reversible conversion of sulfur to Li$_2$S$_n$ (8 > n > 4 for soluble polysulfides and n = 2, 1 for insoluble polysulfides). At the same time, they inhibit the leakage of soluble polysulfides by encapsulation. The potential adsorption of polysulfides into the microporous mesopore walls of the CDC-

MFs reduces shuttling even more and increases the electrochemical contact area between conductive carbon and insulating sulfur. Moreover, the hierarchical structure of this material provides rapid Li-ion transport throughout the composite particles. In consequence, the cathodes show promising rate capability (Figure 55(C)). Capacities exceeding 600 mAh/g$_{Sulfur}$ are obtained up to high current densities of 2.61 mAh/g (0.5 C) even after more than 100 total cycles. At a rate of 1 C the capacity drops. This is most likely caused by the high polarization of the plane lithium metal anode. However, if the large thickness of the active material layer and the high sulfur content of the cathode are considered, the capacities related to the mass of the whole cathode including CDC-MF, binding agent, and conductive additive of 400 mAh/g at 0.5 C and 200 mAh/g at 1 C are impressive.

5.2.2 Hierarchical CDC Monoliths (CDC-Ms)

Synthesis and Structure

Monolithic appearance is a highly desired feature of porous materials for practical applications because it allows to shape them into a particular form without the addition of a binding agent. These additives are associated with the introduction of additional mass and can lead to unfavorable modifications of the chemical properties of the materials. Furthermore, monolithic appearance can significantly enhance the volumetric efficiency of the porous material in a given application.

As long as CDCs are considered, chlorination of monolithic carbide precursors is so far limited to the synthesis of predominantly microporous materials with poor mass transfer characteristics.[58] CDC monoliths with a hierarchical micro-mesoporous structure can be obtained by binder-assisted compression of OMS/PCS composites followed by pyrolysis, template removal, and high-temperature chlorine treatment.[57] Within this thesis, binder-free monolithic CDCs with trimodal micro-meso-macropore structure obtained by soft-templating or template-free approaches are described for the first time (see sections 5.1.1 and 5.3). However, neither PolyHIPE-CDCs nor CDC aerogels contain perfectly uniform distribution of macropores and therefore mass transport within these materials could be of different magnitude at different positions within the monoliths.

Nanocasting is the method of choice to realize a CDC material with perfectly defined pore structure on all hierarchy levels. The direct use of monolithic silica templates

further overcomes the need of an additional compression step as described by Wang and co-workers.[57] Hierarchical meso-macroporous silica monoliths can be obtained by spinodal decomposition (also known as Nakanishi-type synthesis) starting form tetramethoxysilane as SiO_2 precursor.[221] These monoliths contain a three-dimensional connected structure of 1-2 μm-sized macropores which additionally contain mesopores of 5-10 nm in size within their walls. These mesopores are responsible for the high SSA of 680 m^2/g of the silica templates (Table 11).

Table 11. *Porosity data summary of CDC-Ms, the related materials in the different synthesis stages, and a microporous CDC reference material.*

Sample	SSA$_{BET}$ (m^2/g)[a]	V$_{Micro+Meso}$ (cm^3/g)[b]	V$_{Micro}$ (cm^3/g)[c]	Average Pore Size(s) (nm)
SiO_2 Monolith[d]	680	1.01	0.002	7.3
SiC Monolith[e]	365	0.38	0.03	4.8
CDC Monolith[e]	2662	2.28	0.6	1.0/6.5
Microporous CDC[f]	2342	1.07	0.94	0.9-1.0

[a] Specific surface area calculated using the BET equation (p/p_0 = 0.05-0.2).
[b] Micro- and mesopore volume calculated at p/p_0 = 0.99.
[c] Micropore volume calculated from the cumulative pore volume up to a diameter of 2 nm.
[d] PSD calculated with the NLDFT method (nitrogen on silica with cylindrical pores at -196°C, adsorption branch kernel).
[e] PSD calculated with the QSDFT method (nitrogen on carbon with slit/cylindrical pores at -196°C, adsorption branch kernel).
[f] PSD calculated with the QSDFT method (nitrogen on carbon with slit pores at -196°C, equilibrium branch kernel).

For the replication to CDC monoliths, these silica materials are cut in disks of ~1 cm diameter and 0.5 cm height and infiltrated with SMP-10 under vacuum (Figure 56(A)). The resulting yellow composite is then transformed to the silicon carbide replica of the SiO_2 monolith by pyrolysis and template removal in hydrofluoric acid solution. Finally, the SiC is converted to CDC-Ms by silicon etching during the chlorine treatment at 800°C. The monolithic appearance of the silica monoliths can be kept intact over the entire synthesis pathway (Figure 56(A)). A linear shrinkage of ~20% is observed during the conversion from polymer to silicon carbide while the high-temperature chlorine treatment is fully conformal, i.e. the texture of the carbide is precisely transformed to the carbon. EDX measurements of the CDC-Ms show a carbon content of more than 99.9 atom% and thermogravimetric analysis under air atmosphere leads to quantitative

carbon combustion due to complete removal of silicon during chlorine treatment (Appendix 3).
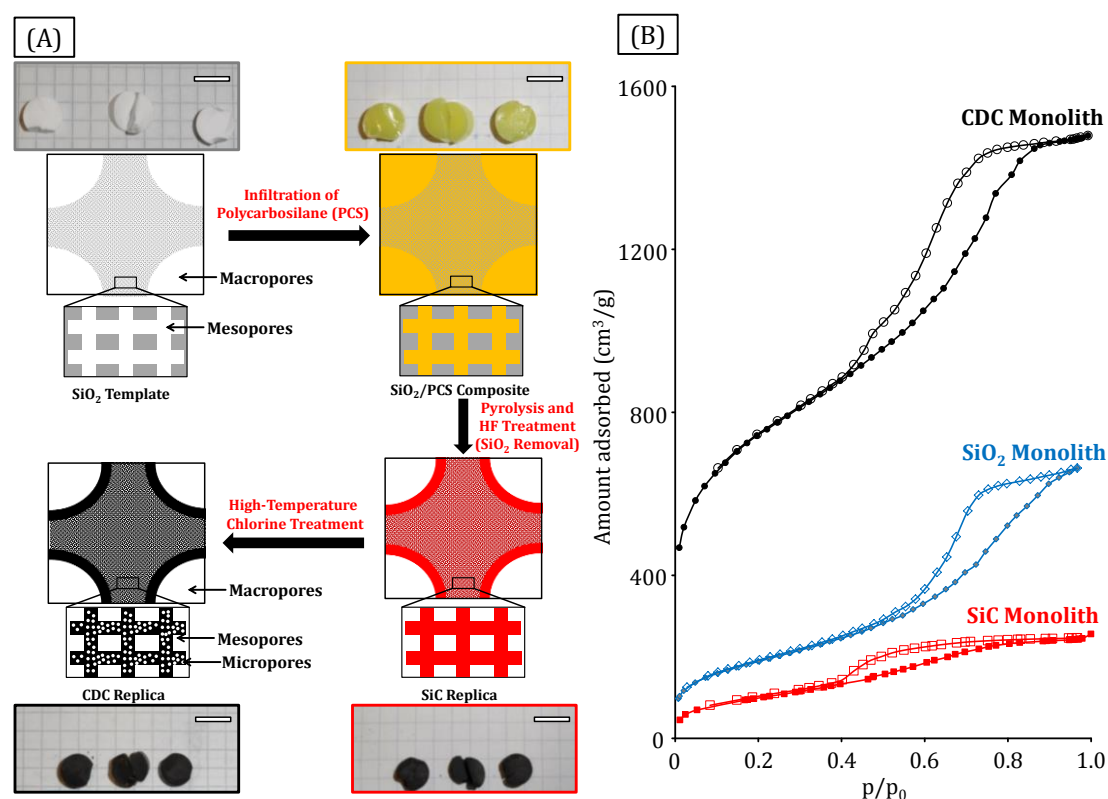
Figure 56. Preparation of CDC monoliths along with photographs (scale bar: 1 cm) (A) and nitrogen physisorption isotherms (-196°C) of the materials in different synthesis stages.

After pyrolysis and template removal, a monolithic mesoporous SiC material with a SSA of 365 m^2/g and a micro- and mesopore volume of 0.38 cm^3/g is obtained (Figure 56(B)) and Table 11). Silicon removal is associated with the implementation of 0.6 cm^3/g micropores as calculated from the cumulative QSDFT pore volume. The specific surface area significantly increases to 2662 m^2/g. The well-defined mesopore system provided by the silicon carbide precursor is fully recovered as shown by the distinct hysteresis loop in the nitrogen physisorption isotherm of the CDC-M (Figure 56(B)). The large uptake of nitrogen over the entire range of relative pressure is associated with the presence of micro-mesopore volumes as high as 2.28 cm^3/g.

In accordance to the shape of the isotherm of CDC-Ms, the QSDFT pore size analysis of a low-pressure measurement (Figure 57(A,B)) shows the presence of micropores of 1.0 nm in size. The mesopores are narrowly distributed in the range of 3-12 nm and centered at a diameter of 6.5 nm. The PSDs obtained from the adsorption and desorption branches do not significantly differ in size and volume of the pores (Figure 57(C,D)).

These calculations indicate that desorption of nitrogen from the majority of the mesopores takes place under equilibrium conditions. Hence, they are highly accessible compared to other mesoporous CDCs with similar pore diameters, such as the CDC mesofoams (see section 5.2.1). However, the presence of minor cavitation effects cannot be ruled out due to the slight step in the desorption branch at $p/p_0 = 0.42$.
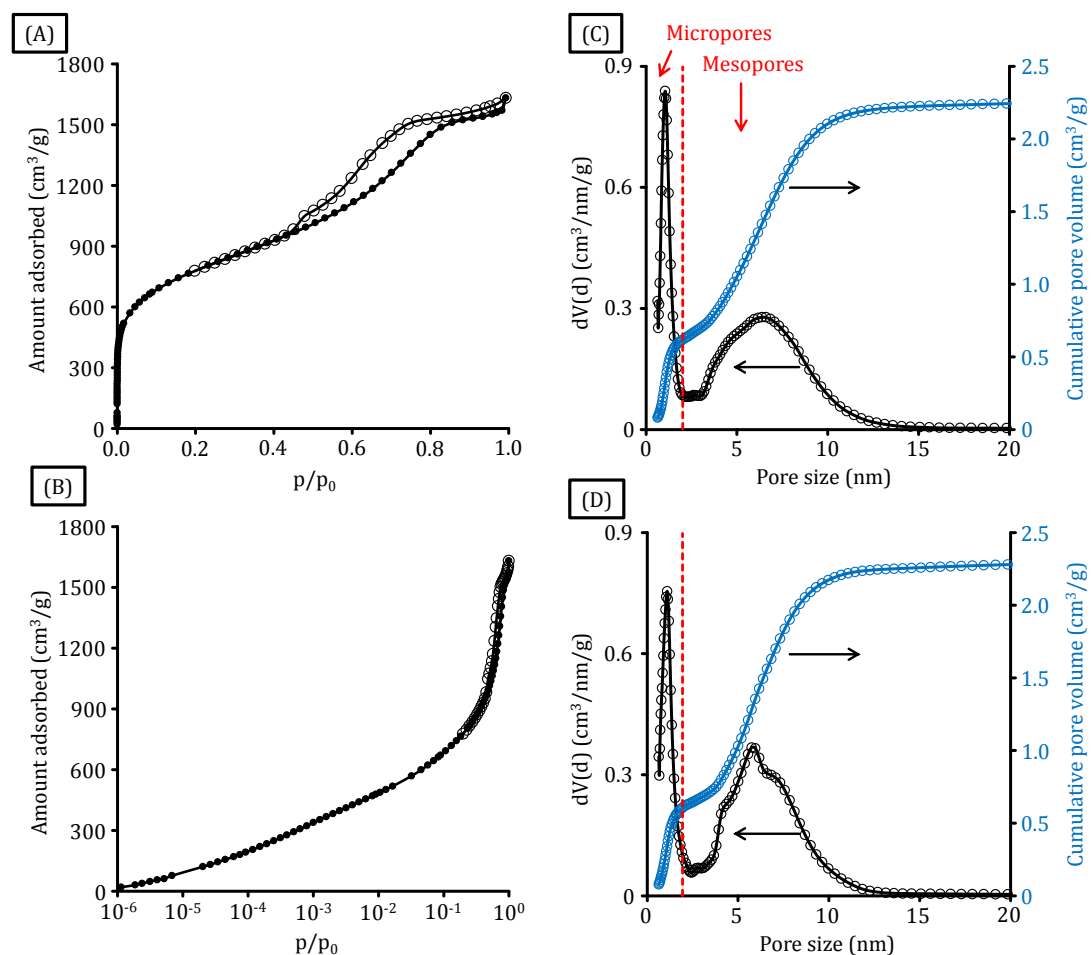
Figure 57. *Linear (A) and semi-logarithmic (B) plots of low-pressure nitrogen physisorption (-196°C) isotherms of the CDC-Ms and corresponding QSDFT (nitrogen on carbon with slit/cylindrical pores at -196°C) pore size distributions calculated from the adsorption (C) and equilibrium (D) kernel of CDC-Ms.*
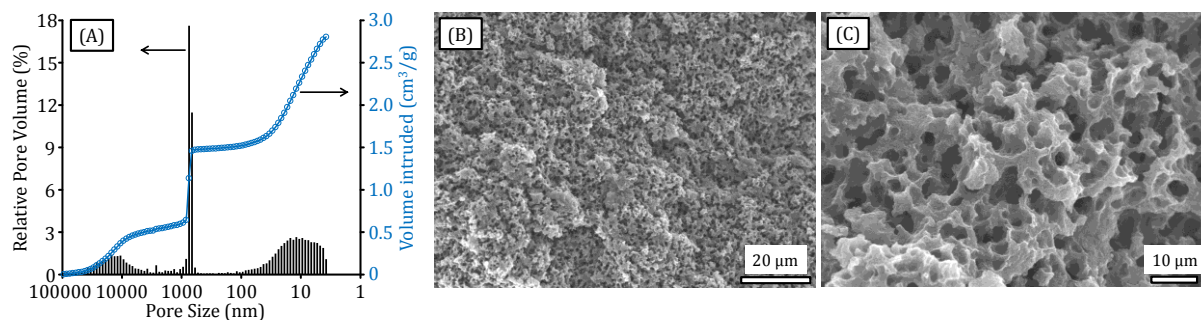
Figure 58. *Mercury intrusion curve (blue) and corresponding relative pore volumes (black) (A) as well as SEM micrographs (B and C) of CDC-Ms.*

The μm-sized pores in the CDC-Ms arise from the replication of the macropore walls present in the SiO_2 templates and are characterized by mercury intrusion porosimetry (Figure 58(A)). The intrusion at low pressures (i.e. at larger pore size) might be related to inter-particular spaces. The sharp increase of the intruded volume at a pore size of 750 nm shows that the macropores in the CDC monoliths are well-defined in size. These pores contribute 0.97 cm^3/g to the total pore volume of the CDC-Ms. In accordance to the nitrogen physisorption experiments (Figure 56(B)), the presence of mesopores causes additional intrusion of 1.2 cm^3/g mercury in the pore size range of 50-4 nm. If the QSDFT cumulative pore volume up to a diameter of 4 nm is taken into consideration (Figure 57(C)), the overall pore volume of the CDC monoliths is as high as 3.14 cm^3/g. The ratio of open meso- and macroporosity of the CDC-Ms obtained from mercury intrusion porosimetry is ~76%. This indicates a good accessibility of the microporous walls throughout the entire material and the absence of large volumes of closed macro- or mesopores.

The geometry of the large-pore system can be seen in SEM images (Figure 58(B,C)). In good accordance with the mercury intrusion measurements, the diameter of the wormlike macropores is in the range of 0.5-1.0 μm. They are surrounded by the micro- and mesoporous CDC walls. Their thickness of ~1 μm is close to the macropore size of the former monolithic silica templates which precisely dictate the pore structure of the replica materials within the nanocasting procedure.

n-Butane Adsorption Studies

The controllable shape as well as the large volume of micro- and mesopores in combination with the hydrophobic surface properties and the large volume of micro- and mesopores qualifies CDC-Ms as highly attractive materials for the removal of hydrophobic organic molecules (e.g. *n*-butane) from gas mixtures. The presence of the hierarchical pore system might further enhance rapid mass transport throughout the monoliths. This is equally important as high uptake for effective gas filtration. Compared to the PolyHIPE-CDCs, CDC-MFs also provide a trimodal pore system with significant contributions of micro-, meso-, and macropores but offer the advantage of a higher material density of ~0.3 g/cm^3 due to the smaller diameter and thicker walls of the macropores. Therefore, a comparably high volumetric adsorption capacity is provided while the hierarchical pore structure still ensures efficient mass transfer.

The volumetric *n*-butane physisorption isotherms of the CDC-Ms and a purely microporous CDC reference material measured at 5°C (Figure 59(A)) show the same shape as the nitrogen physisorption isotherms at -196°C (Figure 57(A)) and Appendix 4(A)). The microporous material shows a type I isotherm with complete pore filling at low relative pressure. This is followed by the formation of a plateau due to the absence of meso- and macropores. In contrast, a type IV isotherm including a narrow hysteresis loop is obtained for the CDC-Ms in agreement with the physisorption of nitrogen. The SSA and the total pore volume of the reference material are 2342 m^2/g and 1.07 cm^3/g, respectively (Table 11). According to the QSDFT pore size analysis, its micropore diameter is centered at 0.9-1.0 nm which is comparable to the micropore size of CDC-Ms.
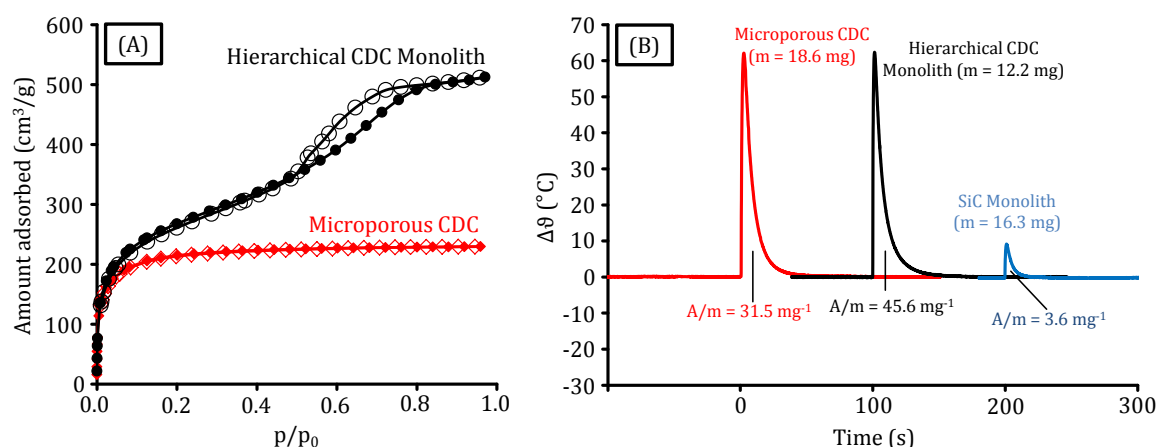
Figure 59. *Volumetric n-butane physisorption isotherms (5°C) of the hierarchical CDC-Ms (black circles) and the microporous CDC reference material (red diamonds) (A) and thermal response measurements of n-butane adsorption (1 bar, 25°C) in the microporous CDC reference material (red), CDC-Ms (black, horizontally shifted by 100 s), and the mesoporous SiC monolith (blue, horizontally shifted by 200 s) (B).*

Thermal response measurements (see section 3.2) are used for the determination of the adsorption properties of the CDC materials towards *n*-butane. They are an efficient tool for the screening of materials properties, such as SSA, adsorption capacities, and adsorption kinetics.[205] In the InfraSORP technology, an infrared sensor directly measures the temperature increase of the adsorbent caused by the released heat of adsorption in a dynamic flow cell when the inert gas (typically nitrogen) is switched to the adsorbing gas (e.g. *n*-butane at 1 bar). The integrated thermal response signal is proportional to the *n*-butane uptake. Under the elevated conditions (1 bar and 25°C), the relative pressure of *n*-butane is p/p_0 ~0.4. Hence, a significant amount of gas is also adsorbed in the mesopores of the CDC-Ms. In consequence, the mass-related integrated

intensity (A/m) of the first thermal response peak has a higher value compared to the microporous reference material (Figure 59(B)) which is in accordance to the volumetric *n*-butane physisorption isotherms. Under the elevated conditions, the temperature increase due to the adsorption of *n*-butane in micropores might be higher due to the higher adsorption potential compared to mesopores. In consequence, the temperature increase and the mass-related integrated intensity of the signal of the mesoporous silicon carbide material is far below the CDCs. This is related to its lower specific surface area and purely mesoporous structure (Figure 59(B)). The measurements further indicate that there is also a significant contribution to the temperature increase from adsorption in the mesopore system of the CDC-Ms, especially if the higher specific mesopore volume compared to the SiC monoliths is taken into consideration.

In terms of adsorption kinetics, the InfraSORP measurements demonstrate the higher adsorption/desorption rates in the CDC-Ms compared to the microporous reference material. This is evident from adsorption/desorption cycles when starting from freshly activated materials and systematically varying the equilibration time for desorption. After desorption times of 120 and 150 s, the CDC-Ms reach 86% and 88% of their initial adsorption capacity, respectively. In contrast, only 74% and 79% of the initial peak area are reached by the microporous CDC reference material after equal desorption time (Figure 60). This indicates a too slow desorption kinetics for the purely microporous system causing incomplete pore emptying and thus a lower signal intensity with decreasing equilibration time.

The larger decrease in temperature during desorption of *n*-butane from the CDC-Ms further indicates a more rapid removal of the molecules in the hierarchical CDC structure. These advanced adsorption kinetics in the CDC-Ms are related to the additional mesopores which are not present in the microporous CDC and also contribute to the *n*-butane adsorption with advanced accessibility due to their larger diameter. Furthermore, the meso- and macropores in the CDC-Ms ensure rapid diffusion of the test gas molecules to the micropores where the adsorption mainly takes place. This feature is not provided by the purely microporous material.

These assumptions are further confirmed by the adsorption/desorption cycling of the purely mesoporous SiC monoliths (Figure 60). In contrast to the CDCs, the SiC monoliths reach 100% of their initial adsorption capacity even after desorption time of 120 s. Furthermore, the decrease of the temperature during desorption is larger than the

increase during adsorption and equilibrium is reached more rapidly. This indicates extremely rapid desorption of n-butane from the SiC monoliths due to their highly accessible mesopores.
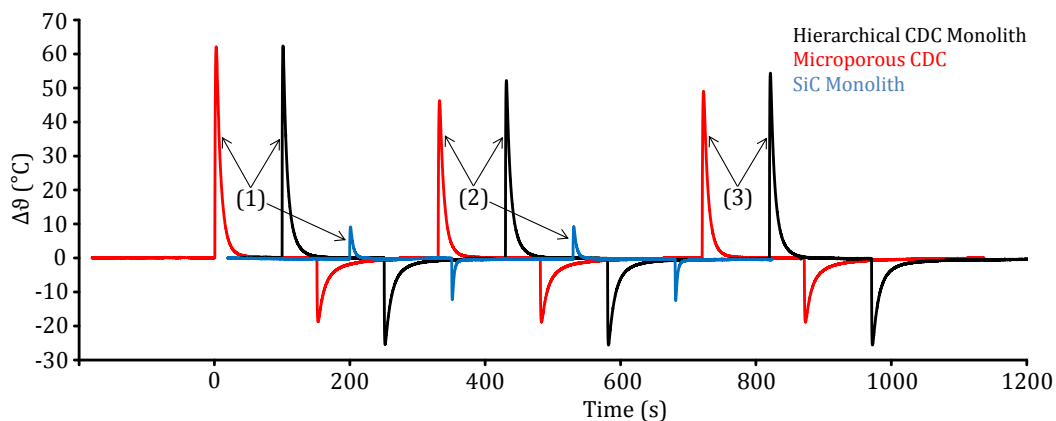
Figure 60. *Thermal response measurements of n-butane adsorption (1 bar, 25°C) in the microporous CDC reference material (red), CDC-Ms (black, horizontally shifted by 100 s), the mesoporous SiC monolith (blue, horizontally shifted by 200 s) in fully activated state (1) and after desorption times of 120 s (2) and 150 s (3).*

In summary, the thermal response measurements show the advantage of the pore structure of CDC-Ms in terms of rapid mass transfer due to meso- and macropores combined with high adsorption capacities provided by micro- and mesopores. This hierarchical pore structure along with the monolithic shape and well-defined pore sizes is highly desirable for efficient adsorption of hydrophobic organic molecules.

5.3 CDC Aerogels
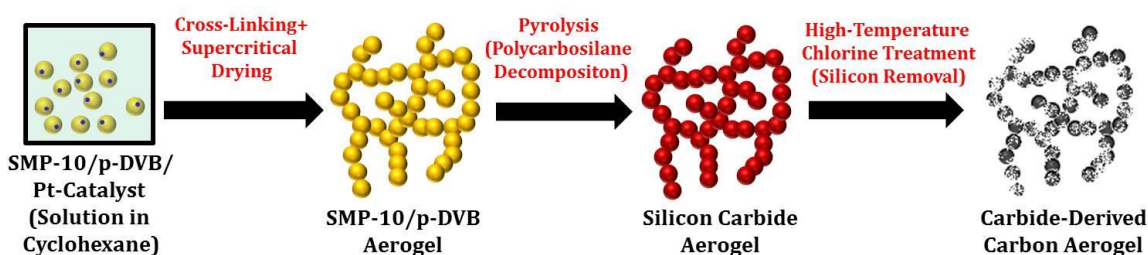
Figure 61. *Preparation of CDC aerogels.*

Well-defined hierarchical CDC structures can also be synthesized without the use of soft- or hard templates when starting from PCS aerogels. These materials can be prepared by cross-linking of the preceramic polymer and p-DVB in the presence of a platinum catalyst in cyclohexane solution by a hydrosilylation mechanism. This is followed by

drying in supercritical carbon dioxide, pyrolysis, and high-temperature chlorine treatment (Figure 61).[222] Post-synthesis activation with carbon dioxide can be applied to further increase the specific surface area as well as the volume of micro- and narrow mesopores. Activated and pristine CDC aerogel materials can be used as versatile electrode materials in EDLCs based on aqueous and organic electrolytes.

5.3.1 Pore Structure and Carbon Dioxide Adsorption of CDC Aerogels

Synthesis and Structure

After drying in supercritical carbon dioxide, the PCS aerogels (produced according to a method reported by Sorarù and co-workers)[135] offer high porosity with a SSA of 507 m^2/g (Table 12). Linear volume shrinkage of 30 and 40% takes place during the conversion from the polymer to silicon carbide at maximum temperatures of 700 and 1000°C, respectively (Figure 62(A-C)). The nitrogen physisorption isotherm shows the shape that is typical for the open-cell pore structure present in all aerogel materials independent of the synthesis stage.[12] The high uptake of nitrogen at $p/p_0 > 0.9$ is due to adsorption in the aerogel macropore system (Figure 62(D)). The larger shrinkage of the material at the higher pyrolysis temperature is related to the rather distinct crystallization of silicon carbide compared to the low-temperature sample (see section 5.2.1). In consequence, the decrease of the SSA is higher for the SiC aerogel prepared at 1000°C (307 m^2/g) compared to the material obtained at 700°C (463 m^2/g) (Table 12).

**Table 12.** *Porosity data summary of PCS aerogel, as well as of the SiC- and CDC aerogels prepared at different temperatures.*

Material	SSA_{BET} (m^2/g)[a]	V_{Micro} (cm^3/g)[b]	$V_{<0.7\,nm}$ (cm^3/g)[c]	$V_{Meso+Macro}$ (cm^3/g)[d]
PCS aerogel	507	0.03	n. d.	n. d.
SiC aerogel 700°C	463	0.06	0.05	4.56
SiC aerogel 1000°C	307	0.03	0.003	3.26
CDC aerogel 700°C	2122	0.50	0.16	8.43
CDC aerogel 1000°C	1675	0.51	0.21	5.01

[a]   Specific surface area calculated using the BET equation ($p/p_0 = 0.05$-0.2).

[b]   Micropore volume calculated from the cumulative pore volume up to a diameter of 2 nm (QSDFT method for nitrogen on carbon with slit/cylindrical pores at -196°C, adsorption branch kernel).

[c]   Cumulative volume of pores < 0.7 nm calculated from carbon dioxide physisorption (NLDFT method for carbon dioxide on carbon at 0°C).

[d]   Meso- and macropore volume calculated from mercury intrusion porosimetry (pores > ~3 nm).
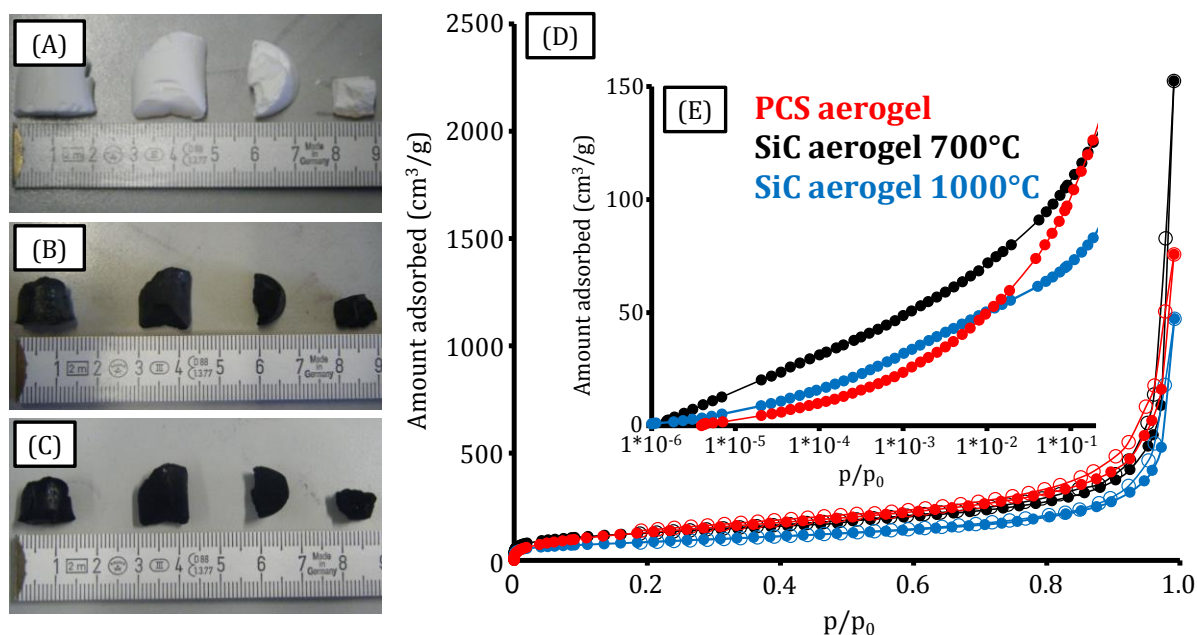
Figure 62. *Photographs of PCS aerogel monoliths (A), SiC aerogel monoliths prepared at 700°C (B), and CDC aerogel monoliths pyrolized at 700°C and chlorinated at 700°C (C). Linear (D) and semi-logarithmic (E) plots of low-pressure nitrogen physisorption isotherms (-196°C) of the PCS aerogel (red) and the SiC aerogels pyrolyzed at 700°C (black) and 1000°C (blue).*
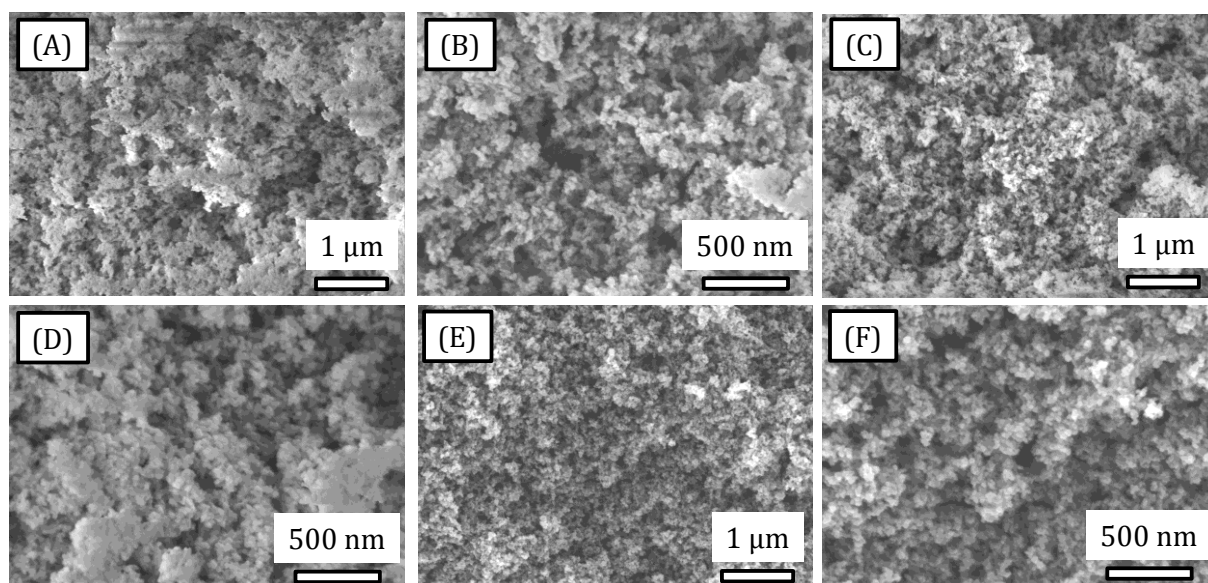
Figure 63. *SEM micrographs of the PCS aerogel (A and B), SiC aerogel prepared at 700°C (C and D), and SiC aerogel prepared at 1000°C (E and F).*

In spite of the shrinkage occurring, the typical aerogel-type shape of the isotherms is still present after the carbide formation. The low amount of nitrogen adsorbed at low relative pressures indicates the absence of large amounts of micropores in the PCS and SiC aerogels (Figure 62(E)).

The large SSA of these materials is mostly related to the open cell foam morphology consisting of interconnected nm-sized primary particles. Due to the lower degree of

volume shrinkage at a pyrolysis temperature of 700°C, the particle size is larger and a more distinct inter-particular and open porosity can be observed as compared to the SiC aerogel obtained at 1000°C (Figure 63) leading to a larger amount of adsorbed nitrogen at high relative pressure in the nitrogen physisorption measurement (Figure 62(D)).

In accordance, SEM images show the presence of the typical open cell foam structure in the aerogels (Figure 63). The SiC aerogel prepared at 1000°C shows a lower porosity and the diameter of the agglomerated colloidal particles is smaller compared to the low-temperature analogue.
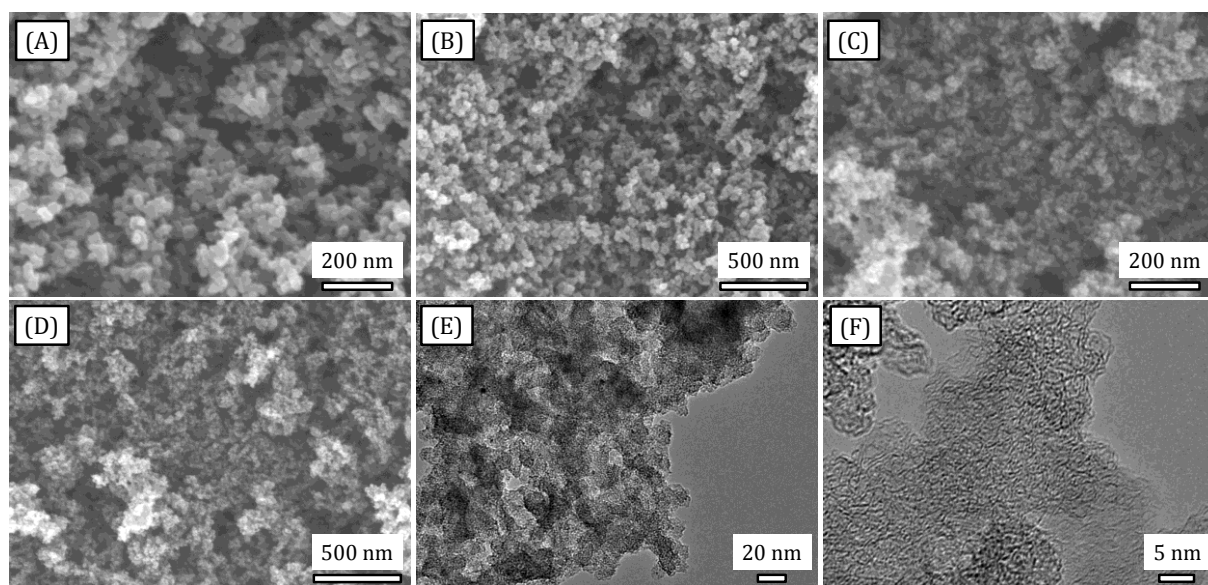
Figure 64. *SEM (A-D) and TEM micrographs (E and F) of the CDC aerogels prepared at 700°C (A, B, E, and F), and 1000°C (C and D).*

The CDC aerogels show the same monolithic appearance as their SiC precursors because the high-temperature chlorine treatment is fully conformal and no macroscopic changes occur during the carbide-to-carbon transformation (Figure 62(B,C)). As the particle size, the macropore structure of the CDC aerogels is also similar to the SiC precursors containing rather open porosity in the monoliths prepared at lower temperatures (Figure 64(A-D)). Transmission electron microscopy images (Figure 64(E,F)) illustrate the amorphous carbon microstructure consisting of mostly disordered sp^2 carbon fringes. CDC aerogels do not show distinctive graphitic stacking as it is typical for polymer-based carbide-derived carbons prepared within the investigated synthesis temperature range (see section 5.2.1).

Nitrogen physisorption isotherms measured at -196°C (Figure 65(A,B)) show the typical aerogel-type shape with a large gas uptake at high relative pressures ($p/p_0 > 0.9$)

associated with the filling of the large meso-and macropores, which are responsible for the very high pore volumes. Silicon extraction during the high-temperature chlorine treatment significantly increases the micropore volume compared to the SiC precursors as indicated by the larger amount of nitrogen adsorbed in the low pressure area (Figure 65(B)). In consequence, the SSAs of the CDCs are as high as 2122 m^2/g and 1675 m^2/g for synthesis temperatures of 700 and 1000°C, respectively. These values considerably exceed those of the SiC aerogels (Table 12). While the total volume of pores with a diameter below 2 nm does not significantly change at higher synthesis temperatures (Table 12), the SSAs are strongly dependent on the conditions during pyrolysis and silicon extraction indicating their strong influence on the carbon microstructure and porosity.
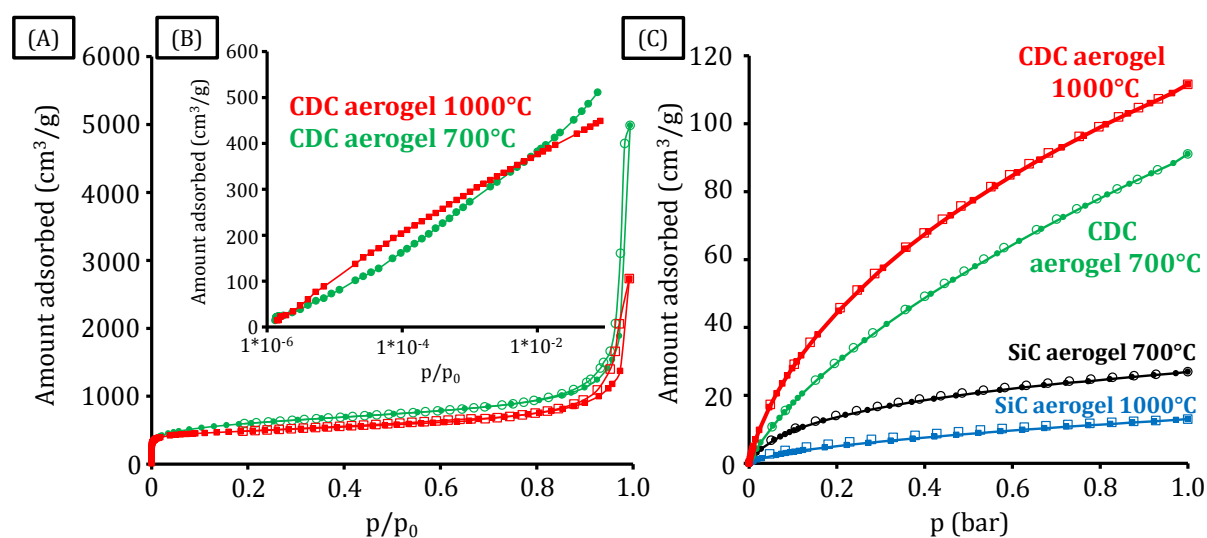
Figure 65. *Linear (A) and semi-logarithmic (B, low pressure region) plots of nitrogen physisorption (-196°C) isotherms of the CDC aerogels prepared at 700°C (green) and 1000°C (red) as well as carbon dioxide physisorption (0°C) isotherms (C) of the CDC aerogels and the SiC aerogel precursors pyrolyzed at 700°C (black) and 1000°C (blue).*

The temperature-dependent structure of the CDC aerogels was additionally characterized by carbon dioxide physisorption at 0°C up to atmospheric pressure (Figure 65(C)). This technique can be used to particularly investigate the narrow micropore structure due to the low relative pressure of CO_2 (p/p_0 ~0.03) and its small kinetic diameter (0.33-0.36 nm). In consequence, large volumes of pores with a diameter below 0.7 nm are required for the adsorption of large quantities of this molecule.[71] CDC aerogels adsorb larger quantities of CO_2 compared to the SiC precursors due to the presence of higher micropore volumes after the high-temperature chlorine treatment.

As the micropore structure is very sensitive to the elevated conditions of the chlorine treatment, the CDC sample prepared at 1000°C adsorbs a higher amount of CO_2 compared to the low-temperature material due to the presence of a larger volume of narrow micropores. The study of the micropore structure of the CDC aerogels is performed by using DFT analysis of combined carbon dioxide (0°C) and nitrogen physisorption (-196°C) analysis. With this combination it is possible to accurately investigate pore sizes below and above 0.7 nm. As already indicated by the larger uptake of CO_2 at ambient pressure, the combined PSD shows the presence of a larger amount of pores < 0.7 nm in the CDC aerogel obtained at 1000°C (Figure 66(A,B) and Table 12). This result is in accordance with the larger uptake of nitrogen in the low pressure region (p/p_0 < 0.001) compared to the low-temperature material (Figure 65(B)), which is associated with the filling of these ultra-micropores. The rather amorphous character of the SiC precursor and the lower temperature of silicon extraction cause the presence of rather amorphous carbon instead of graphitic nanodomains in the material obtained at 700°C. This leads to its higher micropore volume, larger micropores, and higher SSA. In contrast, a lower SSA but a higher volume of narrow micropores suitable for CO_2 storage is obtained at higher temperature.
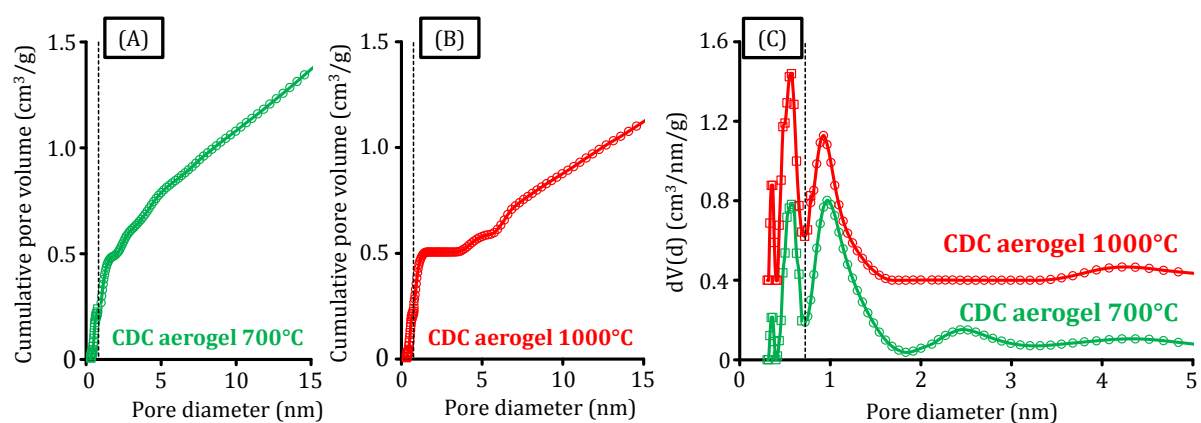
Figure 66. *Cumulative (A and B) and differential (C) pore size distributions of the CDC aerogels prepared at 700°C (green) and 1000°C (red) obtained from combined nitrogen physisorption (circles, QSDFT for nitrogen on carbon with slit/cylindrical pores at -196°C, adsorption branch kernel) and carbon dioxide (squares; NLDFT for carbon dioxide on carbon at 0°C) analysis. The PSD of the aerogel CDC prepared at 1000°C is vertical offset by 0.4 cm³/nm/g.*

As indicated by the large uptake of nitrogen at high relative pressures, the total pore volumes of the silicon carbide precursors increase during the high-temperature chlorine treatment as a result of the micropore formation and the decreasing weight due to the removal of the silicon atoms. The CDC micropores in combination with the aerogel

structure cause extremely low density and at the same time very high total pore volume. From the amount of adsorbed nitrogen at a relative pressure $p/p_0 = 0.99$, total pore volumes of 7.7 and 4.2 cm^3/g are calculated for the CDC aerogels prepared at 700 and 1000°C, respectively (Figure 65(A)). However, the isotherms do not reach a plateau and the amount of adsorbed gas at such high relative pressure can be largely influenced by minor temperature variations. DFT methods for pore size analysis fail to operate precisely at such high relative pressures and hence the quantitative analysis of the large-pore system present in the CDC aerogels is not very precise based on the nitrogen physisorption data.
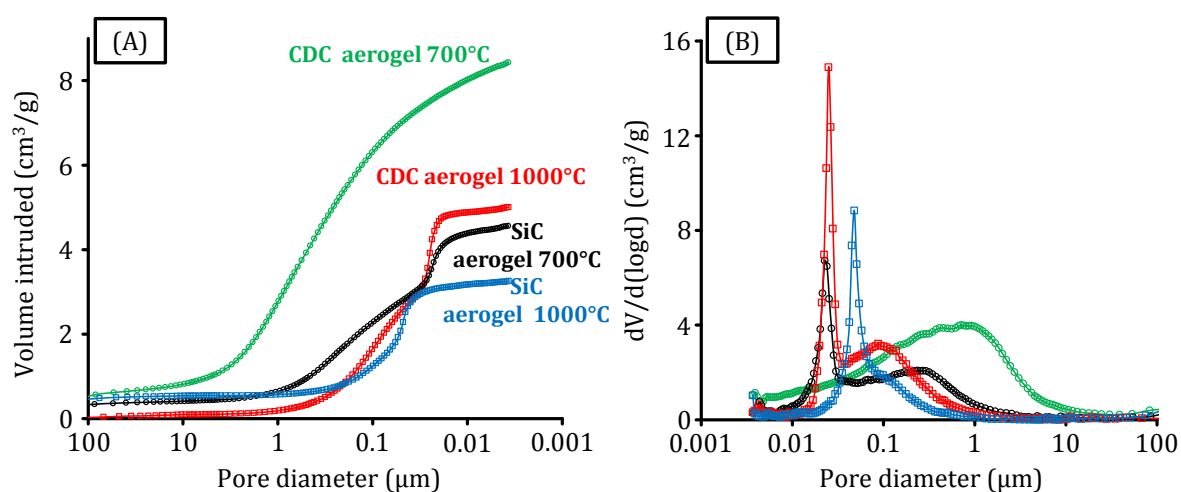
Figure 67. *Mercury intrusion curves (A) and corresponding pore size distributions (B) of the CDC aerogels prepared at 700°C (green) and 1000°C (red) as well as the SiC aerogel precursors pyrolyzed at 700°C (black) and 1000°C (blue).*

Mercury intrusion porosimetry measurements are additionally applied to determine the porosity within the SiC and CDC aerogel monoliths (Figure 67(A)). In terms of the total pore volume, the mercury intrusion curves show the same trend as the nitrogen physisorption measurements. A larger volume of liquid is intruded in the CDCs compared to the SiC aerogels. The highly open and well-accessible pore structure present in the CDC aerogels causes meso- and macropore volumes as high as 8.43 and 5.01 cm^3/g for the materials synthesized at 700 and 1000°C, respectively (Table 12). The micropores present in the materials are not detected by this method and therefore the total pore volume of the CDC aerogel prepared at 700°C is close to 9 cm^3/g. The lower amount of intruded mercury in the carbide and carbon aerogels prepared at higher temperatures is likely related to the higher volume shrinkage during synthesis associated with the formation of rather dense materials as already indicated by SEM

investigations (Figure 64). All aerogels except the CDC material prepared at 700°C show the presence of broadly distributed macropores in the range of 0.5-1 µm and a narrow maximum centered at 0.025-0.05 µm (Figure 67(B)). The larger pores are formed by the open cell foam macrostructure of the aerogels while the maximum centered at smaller pore size is related to mercury intrusion in the empty spaces between the agglomerated nanoparticles which are in direct contact. The monomodal distribution of pores in the CDCs prepared at 700°C as well as the distinct intrusion of mercury at larger pore diameter (lower pressure) indicates some structural change of this material (e.g. the collapse of the nanoparticle chains) during the mercury intrusion. Therefore, a reliable pore size distribution cannot be determined for this material.

Carbon Dioxide Adsorption with the InfraSORP Technology

Due to their high SSA in combination with the controllable and hierarchical pore structure, CDC aerogels are attractive candidates for the rapid adsorption of large amounts of carbon dioxide. The benefit of the aerogel-type pore structure appears obvious when the carbon dioxide adsorption properties of these CDCs are compared with purely microporous reference materials. The latter are prepared by pyrolysis of pristine SMP-10 at 700 or 1000°C followed by chlorine treatment at equal temperature. Due to their purely microporous structure, both reference materials show a nitrogen physisorption isotherm of type I at -196°C (Appendix 5). The micropore volume of the microporous CDCs (1.04 cm^3/g for the material prepared at 700°C and 0.84 cm^3/g for the material prepared at 1000°C) is slightly above the CDC aerogels due to the higher silicon/carbon ratio before high-temperature chlorine treatment. In accordance, the SSAs of the reference materials are slightly above the values obtained for the CDC aerogels at the same synthesis temperature. The presence of narrow micropores strongly depends on the conditions during pyrolysis and silicon removal. The uptake of nitrogen reaches saturation at lower relative pressure in the high-temperature sample due to the higher volume of small ultramicropores leading to higher carbon dioxide adsorption capacity (Appendix 5) compared to the material prepared at 700°C. At the same synthesis temperature, both microporous samples offer slightly higher carbon dioxide uptake compared to the CDC aerogels and seem to be the more attractive candidates for the adsorptive removal of carbon dioxide on the first view (Appendix 6). However, besides a high storage capacity, rapid adsorption kinetics are another

important requirement to an adsorbent material and the more compact the material, mass transfer restrictions are likely to occur.
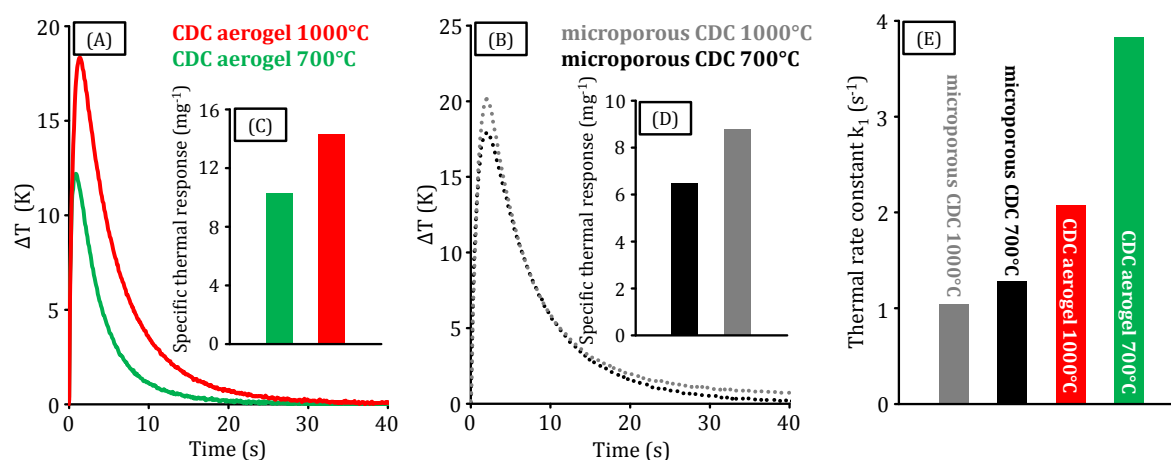
Figure 68. *Thermal response measurements (A and B), corresponding specific thermal responses (C and D) as well as thermal rate constants for adsorption process of 1st order (E) of the CDC aerogels prepared at 700°C (green) or 1000°C (red) and the microporous CDC material prepared at 700°C (black) or 1000°C (grey).*

Thermal response measurements based on the InfraSORP technology using the adsorption of carbon dioxide at 25°C and atmospheric pressure (p/p$_0$ ~0.02) are used to investigate the adsorption properties of the CDC aerogels in comparison to the reference materials. As for the measurements at 0°C under equilibrium conditions (Figure 65(C)), the specific thermal response peak areas of the CDC aerogel and the microporous CDC prepared at 1000°C are about 1.3 fold larger compared to the low-temperature samples. This indicates their larger uptake at 25°C due to the presence of larger volumes of narrow micropores (Figure 68(A-D)).

The InfraSORP technology allows to measure the temperature increase in real-time (the time constant for the optical calorimeter is negliable) and therefore the temperature signal can be directly evaluated in terms of adsorption kinetics. Leistner and co-workers proposed a thermal response function assuming that the adsorption process follows kinetics of first order according to Equation 24 (ΔT: measured temperature change, ΔT_1: maximum adiabatic temperature, k_1: thermal rate constant, k_2: rate of heat transfer).[205]

$$\Delta T(t) = \Delta T_1[(1 - e^{-k_1 t}) - (1 - e^{-k_2 t})] \qquad (24)$$

The thermal adsorption rate constant is obtained by fitting Equation 24 to the measured thermal response curve (Appendix 7). The fit quality R^2 is > 0.998 for all samples except

for the microporous CDC prepared at 1000°C with $R^2 = 0.988$. If the model sufficiently describes the measured data, integration of Equation 24 should give the same peak area obtained by numerical integration of the signal. This is the case for the microporous CDC prepared at 700°C and the CDC aerogels prepared at 700 and 1000°C where the peak areas (calculation from function vs. numerical integration) show deviations of only 5.0%, 1.4%, and 4.4% respectively. For the microporous sample obtained at 1000°C a much larger deviation of 33% is calculated because the function does not sufficiently describe the long term equilibration behavior of the measured data for this material containing the narrowest micropores and no transport pore arrangement.

In accordance to the work of Reucroft and Rivin, the thermal response function can be modified by a second process which describes the migration of molecules adsorbed in easily accessible larger pores to the stronger adsorption sites in the more narrow micropores.[223] In consequence, an additional thermal response peak is introduced in Equation 24, giving Equation 25 (*T₂*: maximum adiabatic temperature of the migration process, k₃: thermal rate constant of the migration, k₄: rate of heat transfer for the migration process).

$$\Delta T(t) = \Delta T_1 \left[\left(1 - e^{-k_1 t} \right) - \left(1 - e^{-k_2 t} \right) \right] + \Delta T_2 \left[\left(1 - e^{-k_3 t} \right) - \left(1 - e^{-k_4 t} \right) \right] \qquad (25)$$

Using Equation 25 for fitting the thermal response of the microporous reference sample prepared at 1000°C gives a good quality for entire range of the data (Appendix 8). The disappearance of the second peak for the CDC aerogel obtained at 1000°C indicates enhanced kinetics in carbon dioxide adsorption due to superior accessibility of the micropores provided by the meso-macropore system. Moreover, the obtained overall adsorption rate constants k_1 show a direct correlation between the pore structure of the investigated materials and their adsorption kinetics. Independent of the synthesis temperature, strictly microporous CDCs show significantly slower adsorption constants ($k_1 = 1.04$/s for synthesis at 1000°C and $k_1 = 1.28$/s for synthesis at 700°C) compared to CDC aerogels ($k_1 = 2.07$/s for synthesis at 1000°C and $k_1 = 3.83$/s for synthesis at 700°C, Figure 68(E)). For both systems, rather rapid adsorption can be observed in the samples prepared at the lower temperature indicating that the presence of larger micropores enhances the kinetics as well.

In conclusion, CDC materials with an aerogel-type pore structure, SSAs of more than 2100 m²/g, and total pore volumes close to 9 cm³/g can be prepared by hydrosilylation

of polycarbosilanes in the presence of a platinum catalyst followed by supercritical drying, ceramic conversion and high-temperature chlorine treatment. Due to the simultaneous presence of a high volume of micropores with the size controllable by the synthesis temperature and the aerogel-type structure of agglomerated nanoparticles, CDC aerogels combine high capacities with advanced kinetics in carbon dioxide adsorption compared to reference materials without transport pores but comparable microstructure.

5.3.2 CO_2 Activation and EDLC Performance of CDC Aerogels

CO_2 Activation of CDC Aerogels

The porosity of the CDC aerogels can be further increased by post-synthetic activation in carbon dioxide. With an activation carried out at a temperature of 950°C for the duration of 4 h and by using a large batch of CDC aerogel obtained at 700°C as the parent material, the specific surface area and the micropore volume can be increased to 2498 m^2/g and 0.63 cm^3/g, respectively (Figure 69(A,B)).
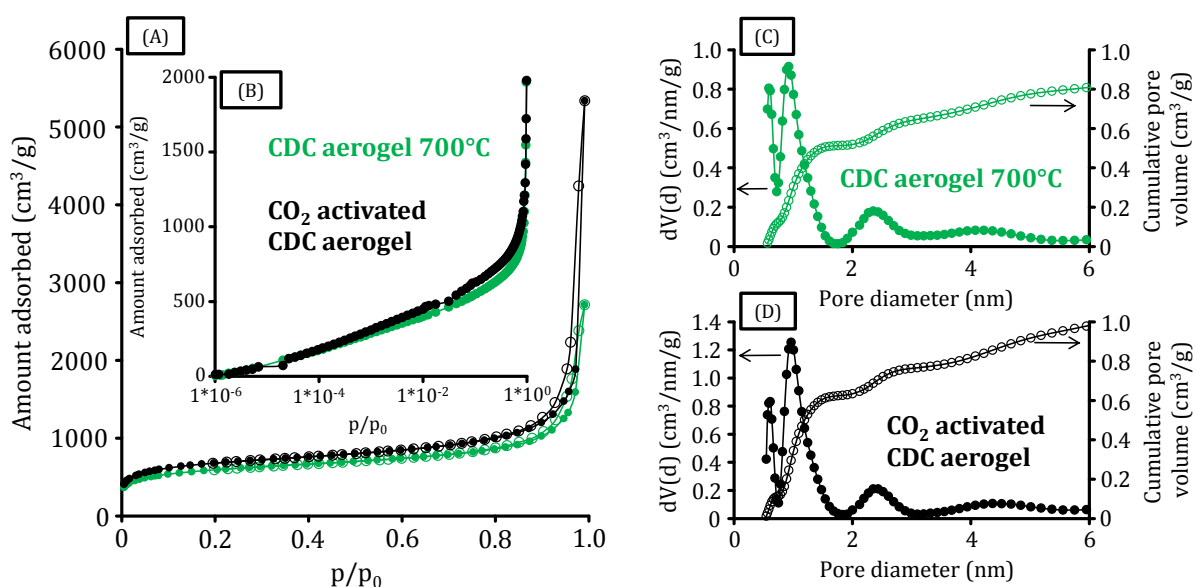
Figure 69. *Linear (A) and semi-logarithmic (B, low pressure measurement) plots of nitrogen physisorption (-196°C) isotherms and corresponding QSDFT (nitrogen on carbon with slit/cylindrical pores at -196°C, adsorption branch kernel) pore size distributions (C and D) of a CDC aerogel prepared at 700°C (green) and the CO_2 activated CDC aerogel (black).*

During activation, slight widening of the micropores takes place (Figure 69(C,D)). A higher volume of larger micropores centered at 0.9-1.0 nm is present in the activated material compared to the as-made CDC aerogel. However, in spite of the CO_2 activation,

the general shape of the isotherm is still similar to the parent material. The large uptake at relative pressures ($p/p_0 > 0.9$) indicates that the aerogel-type system is still intact even after the oxidation process. This observation is confirmed by SEM investigations of the CO_2 activated samples, which show the presence of a meso-macropore structure comparable to the parent material (Figure 70).
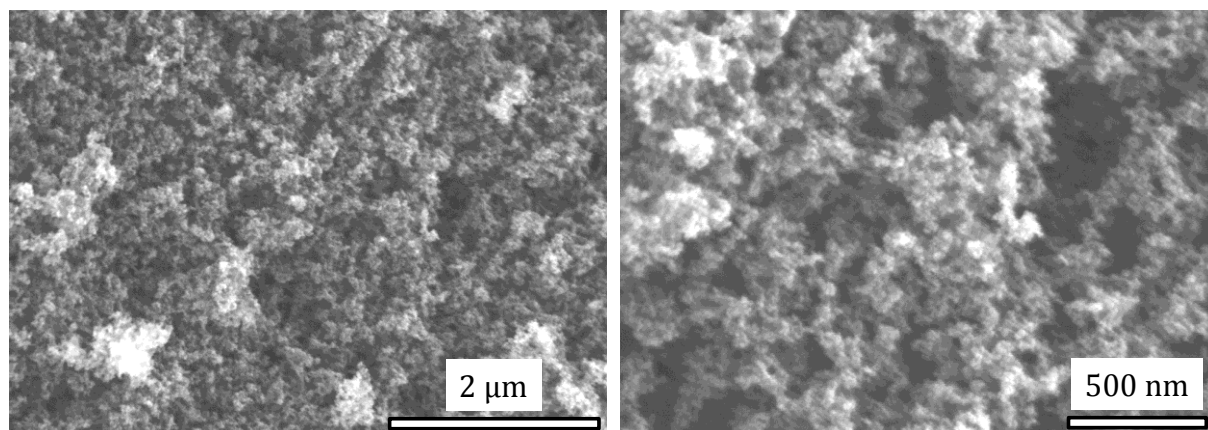
Figure 70. *SEM micrographs of the CO_2 activated CDC aerogel.*
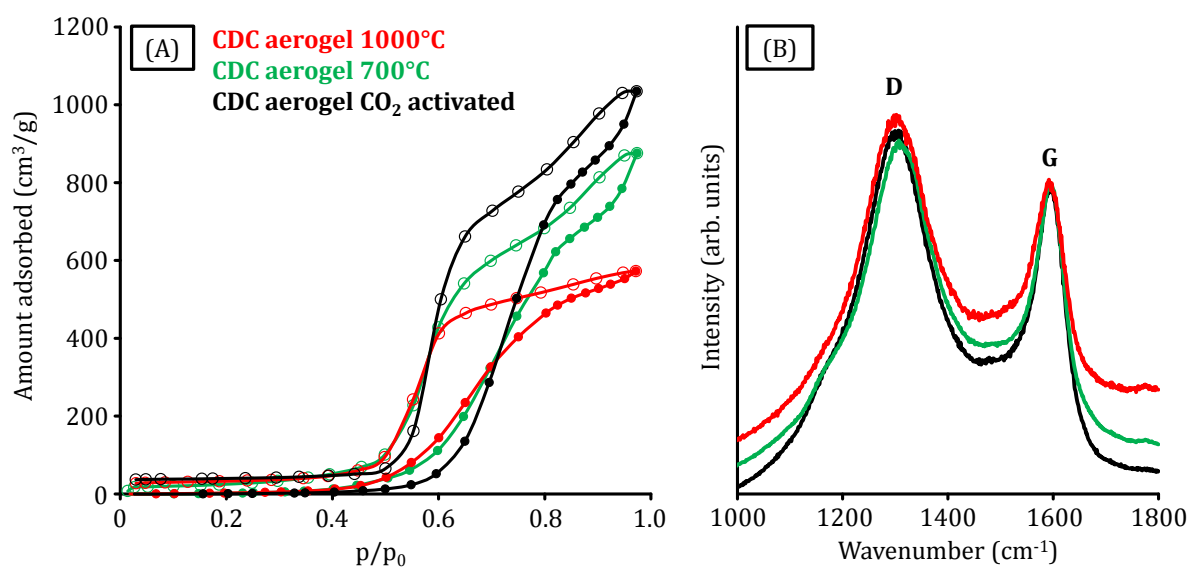
Figure 71. *Water vapor physisorption (25°C) isotherms (A) and Raman spectra of the CDC aerogel prepared at 700°C (green), 1000°C (red), and the CO_2 activated CDC aerogel (black).*

The water vapor physisorption isotherms of the CO_2 activated CDC aerogel and the as-made CDC aerogels obtained at 700°C and 1000°C (Figure 71(A)) show a large uptake at medium relative pressures ($p/p_0 > 0.5$ for the as made CDCs and $p/p_0 > 0.6$ for the CO_2 activated sample). The starting point of water adsorption in porous carbon materials is influenced by the pore size and the presence of hydrophilic surface functional groups.[158]

The higher relative pressure of the initial adsorption for the activated sample is likely related to more hydrophobic surface properties compared to the CDC aerogel obtained at 700°C as their micropores are similar in size (Figure 69(C,D)). The similar onset point of the vapor uptake of the CDC aerogel prepared at 700°C compared to the material obtained at 1000°C is, in view of its larger pore size, likely related to the higher number of surface functional groups as it is typical for CDCs prepared at such low temperatures. The maximum vapor uptake at high relative pressure which increases from the CDC aerogel obtained at 1000°C to the material prepared at 700°C and the CO_2 activated sample reflects the trend in the micropore and narrow mesopore volumes determined by nitrogen physisorption.

The post-synthesis treatment does not drastically change the carbon microstructure of the CDC aerogels. The Raman spectra of all materials are comparable in shape and the I_D/I_G ratios are ranging from 1.55 for the CDC aerogel prepared at 700°C to 1.58 for the CO_2 activated CDC aerogel (Figure 71(B)). A slightly higher degree of graphitization in the CDC aerogel prepared at 1000°C is indicated by the lower FWHM of the D-band of 117 cm^{-1} compared to the material prepared at 700°C (133 cm^{-1}) and the activated sample (134 cm^{-1}).

EDLC Performance of CDC Aerogels

The CDC aerogels are tested as electrode materials in symmetrical EDLCs in different types of electrolyte systems (Figure 72). Due to the large variety of potential aqueous electrolytes, the CDC aerogel prepared at 700°C is used in different electrolytes (1 M aqueous solutions of H_2SO_4, Li_2SO_4, HCl, and LiCl) to evaluate the optimum system.

All the cyclic voltammogramms are of nearly perfect rectangular shape over the applied potential range of -0.6-0.6 V independent of the elevated scan rate. This indicates the absence of a large number of surface functional groups and proofs the high purity of the CDC aerogel. In case of the 1 M H_2SO_4 and 1 M HCl electrolyte, a very minor contribution of pseudocapacitive contributions is observed. From both the cyclic voltammogramms and the charge-discharge tests it can be concluded that the highest capacitance values are achieved in the 1 M H_2SO_4 solution. At the lowest scan rate (1 mV/s) and current density (0.1 A/g), specific capacities of 147 and 151 F/g are achieved, respectively. Furthermore, high capacitance retentions at high current densities and scan rates are observed in this electrolyte system. The 1 M Li_2SO_4 electrolyte leads to comparably

stable rate performance but the maximum capacitance values are significantly below the 1 M H_2SO_4 electrolyte. This is likely related to the diameter of the Li^+ cation. Due to its larger size, fewer ions can be stored within the pore system of the CDC aerogel and lower capacity is achieved. Furthermore, both electrolytes with chloride as the anion offer high capacities at low scan rates and current density but fail to operate at higher charge-discharge rates. Especially the EDLC based on the 1 M HCl electrolyte can utilize only 21% and 10% of its initial capacity of 129 F/g at high scan rates of 500 mV/s and 1000 mV/s, respectively.
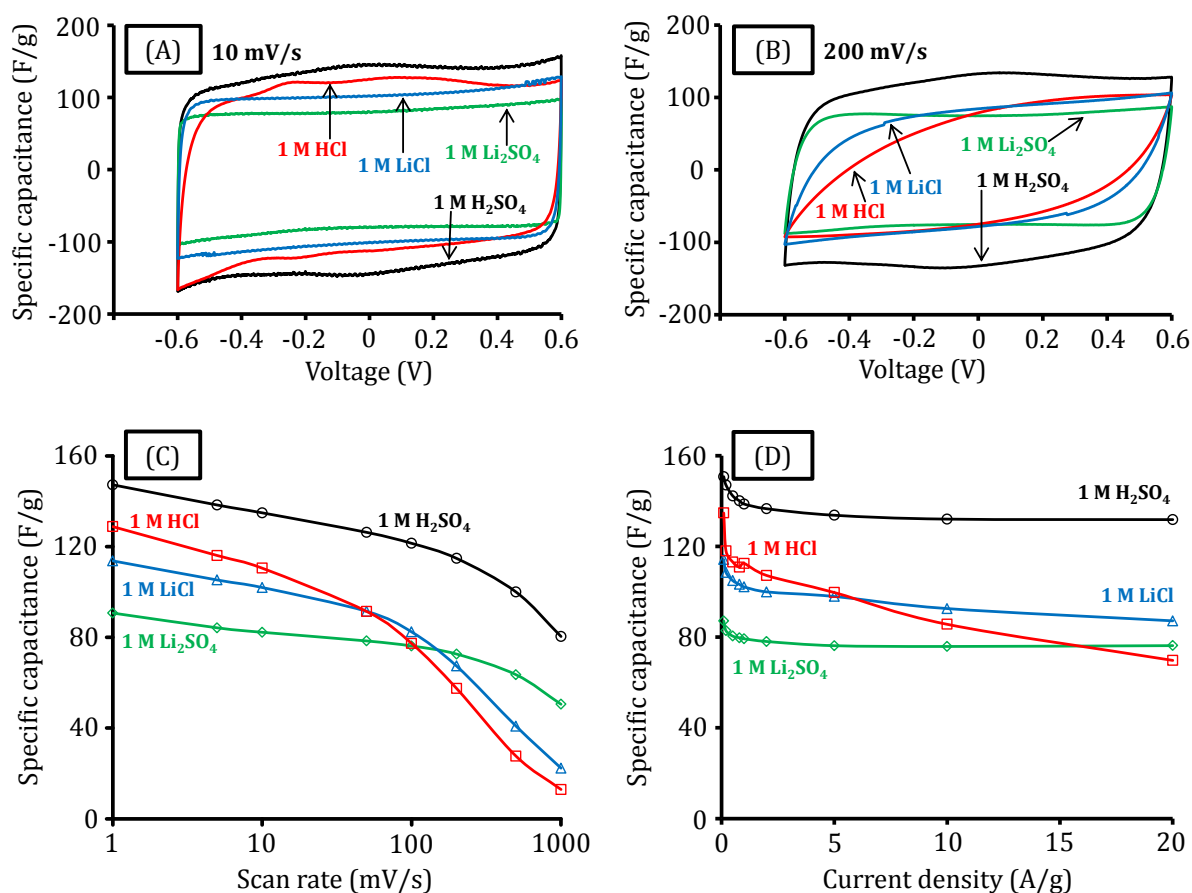
Figure 72. *Cyclic voltammograms at scan rates of 10 mV/s (A) and 200 mV/s (B) and specific capacities at different scan rates (C) as well as specific capacities obtained from galvanostatic charge-discharge tests (D) of the CDC aerogel prepared at 700°C in different 1 M aqueous electrolytes.*

Electrochemical impedance spectroscopy measurements (Figure 73) underline beneficial characteristics of the EDLC operating in the 1 M H_2SO_4 electrolyte. The abrupt drop in capacitance starts at one order of magnitude higher frequency compared to the chloride-containing electrolytes (Figure 73(A)). In contrast, only a marginal difference can be observed when compared to the EDLC based on the 1 M Li_2SO_4 electrolyte. In

consequence, it can be assumed that the favorable high-rate performance of these electrolytes is related to the sulfate-anion rather than to the cations. The Nyquist plots (Figure 73(B)) show the presence of higher resistance in the chloride-containing electrolytes indicated by the rather distinct semicircle. This additional resistance is responsible for the worse high-rate performance of these electrolytes. From these measurements it can be concluded that the 1 M H_2SO_4 electrolyte is favorable for the use of the CDC aerogels in aqueous EDLCs as they provide both the highest capacity and stability.
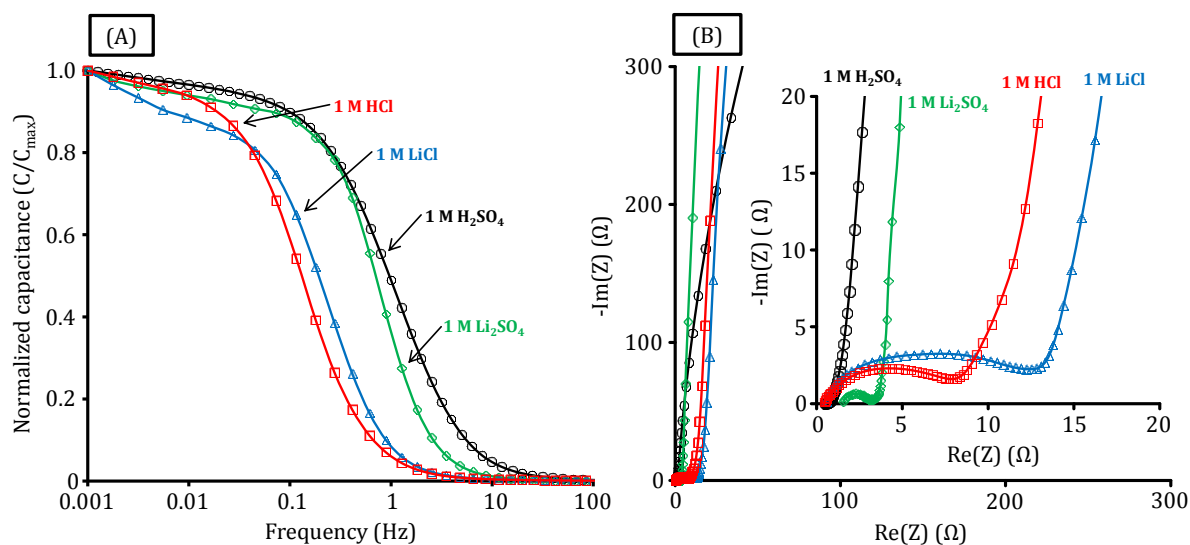
Figure 73. *Frequency responses (A) and Nyquist plots (B) of the CDC aerogel prepared at 700°C in different 1 M aqueous electrolytes.*

Characterization of the three different CDC aerogels in EDLCs based on 1 M H_2SO_4 electrolyte clearly reflects the influence of their pore structure on the EDLC performance (Figure 74). Compared to the CDC aerogel prepared at 700°C (147 F/g), the CO_2 activated material and the CDC aerogel prepared at 1000°C exhibit slightly lower capacities of 135 F/g and 109 F/g, respectively (calculated from cyclic voltammogramms at 1 mV/s scan rate). At very high scan rates of up to 1000 mV/s, the materials still provide sufficient capacitance due to their aerogel-type pore structure with high macropore volume for sufficient ion transportation and nano-sized CDC domains which serve for short diffusion pathways to reach the adsorption sites (micropores). The specific capacities calculated from charge-discharge tests (Figure 74(E)) are in good accordance to the values obtained from CV and also prove the outstanding high-power capability of the CDC aerogels. In spite of its higher SSA, the

initial capacitance of the activated CDC aerogel is slightly below the CDC aerogel prepared at 700°C. This is likely related to the lower amount of surface functional groups and hence less contribution of faradic redox reactions to the capacitance of the activated material. Independent of the scan rate, the CV of this material is of a more rectangular shape compared to the non-activated material (Figure 74(A,C)). At higher scan rates, when surface reactions are too slow to contribute to the capacitance, the values of the activated material are higher than those for the CDC aerogel prepared at 700°C according to its higher SSA and micropore volume.
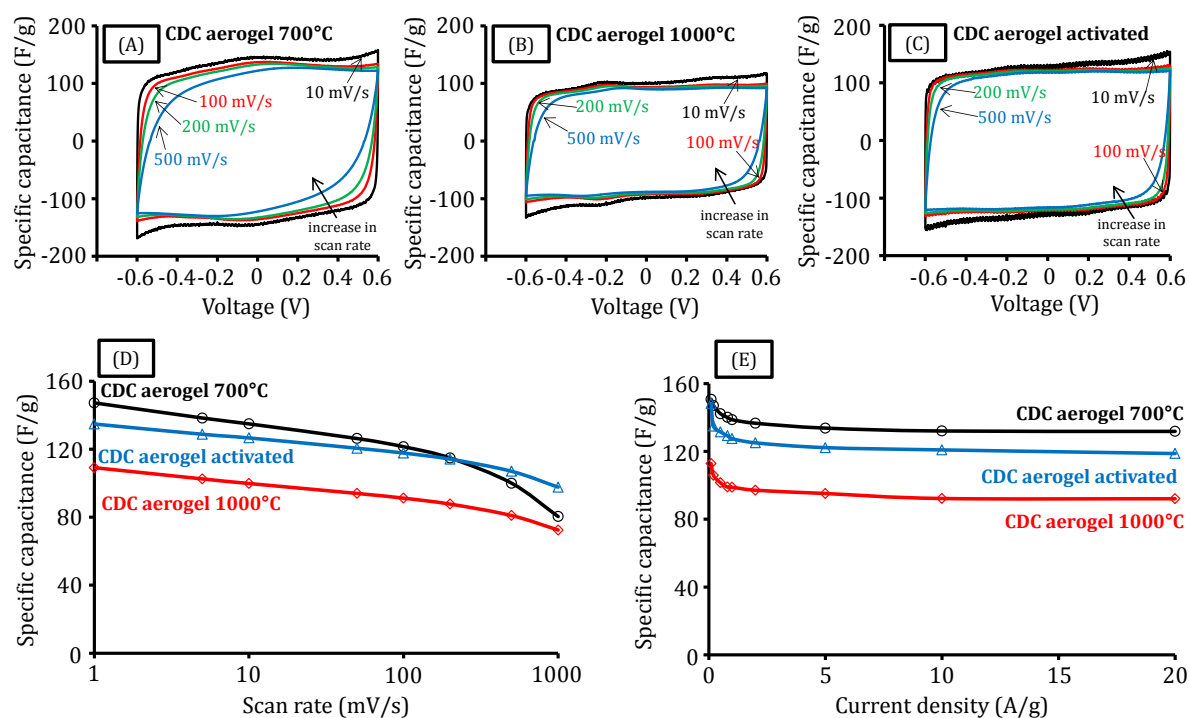
Figure 74. *Cyclic voltammograms at different scan rates of the CDC aerogel prepared at 700°C (A), the CDC aerogel prepared at 1000°C (B) and the CO_2 activated CDC aerogel (C) as well as corresponding specific capacities (D) and specific capacities obtained from galvanostatic charge-discharge tests (E) in 1 M aqueous H_2SO_4 electrolyte.*

From the impedance spectroscopic analyses of the CDC aerogels, it can be concluded that the resistance of all materials is relatively low as it is typical for aqueous electrolyte systems.[145] The material prepared at 700°C has a slightly higher resistance as indicated by the capacitance drop occurring at lower frequencies (Figure 75(A)) as well as the higher resistance in the Nyquist plot (Figure 75(B)). This could be related to the slightly lower conductivity of the CDC aerogel prepared at the lowest temperature of 700°C as indicated from the lowest I_D/I_G ratio of all samples determined by Raman spectroscopy

(Figure 71(B)). The electrical conductivity of the carbon material is an important factor for the performance in EDLCs, especially at high charge-discharge rates.

Figure 75. *Frequency responses (A) and Nyquist plots (B) of the CDC aerogel prepared at 700°C (black), the CDC aerogel prepared at 1000°C (red) and the CO$_2$ activated CDC aerogel (blue) in aqueous 1 M H$_2$SO$_4$ electrolyte.*

Figure 76. *Cyclic voltammograms at a scan rate of 50 mV/s (A), specific capacities from cyclic voltammogramms at different scan rates (B), specific capacities from charge-discharge tests (C), and freq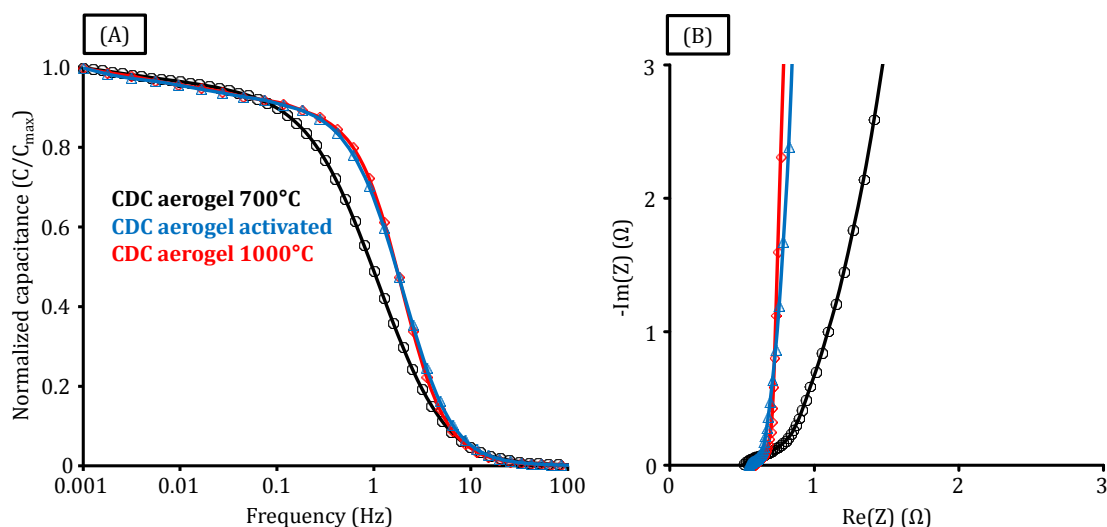uency responses (D) of the CDC aerogel prepared at 700°C (black), the CDC aerogel prepared at 1000°C (red), and the CO$_2$ activated CDC aerogel (blue) in organic 1 M TEABF$_4$ in AN electrolyte.*
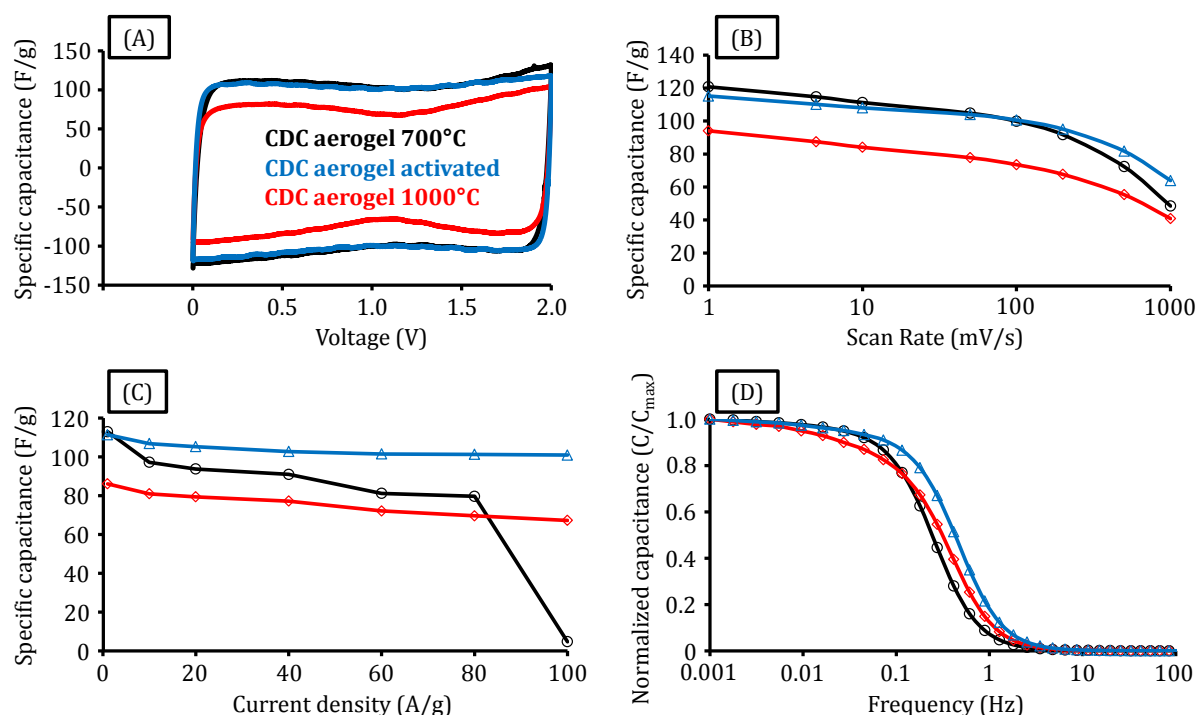
In contrast to aqueous electrolytes, salts dissolved in organic solvents offer the advantage of a higher stability window usually in the range of 2.2-3.0 V and thus the

achievable specific energy is significantly beyond that of aqueous solutions. The CDC aerogels also show good performance if a 1 molar solution of tetraethylammonium tetrafluoroborate (TEABF$_4$) in acetonitrile (AN) is used as the electrolyte. In cyclic voltammogramms (Figure 76(A,B)), specific capacities of up to 121 F/g are obtained by the CDC aerogel prepared at 700°C at the lowest scan rate of 1 mV/s. The activated sample offers comparable capacity values independent of the scan rate while the CDC aerogel prepared at 1000°C provides lower capacity due to its slightly lower SSA.

Charge-discharge measurements, which are most accurate to characterize EDLCs under relevant conditions, proof the advanced electron transport properties of the CDC aerogels (Figure 76(C)). In principle, an ideal EDLC must deliver the same energy independent of the current density. However, even at current densities below 10 A/g, capacitance drops often occur for systems which are not optimized for ion adsorption (e.g. activated carbons).[157] In case of the activated CDC aerogel, more than 100 F/g can be achieved at a current density of 100 A/g. Such high capacitance retentions are usually only achieved by materials with sufficiently large external SSA, such as carbon onions or carbon nanotubes.[15] The CO$_2$ activated CDC aerogel provides a combination of hydrophobic surface properties, sufficiently large micropores and the aerogel-type transport pore system and is therefore optimal for efficient ion transportation. The CDC aerogel prepared at 1000°C can also operate at such high current densities but shows a lower capacitance and higher capacitance drop due to the lower SSA and smaller micropores, respectively. The CDC aerogel prepared at 700°C fails to operate at current densities above 80 F/g, likely related to their more hydrophilic surface properties which hinder sufficient wetting of the pore system with the non-polar organic electrolyte.

These trends between the different carbon materials are reconfirmed by the frequency responses obtained from impedance spectroscopy analysis (Figure 76(D)). The activated CDC aerogel shows the drop of the capacitance at higher frequencies compared to the non-activated samples in accordance to its higher capacitance retentions at high current density.

In summary, it has been shown that CDC aerogels are outstanding electrode materials in EDLCs in both aqueous and organic electrolyte systems. They simultaneously provide high SSA and the aerogel-type pore structure. Hence, high capacities in combination with excellent capacitance retentions at high current densities and high scan rates can be achieved.

5.4 CDCs from Sacrificial Templates

Various CDC materials with hierarchical pore structure (e.g. CDC mesofoams, see section 5.2.1), show promising results as conductive sulfur hosts in Li-S battery cathodes. These carbons can mitigate polysulfide dissolution via physical adsorption and electrically connect nano-sized sulfur, which suffers from low intrinsic electric conductivity. Micro- and mesoporous CDCs are advantageous for this purpose as their mesopores provide large pore volume for sulfur storage and allow for the rapid ion transport (and thus faster charge-discharge rates). At the same time, micropores induce reduced polysulfide dissolution and provide high surface area for sufficient electrical contact between the active material and carbon.

However, the syntheses of these advanced CDC structures require the use of hard- or soft-templating approaches based on solid-state templates or amphiphilic structure-directing agents, respectively. The removal of the template requires an additional synthesis step in hard-templating routes (often accompanied with the use of extremely toxic substances such as hydrofluoric acid). Soft-templating approaches most often make use of large amounts of organic solvents and polluting surfactants which end up in an evaporated or decomposed state. Sacrificial templating is an attractive alternative as no surfactant is needed and the template removal does not require an additional synthesis step. The elimination of the pore-forming templates takes place in parallel to the thermal conversion of the precursor.

Synthesis and Structure

Micro- and mesoporous CDC materials (PMMA-CDCs) can be prepared from poly(methylmethacrylate) (PMMA) spheres (synthesized by a miniemulsion technique) as pore-forming material.[224] These PMMA spheres are mixed with polycarbosilane polymer precursor followed by simultaneous carbide formation/template removal and by a high-temperature chlorine treatment for CDC formation (Figure 77(A)). They exhibit a narrow size distribution centered at 90 nm as determined by DLS measurements (Appendix 9(A)). SEM images of the PMMA spheres show that the polymeric placeholders are of a near-spherical shape and that the single PMMA nanoparticles obtained after polymerization and drying are agglomerated and contain distinct contact areas. The latter are important for advanced connectivity of the mesopores in the finally obtained carbon material (Appendix 9(B)).
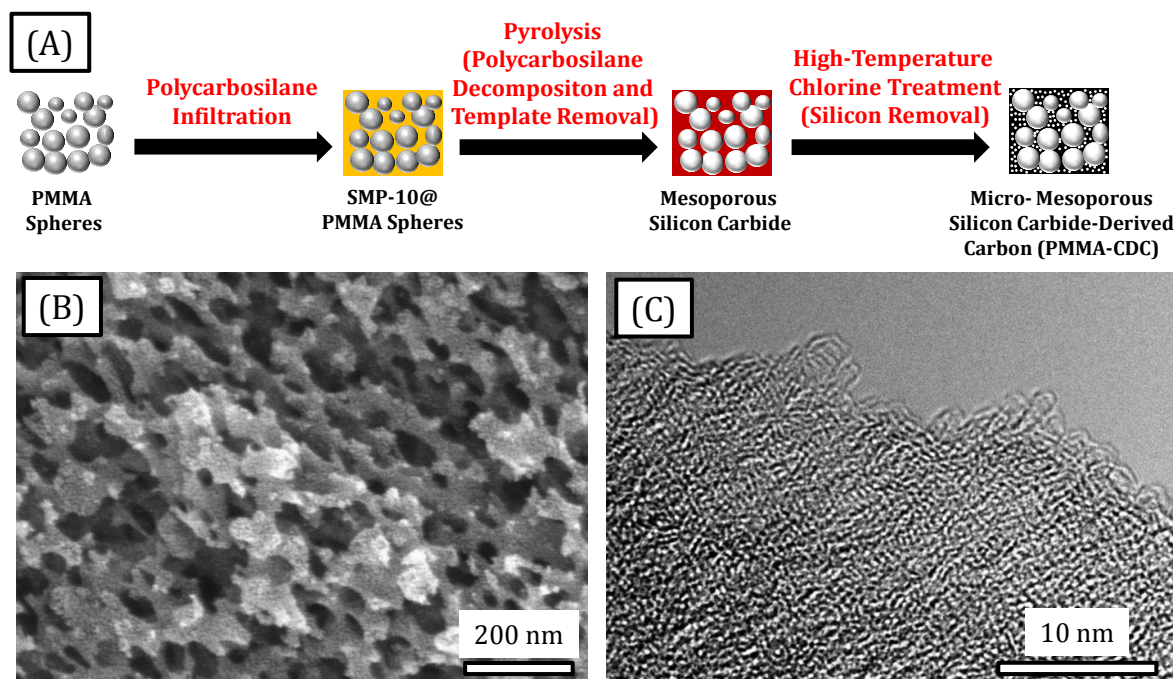
Figure 77. *Procedure for the preparation (A), SEM (B), and TEM micrograph (C) of PMMA-CDC.*
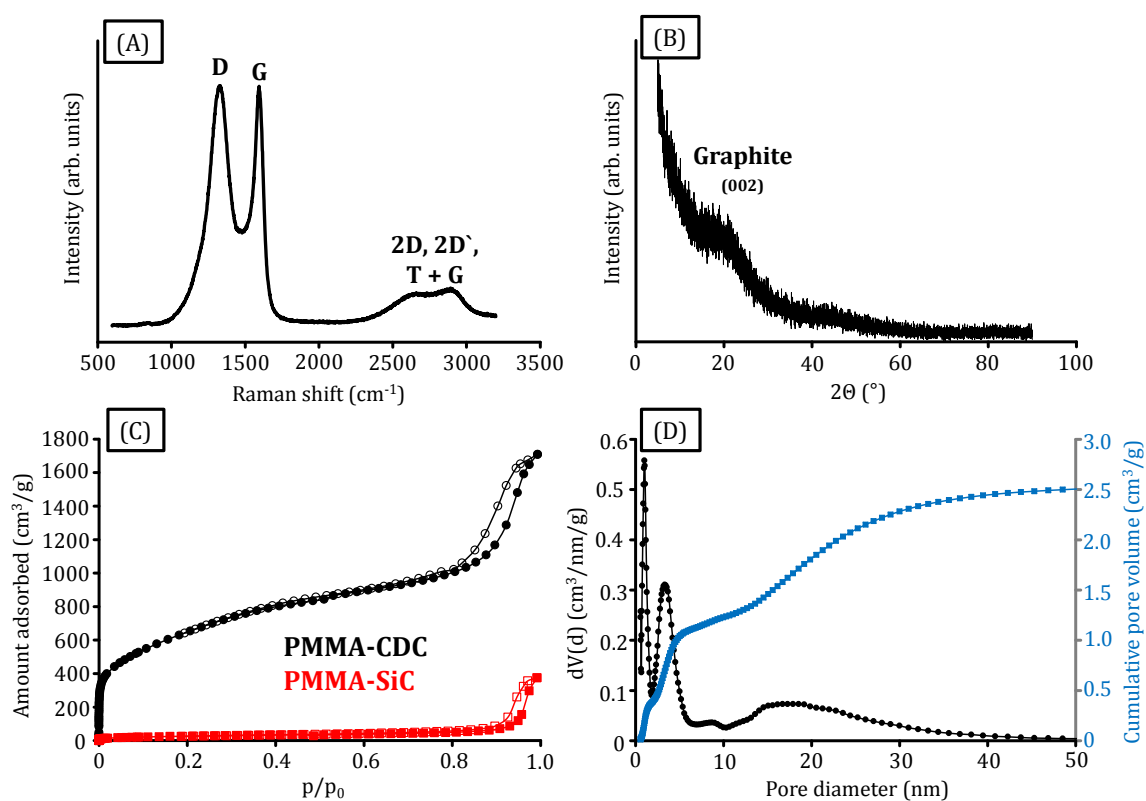
Figure 78. *Raman spectrum (A) and wide-angle XRD pattern (B) of PMMA-CDC as well as nitrogen physisorption (-196°C) isotherms (C) of the PMMA-CDC (black circles) and the mesoporous SiC precursor (red squares) as well as corresponding QSDFT (nitrogen on carbon with slit/cylindrical pores at -196°C, equilibrium branch kernel) pore size distribution of the PMMA-CDC (D).*

The large pores in the CDC materials are comparable in size to the template particles indicating the precise control over the pore size provided by the sacrificial template

route (Figure 77(B)). TEM studies show the highly disordered microstructure of the templated CDC (Figure 77(C)). It mainly consists of randomly oriented sp^2 carbon fringes and no graphitic nanodomains can be observed as it is typical for polymer-based CDCs synthesized at comparable temperatures.

In accordance, the Raman spectrum of the CDC material (Figure 78(A)) shows the characteristic D-band at $\sim$1350 cm^{-1} which is typical for a disordered carbon structure with a high degree of sp^2 atoms (i.e. non-parallel curved graphene sheets). The (peak height) intensity ratio I_D/I_G of the D- and G band of 1.26 and the FWHM of the D-band of 150 cm^{-1} are close to other CDC structures prepared at comparable temperatures (see section 5.3). It is well-known that these carbon materials provide sufficient electric conductivity for the use as electrode materials due to their sp^2-rich structure. As the graphene sheets are highly disordered at the same time and distinct graphitization does not take place, the typical graphite (002) peak appears only with moderate intensity in the XRD pattern of the CDCs (Figure 78(B)).

The hierarchical character of the produced CDCs is proven by nitrogen physisorption measurements (Figure 78(C)). The high specific surface area of 2434 m^2/g and the large micropore volume are responsible for the high uptake of nitrogen in the low-pressure area (p/p$_0$ < 0.2). A distinct hysteresis loop can be observed at high relative pressure (p/p$_0$ = 0.8-0.99) which arises from the larger pores induced by the PMMA template particles. This leads to a high total pore volume of 2.64 cm^3/g. Furthermore, the absence of cavitation or pore blocking effects indicates the high accessibility of the mesopores which is favorable for homogeneous infiltration of sulfur and enhanced electrolyte penetration. In accordance, the QSDFT pore size distribution shows the presence of large mesopores of 10-50 nm combined with micropores of 1.0 nm in size (Figure 78(D)). Minor contributions of small mesopores (3.3 nm) are observed as it is typical for polymer-based carbide-derived carbons (see sections 5.1.1. and 5.3). As it can be seen by the hysteresis loop in the physisorption isotherm, the large mesopores are already present in the silicon carbide materials obtained after PMMA decomposition, which show a moderate specific surface area of 99 m^2/g. In contrast, the micropores are inserted during the removal of silicon during high-temperature chlorine treatment.

The silicon content of the finally obtained CDCs (determined by EDX measurements) is below 0.1 atom%. The comparably high oxygen content of the mesoporous silicon carbide precursors ($\sim$18 atom%) is likely originating from the oxygen-containing

groups of the sacrificial template particles. However, this effect does not negatively influence the purity of the finally obtained CDCs as they show oxygen content of only ~0.5 atom%.

PMMA-CDCs in Li-S Battery Cathodes

The CDCs obtained from PMMA templates simultaneously provide high micropore volume and high conductivity. Together with the precisely defined mesopores and the facile synthesis scheme, PMMA-templated CDCs are highly suitable materials for hosting the electrically insulating sulfur in Li-S battery cathodes.
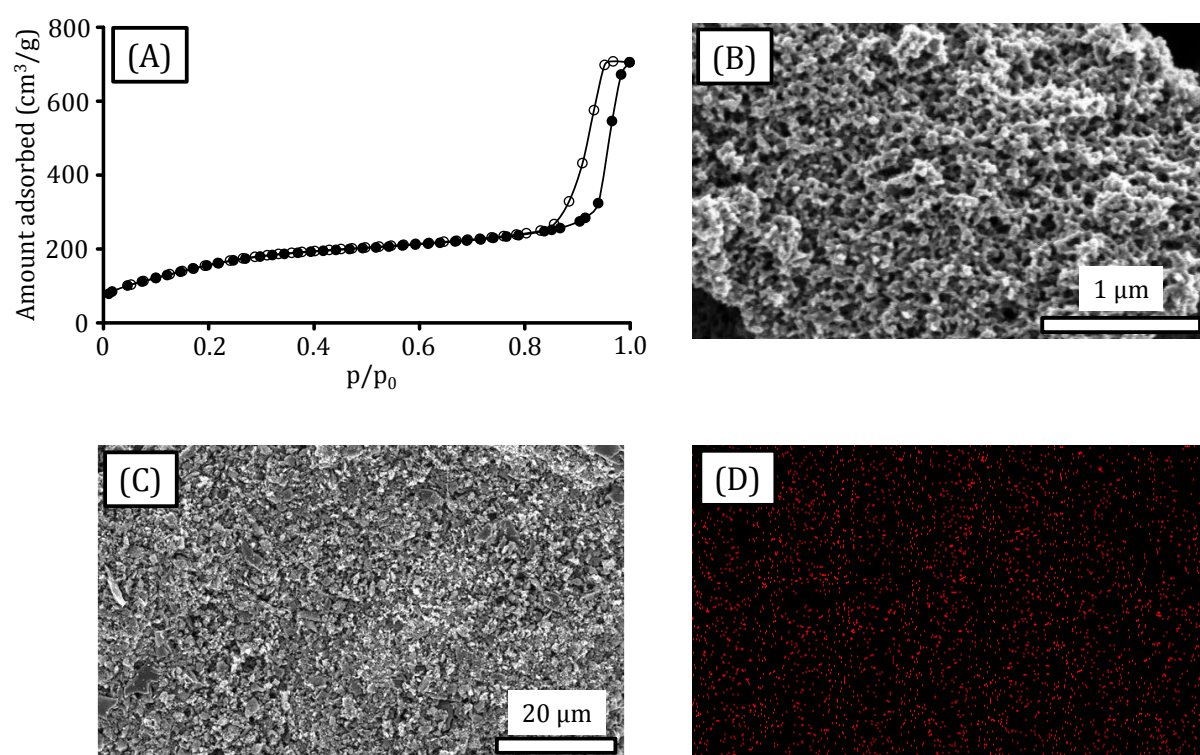
Figure 79. *Nitrogen physisorption (-196°C) isotherm (A) and SEM micrographs (B and C) of the PMMA-CDC/S composite as well as EDX mapping (D) of the sulfur distribution (red).*

After the incorporation of ~45 wt.% sulfur into the pore system of the PMMA-CDC, a nitrogen physisorption measurement of the S/PMMA-CDC composite proofs the strong confinement of the active material into the carbon micropores (Figure 79 (A)). Compared to the pristine PMMA-templated CDC, the specific surface area is decreased to 586 m²/g. The micropore volume remaining after sulfur loading is as low as 0.068 cm³/g. This shows the preferred adsorption of the active material in the carbon micropores and proofs the presence of large electrochemically active surface area. However, a relatively high mesoporosity is still available as indicated by the remaining

hysteresis loop at high relative pressure. The total pore volume of 1.09 cm^3/g serves for sufficient Li diffusion to the active material and can balance the volume expansion of up to 74% during the conversion of sulfur to Li$_2$S. Scanning electron microscopy micrographs of the S/PMMA-CDC powder reveal almost no morphological changes after sulfur infiltration (Figure 79(B)). No agglomerated or large sulfur residues on the particles` external surface are observed. The uniform distribution of sulfur inside the micro and mesopores is confirmed by EDX mapping (Figure 79(C,D)).

The S/PMMA-CDC cathodes exhibit relatively stable cycling performance and high capacity utilization at a current rate of 0.5 C in various electrolyte concentrations (1, 3, and 5 M lithium bis(trifluoromethanesulfonyl)imide (LiTFSI) in dimethoxyethane (DME):1,3-dioxolane (DIOX) (1:1 by volume) (Figure 80(A)). The cathode in 1 M electrolyte exhibits a high initial discharge capacity of 1209 mAh/g$_{Sulfur}$ followed by a distinct capacity drop in the first cycles. 44% of the initial capacity is retained after 50 cycles. The S/PMMA-CDC cathodes in 3 M and 5 M electrolyte exhibit comparable initial discharge capacities of 1324 mAh/g$_{Sulfur}$ and 1404 mAh/g$_{Sulfur}$, respectively. However, these cells exhibit largely improved capacity retention of 55% (3 M electrolyte) and 72% (5 M electrolyte) at the end of 50 cycles. Especially within the first ten cycles the capacitance drops increase at lower electrolyte concentration. This indicates that the polysulfide dissolution is largely suppressed in high-molarity electrolytes due to the reduced solubility of polysulfides which is related to the so-called "common ion effect".[72] The higher concentration of Li-ions in the electrolyte suppresses the solubility of the precipitate according to Le Chatelier's principle. Moreover, lower amount of free solvent molecules in the electrolyte further reduces polysulfide dissolution. In consequence, the unfavorable polysulfide shuttle mechanism is less pronounced as also indicated by SEM micrographs of the cathodes after cycling. The electrode cycled in 1 M electrolyte solution (Figure 80(B)) shows a significant amount of dissolved polysulfides precipitated on the surface of the CDC particles and therefore, many pores are blocked by insoluble low order polysulfides. In contrast, in 5 M electrolyte (Figure 80(C)), the morphology of S/PMMA-CDC cathode is almost identical with its original state (Figure 79(B)). This indicates that the polysulfide dissolution is effectively suppressed in high-molarity electrolytes. This observation is reconfirmed by EDX analysis which reveals that the cathode cycled in 1 M electrolyte exhibits only 43% of its initial sulfur content while the amount of sulfur in the cathode cycled in 5 M electrolyte is still 55% of

the initial value. The continued capacity degradation can be explained by precipitation of low-order insulating polysulfides on the lithium metal anode.

In comparison to the purely microporous activated carbon material YP17D, PMMA-CDC shows much higher capacities due to the advanced pore structure for the use in Li-S battery cathodes. The activated carbon material shows very stable cycling performance because the dissolution of polysulfides is suppressed in small micropores but at the same time the specific capacitance is significantly lower due to reduced sulfur utilization as a result of the increased ionic resistance and incomplete electrolyte accessibility. Random, small, and bottle-neck pore structures present in activated carbons derived from natural sources (e.g. coconut) can be easily clogged with electrically insulating and insoluble low order polysulfides. In contrast to the PMMA-CDC, less sulfur can be utilized in high-molarity electrolyte due to the higher ionic resistance and higher viscosity. These results clearly indicate the importance of the carbon pore structure on the properties as a sulfur host material in Li-S battery cathodes.
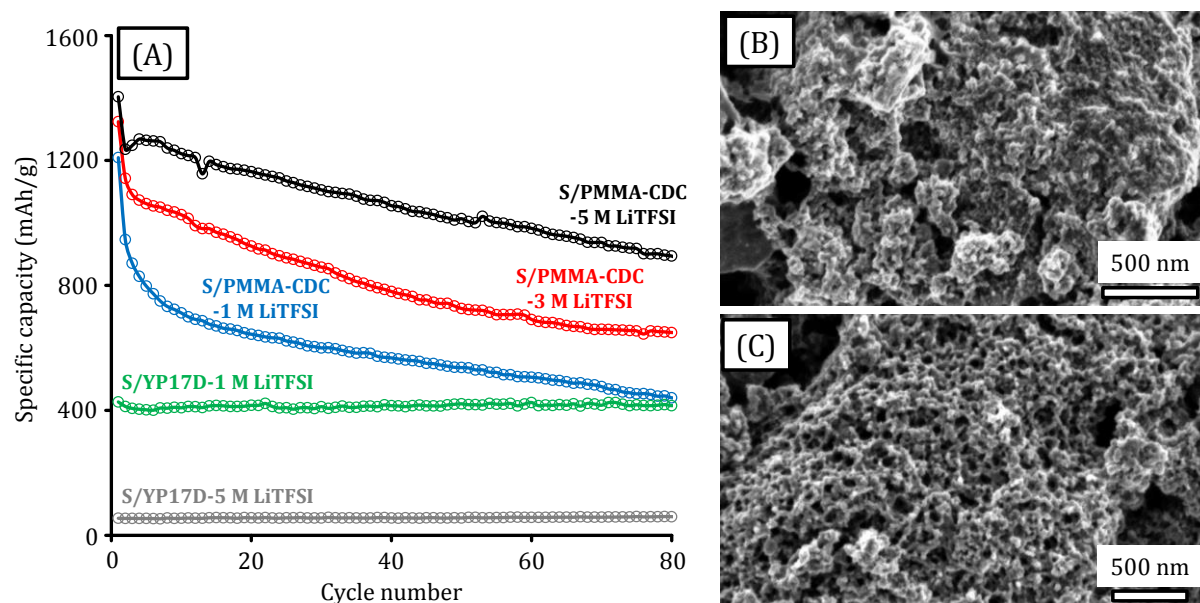
Figure 80. *Discharge capacities (A) of the S/PMMA-CDC cathodes at a current rate of 0.5 C in 1 M (blue), 3 M (red), and 5 M (black) LiTFSI electrolyte in comparison to S/YP17D activated carbon electrodes 1 M (green) and 5 M (grey) electrolyte as well as SEM micrographs of the S/PMMA-CDC cathodes after cycling in 1 M (B) and 5 M (C) electrolyte.*

5.5 Fundamental Adsorption Studies Based on Well-Defined Carbons

As described in the previous sections, polymer-based CDCs can be tailored in their pore structure over a wide range. Depending on their appearance, they show excellent performance in applications related to gas adsorption or electrochemistry. Besides the use in the actual devices, there is also an enormous interest in a better understanding of

the principle phenomena within these processes. CDCs and templated carbons can be applied as model substances for a better understanding of these fundamental processes due to their precisely controllable pore structure. In this chapter, three different methods for the investigation of adsorption processes on the surface of CDCs and templated carbon are presented. In section 5.5.1, solid-state NMR experiments are reported as a useful tool for the investigation of the interactions between carbon-based materials and electrolyte solutions on the atomic level. A study on *in-situ* high-pressure ^{129}Xe NMR spectroscopy in combination with volumetric adsorption measurements is presented in section 5.5.2. The InfraSORP technology is a useful tool for the rapid characterization of porous materials based on the optical adsorption calorimetry. Carbon materials with different pore sizes and pore hierarchies can be distinguished and characterized by this method as reported in section 5.5.3.

5.5.1 Solid-State NMR Spectroscopy Investigations on Ion Adsorption

Although major progress and improvement of EDLCs has been achieved in recent years, a better and more detailed understanding of the basic mechanisms in these devices is still lacking. Therefore, especially *in-situ* characterization and modelling techniques, (often based on CDC structures) receive considerable attention.[225] While the earliest studies are of mainly empirical character (based on electrochemical measurements), *in-situ* techniques are more and more in focus (see section 2.4.1).

The influence of the pore size of the carbon electrode material on the overall performance of EDLCs remains a key question. For a long time, the capacitance of EDLCs was fully ascribed to the formation of an electrochemical Helmholtz double-layer of electrolyte molecules on the carbon pore wall. The carbon pores had to fulfill the requirement that the ion with its complete intact solvent shell has to have full access to their interior. More recent studies report on the significant enhancement of the capacitance when the carbon pore size falls below the solvent shell size of the electrolyte ions and the formation of a double-layer would not be possible from a theoretical point of view.[74] This disagreement and the anomalous increase in capacitance is explained by the distortion of the ion solvation shell in aqueous and organic electrolyte solutions and a reduction of the coordination number in ILs. This leads to a rather close approach of the ions onto the carbon surface and increases the specific capacitance according to Equation 10.

One very attractive technique for the investigation of the interactions between carbon-based materials and electrolyte solutions on the atomic level is the nuclear magnetic resonance (NMR) spectroscopy.[163] It is possible to clearly distinguish between adsorbed ions and those in free solution because the ring currents in the π-electron system within the carbon pore walls give rise to a shielding effect for spins of atoms located between the disordered graphene sheets (i.e. in the pores). Many of these studies make use of activated carbon materials with very disordered pore structure but only very few concentrate on CDCs and templated carbons as appropriate model substances.

In this chapter, carbon materials with well-defined porosity, namely two microporous TiC-derived carbons (prepared at 600°C and 1000°C), ordered mesoporous SiC-CDC (OM-SiC-CDC, see section 2.3.1, in the following denoted as "OM-CDC"), and the hexagonal ordered mesoporous carbon CMK-3 (see section 2.1) are characterized with ^{1}H, ^{13}C, and ^{11}B magic angle spinning (MAS) solid-state NMR after loading with a 1 M solution of TEABF$_4$ in AN with regard to establish a correlation between the NMR parameters and the pore diameter.[226]
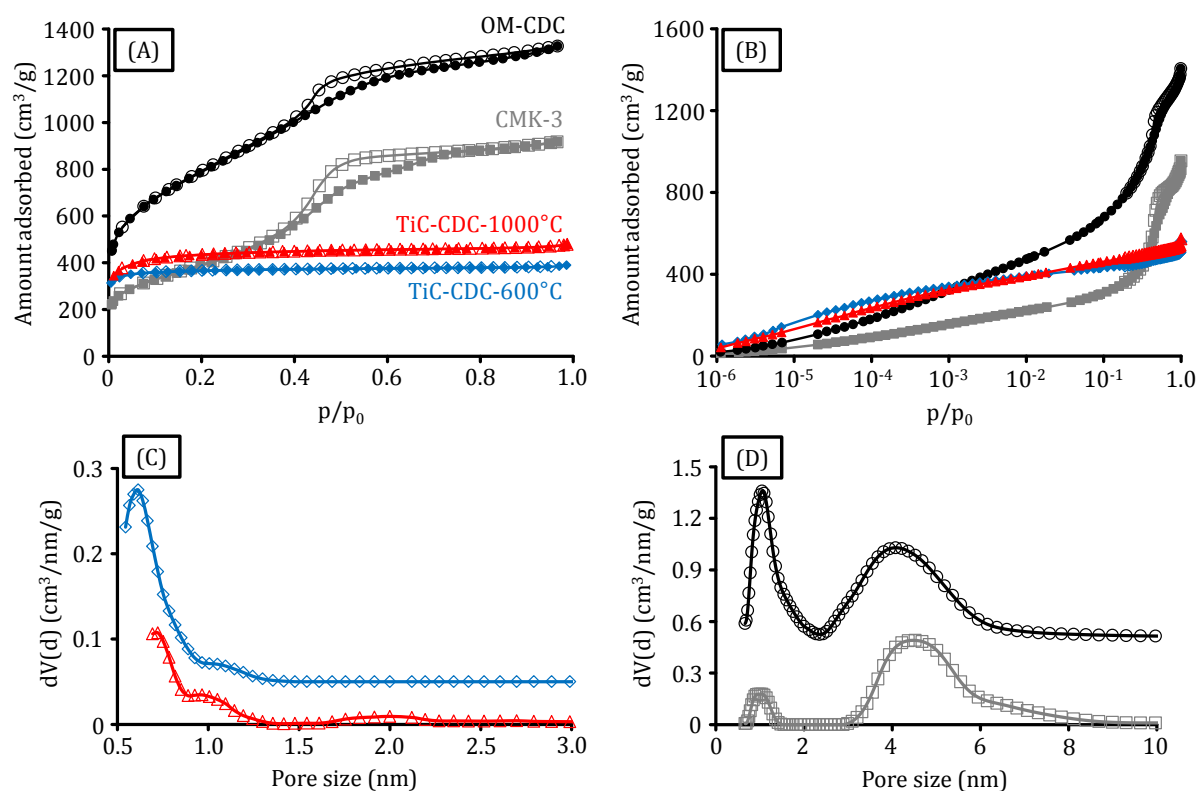

Figure 81. *Linear (A) and semi-logarithmic (B, low pressure measurement) plots of nitrogen physisorption isotherms (-196°C) and corresponding QSDFT (nitrogen on carbon with slit/cylindrical pores at -196°C, adsorption branch kernel) pore size distributions (C and D) of OM-CDC (black), CMK-3 (grey), TiC-CDC-600°C (blue), and TiC-CDC-1000°C (red). PSDs are vertical offset.*

Table 13. Porosity data summary of OM-CDC, CMK-3, and the TiC-CDCs prepared at different temperatures.

Sample	SSA$_{BET}$ (m^2/g)[a]	V$_{Micro+Meso}$ (cm^3/g)[b]	V$_{Micro}$ (cm^3/g)[c]	Average Pore Size(s) (nm)
OM-CDC	2838	2.05	0.55	1.0/4.1
CMK-3	1396	1.42	0.1	(0.9)/4.5
TiC-CDC-1000°C	1652	0.74	0.59	0.8[d]
TiC-CDC-600°C	1412	0.6	0.54	0.6[e]

[a] Specific surface area calculated using the BET equation (p/p$_0$ = 0.05-0.2).
[b] Micro-and Mesopore volume calculated at p/p$_0$ = 0.95.
[c] Micropore volume calculated from the cumulative pore volume up to a diameter of 2 nm (QSDFT method for nitrogen on carbon with slit/cylindrical pores at -196°C, adsorption branch kernel).
[d] Apart from the main pore size, two smaller local maxima in the PSD occur at 1.2 nm and 2.2 nm.
[e] Apart from the main pore size, a shoulder in the PSD is observed at 1.2 nm.

The TiC-CDCs are produced by high-temperature chlorine treatment of bulk TiC powder at different temperatures and in consequence their nitrogen physisorption isotherms (Figure 81(A)) are of type I as it is typical for a purely microporous material. As can be seen in the semi-logarithmic plots of the isotherms (Figure 81(B)), both materials show a high uptake of nitrogen at low relative pressures (p/p$_0$ < 0.1) associated with the filling of the micropores. The strongest adsorption of nitrogen takes place in the TiC-CDC-600°C sample due to the presence of rather narrow micropores when compared to TiC-CDC-1000°C and OM-CDC. Accordingly, the QSDFT-PSD of this sample shows the presence of micropores with a diameter of 0.6 nm (Figure 81(C) and Table 13). Due to the presence of larger micropores, the nitrogen uptake takes place at slightly higher relative pressures in the TiC-CDC-1000°C and the total amount adsorbed is increased as compared to the material prepared at 600°C. Therefore, the maximum in the PSD is shifted to a diameter of 0.8 nm and minor contributions of slightly larger pores are present (Table 13). In contrast to these microporous CDCs, CMK-3 and OM-CDC show a hysteresis loop at p/p$_0$ = 0.4-0.7 as it is typical for materials with hexagonal ordered nanorods. CMK-3 is almost exclusively mesoporous as indicated by the low uptake of nitrogen at low relative pressure (Figure 81(B)). It exhibits a low micropore volume of 0.1 cm^3/g (Table 13) which is mostly caused by the presence of random defects on the surface and within the carbon nanorods related to the decomposition of the carbon precursor. At higher relative pressures, CMK-3 shows high uptake due to the complete filling of the 4.5 nm-sized mesopores with nitrogen. In contrast, OM-CDC contains a hierarchical pore structure of micro- and mesopores. Hence, it exhibits a higher specific

surface area and total pore volume compared to CMK-3. The pore structure of the OM-CDC can therefore be seen as a combination of CMK-3 and the TiC-CDCs as it contains micropores and mesopores centered at 1.0 and 4.1 nm, respectively (Figure 81(D) and Table 13).
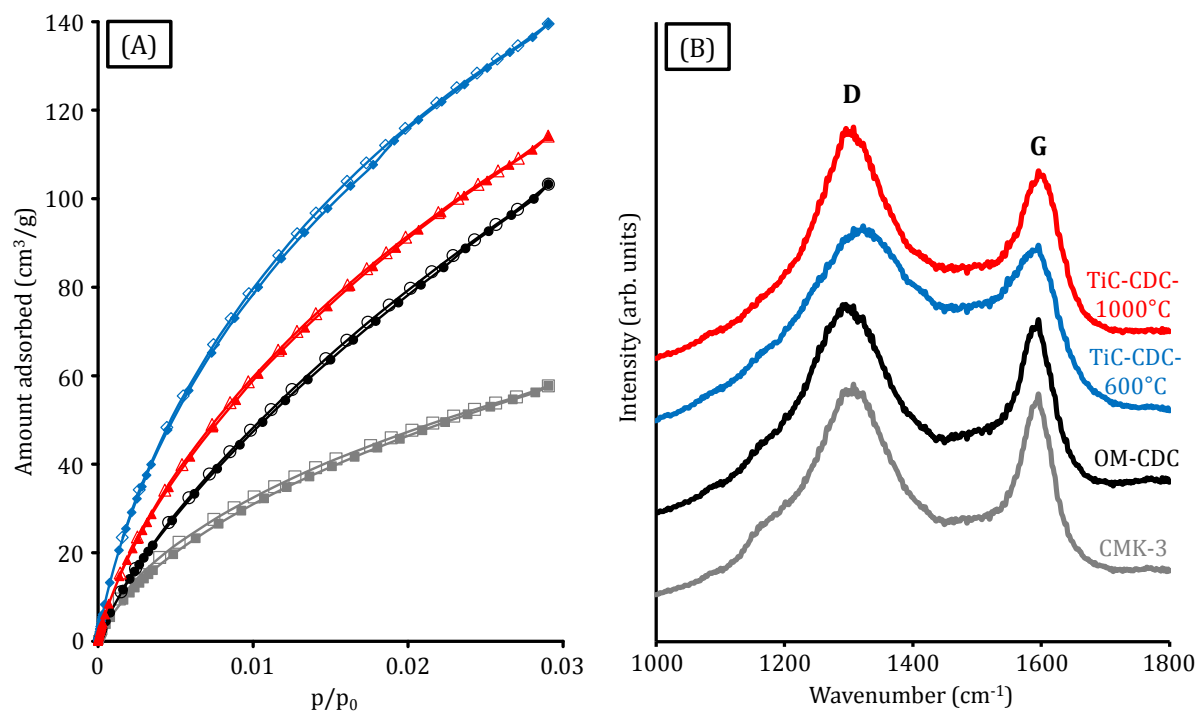
Figure 82. *Carbon dioxide physisorption (0°C) isotherms (A) and Raman spectra of OM-CDC (black), CMK-3 (grey), TiC-CDC-600°C (blue), and TiC-CDC-1000°C (red).*

Carbon dioxide measurements at 0°C up to 1 bar (p/p_0 ~0.03) additionally show the large differences in the micropore structure of the investigated samples (Figure 82(A)). Under these conditions, CO_2 adsorption is very sensitive to the presence of narrow micropores. As a consequence, the highest amount of gas is adsorbed in the pore system of the TiC-CDC-600°C due to the presence of the narrowest micropores followed by TiC-CDC-1000°C and OM-CDC in agreement with their increasing micropore size. CMK-3 shows the lowest uptake due to the lower micropore volume and relatively large micropore diameter of 1.0 nm.

Another important structural difference between the different carbon materials under investigation is their degree of graphitization. Raman spectroscopic investigations show the typical appearance for carbon materials with disordered nanostructure including the disorder-induced D-band and the graphitic G-band arising from a double-resonance process (inter-valley scattering) and in-plane stretching vibrations of sp^2-bonded sites,

respectively (Figure 82(B)). The increasing intensity of both bands in carbon materials prepared at higher temperature indicates an increasing graphitization (i.e., the growth and enlargement of the sp^2-bonded sites in the pore walls). According to the most disordered carbon microstructure (i.e. the lowest degree of graphitization), TiC-CDC-600°C shows the lowest (intensity related) I_D/I_G ratio (1.26) of all samples while OM-CDC (1.43) and CMK-3 (1.43) are comparable in graphitization to TiC-CDC-1000°C (1.44).
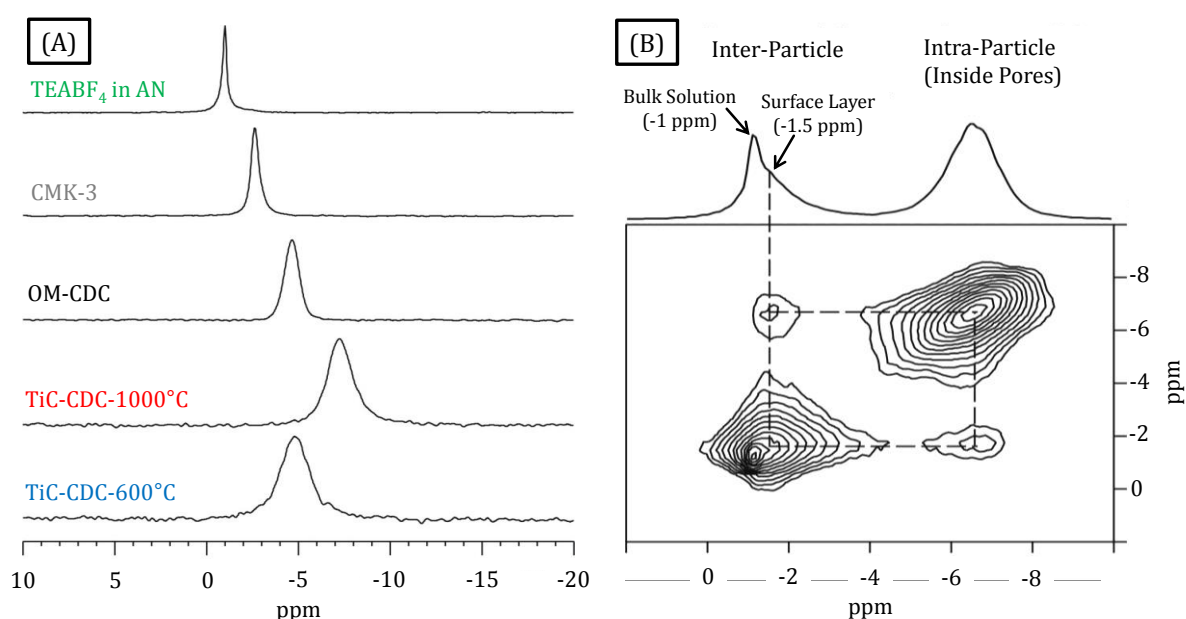
Figure 83. ^{11}B MAS NMR spectra of the carbon materials and the pure electrolyte solution (A) as well as ^{11}B-^{11}B exchange spectroscopy (2D EXSY) of TiC-CDC-1000°C loaded with an excess of 1 M TEABF$_4$ in AN (according to 1.5 times the total pore volume) measured at a mixing time of 5 ms (B).

Table 14. ^{11}B NMR chemical shifts, diamagnetic shift ($\Delta\delta = \delta_{Bulk} - \delta$) of BF$_4$, and line widths of the bulk electrolyte solution and the porous carbons loaded with 1 M TEABF$_4$ in AN.

Sample	δ (ppm)	Δδ (ppm)	FWHM (ppm)
TEABF$_4$ in AN	-1.0	-	0.25
CMK-3	-2.7	1.7	0.45
OM-CDC	-4.6	3.6	1.3
TiC-CDC-1000°C	-7.2	6.2	1.55
TiC-CDC-600°C	-4.7	3.7	1.9

After loading with a 1 M solution of TEABF$_4$ in AN according to the pore volumes of the corresponding carbon samples, the ^{11}B MAS NMR spectra (Figure 83(A)) exhibit one signal only as it is also the case for the bulk electrolyte solution. Compared to the

pristine 1 M TEABF$_4$ in AN, the spectra of the electrolyte solutions in the carbon materials show a different chemical shift and larger FWHM (Table 14). The latter increases steadily with decreasing pore diameter. This is likely due to the increasing immobilization (i.e. stronger adsorption) of the BF$_4^-$ ions in smaller pores since the fraction of ions close to the pore walls becomes larger for decreasing pore diameters. The chemical shift of the ^{11}B in all samples is smaller compared to the pure electrolyte solution (Figure 83(A) and Table 14). This is due to the fact that the ions are located inside the pores and experience the characteristic downfield shift ($\Delta\delta = \delta_{Bulk} - \delta$). The latter is caused by the above-described shielding effect of the pore walls affecting the adsorbed ions. For the samples with comparable graphitization, the strength of this shift is related to the pore diameter. The sample with the largest pores (CMK-3) shows the lowest diamagnetic shift and the sample with the smallest pores (TiC-CDC-1000°C) shows the largest shift due to a stronger confinement of the ions into the micropores. In case of the hierarchical OM-CDC, the signal does not split into two lines as it would be expected for ions adsorbed in micropores and mesopores. This can be explained by the rapid exchange of BF$_4^-$ ions between the well-connected pore systems. Otherwise, two signals would occur at ~-3 and ~-7 ppm because the pore diameters of OM-CDC (4.1 and 1.0 nm) are close to the values for CMK-3 (4.5 nm) and TiC-CDC-1000°C (1.0 nm).

The critical exchange time resulting from the frequency difference between these two chemical shifts is ~0.4 ms. Hence, the exchange between the two pore systems must take place with a characteristic exchange time below 0.4 ms. This hypothesis is reconfirmed by a two-dimensional ^{11}B-^{11}B exchange spectroscopy (2D EXSY) measurement of TiC-CDC-1000°C loaded with 1 M TEABF$_4$ in AN at a mixing time of 5 ms (Figure 83(B)). In this case, the volume of the electrolyte solution added to the carbon material is higher than the total pore volume. This results in the additional presence of a relatively broad signal at -1.5 ppm and a narrow signal at -1 ppm. As these signals only occur for loadings exceeding the internal pore volume and based on the chemical shift, both signals are ascribed to BF$_4^-$ located outside the pores (i.e. in the inter-particle space). The species giving rise to the broad signal at -1.5 ppm exchange with the species adsorbed inside the pores even at a mixing time of only 5 ms as can be seen from the corresponding cross peaks. The broad signal at -1.5 ppm is therefore ascribed to BF$_4^-$ outside the particles but in close contact with the outer surface (i.e. they represent the outer surface layer covering the particles). The narrow signal at -1 ppm is ascribed to BF$_4^-$ in the inter-

particle space without surface contact. As the ions on the outer surface of the particles exchange with the species adsorbed inside the pores under these conditions, the averaged signal of OM-CDC due to this effect is reasonable, especially if the fact that the exchange processes between narrow and large pores within the pore system of an OM-CDC particle should be much faster is taken into consideration. The presence of this inter-pore exchange process proves the strongly hierarchical character of this material.
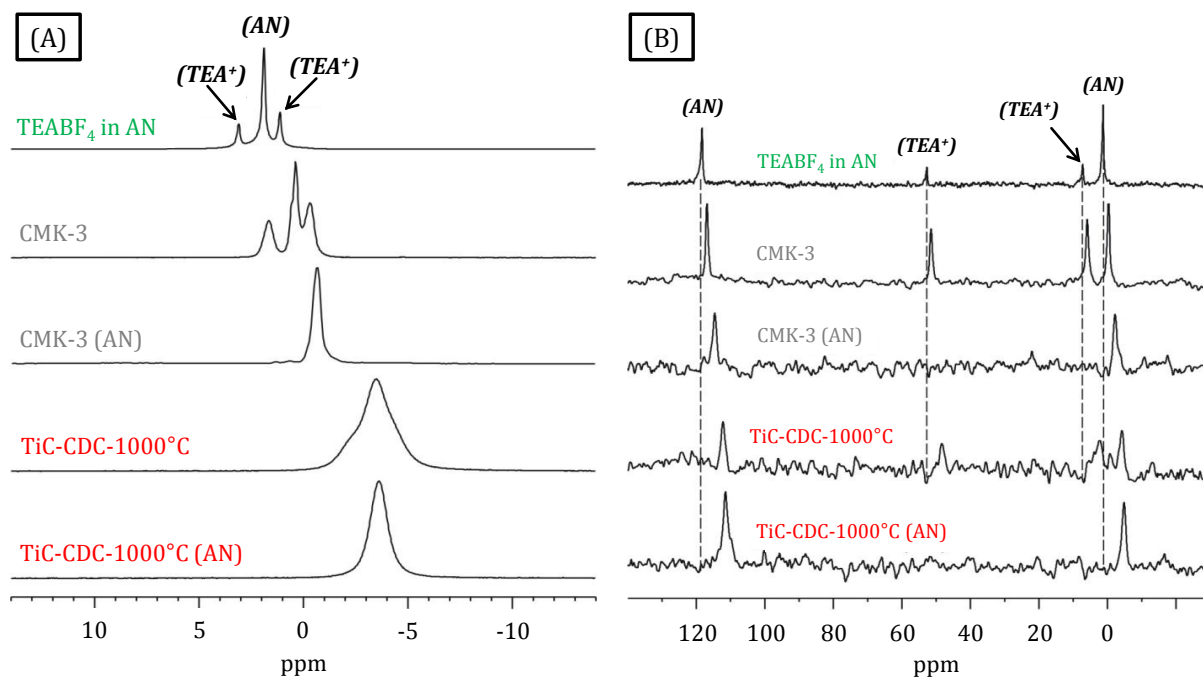
Figure 84. ^1H (A) and ^{13}C (B) MAS NMR spectra of CMK-3 and TiC-CDC-1000°C loaded with AN and 1 M TEABF$_4$ dissolved in AN as well as spectra of the pure electrolyte solution.

In accordance with the results of the ^{11}B spectra, ^1H (Figure 84(A) and Table 15) and ^{13}C ((Figure 84(B) and Table 15) MAS NMR investigations of the carbon materials loaded with electrolyte solution and the pristine AN solvent without TEABF$_4$ ions show a pore size-dependency of the adsorption state of ions into the carbon pores. As already observed in the ^{11}B spectra, all signals exhibit a different diamagnetic shift compared to the pure electrolyte without carbon. With the exception of TiC-CDC-600°C, the shift increases with decreasing pore size (Table 15). The fact that the low-temperature CDC does not follow the pore size dependency of the chemical shift is caused by its less ordered and less graphitized carbon nanostructure. The carbon atoms in this material exhibit a higher degree of sp³ hybridization than in the other samples. Therefore, the ring currents in the pore walls are less pronounced leading to a lower diamagnetic shift for all signals measured in TiC-CDC-600°C. Besides the chemical shift, the line width of

the ^{1}H spectra is also dependent on the pore diameter (Figure 84(A)). It increases with decreasing pore diameter again due to the fact that the adsorbed molecules are indeed increasingly immobilized in pores of decreasing size.

Table 15. *^{1}H and ^{13}C NMR chemical shifts of AN or AN with 1 M TEABF$_4$ adsorbed in porous carbon samples as well as the pure compounds.*

Sample	^{1}H Chemical shift		^{13}C Chemical shift			
	$\delta_{\text{Pure AN}}$ (ppm)	$\Delta_{\text{Electrolyte}}$ (ppm)	$\delta_{\text{Pure AN}}$ (ppm)		$\Delta_{\text{Electrolyte}}$ (ppm)	
			Signal 1	Signal 2	Signal 1	Signal 2
TEABF$_4$ in AN	1.9	1.9	1.4	118.1	1.4	118.3
CMK-3	-0.6	0.5	-2.4	114.7	-0.2	116.8
OM-CDC	-3.0	-1.3	-4.6	111.5	-2.1	114.9
TiC-CDC-1000°C	-3.6	-3.4	-4.8	111.4	-4.3	112.1
TiC-CDC-600°C	-1.9	-1.9	-1.9	113.6	-2.0	114.0

Further interesting effects can be seen if the samples loaded with the electrolyte solution and pure AN are compared. The diamagnetic shift of the ^{1}H and ^{13}C NMR signals of AN is less pronounced in the presence of 1 M TEABF$_4$ especially for CMK-3 and OM-CDC with the larger pore diameter (Table 15). As it is not very likely that the presence of TEABF$_4$ has an influence on the ring currents in the pore walls, it can be assumed that the observed effect is due to a decreasing concentration of AN molecules close to the pore walls in presence of the electrolyte salt. This would be the case if the BF$_4^-$ and TEA$^+$ ions are not homogeneously distributed within the pores. In the case of a concentration gradient (i.e. if these ions tend to reside closer to the walls), the available space for AN in the strongly influenced interface layer would be reduced and AN would exhibit a higher concentration in the middle of the pore. However, in the narrow pores of the microporous CDCs, this model does not apply anymore because the pores are too small for such an arrangement and the entire pore volume must be considered as strongly influenced by the ring current effects in the walls. Indeed, the chemical shift of AN in these materials is almost independent of the presence of TEABF$_4$ (Table 15).

According to the proposal of Chmiola and co-workers,[74] the solvent shell surrounding TEA$^+$ must be strongly perturbed or even "stripped off" inside pores smaller than 1 nm as a result of the ion diameter (1.30 nm with AN solvation shell, 0.67 nm without solvation shell).[142] To further substantiate this idea, the influence of solvent removal on the ^{13}C CP (cross-polarization) MAS NMR spectra of CMK-3 and TiC-CDC-1000°C (i.e. a large-pore and a narrow-pore sample) is investigated (Figure 85). In all spectra, the presence of TEABF$_4$ is detected independent of the presence of the solvent molecules. Evacuation of the materials under high vacuum then results in the disappearance of the signal related to AN and leads to a significant broadening of both TEA$^+$-signals. In case of the purely microporous TiC-CDC-1000°C, the chemical shifts of the TEA$^+$ signals are practically independent of the presence of AN, i.e. the presence of the solvent does not significantly influence the TEA$^+$ chemical shift. From this it can be concluded that the molecules adsorbed in the micropores do not exhibit an unperturbed solvation shell. In contrast, in CMK-3, solvent removal leads to a further diamagnetic shift as the removal of the solvation shells brings the ions closer to the mesopore walls and they are rather strongly influenced by the shielding effect of the sp^2 carbon ring forces. These results prove that under the elevated conditions, ions adsorbed in mesopores contain their solvation shell completely intact while ions at least partially loose the surrounding shell in carbon micropores which is an experimental proof for the theory developed by Chmiola and co-workers.
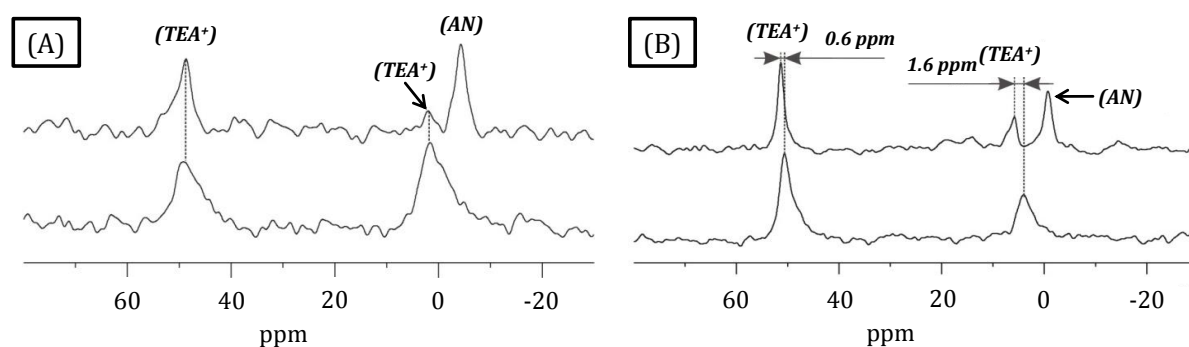
Figure 85. ^{13}C(^{1}H)CP MAS NMR spectra of TiC-CDC-1000°C (A) and CMK-3 (B) loaded with 1 M TEABF$_4$ in AN before (top) and after (down) AN removal.

In summary, solid-state MAS NMR is a highly useful tool for characterization of the adsorption state of ions onto carbon nanopores. If well-defined carbon materials with different pore sizes and pore architectures are used as model electrode materials, important conclusions can be derived from these measurements. i) Only one NMR signal

is detected for all nuclei located at molecules adsorbed inside the pore system. This is even true for hierarchical carbons with bimodal pore size distribution. That means that the adsorbed molecules move and exchange rapidly inside the pores and between the different pore systems. ii) The chemical shift of molecules adsorbed in porous carbon materials of comparable degree of sp^2 hybridization is correlated with the pore size. The molecules are increasingly immobilized in smaller pores. (iii) In carbon materials with sufficiently large pores, electrolyte molecules tend to reside closer to the pore walls than the solvent molecules. Removal of the solvent by evacuation results in a removal of the solvent shell and brings the electrolyte molecules into even closer contact with the pore walls. (iv) If adsorbed in pores smaller than 1 nm diameter, solvent removal does not result in a further increase of the diamagnetic shift.

5.5.2 In-Situ High-Pressure ^{129}Xe NMR Spectroscopy

The adsorption of gases on the surface of porous materials is the most widely applied characterization tool for their characterization. It will likely remain the most frequently used technique for textural imaging of porous solids because it enables the calculation of important properties such as the specific surface area, total pore volume and pore size distribution.[189]

One very useful method for the adsorptive characterization of porous materials is the *in-situ* ^{129}Xe NMR spectroscopy of adsorbed xenon because it allows the direct investigation of the physical state of adsorbed molecules. Xenon is an inert, nonpolar spin-1/2 atom with a high NMR sensitivity and a large electron cloud which is very sensitive to different interactions with various environments. This results in a wide chemical shift range. In consequence, ^{129}Xe NMR spectroscopy, which was firstly described in 1980 by Ito and Fraissard,[227] offers many parameters that can be correlated to structural properties of the porous materials (e.g. the chemical shift, the line width, the chemical shift anisotropy, and the longitudinal relaxation time T_1). In general, the overall chemical shift of adsorbed ^{129}Xe depends on xenon-surface interactions and density-dependent xenon-xenon interactions. As the xenon-xenon interaction is negligible at low xenon densities, the extrapolation of the chemical shift to relative pressure $p/p_0 = 0$ yields the xenon-surface interaction contribution. For porous carbon materials, the latter depends on structural parameters such as the concentration of acidic groups, strong adsorption sites, heteroatoms, and the average pore size. However,

most of the studies on *in-situ* [129]Xe NMR spectroscopy are focused on less-defined materials, such as activated carbons and are limited to low relative pressures.[228, 229]

In this chapter, [129]Xe NMR studies at -36°C up to 18 bar on a series of well-defined CDC and templated carbon materials, namely OM-CDC, CMK-3, TiC-CDC-600°C, and TiC-CDC-1000°C (see section 5.5.1), are described.[230] These conditions allow the study of adsorption/desorption isotherms up to a relative pressure close to $p/p_0 = 1$. The [129]Xe NMR spectra measured at a temperature of -36°C and a xenon pressure of 11 bar show at least two [129]Xe NMR signals (Figure 86(A)). The signals at low chemical shifts of ~0-20 ppm are due to xenon in the gas phase. The signals of adsorbed xenon occur at higher chemical shifts of 100-300 ppm. In addition to the intense signal of adsorbed xenon and the gas phase signal, a third signal appears for TiC-CDC-600°C (denoted by an asterisk in Figure 86(A)) at ~35 ppm. Its intensity amounts to only 4% of the signal of adsorbed xenon at 264 ppm. Due to the low chemical shift and intensity, the signal can be attributed to macropores (e.g. pores between the particles). Xenon in these macropores interacting with the outer surface of the TiC-CDC-600°C particles would give rise to such a chemical shift.
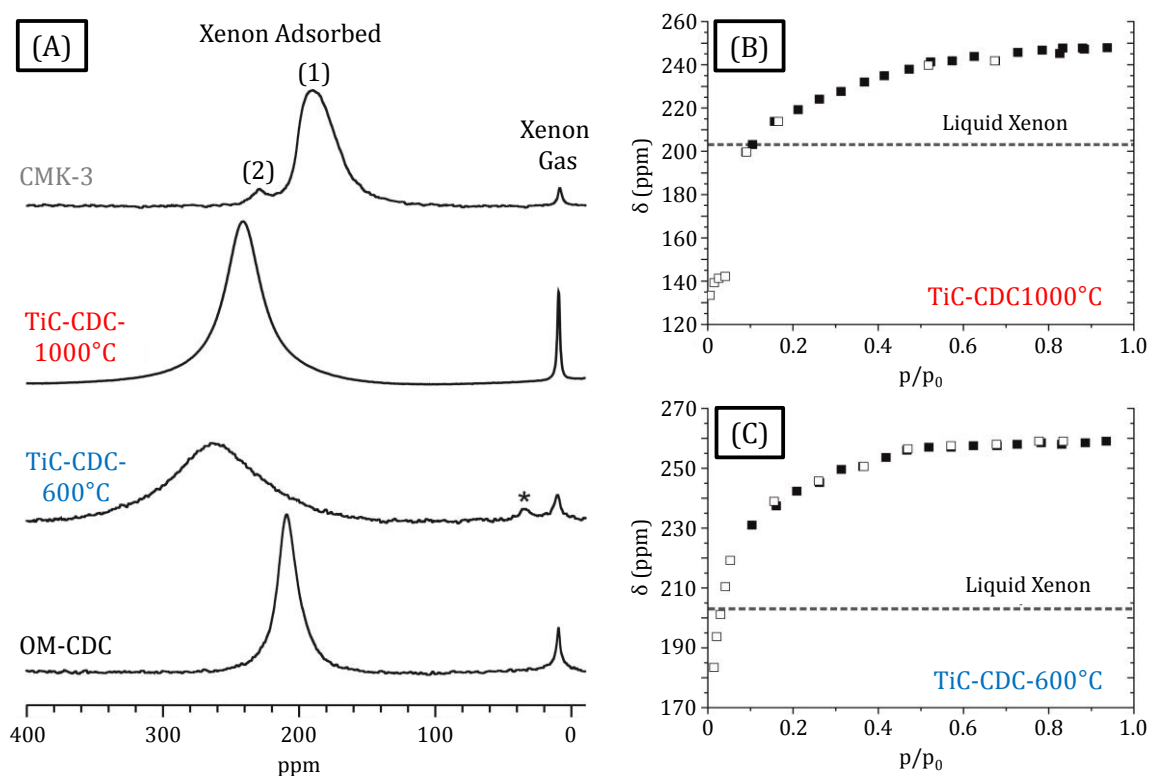
Figure 86. *[129]Xe NMR spectra for isothermal xenon adsorption on OM-CDC, CMK-3, TiC-CDC-1000°C, and TiC-CDC-600°C measured at -36°C at a xenon pressure of 11 bar (p/p₀ = 0.64) (A) as well as [129]Xe NMR chemical shift for TiC-CDC-1000°C (B) and TiC-CDC-600°C (C) measured at -36°C as a function of relative pressure (filled symbols: adsorption; empty symbols: desorption).*

According to their monomodal pore size distribution, the two microporous CDCs exhibit only one signal due to xenon adsorbed in the micropores. The highest chemical shift among all samples is observed for gas adsorbed in TiC-CDC-600°C. Such an inverse correlation between the chemical shift and the pore size is well-known (e.g. for zeolites)[231] and therefore indicates that the micropore size of this sample is smaller than in TiC-CDC-1000°C. This is in agreement with the nitrogen and carbon dioxide adsorption data (see section 5.5.1). It can also be observed that the line width of the xenon adsorbed in TiC-CDC-600°C significantly exceeds the line width of the other samples (Figure 86(A)). This can be explained by the rather strong adsorption of gas in the pores of the low-temperature CDC of 0.6 nm in size which are close to the kinetic diameter of xenon (0.44 nm). In addition, despite the well-defined pore size, surface inhomogeneities due to the rather amorphous carbon microstructure in this sample (see section 5.5.1) can be another reason for line broadening. Finally, xenon clusters of different size may be formed within the micropores which would give rise to a chemical shift distribution.

In contrast to the microporous CDCs, two distinct signals are detected for xenon adsorbed in the pores of CMK-3 (Figure 86(A)). Signal (1) at ~190 ppm and signal (2) at ~230 ppm (with an intensity ratio of approximately 90:10) are due to gas adsorbed in mesopores (1) and micropores (2). The chemical shift of the micropore signal is lower than those observed for the micropores in the TiC-CDCs due to the larger micropores in CMK-3 (see section 5.5.1). The intensity ratio of the signals is also reasonable because the mesopores represent a more than ten times higher fraction of the total pore volume than the micropores.

The plots of the chemical shift of the xenon adsorbed in the microporous CDCs versus the relative pressure of xenon (Figure 86(B,C)) resemble a type I adsorption/desorption isotherm. After a steeply increase of the chemical shift up to a relative pressure of p/p_0 ~0.2, the chemical shift finally levels off at higher pressure and reaches a plateau value. Besides the signal intensity, which represents the amount of adsorbed xenon, this can also be expected for the chemical shift value as it is correlated with the xenon density. Therefore, the plot of the chemical shift versus the relative pressure indeed resembles the shape of the adsorption/desorption isotherm. TiC-CDC-600°C, due to its smaller average pore diameter, shows a higher chemical shift compared to TiC-CDC-1000°C over the entire range of relative pressures. As xenon-wall interactions are

predominating even if the micropores are completely filled, the "saturation value" of the chemical shift of xenon in micropores clearly exceeds the chemical shift of 203 ppm observed for liquid xenon at -36°C.
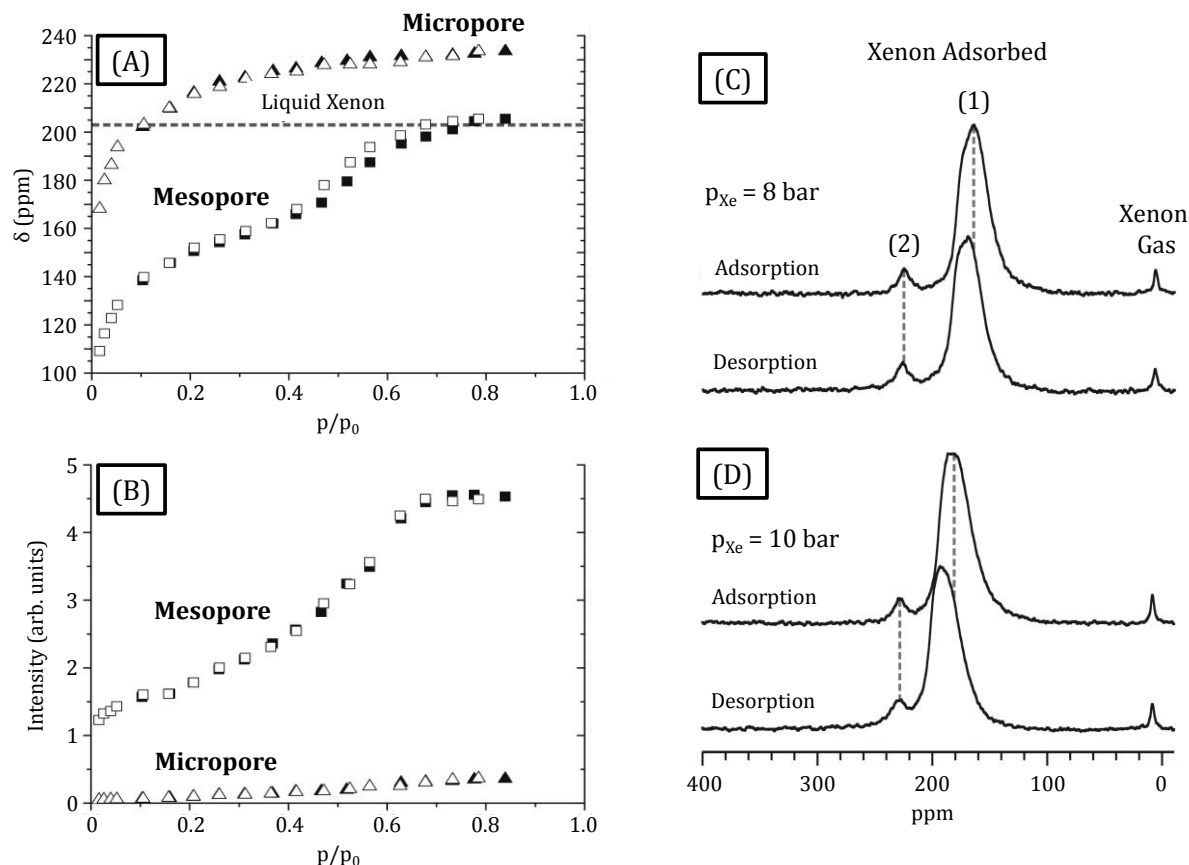
Figure 87. *^{129}Xe NMR chemical shifts (A) and intensities (B) of xenon adsorbed in mesopores and micropores of CMK-3 measured at -36°C as a function of relative pressure (filled symbols: adsorption; empty symbols: desorption) as well as ^{129}Xe NMR spectra of CMK-3 measured during xenon adsorption and during xenon desorption at -36°C at 8 bar (p/p_0 = 0.46) (C) and 10 bar (p/p_0 = 0.58) (D).*

In contrast, the final chemical shift values for xenon inside mesopores of CMK-3 is close to 200 ppm because the condensed xenon is similar to the bulk liquid (Figure 87(A)). For signal (2), the curves resemble a type I adsorption isotherm which is characteristic for microporous materials. Over the entire range of relative pressure, the chemical shift of this signal is lower compared to the TiC-CDCs due to the larger size of the micropores in CMK-3. Compared to the measurement of the signal intensity (Figure 87(B)), the huge advantage of the determination of the chemical shift is its inherently high accuracy. At the chosen measurement temperature of -36°C, the ^{129}Xe NMR signal intensity measurements do not show a hysteresis loop. However, the very sensitive ^{129}Xe NMR chemical shift clearly reflects the onset of a hysteresis at p/p_0 ~0.4-0.7 (Figure 87(C,D)).

While the signal due to mesopores is located at different positions in the spectra of the adsorption and desorption measurements, the chemical shift of xenon adsorbed in the micropores remains constant independent of the relative pressure.
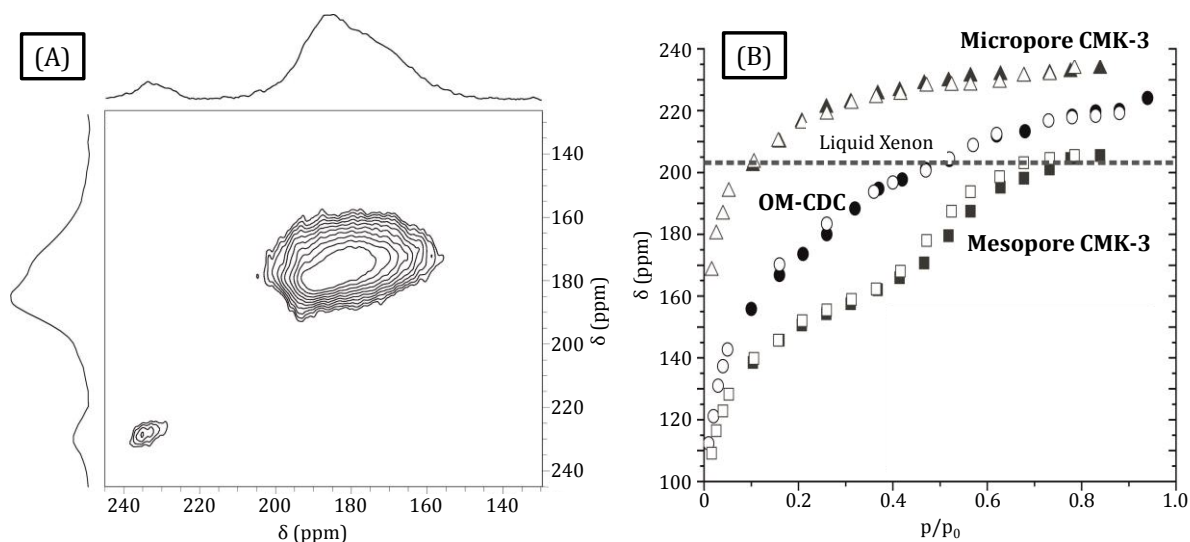
Figure 88. *129Xe NMR EXSY spectrum for isothermal xenon adsorption on CMK-3 measured at -36°C and a xenon pressure of 10 bar with 0.5 s mixing time (A) as well as 129Xe NMR chemical shift for OM-CDC (spheres) measured at -36°C as a function of relative pressure (filled symbols: adsorption; empty symbols: desorption). The data of CMK-3 (triangles and squares) is shown for comparison.*

OM-CDC, which contains a significant amount of both micro- and mesopores, shows only one signal for adsorbed xenon (Figure 86(A)). The chemical shift of the signal is 209 ppm, i.e. it is located in between the micropores (230-260 ppm) and mesopores (190 ppm) of CMK-3 at 11 bar and -36°C. The presence of two distinct signals for mesopores and micropores in CMK-3 shows that the exchange between the two pore systems must be slow at the NMR time scale. Accordingly, 2D exchange spectroscopy (EXSY) at a mixing time of 0.5 s is unable to detect any exchange between the different pore systems (Figure 88(A)). In contrast to CMK-3, the well-interconnected micro- and mesopores in OM-CDC obviously allow a fast exchange of adsorbed xenon between micro- and mesopores. As a result of this fast exchange, a signal at the averaged chemical shift is detected as already observed in the ion adsorption experiments (see section 5.5.1). This averaged chemical shift is observed over the entire relative pressure range (Figure 88(B)). The chemical shift value at the highest relative pressure of 225 ± 3 ppm is located between micro- and mesopores which is in line with the assumption of rapid exchange between the pore systems in this hierarchical material. Moreover, the observed average signal exhibits a lower line width than the other samples under study.

This also indicates a high mobility of the xenon and a well-defined pore size and surface chemistry of this material.
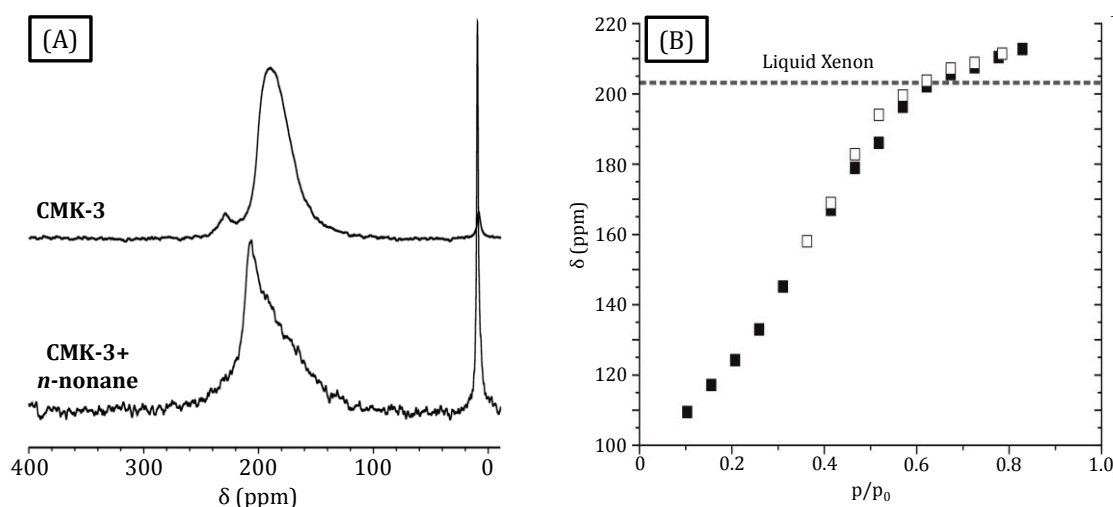
Figure 89. *^{129}Xe NMR spectra of CMK-3 before and after n-nonane preadsorption measured at -36°C at a xenon pressure of 11 bar (p/p$_0$ = 0.64) (A) and ^{129}Xe NMR chemical shift for n-nonane loaded CMK-3 measured at -36°C as a function of relative pressure (filled symbols: adsorption; empty symbols: desorption).*

In addition to xenon adsorption in the pristine materials, the effect of *n*-nonane preadsorption on the pore system of CMK-3 is studied. This treatment preferentially closes the micropores and makes them inaccessible for other molecules whereas the larger pores remain accessible.[120] The ^{129}Xe NMR spectrum of CMK-3 after loading with the hydrocarbon molecules (Figure 89(A)) proves the quantitative blocking of the micropores due to the disappearance of the signal caused by xenon adsorbed in these cavities at ~230 ppm. The signal of xenon adsorbed in the mesopores is located at higher chemical shift after *n*-nonane loading. This observation indicates that the mesopores are also modified by the hydrocarbon molecules. The pressure-dependence of the chemical shift (Figure 89(B)) shows that the hysteresis loop shifts towards slightly lower relative pressure compared to the nonane-free material. These observations indicate that the mesopores become smaller during *n*-nonane loading. Moreover, the maximum chemical shift value of the xenon adsorbed in the mesopores extrapolated to relative pressures of p/p$_0$ = 1 is also slightly larger than before *n*-nonane loading indicating a stronger influence of xenon-wall interactions caused by the presence of *n*-nonane in the mesopores (Figure 89(B)). It is known for hierarchically structured materials (especially for those with an ordered mesopore structure), that *n*-nonane molecules blocking the micropores in the neighborhood of mesopores can also

partly penetrate into the larger pores explaining the shift of the hysteresis loop towards lower relative pressure.[232]

It can be summarized that *in-situ* high-pressure [129]Xe NMR spectroscopy is a very useful method for the characterization of porous carbon materials. The chemical shift extrapolated to a relative pressure of $p/p_0 = 1$ can be used for a precise estimation of the micropore diameter as shown by the isotherms recorded for the two purely microporous TiC-CDCs and the micropores in CMK-3. While xenon adsorbed in the micro- and mesopores of CMK-3 causes two different signals due to their spatial separation, only one averaged signal can be observed in the strongly hierarchical OM-CDC as a result of the well-connected pore systems which allow fast exchange of adsorbed xenon. Finally, the changes in the spectra after the blocking of the micropores with *n*-nonane provide information about the adsorption state of the hydrocarbon molecules in the carbon structure leading to a better understanding of the connectivity of micro- and mesopores which is of interest for various applications.

5.5.3 InfraSORP Studies

A third example for the usefulness of CDCs and templated carbon materials as model substances is their characterization by the so-called InfraSORP technology (see sections 3.2 and 5.2.2). This technique is an efficient tool for the rapid screening of materials properties, such as SSA, adsorption capacities, and adsorption kinetics. In the InfraSORP technology, an infrared sensor directly measures the temperature increase of the adsorbent caused by the released heat of adsorption in a dynamic flow cell when the inert gas (typically nitrogen) is switched to the adsorbing gas (e.g. *n*-butane at 1 bar). So far, studies using this technology mainly focused on microporous metal-organic frameworks or zeolites.[203-205] However, the advanced pore structure of CDCs as well as templated carbide- and carbon materials makes them attractive candidates for the evaluation of the potential of this novel technology. Furthermore, their use as model substances in such measurements can lead to a better understanding of the fundamental principles of the thermal response method and finally also to a more detailed image of the structure of the materials.

In this study, three different microporous CDCs as well as three templated carbide and carbon materials with mesopores are investigated. Microporous CDCs are obtained by chlorine treatment of TiC powder at 600 and 1000°C (see section 5.5.1) and by pyrolysis

with subsequent chlorine treatment of the allylhydridopolycarbosilane SMP-10 at 700°C (see section 5.2.2). With these synthesis procedures, CDCs with average micropore sizes ranging from 0.6 nm to 1.0 nm are obtained (Table 16). Besides OM-CDC and CMK-3 (see section 5.5.1), a purely mesoporous OM-SiC is used as templated material with well-aligned mesopores. In contrast to the mesoporous carbon CMK-3, the carbide structure is completely free of micropores (Table 16).

Table 16. *Porosity data summary obtained from nitrogen physisorption measurements (-196°C) of the TiC-CDCs prepared at different temperatures, the microporous (MP) SMP-10-CDC, OM-SiC, CMK-3, and OM-CDC used for the thermal response measurements.*

Sample	SSA_{BET} (m^2/g)[a]	$V_{Micro+Meso}$ (cm^3/g)[b]	V_{Micro} (cm^3/g)[c]	Average Pore Size(s) (nm)
TiC-CDC-600°C	1412	0.6	0.54	0.6[d]
TiC-CDC-1000°C	1652	0.74	0.59	0.8[e]
MP SMP-10-CDC	2342	1.07	0.94	0.9-1.0
OM-SiC	979	0.79	0.02	4.2
CMK-3	1396	1.42	0.1	(0.9)/4.5
OM-CDC	2838	2.05	0.55	1.0/4.1

[a]   Specific surface area calculated using the BET equation (p/p_0 = 0.05-0.2).

[b]   Micro-and mesopore volume calculated at p/p_0 = 0.95.

[c]   Micropore volume calculated from the cumulative pore volume up to a diameter of 2 nm (QSDFT method for nitrogen on carbon with slit/cylindrical pores (TiC-CDCs, MP-SMP-10-CDC, OM-CDC, and CMK-3) or with cylindrical pores (OM-SiC) at -196°C, adsorption branch kernel)

[d]   Apart from the main pore size, a shoulder in the PSD is observed at 1.2 nm.

[e]   Apart from the main pore size, two smaller local maxima in the PSD occur at 1.2 nm and 2.2 nm.
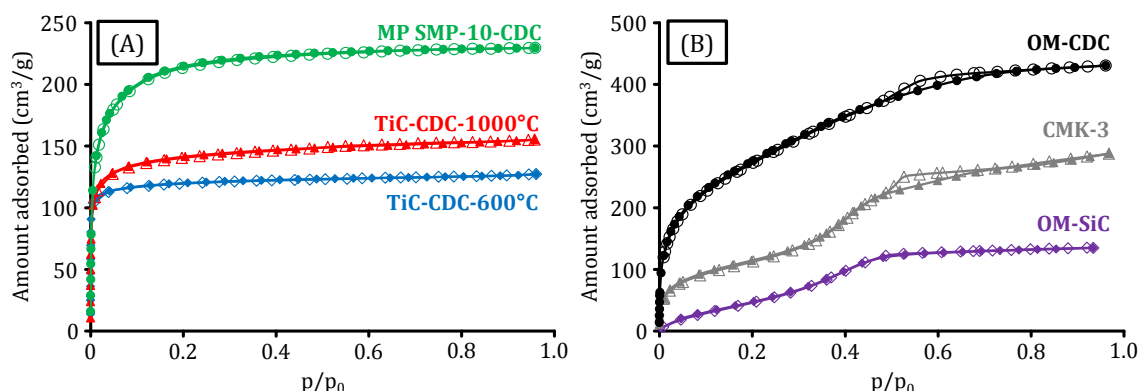
Figure 90. *Volumetric n-butane physisorption isotherms (5°C) of the microporous CDCs (A) and the templated mesoporous materials (B) used for the InfraSORP studies.*

Volumetric *n*-butane physisorption isotherms of the materials measured at 5°C further reveal their porous structure. The isotherms of the microporous CDCs are of type I

according to their pore size (Figure 90(A)). TiC-CDC-600°C shows the lowest *n*-butane uptake as a result of the lowest micropore volume. In contrast, SMP-10-based CDC shows much higher uptake as compared to the TiC-CDCs due to its considerably higher micropore volume and pore size. Because of the microporous character of the samples, the pores are fully saturated with adsorbate even at very low relative pressures. Hence, it can be concluded that under the conditions of the Infrasorp studies (*n*-butane at 1 bar as the test gas and 25°C as the equilibrium temperature corresponding to $p/p_0 \sim 0.4$) complete pore filling will occur. In contrast, the templated samples are not completely filled with *n*-butane at $p/p_0 = 0.4$ according to their mesoporous structure (Figure 90(B)). While it can be expected that micropores present in OM-CDC and CMK-3 will be completely filled during the InfraSORP measurements, the mesopore walls will be covered by a mono- or multilayer of adsorbate molecules and a certain volume of empty pores will be present in equilibrium of *n*-butane adsorption.

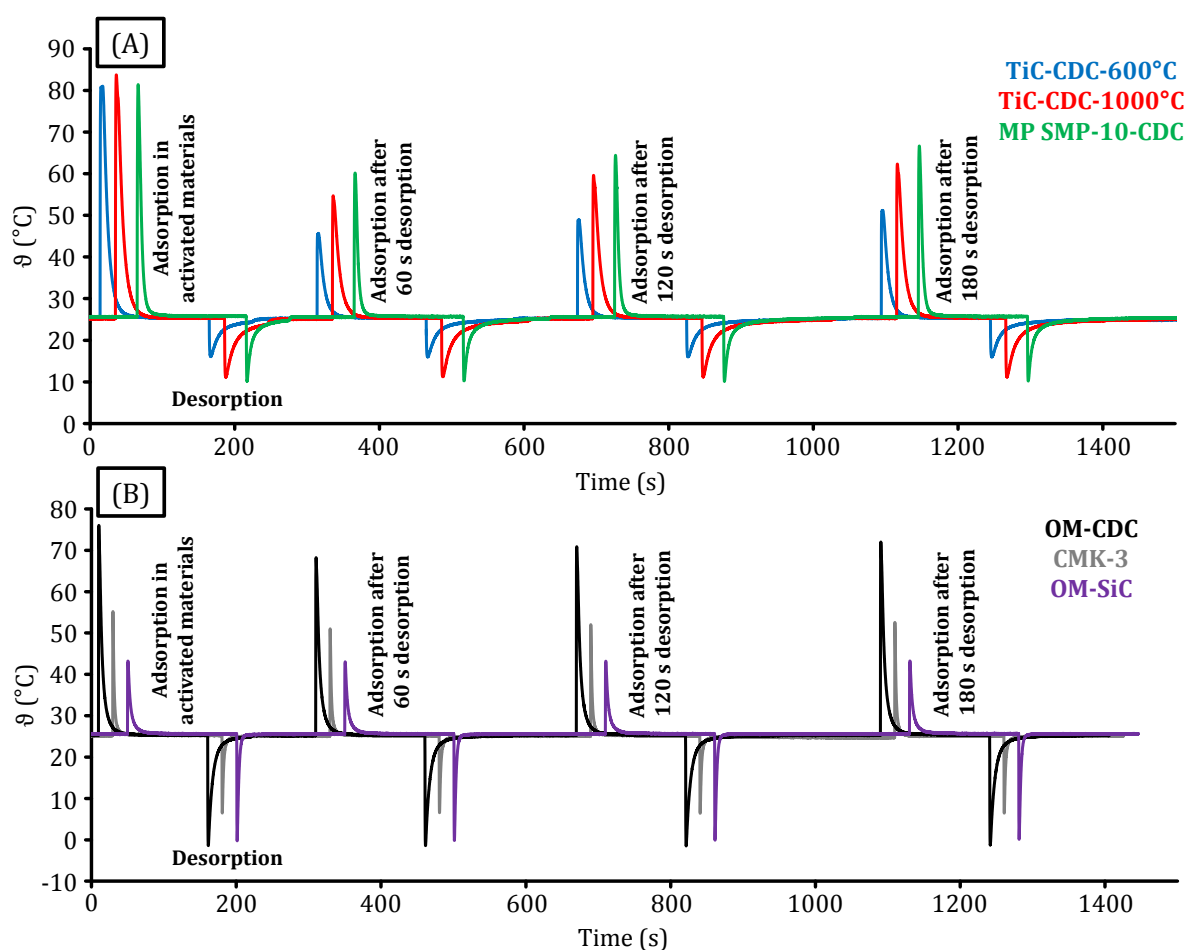***Figure 91.*** *Thermal response measurements (horizontally shifted for better visibility) of n-butane adsorption (1 bar, 25°C) of the microporous CDCs (A) and the templated mesoporous materials (B).*

When these samples are characterized with the InfraSORP technique, the temperature of the microporous CDC materials increases significantly during the first adsorption process due to the release of the high heat of adsorption of the gas molecules in these narrow pores (Figure 91(A)). In contrast, the increase of the temperature is less pronounced for the mesoporous samples CMK-3 and OM-SiC (Figure 91(B)). While CMK-3 is comparable in SSA to the TiC-CDC-600°C and shows even higher uptake of the test gas at p/p_0 = 0.4 under equilibrium conditions (Figure 90), less heat is released during *n*-butane adsorption in a mesopore as compared to the very narrow micropores in the TiC-CDC with their size close to the kinetic diameter of the gas molecules. In terms of the temperature maximum, an intermediate situation can be observed in OM-CDC because it consists of a combination of micro- and mesopores.

The decrease in temperature during desorption (i.e. flushing with nitrogen) is also strongly influenced by the pore structure of the materials. Adsorption and desorption signals of the microporous CDCs are highly asymmetric as the value of temperature decrease during desorption is significantly below the increase in adsorption. The SMP-10-CDC shows the largest decrease of temperature when *n*-butane is removed indicating that the desorption process is more rapid in the sample with the largest micropores. In contrast, *n*-butane removal from the TiC-CDC-600°C with the smallest micropores is rather slow. From a thermodynamic point of view, this difference is related to the stronger adsorption of the test gas in rather narrow pores (i.e. to the higher adsorption enthalpy). In terms of kinetics, the diffusion of the *n*-butane out of the pore system of TiC-CDC-600°C is expected to be slower compared to SMP-10-CDC with the larger pores although it can be expected from the *n*-butane physisorption isotherms that the pore volume of all the microporous samples is completely filled with test gas under the elevated conditions. In contrast to the microporous samples, the desorption signals of the mesoporous materials are rather symmetrical to the adsorption signals and the decrease in temperature is more distinct. In case of the purely mesoporous OM-SiC, the temperature change during desorption is even higher than during adsorption. The adsorption enthalpy of the test gas in large mesopores is much lower and hence, the desorption equilibrium is reached more rapidly. Moreover, the mesopores are not completely filled under the elevated conditions. Only mono- or multilayer formation takes place and capillary condensation can be ruled out. Hence, these samples still provide empty mesopores that ensure rapid diffusion of the test gas out of their interior.

For the hierarchical OM-CDC it can be concluded that desorption equilibrium is still reached slower compared to CMK-3 and OM-SiC due to the presence of high micropore volumes. However, at the same time, the decrease of the temperature is much higher as compared to the purely microporous samples despite the lower temperature increase during adsorption. This underlines the positive effect of the hierarchical micro-mesopore system on the adsorption properties of this material with a combination of high uptakes and rapid adsorption/desorption rates.
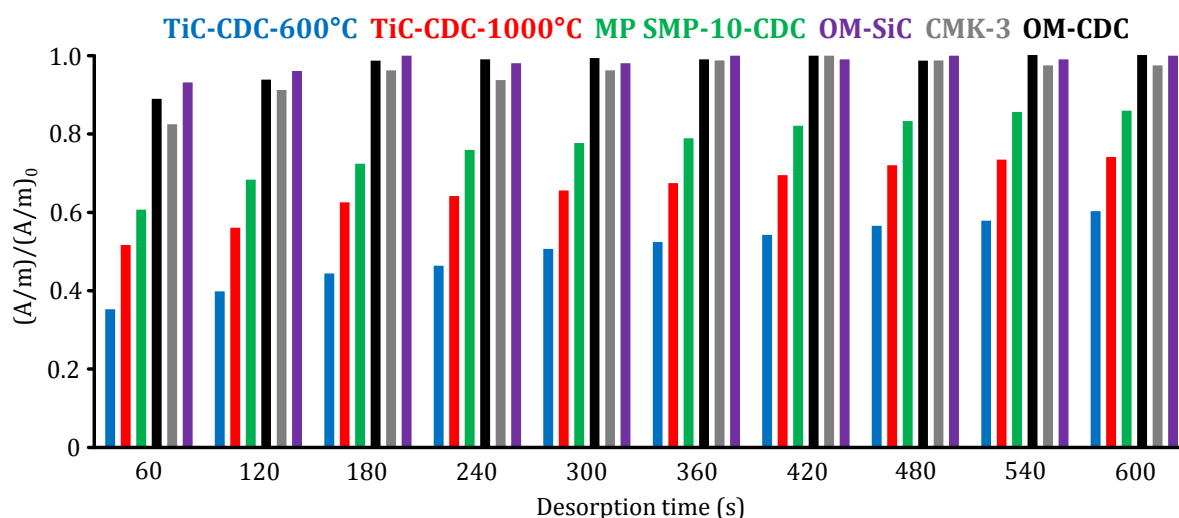
Figure 92. *Mass-related peak areas (A/m) of n-butane adsorption of the investigated samples after different desorption times in relation to the initial peak area ((A/m)$_0$) in fully activated state.*

Continued adsorption/desorption cycling with increasing desorption times further shows the usefulness of the InfraSORP technique for the characterization of porous materials (Figure 92). After the adsorption procedure in the fully activated samples and 60 s desorption by nitrogen purging, the microporous samples only achieve 35% (TiC-CDC-600°C), 51% (TiC-CDC-1000°C), and 61% (SMP-10-CDC) of their initial peak area. With increasing desorption time, a larger fraction of the adsorbed *n*-butane is removed from the pore system of the carbons. 86% of the initial mass-related peak area is achieved by SMP-10-CDC after desorption time of 600 s. In contrast, only 60% of the initial A/m value are achieved in TiC-CDC-600°C due to its smaller pore diameter and hence slower desorption of the test gas during the nitrogen flow. An intermediate situation is observed in the TiC-CDC-1000°C as a result of its pore size centered at 0.8 nm located between TiC-CDC-600°C and SMP-10-CDC. The results obtained with this measuring algorithm render the InfraSORP as a useful technique for the rapid estimation of the micropore size of porous materials. The determination of this

parameter normally requires long time because it is most often calculated with time-consuming gas physisorption measurements at very low pressures and with long equilibration times. Furthermore, the continued adsorption/desorption cycling impressively demonstrates the advantage of the presence of mesopores with regard to achieve high adsorption/desorption rates. OM-CDC, OM-SiC, and CMK-3 achieve more than 95% of their initial peak area even after 180 s desorption time. This is in accordance to the differences in the desorption signals due to the weaker adsorption strength of the test gas into the mesopores and the presence of free pore volume in these samples ensuring sufficient diffusion pathways for the removal of *n*-butane.

In summary, with the model systems presented here, critical issues of this novel method are evaluated and structural parameters of the materials can be estimated. However, it must be noticed that the use of different gases (e.g. carbon dioxide, sulfur hexafluoride, or *iso*-butane) would lead to even deeper understanding of the mechanisms of gas adsorption in porous materials. Measurements with other test gases at different relative pressures, different temperatures, with different adsorption enthalpies, polarities, and kinetic diameters will lead to further insights in the materials porous structure and the corresponding adsorption mechanisms.

5.6 Kroll-Carbons (KCs)

Porous carbon materials are crucial components in a wide range of applications. Their performance is most often a function of their structural properties, such as SSA, pore size, and pore geometry. Microporous carbons can be produced over a wide range of pore sizes by different approaches (e.g. activation, nanocasting of zeolites, or the extraction of metal- or semi-metal atoms from carbides).[9] In contrast, well-defined mesoporous carbon materials are not produced on a large scale. On the one hand, this might be due to the fact that these materials are so far only used in niche applications like the filtration of blood for the removal of inflammatory mediators or in academic research. One area in which the mesoporous carbon materials seem to be very promising is the Li-S battery. However, the cost for the carbon materials hosting the active material is till very high and a major problem for the energy storage system. Another major reason for the rare implementation of these materials in industrially relevant processes is their extremely complex manufacturing. As long as well-defined and narrowly distributed pores are required, mesoporous carbon materials have to be

produced by very complex synthesis methods. The pioneering work of Ryoo and co-workers established the highly ordered CMK-family using infiltration of ordered mesoporous SiO_2 materials with carbon precursors and subsequent template removal by etching in hydrofluoric acid or sodium hydroxide solutions (see section 2.1).[17] However, the wet silica etching process has a low time-space yield and up-scaling is challenging from an economic and ecological point of view. An advantageous soft templating approach for the direct synthesis of mesoporous carbons was developed by Zhao and co-workers avoiding the use of a solid template and hazardous chemicals by using the evaporation induced self-assembly (EISA) method (see section 2.1).[22] Nevertheless, this procedure suffers from the use of large amounts of solvents and non-ionic surfactants, which cannot be reused and are thermally decomposed into gaseous by-products. Furthermore, this method is limited in terms of precursors since mostly synthetic molecules or polymers are used. In contrast to such complex templating approaches, physical or chemical activation processes do not allow precise control over mesopore sizes and therefore a versatile, low-cost, and scalable process for the generation of mesoporous carbons is still not available.

In this chapter, a new chemical method for the production of mesoporous carbon materials with precisely defined pores, high SSA, and high total pore volume is presented based on reactive carbochlorination etching of titania, silica, or alumina nanoparticles inside a dense carbon matrix. For the first time this chemical conversion, known as key-step of the Kroll-process,[233] is applied to remove metal oxide templates in a solid-gas reaction. Accessibility limitations for occluded silica in liquid HF etching processes as present in conventional hard templating approaches are avoided using the highly reactive chlorine gas etching at high temperature. This leads to a scalable production scheme for mesoporous carbons.[234, 235]

5.6.1 KCs from TiO₂ Templates in Li-S Battery Cathodes

Synthesis and Structure

For the production of Kroll-Carbons from TiO_2 templates, commercially available titania nanoparticles (Degussa P25, measured SSA: 50 m²/g) are mixed with sucrose as a natural, renewable, and inexpensive carbon precursor. The hydrocarbon undergoes an acid-catalyzed polymerization around the TiO_2 nanoparticles and is subsequently thermally converted into a carbon network under inert conditions. After rapid heating

and short annealing at 900°C, the titanium dioxide template is removed by dosing chlorine gas to the TiO_2/carbon composite material at 900°C according to Equation 26.

$$TiO_{2(s)} + (2+x)\ C_{(s)} + 2\ Cl_{2(g)} \rightarrow TiCl_{4(g)} + 2\ CO_{(g)} + x\ C_{(s)} \qquad (26)$$
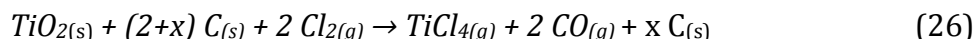
The residual solid carbon represents the Kroll-Carbon (Figure 93). The generated $TiCl_4$ is removable by distillation and can be reused for the production of titanium dioxide nanoparticles by flame pyrolysis or for the production of titanium metal according to the Kroll-process. This new strategy uses the TiO_2 nanoparticles as both hard- and sacrificial template. It is removed directly after the thermal conversion of the carbon precursor leading to precise control over the pore structure in the carbon material due to the definite replication of the template structure.
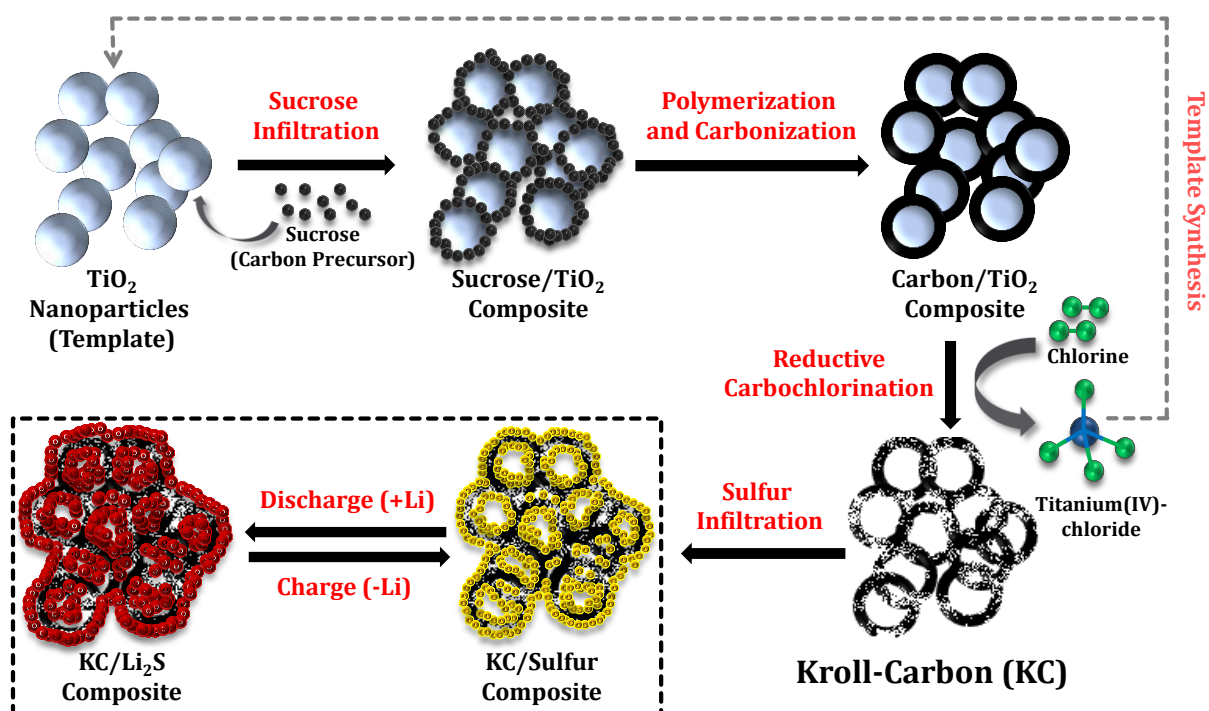
Figure 93. *Preparation of KCs and their use in Li-S battery cathodes.*

If flame-derived TiO_2 nanoparticles (Degussa P25) are utilized as templates, remarkably high specific BET surface areas of 1989 m^2/g are achieved as shown by nitrogen physisorption measurements (Figure 94(A) and Table 17). The resulting mesopores are uniform and highly accessible resulting in a type IV isotherm with a distinctive H1 hysteresis loop. The overall pore volume is as high as 3.1 cm^3/g (Table 17) due to the high volume of large mesopores. Hence, this new material is more suitable for the

infiltration of large amounts of sulfur as compared to previously described CMK-3,[180] spherical OMC nanoparticles,[181] and porous hollow carbon spheres.[182]

The QSDFT pore size distribution (Figure 94(B)) shows a multimodal distribution of pore diameters with maxima at 1, 4.2, and 18 nm. While the large pores originate from the titanium dioxide template particles, the smaller mesopores arise from empty spaces between the TiO_2 nanoparticles due to incomplete filling of the template voids with precursor molecules during infiltration. Additionally, 0.3 cm^3/g micropores of 1 nm in diameter are generated by the CO evolution in the Kroll reaction in analogy to physical activation procedures (Table 17).
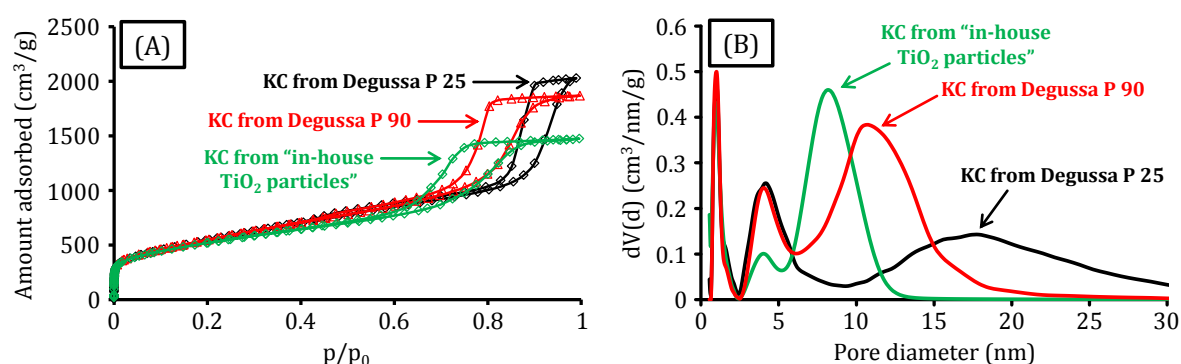
Figure 94. *Nitrogen physisorption (-196°C) isotherms (A) and QSDFT (nitrogen on carbon with slit/cylindrical pores at -196°C, adsorption branch kernel) pore size distributions (B) of the KCs obtained from different templates.*
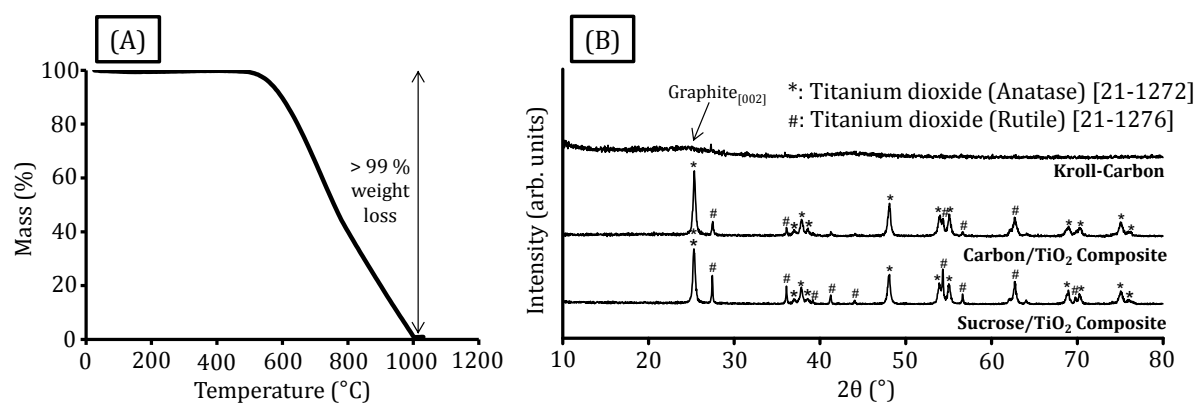
Figure 95. *Thermogravimetrical analysis of the KCs from Degussa P25 templates under air atmosphere with a heating rate of 5 K/min (A) and wide-angle XRD patterns (B) of the sucrose/P25 composite, carbon/P25 composite, and the resulting KCs.*

EDX analyses indicate a high purity of the KC material (more than 99.5 wt% of carbon) while titanium, oxygen, and chlorine are below the detection limit. Thermal analyses (Figure 95(A)) confirm this observation as the residual mass is below 1%. This indicates a complete conversion of the titanium dioxide template to volatile $TiCl_4$ and CO species.

KCs differ significantly in structure compared CDCs. At the temperature of chlorine treatment used for KC synthesis, TiC formation can be ruled out because the powder XRD measurements of a sample annealed without chlorine show no carbide reflections (Figure 95(B)). After the chlorination, the KCs only show the broad characteristic graphite (002) peak at moderate intensity indicating the absence of impurities as well as a certain degree of graphitization in the pore walls of KCs.

Table 17. *Porosity data summary of mesoporous Kroll-Carbons prepared from TiO$_2$ template particles of different size.*

Template	Template SSA$_{BET}$ (m^2/g)[a]	KC SSA$_{BET}$ (m^2/g)[a]	KC V$_{Micro+Meso}$ (cm^3/g)[b]	KC V$_{Micro}$ (cm^3/g)[c]
Degussa P25	50	1989	3.12	0.30
Degussa P90	100	1979	2.89	0.28
In-house made TiO$_2$-NPs	152	1872	2.28	0.32

[a]   Specific surface area calculated using the BET equation (p/p$_0$ = 0.05-0.2).
[b]   Micro- and mesopore volume calculated at p/p$_0$ = 0.99.
[c]   Micropore volume calculated from the cumulative pore volume up to a diameter of 2 nm (QSDFT method for nitrogen on carbon with slit/cylindrical pores at -196°C, adsorption branch kernel).

Figure 96. *SEM (A-C) and TEM (D and E) micrographs of KCs from Degussa P25 templates.*
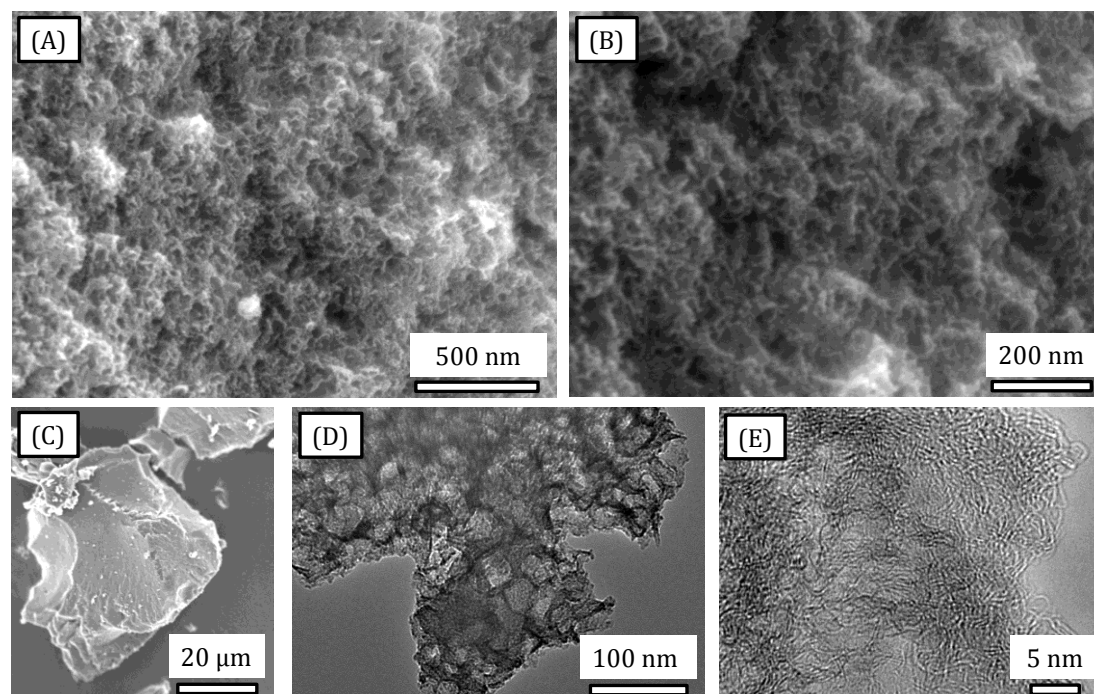
SEM images of the KCs (Figure 96(A,B)) show the presence of a distinctive arrangement of mesopores with block-shaped geometry and a foam-type structure which is

responsible for the high internal pore volume of the carbons. The synthesis of this first generation of Kroll-Carbons produces micro-to millimeter-sized particles (Figure 96(C)). The carbochlorination process shows full macroscopic shape retention since no shrinkage of the particle size from the sucrose/TiO_2 composite to the KC can be observed. The average sizes of the large mesopores in the TEM images (Figure 96(D)) are 15 to 25 nm and in good agreement with the nitrogen physisorption analysis. Moreover, the mesopore size is very close to the template dimensions (Appendix 10) and the presence of some edges and corners of TiO_2 nanoparticles (Figure 96(D)) confirm the carbochlorination reaction as being highly conformal. TEM images at higher magnifications (Figure 96(E)) show the carbon microstructure of the KCs as an arrangement of mostly disordered sp^2 carbon fringes with low degree of graphitization.

Since the performance of porous carbons as key-component in various applications such as lithium-sulfur batteries, electrochemical capacitors, and adsorption strongly depends on the pore size, it is crucial for any synthetic route to allow control over the pore diameter as precise as possible. In addition to Degussa P25, KC synthesis can be carried out with a series of template particles with higher specific surface areas corresponding to smaller particle size (Degussa P90, measured SSA: 100 m^2/g and "in-house made" TiO_2 particles prepared by flame spray pyrolysis, measured SSA: 152 m^2/g). Nitrogen physisorption isotherms clearly show a decreasing diameter of the larger mesopores for the carbons prepared from smaller oxide particles as the hysteresis loops shift towards lower relative pressures (Figure 94(A)). At the same time, the specific surface areas remain at the same level (Table 17). The corresponding QSDFT pore size distributions (Figure 94(B)) confirm the decreasing diameter of the large mesopores from 18 nm (Degussa P25), to 11 nm (Degussa P90), and 8.5 nm (in-house made TiO_2 particles) respectively. This analysis illustrates that the novel synthesis route allows precise control over the mesopore sizes of KCs. The corresponding total pore volumes decrease due to the smaller pore diameters while the micropore sizes and micropore volumes stay at the same level (Figure 94(B) and Table 17). Furthermore, it is noteworthy that the volume of the smaller mesopores in carbons prepared from the smaller in-house particles is significantly lower as compared to the Degussa products. This might be related to a rather complete filling of the narrower inter-particular spaces with sucrose molecules and is also an explanation for the slightly lower SSA of this sample.

KCs from Degussa P25 Templates in Li-S Battery Cathodes

Since Kroll-Carbons from Degussa P25 templates stand out by very high mesopore volume and are electrically conductive, they were infiltrated with different amounts of sulfur by melt infiltration (Table 18) and the resulting composite structures were characterized as Li-S battery cathodes. In the following, the cathodes are denoted as KC/S-53, KC/S-60, KC/S-64 and KC/S-72 according to their sulfur content in wt.% (Table 18). SEM images illustrate the typical morphology of the as-prepared cathodes before electrochemical cycling (Figure 97(A,B)). The cathode surface is smooth but reveals a widely open and highly accessible inter-particular porosity throughout the 83-95 µm thick active material layer. The irregularly-shaped KC/S composite particles of up to 20 µm in size reduce the cathode compressibility (density) and lead to a loosely packed active layer with interconnected cavities.
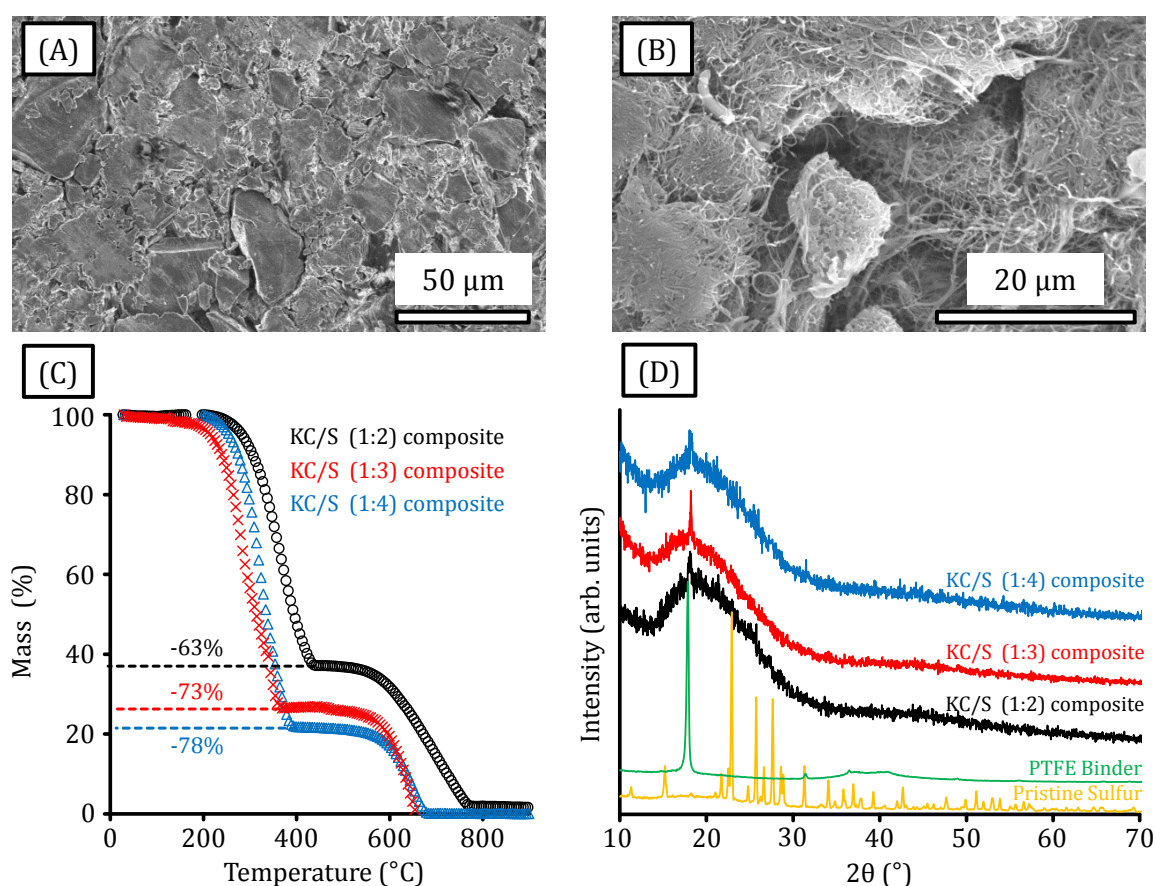
Figure 97. *SEM micrographs (A and B) of the KC/S-64 cathode as well as thermogravimetrical analyses (C) of the KC/S composites with different compositions and wide-angle XRD patterns (D) of the KC/S cathodes with different compositions, the PTFE binder, and pristine sulfur.*

The KC/S weight ratios determined by TGA (Figure 97(C)) are in good accordance with the expected values of 33:67 (1:2 composite), 25:75 (1:3 composite), and 20:80 (1:4

composite) because the melt infiltration strategy allows precise control over the KC/S composite composition. The powder XRD patterns of the KC/S composite cathodes with different sulfur contents, pristine sulfur, and partially crystalline poly(tetrafluorethylene) (PTFE) binder (Figure 97(D)) show the intense PTFE peak for all cathodes but the reflections corresponding to bulk α-sulfur completely disappear even at high loadings of 72 wt.% because sulfur is completely melt-infiltrated and well dispersed inside the KC framework. KCs effectively suppress the crystal growth of sulfur particles due to their high amount of mesopores available for active material storage.

Table 18. *Compositions and textural properties of the KC/S cathodes with different sulfur contents.*

Cathode	KC:S composition (weight ratio)	KC/S:MWCNT:PTFE composition (weight ratio)	Active layer thickness (μm)	S surface loading (mg/cm^2)
KC/S-53	1:2	8:1:1	95	2.83
KC/S-60	1:3	8:1:1	85	3.32
KC/S-64	1:4	8:1:1	89	4.55
KC/S-72	1:4	18:1:1	83	4.92

The cycling stabilities of KC/S composite cathodes with variable sulfur content are characterized by galvanostatic cycling (Figure 98) at a constant rate of 167 mA/g (0.1 C). High initial discharge capacities of 1089 mAh/g$_{Sulfur}$ (KC/S-53), 1115 mAh/g$_{Sulfur}$ (KC/S-60), 1046 mAh/g$_{Sulfur}$ (KC/S-64), and 1038 mAh/g$_{Sulfur}$ (KC/S-72) are determined for all cathodes. After a distinct capacity decay of maximal 18% within the first 10 discharge/charge cycles, the KC/S composites exhibit an excellent cycling stability with highly consistent capacities of 806 mAh/g$_{Sulfur}$ (KC/S-53), 820 mAh/g$_{Sulfur}$ (KC/S-60), 817 mAh/g$_{Sulfur}$ (KC/S-64), and 736 mAh/g$_{Sulfur}$ (KC/S-72) after 80 cycles. For all composites, more than 70% of the initial discharge capacity can be reversibly utilized even at very high sulfur loading of 72 wt.% and at a low rate of 0.1 C although this is a combination which is known to cause extensive active material loss by lithium polysulfide shuttling and rupturing of the electrically conductive carbon backbone.[220]

The KC/S-72 cathode is most suitable for the application in actual energy storage systems since the initial discharge capacity of 747 mAh/g per cathode mass (including binder and conductive additive) is much higher compared to cathodes with lower sulfur content making the high capacity cathode both the more practical and cheaper choice

since less host material is needed. Only a slight decrease in the cell discharge voltage is observed when the cathode is loaded with such a high amount of sulfur (Figure 98(C)). This indicates that sufficient amounts of Li$^+$ ions and electrons can diffuse to all reaction sites facilitating the electrochemical conversion of sulfur at the large C/S interface area within Kroll-Carbon (Figure 98(D)).
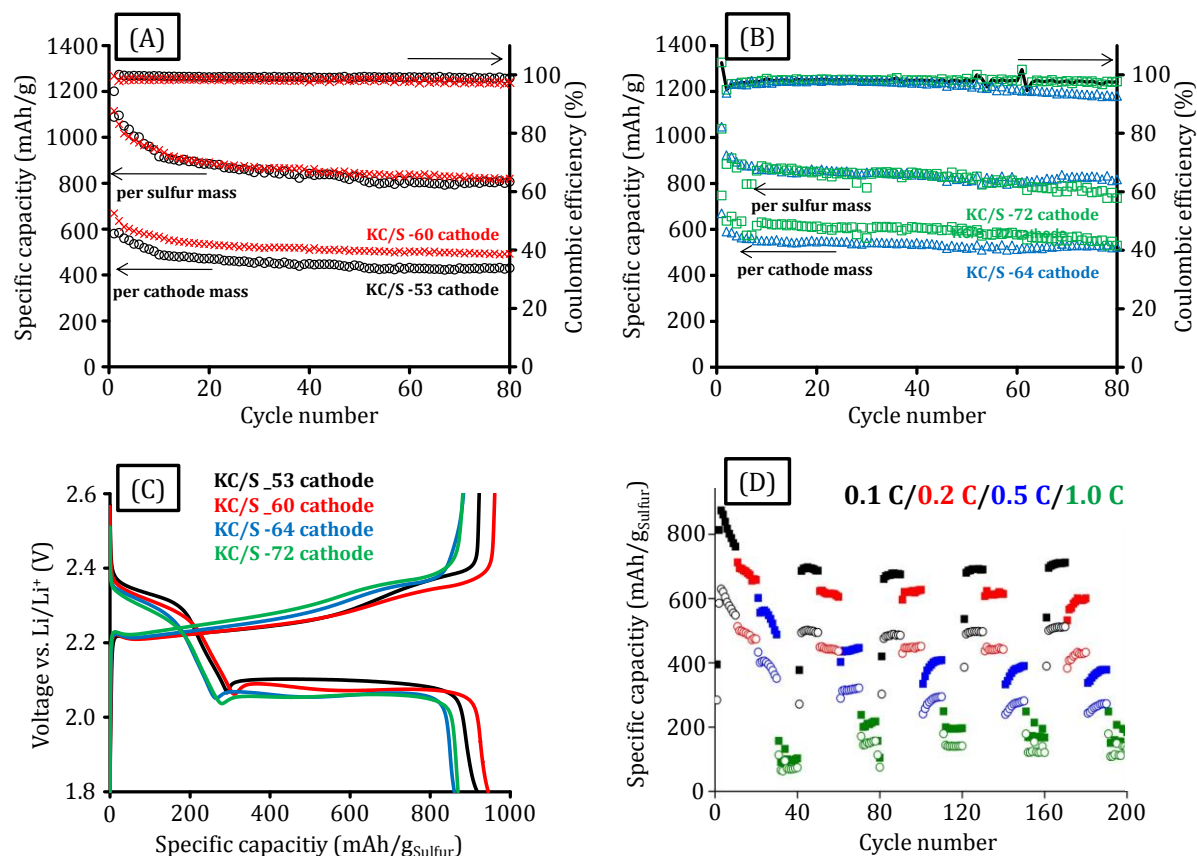
Figure 98. Cycling stabilities (measured at 0.1 C) along with coulombic efficiencies (A and B), discharge/charge voltage profiles (measured at 0.1 C) of the 10th cycles (C) of the KC/S cathodes with different compositions, and C-rate performance (D) of the KC/S-72 cathode (filled symbols represent the capacity related to sulfur, empty symbols represent the capacity related to the overall cathode).

Due to the high total pore volume of the KCs, high sulfur loadings are possible and high capacities related to the mass of the overall cathode can be achieved. Hence, this novel class of mesoporous carbons outperforms many mesoporous materials with promising properties as Li-S cathode material produced by classical soft- or hard-templating approaches. For instance, the performance of KCs is significantly beyond the well-known ordered mesoporous CMK-3 which was identified as promising sulfur host material by Nazar and co-workers.[180] Li-S cells based on the latter show significantly lower capacitance as compared to the KC/S-72 cathode at even lower sulfur loadings. Especially when the capacity related to the mass of the whole cathode is considered, the

performance of Kroll-Carbon-based electrodes significantly exceeds that of CMK-3.[235] This can be explained by the significantly higher pore volume and specific surface area of the KC and therefore a rather complete utilization of encapsulated sulfur due to the large C/S interface and sufficient hollow space for electrolyte penetration and volume expansion. Even though various mesoporous carbon materials show excellent performance as cathode materials in Li–S cells, all of them are derived by classical templating approaches and are hence difficult to produce on a larger scale. The Kroll-process, and especially the reductive carbochlorination, is a valuable new process for upscaling the synthesis of mesoporous carbons with well-defined pore size. Even though chlorination at high temperatures is a dangerous and toxic process, the low price of chlorine and the possibility to reuse the by-product $TiCl_4$ are highly attractive.
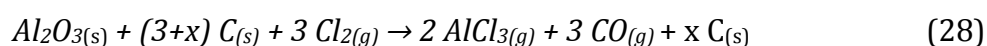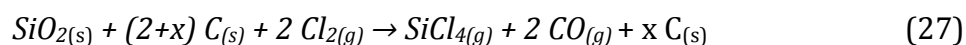
In summary, the Kroll-type reaction scheme using flame derived TiO_2 nanoparticles as templates results in carbons with high specific surface area and pore volumes up to 1980 m^2/g and 3.1 cm^3/g, respectively. The synthesis process is highly versatile and allows for tailoring the pore morphology and diameter in a wide range. The novel materials prepared from a commercially available template material (Degussa P25) show outstanding performance as sulfur host material in high capacity cathodes for lithium-sulfur batteries. Extremely high sulfur contents up to 72 wt.% cause initial discharge capacities as high as 747 mAh/$g_{Cathode}$ and stable cycling with reversible capacities of more than 550 mAh/$g_{Cathode}$.

5.6.2 KCs from SiO₂ and Al₂O₃ Templates as Electrode Material in EDLCs

Synthesis and Structure

The reductive carbochlorination reaction for the synthesis of porous KCs can also be applied to composites of carbon and Al_2O_3 or carbon and SiO_2. Silica and alumina nanoparticulate templates are useful alternatives to titania-based particles as they are available in different textures and, sizes. Hence, KCs with different properties can be produced. As $TiCl_4$ in case of TiO_2 templates (see section 5.6.1), $SiCl_4$ and $AlCl_3$ can be produced as useful by-products according to Equation 27 and Equation 28, if silica and alumina templates are utilized as the templates, respectively.

$$SiO_{2(s)} + (2+x)\ C_{(s)} + 2\ Cl_{2(g)} \rightarrow SiCl_{4(g)} + 2\ CO_{(g)} + x\ C_{(s)} \qquad (27)$$

$$Al_2O_{3(s)} + (3+x)\ C_{(s)} + 3\ Cl_{2(g)} \rightarrow 2\ AlCl_{3(g)} + 3\ CO_{(g)} + x\ C_{(s)} \qquad (28)$$

In this first study, commercially available silica (Aerosil 380 with SSA = 380 ± 30 m^2/g and Aerosil 90 with SSA = 90 ± 15 m^2/g) and alumina (Aeroxide Alu 130 with SSA = 130 ± 20 m^2/g) nanoparticles (purchased from Degussa-Evonik) were utilized as templates. After the infiltration of sucrose and carbonization, reductive carbochlorination of the oxide/carbon composites at 900°C leads to quantitative removal of the template particles and to the formation of KCs with high purity. The carbon content of the samples measured determined by EDX is about 99 atom% and potential impurities of silicon, aluminum, oxygen, and chlorine are below the detection limit. For the SiO$_2$ templates, the complete absence of oxidic residuals is surprising as the reductive carbochlorination at a temperature as low as 900°C is expected to be too slow to lead to sufficient conversion rates. In case of the nanocomposites for the preparation of KCs, the contact area between oxide and carbon is very large and therefore the composite is more reactive as compared to the bulk starting materials.
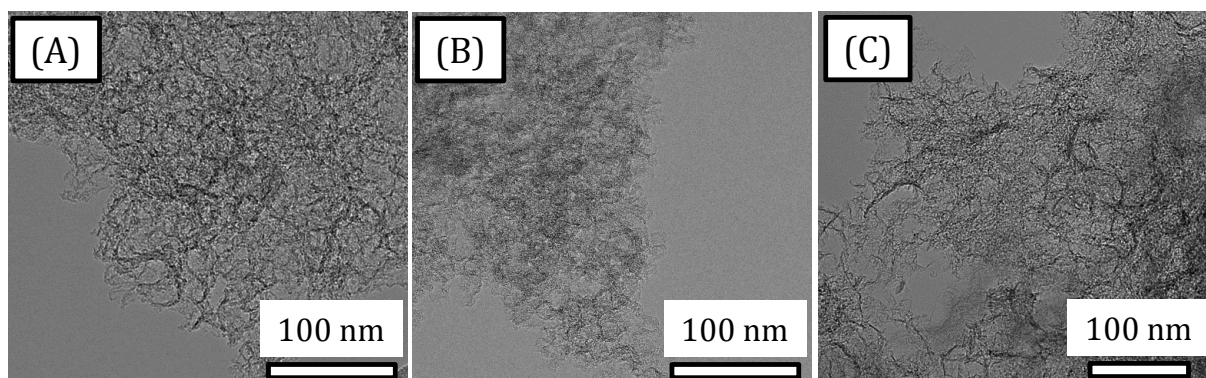
Figure 99. *TEM micrographs of KCs from Alu 130 (A), Aerosil 380 (B), and Aerosil 90 (C) templates.*

Due to the complete template removal, KCs offer a highly open mesopore structure as shown by TEM measurements (Figure 99). The mesopore sizes increase from values below 30 nm in the KCs derived from Alu 130 and Aerosil 380 templates to diameters above 40 nm for the KCs obtained from Aerosil 90 particles. Hence, the template removal by the reductive carbochlorination reaction is highly conformal and allows precise control over the pore sizes of the resulting KCs.

TEM micrographs at higher magnifications show that the carbon microstructure of these KCs consists of an arrangement of mostly disordered sp^2 carbon fringes with low degree of graphitization in analogy to the KCs based on TiO$_2$ templates (see section 5.6.1) due to the equal synthesis temperature (Figure 100(A)). In accordance with the electron microscopic investigations, Raman spectra (Figure 100(B)) indicate a highly defective

carbon structure with a characteristic D-band at ~1350 cm^{-1}. The shoulder D^2-band present in all samples and the absence of sharp peaks in the range from 2400-3000 cm^{-1} further indicates a low graphitization in the KCs obtained at the elevated temperature of 900°C. The overall carbon ordering of these carbon materials is close to CDC materials obtained in the same temperature range (see sections 5.1.1 and 5.4). It can therefore be expected that Kroll-Carbons provide sufficient electrical conductivity for the use in electrochemical energy storage devices. Among the different templates, the KCs based on Alu 130 particles show a slightly higher amount of graphitic ribbon structures due to its higher I_D/I_G ratio (Table 19) as well as FWHM of the D-band (135 cm^{-1}) as compared to the materials based on Aerosil 380 (136 cm^{-1}) and Aerosil 90 (141 cm^{-1}).
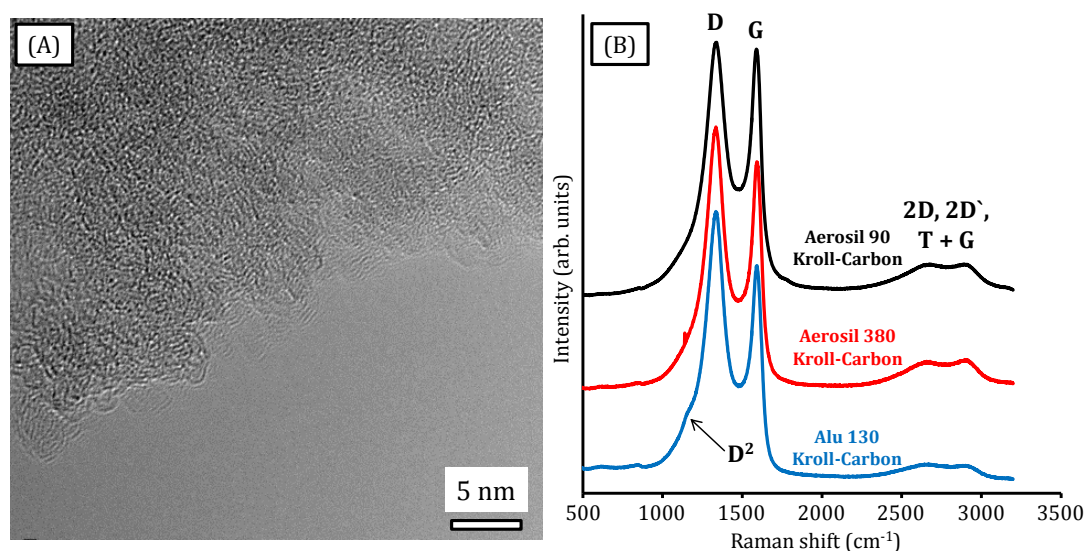
Figure 100. *TEM micrograph of KCs from Alu 130 (A) and Raman spectra (B) of KCs from Alu 130 (blue), Aerosil 380 (red), and Aerosil 90 (black) templates.*

Table 19. *Porosity, Raman, and EDX data summary of Kroll-Carbons prepared from Alu 130, Aerosil 380, and Aerosil 90 templates.*

Template	SSA$_{BET}$ (m^2/g)[a]	V$_{Micro+Meso}$ (cm^3/g)[b]	V$_{Micro}$ (cm^3/g)[c]	Carbon (wt.%)[d]	I_D/I_G
Alu 130	1867	1.92	0.39	99.1	1.54
Aerosil 380	1710	3.24	0.32	98.9	1.40
Aerosil 90	1524	3.25	0.31	99.4	1.24

[a] Specific surface area calculated using the BET equation (p/p$_0$ = 0.05-0.2).
[b] Micro- and mesopore volume calculated at p/p$_0$ = 0.99.
[c] Micropore volume calculated from the cumulative pore volume up to a diameter of 2 nm (QSDFT method for nitrogen on carbon with slit/cylindrical/spherical pores at -196°C, adsorption branch kernel).
[d] Calculated from EDX data.

KCs obtained by using the different SiO_2 and Al_2O_3 particles exhibit high SSAs of up to 1867 m^2/g and total pore volumes exceeding 3 cm^3/g (Figure 101(A) and Table 19). Because the isotherms of the carbons prepared from the silica templates do not reach saturation at p/p_0 = 0.99, these values must be regarded as minimum total pore volumes and the actual values are expected to be even higher. The distinct uptake of nitrogen at low relative pressures (p/p_0 < 0.1) is associated with the filling of narrow micropores which are likely generated by the CO evolution during carbochlorination as described for the titania-templated KCs (see section 5.6.1). The highest micropore volume and SSA of the alumina-based material are a result of the higher molar ratio of carbon etching and therefore the preferred formation of micropores. QSDFT pore size distributions show the presence of 1 nm-sized pores and small volumes of narrow mesopores of 2-6 nm depending on the template (Figure 101(B)). The latter might be a result of the presence of empty spaces between the template nanoparticles which are not entirely filled with the carbon precursor during infiltration (see section 5.6.1). The micropores are ideally sized for the use of the KCs in EDLCs as they are large enough for fast and effective electrosorption of ions and small enough to serve for high surface area available for double-layer formation.

Figure 101. *Nitrogen physisorption (-196°C) isotherms (A) and QSDFT (nitrogen on carbon with slit/cylindrical pores at -196°C, adsorption branch kernel) pore size distr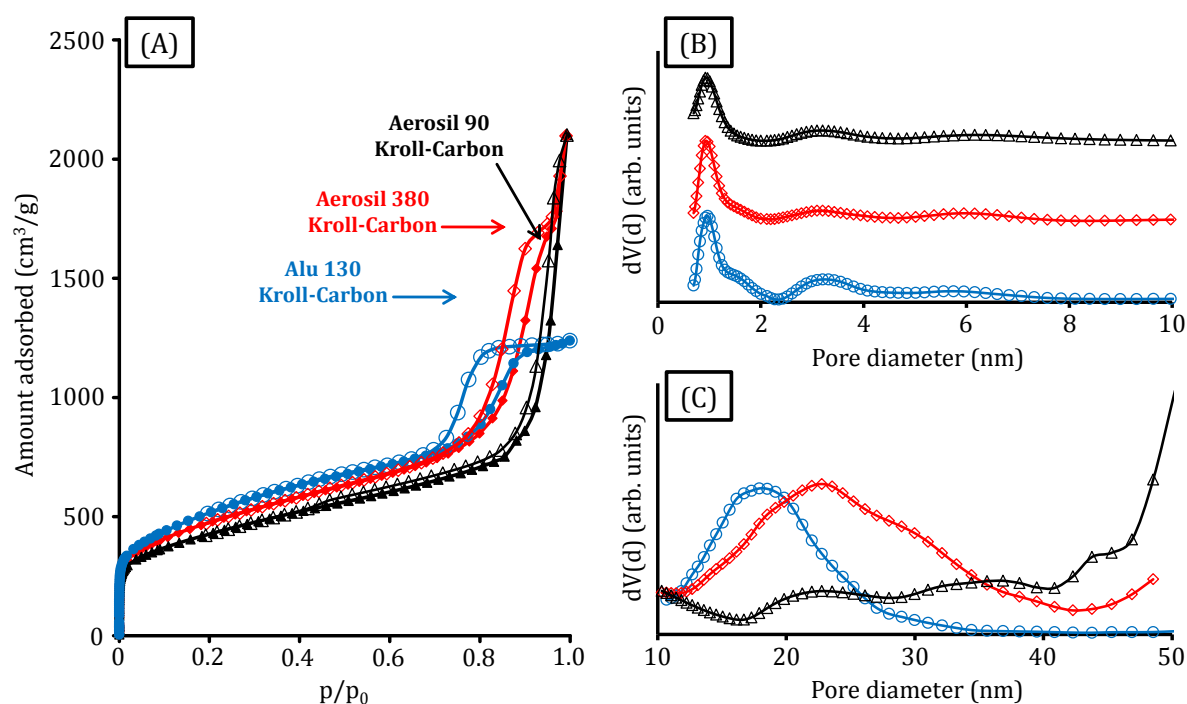ibutions (B and C) of the KCs obtained from Alu 130 (blue), Aerosil 380 (red), and Aerosil 90 (black) templates. PSDs in (B) are vertical offset.*

All KCs show a very distinct and narrow hysteresis loop at high relative pressures ($p/p_0 > 0.7$). This indicates the presence of high volumes of uniformly sized mesopores for all templates. According to the oxides` particle sizes, the largest mesopores are formed in the KCs obtained from Aerosil 90 as the pore condensation occurs at the highest relative pressure. Aerosil 380 and Alu 130 templates result in smaller pore diameters. No blocking or cavitation effects are observed due to the high accessibility of the KC pore system. QSDFT-PSDs in the large mesopore region (Figure 101(C)) show the template-induced mesopores centered at 18 and 23 nm for the Alu 130 and Aerosil 380 templates, respectively. The majority of mesopores present in KCs obtained from Aerosil 90 are too large to be analyzed by the QSDFT model. The distinct mesopore systems of the Kroll-Carbons ensure a high accessibility of the surface area throughout the entire particle. The additional micropores are mainly responsible for the high specific surface area which is not achievable by classical hard-templating approaches based on oxidic hard templates of comparable size.[177]
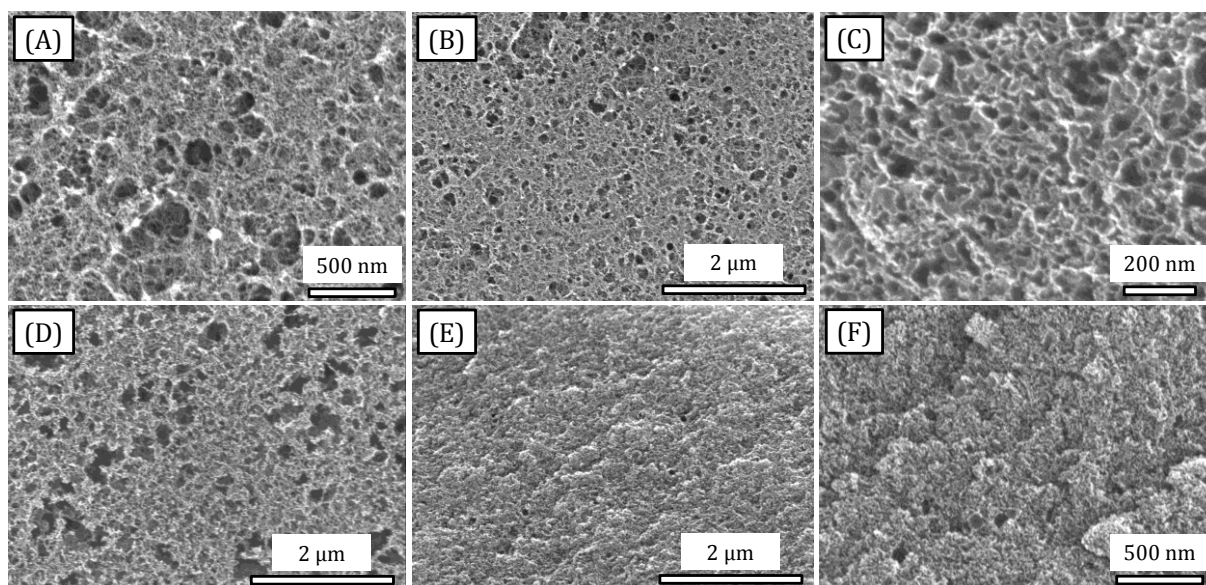
Figure 102. *SEM micrographs of KCs from Aerosil 380 (A and B), Aerosil 90 (C and D), and Alu 130 (E and F) templates.*

SEM micrographs of the silica-based KCs (Figure 102) show the additional presence of macropores already present in the templates which are not infiltrated with the precursor. They are responsible for the additional uptake of nitrogen at high relative pressures and can serve as ion transport pathways and allow rapid access of the entire particle. As already indicated by the saturation of the nitrogen physisorption isotherm (Figure 101(A)), such pores are not present in the alumina-based KCs due to a rather

dense particle structure and the absence of large meso- or macropores. In the KCs derived from Aerosil 90 particles, the large pores can be clearly observed and their size of 40-70 nm is significantly higher as for the Aerosil 380-based sample in accordance with the nitrogen physisorption experiments. This further proves the precise control over the pore sizes provided by the reductive carbochlorination reaction.

Kroll-Carbons as Electrode Materials in EDLCs

The KCs derived from Alu 130 and Aerosil 90 template particles (corresponding to the smallest and largest measures) are characterized as electrode materials in EDLCS based on aqueous (1 M H_2SO_4) and ionic liquid ($EMIBF_4$) electrolytes (Table 20).
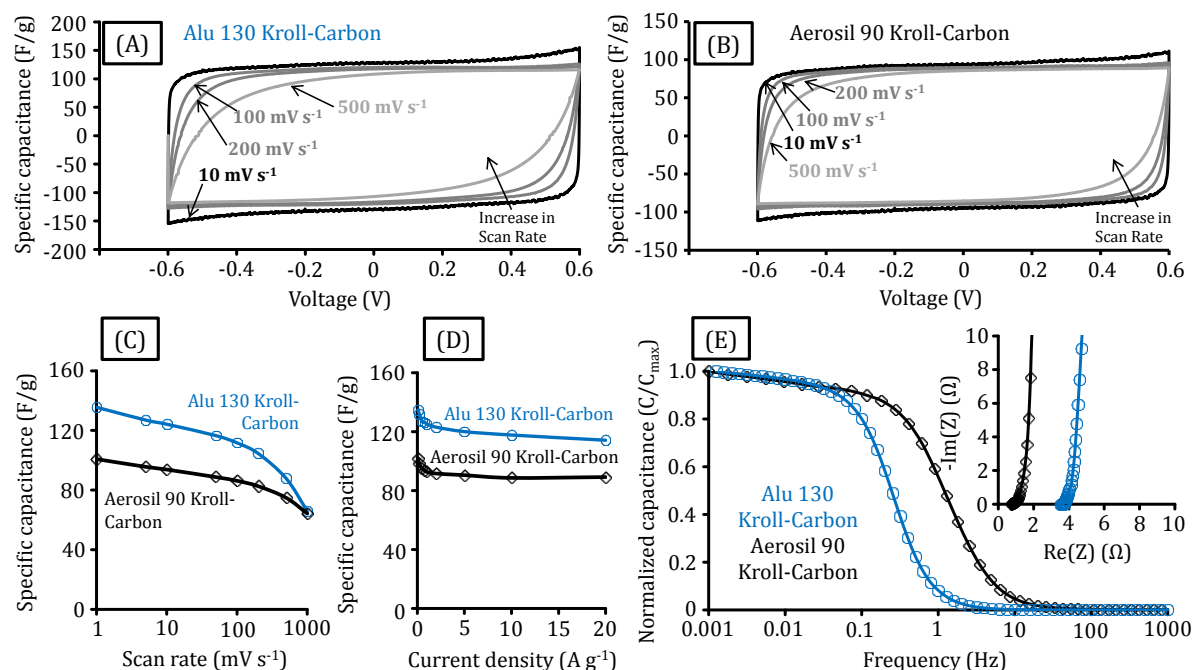
Figure 103. *Cyclic voltammograms at different scan rates of the KCs from Alu 130 (A) and Aerosil 90 (B) as well as specific capacities at different scan rates (C), specific capacities obtained from galvanostatic charge-discharge tests (D), and frequency responses (E) with Nyquist plots (inset in (E)) in aqueous 1 M H_2SO_4 electrolyte.*

The CV curves of the KCs in 1 M aqueous H_2SO_4 are rectangular within the applied potential range (Figure 103(A,B)). This is indicating the absence of a large number of surface functional groups and the high purity of the materials. Specific capacitances as high as 135 F/g are obtained at a scan rate of 1 mV/s for the alumina-templated KCs. Due to their lower SSA, the KCs from silica templates show a 26% lower value. While these are high values, materials with higher micropore volumes but comparable SSA exhibit higher specific capacities in the same electrolyte system (see section 5.1.2). This

difference is likely related to the lower adsorption potential of the ions in mesopores as compared to the rather narrow micropores. This also explains the moderate capacitance per surface area of the KCs (Table 20) in this electrolyte system. 7.2 and 6.6 $\mu F/cm^2$ are provided by the KCs obtained from Alu 130 and Aerosil 90 templates, respectively. The nearly rectangular shape of the CV curves at high sweep rates indicates very rapid ion diffusion in the materials due to their distinctive mesopore system. Specific capacities up to 90 F/g can be utilized at a scan rate as high as 500 mV/s (Figure 103(C)). These values significantly exceed the capacities of purely microporous carbon materials with curved pores that usually exhibit significant capacitance fading at higher scan rates.

The values determined by CV measurements are in good accordance with galvanostatic charge-discharge experiments (Figure 103(D)) showing specific capacitances (at a current rate of 0.1 A/g) up to 134 F/g and 101 F/g for KCs obtained from Alu 130 and Aerosil 90, respectively. Charge-discharge measurements are most accurate to determine the performance of EDLCs in real applications as an ideal EDLC must deliver the same energy independent of the current density applied. KCs provide impressive high power characteristics with up to 88% of the initial capacitance retained at high current densities of 20 A/g. Such high capacitance retentions are not achievable with most commercial activated carbons. These materials, while showing comparable SSA usually retain only 50% of their initial capacitance at high current densities in the same electrolyte system.[157]

Nyquist plots (Figure 103(E)) of the KCs show a nearly vertical line at low frequencies, where the contribution becomes almost exclusively capacitive. The EIS measurements allow for estimation of the capacitance changes with the operating frequency (Figure 103(E)). At low frequencies, the capacitance shows saturation in both materials indicating that they reach the equilibrium in ion adsorption. The maximum operating frequency (f_{max}) is set by the frequency at which the capacitance decreases by not more than 50%. The Aerosil 90-based KCs can operate at higher frequency (> 1 Hz) compared to the Alu 130-based KCs (> 0.2 Hz) due to its larger mesopores leading to enhanced ion diffusion. The f_{max} of the silica-based sample is comparable to previously reported hierarchical materials and significantly surpassing the performance of activated carbons in the same electrolyte system.

The equivalent series resistance (ESR) is a very important characteristic of an EDLC device including the electrical resistance of the electrodes and the current collector

interfaces as well as the portion of the ionic resistance related to the ion transport outside the carbon pore channels. It can be determined at very high frequencies when the imaginary component of the complex impedance becomes zero (intersection of the Nyquist plot with the x-axis). The microstructure of Aerosil 90-derived KC architecture allows smaller equivalent series resistance to be attained, likely originating from the smaller current collector/electrode contact resistance (Figure 103(E)).

Table 20. EDLC data summary of the KCs determined from the CV measurements at a scan rate of 1 mV/s.

Template/ Electrolyte	Capacitance per KC weight (F/g)	Capacitance per electrode volume (F/cm^3)	Capacitance per KC SSA (µF/cm^2)
Alu 130/1 M H$_2$SO$_4$	135	31.1	7.2
Aerosil 90/1 M H$_2$SO$_4$	100	21.1	6.6
Alu 130/EMIBF$_4$	141	31.1	7.6
Aerosil 90/EMIBF$_4$	124	26.5	8.1

Figure 104. Cyclic voltammograms at different scan rates of the KCs from Alu 130 (A) as well as Cycling stabilities during galvanostatic charge/discharge cycling in the potential range -2.0-2.0 V (B), specific capacities at different scan rates (C), specific capacities obtained from galvanostatic charge-discharge tests at 20 and 70°C (D), and frequency responses (E) with Nyquist plots (inset in (E)) of the KCs from Alu 130 (blue) and Aerosil 90 (black) in EMIBF$_4$ IL electrolyte.

The CV curves of the KC-based electrodes in the IL electrolyte show some pseudocapacitive contributions at ~1.7 V in the symmetrical EDLC (Figure 104(A)). These peaks can either result from impurities in the $EMIBF_4$ or from reactions of the IL with functional groups on the carbon surface. However, these faradic processes do not negatively affect the cycle stability of the EDLC showing complete retention of the initial capacitance after 10000 galvanostatic charge/discharge cycles in the potential range from -2.0-2.0 V (Figure 104(B)). High specific capacitance values of 141 F/g (7.6 µF/cm^2 when related to the carbon surface area) for KCs prepared from Alu 130 and 124 F/g (8.1 µF/cm^2) for KCs prepared from Aerosil 90 templates are determined from the CV measurements at low scan rates ((Figure 104(C) and Table 20). When the rate is increased up to 100 or even 500 mV/s, high specific capacitances can be retained and the CV curves exhibit a nearly rectangular shape as it is typical for pure EDLCs with low electrolyte diffusion limitations. At scan rates of 50 mV/s and higher, redox reactions are too slow to contribute to the capacitance leading to the disappearance of the redox peaks.

C-D measurements (Figure 104(D)) at 20°C and a current density of 0.1 A/g in the potential range -2.0-2.0 V confirm the values calculated from CV investigations. High specific capacitances of 135 and 121 F/g are determined for the KCs from Alu 130 and Aerosil 90 templates, respectively. As for the 1 M H_2SO_4 electrolyte, remarkable capacitance retentions of 75% are determined at high current densities of 20 A/g. The relative capacitance retentions of KCs significantly surpass those observed for high performance polypyrrole-derived activated carbons, and other tuned mesoporous materials.[236] C-D measurements of the KC-based EDLCs at a high temperature of 70°C (Figure 104(D)) show a ~10% increase of the specific capacitance over the entire current density range due to the reduction of the viscosity of the electrolyte and an increase of its ionic conductivity at higher temperatures. Compared to activated carbons with a 20% increase of the capacitance at 60°C, the enhancement of the KC performance is moderate due to their enhanced electron transport performance even at room temperature. In contrast to the aqueous electrolyte system, EIS measurements of the KC-based EDLCs in $EMIBF_4$ electrolyte show the presence of the typical 45° segment due to the resistance of ions during diffusion into the bulk of electrode particles (Figure 104(E)). The ESRs of the KCs are relatively equal due to their high purity and similar surface chemistry. Regarding the values of f_{max}, both of the KCs show promising

behavior in the IL electrolyte system (Figure 104(E)). They can operate at frequencies as high as 0.15 Hz (KC from Alu 130) and 0.1 Hz (KC from Aerosil 90) being comparable with the high values of OM-SiC-CDCs and significantly exceeding those of many activated carbons, even in cases where small mesopores are present.[157, 236]

Table 20. *EDLC data summary of the KCs determined from the CV measurements at a scan rate of 1 mV/s.*

Template/ Electrolyte	Capacitance per KC weight (F/g)	Capacitance per electrode volume (F/cm^3)	Capacitance per KC SSA (μF/cm^2)
Alu 130/1 M H_2SO_4	135	31.1	7.2
Aerosil 90/1 M H_2SO_4	100	21.1	6.6
Alu 130/EMIBF$_4$	141	31.1	7.6
Aerosil 90/EMIBF$_4$	124	26.5	8.1

If the CV voltage range is extended to -2.5 V-2.5 V for the Alu 130-templated hierarchical KC, the specific capacitance reaches even higher values of 174 F/g (at 1 mV/s) because the observed surface reactions now fully contribute to the capacitance values (Figure 105). However, at higher scan rates the CV still becomes rectangular indicating a reasonable stability. In spite of redox contributions present, it is known that the EMIBF$_4$ ionic liquid can operate in a wide voltage window leading to high energy density.
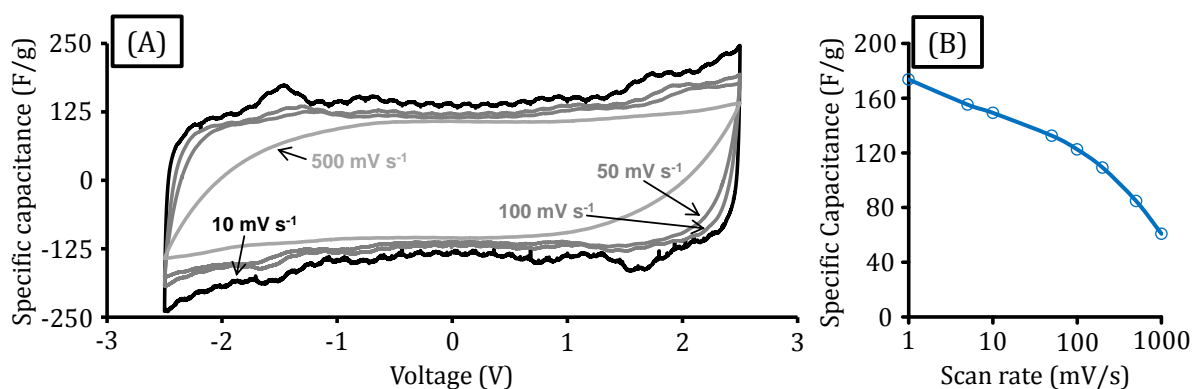

Figure 105. *Cyclic voltammograms at different scan rates of the KCs from Alu 130 in the potential range -2.5-2.5 V (A) and specific capacities at different scan rates (B).*

6. Summary and Outlook

Numerous methods for the targeted synthesis of carbon materials with tailored pore systems and for the production of structures with well-defined hierarchical pore architectures were developed within this thesis (Figure 106).

PolyHIPE-CDCs with porosity on three hierarchy levels and total pore volumes as high as 8.5 cm^3/g were prepared by a high internal phase emulsion technique. Especially after CO_2 activation, which increases the SSA to values above 3100 m^2/g, these materials are highly promising for the filtration of non-polar organic compounds from gas mixtures. Perfectly shaped CDC nanospheres with diameters below 200 nm were obtained from miniemulsions. Their pore structure is highly dependent on the emulsion composition and their high capacitance in aqueous symmetrical EDLCs (up to 175 F/g) makes them promising candidates for electrochemical flow capacitors.

The nanocasting concept was presented as an efficient approach for the synthesis of CDC mesofoam powders and meso-macroporous CDC monoliths. These materials are highly versatile in terms of application. Due to their high nanopore volume, well-defined mesopores and large SSA, they show outstanding properties as electrode material in EDLCs or in Li-S batteries as well as high and rapid uptake in gas adsorption processes.

CDC aerogels were produced by pyrolysis and high-temperature chlorine treatment of cross-linked polycarbosilane aerogels. These materials can be tailored for efficient CO_2 adsorption and show outstanding performance in EDLC electrodes at high current densities of up to 100 A/g due to the very short electron diffusion pathways within the aerogel-type pore system.

It was further shown that CDCs can be combined with mesopores by the sacrificial template method starting from PMMA particles as the pore-forming material. The use of highly toxic hydrofluoric acid and large amounts of organic solvents as typical for hard- and soft-templating approaches can be overcome. SSAs and total pore volumes of 2434 m^2/g and 2.64 cm^3/g are achieved. The PMMA-CDCs show high performance in Li-S battery cathodes, especially in high-molarity electrolytes.

The reported CDC synthesis pathways are very attractive with regard to the finally obtained products and exhibit serious advantages compared to previously reported methods for the production of hierarchical carbon materials and CDCs. As both the micropore size and the diameter of the larger pores can be precisely controlled, it is highly attractive to further tailor their pore structure for the use in the adsorption of

proteins or catalytic conversions which often make use of carbon-supported catalysts. However, it must be concluded that all the discussed materials and synthesis methods are all still beyond the approaches for activated carbon production in terms of economic and ecological efficiency. Therefore, it can be expected that CDC will likely remain a niche product as long as mass-production of devices is considered.

However, their use as model substances in energy- and environmentally relevant applications might be equally important. The questions "How does it work?" and "What do we need?" must be clearly answered before any material can be tailored for a specific application under the consideration of economic and ecological perspectives. The high potential of CDCs and templated carbon materials for this purpose was shown in this thesis. These carbons were used as model substances in combination with NMR techniques for a better understanding of the fundamentals of adsorption processes on porous carbon surfaces. However, such investigations strongly require the use of model substances with a tailored and well-defined pore structure to clearly differentiate physical states of adsorbed species by the spectroscopic method and hence to understand fundamental mechanisms. The characterization of the interaction of electrolyte molecules with the carbon surface was performed with solid-state NMR experiments. The materials were also studied in the high-pressure adsorption of ^{129}Xe using an *in-situ* NMR technique. Both NMR studies enable the analysis of ions or gas atoms adsorbed on the carbon surface on an atomic level and experimentally demonstrate different strength of interaction with pores of variable size and connectivity. In addition, the novel InfraSORP technology was used for the investigation of the thermal response of CDCs and templated carbon and carbide materials during *n*-butane adsorption. These well-defined model systems lead to a more profound understanding of this technique for the very rapid characterization of porous materials. Experiments like these are further expandable with CDCs as the model substances to different other topics under discussion, such as the mechanism of the polysulfide shuttle in Li-S batteries or the mechanism of water adsorption on porous carbon surfaces.

In contrast to hierarchical CDCs, which are obtained by quite complex templating approaches, and which are therefore not suitable for mass-production, the Kroll-Carbon concept is a highly attractive alternative for the synthesis of well-defined carbons on the large scale. Within this thesis, first materials were produced with high SSA close to 2000 m^2/g and total pore volumes exceeding 3 cm^3/g. The versatility of this method was

shown with regard to different template particle dimensions as well as by using various types of oxides (silica, alumina, titania) which are all usable for the reductive carbochlorination mechanism. Hence, porous carbon materials with various textural parameters are approachable. The first generation of KCs shows attractive properties for the use in Li-S battery cathodes and as electrode materials in EDLCs. Their use in other fields where mesoporous carbon materials are required, such as the adsorption of cytokines from blood plasma, is promising. Novel KC structures with even ordered mesopore systems can be generated if ordered mesoporous oxides are utilized as the template and if the reductive carbochlorination is used for the treatment of ordered mesoporous carbon/metal oxide composites obtained by soft-templating. Furthermore, composites with atomically dispersed metal oxide domains within a carbon structure are attractive precursor systems as they would lead to microporous KCs with even higher SSAs and micropore volumes and will therefore expand their fields of potential applications.
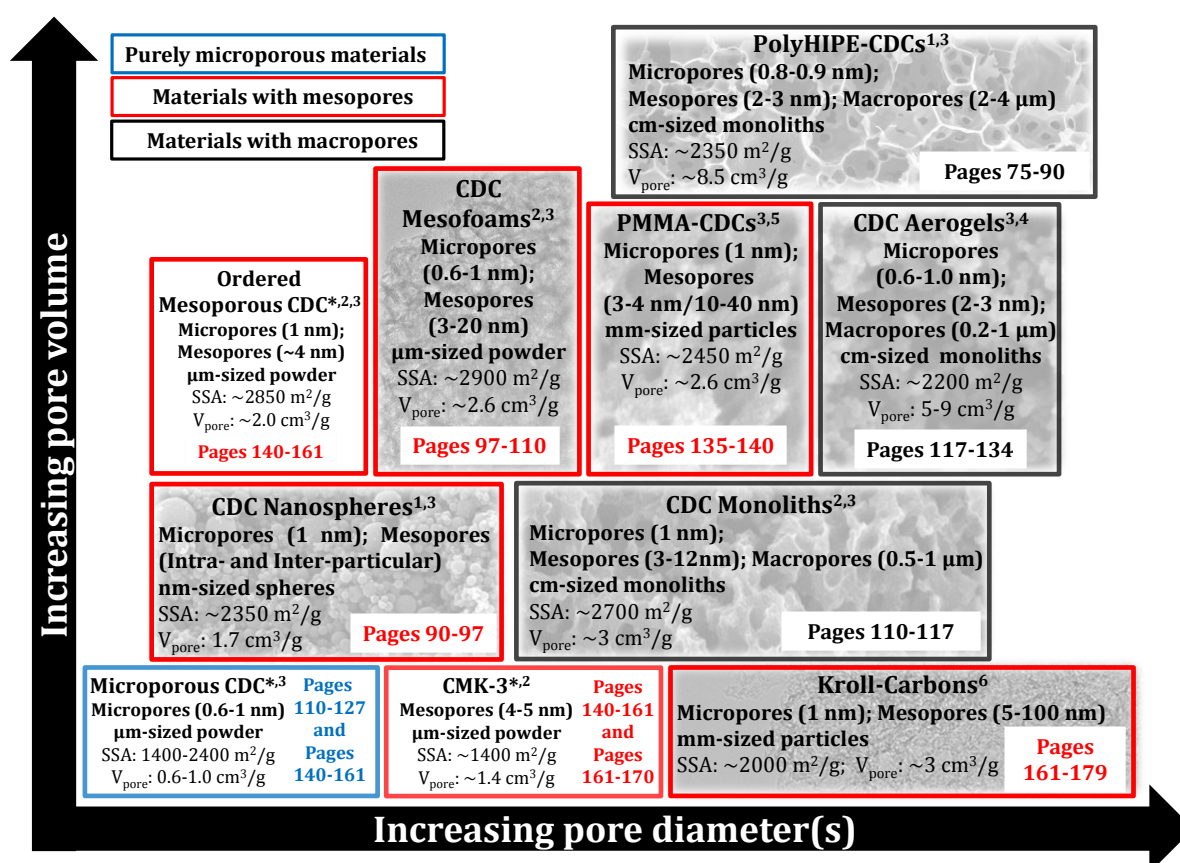
Figure 106. *Carbon materials with different textural parameters and synthesized by various techniques discussed within this thesis (*: reference material not developed within this thesis; [1]: material obtained by soft-templating; [2]: material obtained by hard-templating; [3]: material obtained by high-temperature chlorine treatment; [4]: material obtained by sol-gel technique; [5]:material obtained by sacrificial templating; [6]:material obtained by reductive carbochlorination).*

7. References

1.	Y. Gogotsi and V. Presser (Eds.), Carbon Nanomaterials, 2nd Edition, CRC Press, **2014**.
2.	M.-M. Titirici (Ed.), Sustainable Carbon Materials From Hydrothermal Processes, John Wiley & Sons, **2013**.
3.	P. Serp and J. L. Figueiredo (Eds.), Carbon Materials For Catalysis, John Wiley & Sons, **2009**.
4.	K. Müllen, *ACS Nano*, **2014**, *8*, 6531-6541.
5.	S. Iijima, *Physica B*, **2002**, *323*, 1-5.
6.	L. T. Scott, *Angew. Chem. Int. Ed.*, **2004**, *43*, 4994-5007.
7.	K. Kaneko, *J. Membr. Sci.*, **1994**, *96*, 59-89.
8.	T. Kyotani, *Carbon*, **2000**, *38*, 269-286.
9.	J. Lee, J. Kim and T. Hyeon, *Adv. Mater.*, **2006**, *18*, 2073-2094.
10.	L. Borchardt, M. Oschatz and S. Kaskel, *Mater. Horiz.*, **2014**, *1*, 157-168.
11.	A. F. Gross and A. P. Nowak, *Langmuir*, **2010**, *26*, 11378-11383.
12.	J. Biener, M. Stadermann, M. Suss, M. A. Worsley, M. M. Biener, K. A. Rose and T. F. Baumann, *Energy Environ. Sci.*, **2011**, *4*, 656-667.
13.	S. Zhang, L. Chen, S. Zhou, D. Zhao and L. Wu, *Chem. Mater.*, **2010**, *22*, 3433-3440.
14.	S. Dörfler, I. Felhoesi, T. Marek, S. Thieme, H. Althues, L. Nyikos and S. Kaskel, *J. Power Sources*, **2013**, *227*, 218-228.
15.	D. Pech, M. Brunet, H. Durou, P. Huang, V. Mochalin, Y. Gogotsi, P.-L. Taberna and P. Simon, *Nat. Nanotechnol.*, **2010**, *5*, 651-654.
16.	C. R. Perez, S.-H. Yeon, J. Segalini, V. Presser, P.-L. Taberna, P. Simon and Y. Gogotsi, *Adv. Funct. Mater.*, **2013**, *23*, 1081-1089.
17.	S. Jun, S. H. Joo, R. Ryoo, M. Kruk, M. Jaroniec, Z. Liu, T. Ohsuna and O. Terasaki, *J. Am. Chem. Soc.*, **2000**, *122*, 10712-10713.
18.	R. Ryoo, S. H. Joo and S. Jun, *J. Phys. Chem. B*, **1999**, *103*, 7743-7746.
19.	M. Kruk, M. Jaroniec, T.-W. Kim and R. Ryoo, *Chem. Mater.*, **2003**, *15*, 2815-2823.
20.	R. Ryoo, S. H. Joo, S. Jun, T. Tsubakiyama and O. Terasaki, *Stud. Surf. Sci. Catal.*, **2001**, *135*, 1121-1128.
21.	J. Lee, K. Sohn and T. Hyeon, *J. Am. Chem. Soc.*, **2001**, *123*, 5146-5147.
22.	Y. Meng, D. Gu, F. Zhang, Y. Shi, H. Yang, Z. Li, C. Yu, B. Tu and D. Zhao, *Angew. Chem. Int. Ed.*, **2005**, *44*, 7053-7059.
23.	H. Marsh and F. Rodriguez-Reinoso (Eds.), *Activated Carbon*, 1st Edition, Elsevier, **2006**.
24.	A. C. Pastor, F. Rodriguez-Reinoso, H. Marsh and M. A. Martinez, *Carbon*, **1999**, *37*, 1275-1283.
25.	F. Rodriguez-Reinoso, *Production and Applications of Activated Carbons*, in: *Handbook of Porous Solids*, Wiley-VCH, **2002**, 1766-1827.
26.	J. Wang and S. Kaskel, *J. Mater. Chem.*, **2012**, *22*, 23710-23725.
27.	Y. Lv, F. Zhang, Y. Dou, Y. Zhai, J. Wang, H. Liu, Y. Xia, B. Tu and D. Zhao, *J. Mater. Chem.*, **2012**, *22*, 93-99.
28.	H. Nishihara and T. Kyotani, *Adv. Mater.*, **2012**, *24*, 4473-4498.

29. Y. Zhai, Y. Dou, D. Zhao, P. F. Fulvio, R. T. Mayes and S. Dai, *Adv. Mater.*, **2011**, *23*, 4828-4850.

30. H. Nishihara, H. Itoi, T. Kogure, P.-X. Hou, H. Touhara, F. Okino and T. Kyotani, *Chem. Eur. J.*, **2009**, *15*, 5355-5363.

31. V. Presser, M. Heon and Y. Gogotsi, *Adv. Funct. Mater.*, **2011**, *21*, 810-833.

32. W. A. Frad, *Advan. Inorg. Chem. Radiochem.*, **1968**, *11*, 153-247.

33. R. Riedel and I. W. Chen (Eds.), *Ceramics Science and Technology; Volume 1: Structures*, Wiley-VCH, **2008**.

34. E. Riedel (Ed.), *Inorganic Chemistry*, 6th Edition, de Gruyter, **2004**.

35. L. Borchardt, C. Hoffmann, M. Oschatz, L. Mammitzsch, U. Petasch, M. Herrmann and S. Kaskel, *Chem. Soc. Rev.*, **2012**, *41*, 5053-5067.

36. P. Colombo, G. Mera, R. Riedel and G. D. Soraru, *J. Am. Ceram. Soc.*, **2010**, *93*, 1805-1837.

37. R. Riedel (Ed.), Handbook of Ceramic Hard Materials, Wiley-VCH, **2000**.

38. H. Klemm, *J. Am. Ceram. Soc.*, **2010**, *93*, 1501-1522.

39. H. O. Pierson, *High Temp. Mater. Processes*, **1993**, *11*, 239-246.

40. A. W. Weimer, K. J. Nilsen, G. A. Cochran and R. P. Roach, *AIChE J.*, **1993**, *39*, 493-503.

41. M. J. Ledoux and C. Pham-Huu, *CATTECH*, **2011**, *4*, 226-246.

42. R. Koc, *J. Mater. Sci.*, **1998**, *33*, 1049-1055.

43. I. M. Berger, E. Langholf, K. Jaenicke-Rossler and G. Leitner, *J. Mater. Sci. Lett.*, **1999**, *18*, 1409-1412.

44. G. A. Swift and R. Koc, *J. Mater. Sci.*, **1999**, *34*, 3083-3093.

45. R. Riedel, E. Horvath-Bordon, S. Nahar-Borchert and E. Kroke, *Key Eng. Mater.*, **2003**, *247*, 121-128.

46. P. A. Storozhenko and G. I. Shcherbakova, *Mendeleev Commun.*, **2014**, *24*, 133-137.

47. D. Y. Son, *Adv. Silicon Sci.*, 2009, 2, 391-400.

48. M. Chen, P. Xiong, Q. Zhou, L. Ni and G. Wang, *Polym. Int.*, 2014, 63, 1531-1536.

49. M. Berbon and M. Calabrese, *J. Am. Ceram. Soc.*, **2002**, *85*, 1891-1893.

50. E. Kockrick, R. Frind, M. Rose, U. Petasch, W. Böhlmann, D. Geiger, M. Herrmann and S. Kaskel, *J. Mater. Chem.*, **2009**, *19*, 1543-1553.

51. S. Kaur, R. Riedel and E. Ionescu, *J. Eur. Ceram. Soc.*, **2014**, *34*, 3571-3578.

52. M. Oschatz, L. Borchardt, K. Pinkert, S. Thieme, M. R. Lohe, C. Hoffmann, M. Benusch, F. M. Wisser, C. Ziegler, L. Giebeler, M. H. Rümmeli, J. Eckert, A. Eychmüller and S. Kaskel, *Adv. Energy Mater.*, **2014**, *4*, 1300645/1300641-1300645/1300649.

53. O. Hutchins, *Silicon tetrachloride*, US1271713, **1918**.

54. W. A. Mohun, *Mineral active carbon*, US3066099, **1962**.

55. M. Kusunoki, M. Rokkaku and T. Suzuki, *Appl. Phys. Lett.*, **1997**, *71*, 2620-2622.

56. A. J. Van Bonnel, J. E. Crombeen and A. Van Tooren, *Surf. Sci.*, **1975**, *48*, 463-472.

57. J. Wang, M. Oschatz, T. Biemelt, L. Borchardt, I. Senkovska, M. R. Lohe and S. Kaskel, *J. Mater. Chem.*, **2012**, *22*, 23893-23899.

58. S.-H. Yeon, I. Knoke, Y. Gogotsi and J. E. Fischer, *Microporous Mesoporous Mater.*, **2010**, *131*, 423-428.

59. T. Knorr, A. Schwarz and B. J. M. Etzold, *Chem. Eng. Technol.*, **2014**, *37*, 453-461.

60. F. Glenk, T. Knorr, M. Schirmer, S. Guetlein and B. J. M. Etzold, *Chem. Eng. Technol.*, **2010**, *33*, 698-703.

61. M. Kormann, H. Ghanem, H. Gerhard and N. Popovska, *J. Eur. Ceram. Soc.*, **2008**, *28*, 1297-1303.

62. T. Fey, B. Zierath, A. M. Kern, P. Greil and B. J. M. Etzold, *Carbon*, **2014**, *70*, 30-37.

63. V. Ruiz, C. Blanco, E. Raymundo-Pinero, V. Khomenko, F. Beguin and R. Santamaria, *Electrochim. Acta*, **2007**, *52*, 4969-4973.

64. M. Rose, E. Kockrick, I. Senkovska and S. Kaskel, *Carbon*, **2009**, *48*, 403-407.

65. V. Presser, L. Zhang, J. J. Niu, J. McDonough, C. Perez, H. Fong and Y. Gogotsi, *Adv. Energy Mater.*, **2011**, *1*, 423-430.

66. J. Chmiola, C. Largeot, P.-L. Taberna, P. Simon and Y. Gogotsi, *Science*, **2010**, *328*, 480-483.

67. M. Heon, S. Lofland, J. Applegate, R. Nolte, E. Cortes, J. D. Hettinger, P.-L. Taberna, P. Simon, P. Huang, M. Brunet and Y. Gogotsi, *Energy Environ. Sci.*, 2011, *4*, 135-138.

68. R. Jager, P. E. Kasatkin, E. Hark and E. Lust, *Electrochem. Commun.*, **2013**, *35*, 97-99.

69. L. Borchardt, F. Hasche, M. R. Lohe, M. Oschatz, F. Schmidt, E. Kockrick, C. Ziegler, T. Lescouet, A. Bachmatiuk, B. Büchner, D. Farrusseng, P. Strasser and S. Kaskel, *Carbon*, **2012**, *50*, 1861-1870.

70. E. Kockrick, C. Schrage, L. Borchardt, N. Klein, M. Rose, I. Senkovska and S. Kaskel, *Carbon*, **2010**, *48*, 1707-1717.

71. A. Silvestre-Albero, S. Rico-Frances, F. Rodriguez-Reinoso, A. M. Kern, M. Klumpp, B. J. M. Etzold and J. Silvestre-Albero, *Carbon*, **2013**, *59*, 221-228.

72. J. T. Lee, Y. Zhao, S. Thieme, H. Kim, M. Oschatz, L. Borchardt, A. Magasinski, W. I. Cho, S. Kaskel and G. Yushin, *Adv. Mater.*, **2013**, *25*, 4573-4579.

73. S. Thieme, J. Brückner, I. Bauer, M. Oschatz, L. Borchardt, H. Althues and S. Kaskel, *J. Mater. Chem. A*, **2013**, *1*, 9225-9234.

74. J. Chmiola, G. Yushin, Y. Gogotsi, C. Portet, P. Simon and P. L. Taberna, *Science*, **2006**, *313*, 1760-1763.

75. J. Torop, M. Arulepp, J. Leis, A. Punning, U. Johanson, V. Palmre and A. Aabloo, *Materials*, **2010**, *3*, 9-25.

76. F. Hippauf, D. Lunow, L. Borchardt, T. Henle and S. Kaskel, *Carbon*, **2014**, *77*, 191-198.

77. G. Yushin, E. N. Hoffman, M. W. Barsoum, Y. Gogotsi, C. A. Howell, S. R. Sandeman, G. J. Phillips, A. W. Lloyd and S. V. Mikhalovsky, *Biomaterials*, **2006**, *27*, 5755-5762.

78. V. Presser, S.-H. Yeon, C. Vakifahmetoglu, C. A. Howell, S. R. Sandeman, P. Colombo, S. Mikhalovsky and Y. Gogotsi, *Adv. Healthcare Mater.*, **2012**, *1*, 796-800.

79. S. Porada, L. Borchardt, M. Oschatz, M. Bryjak, J. S. Atchison, K. J. Keesman, S. Kaskel, P. M. Biesheuvel and V. Presser, *Energy Environ. Sci.*, **2013**, *6*, 3700-3712.

80. S. Porada, L. Weinstein, R. Dash, A. van der Wal, M. Bryjak, Y. Gogotsi and P. M. Biesheuvel, *ACS Appl. Mater. Interfaces*, **2012**, *4*, 1194-1199.

81. K. Motzfeldt and M. Steinmo, *Proc. Electrochem. Soc.*, **1997**, *97-39*, 523-528.

82. Y. Gogotsi, A. Nikitin, H. Ye, W. Zhou, J. E. Fischer, B. Yi, H. C. Foley and M. W. Barsoum, *Nat. Mater.*, **2003**, *2*, 591-594.

83. M. R. Lukatskaya, J. Halim, B. Dyatkin, M. Naguib, Y. S. Buranova, M. W. Barsoum and Y. Gogotsi, *Angew. Chem. Int. Ed.*, **2014**, *53*, 4877-4880.

84. G. Yushin, A. Nikitin and Y. Gogotsi, *Carbide-derived carbon*, in: *Carbon Nanomaterials*, CRC Press, **2006**, 211-254.

85. W. C. Schumb and J. R. Aronson, *J. Am. Chem. Soc.*, *1959*, *81*, 806-807.

86. N. Batisse, K. Guerin, M. Dubois, A. Hamwi, L. Spinelle and E. Tomasella, *Thin Solid Films*, **2010**, *518*, 6746-6751.

87. R. K. Dash, G. Yushin and Y. Gogotsi, *Microporous Mesoporous Mater.*, **2005**, *86*, 50-57.

88. P. Becker, F. Glenk, M. Kormann, N. Popovska and B. J. M. Etzold, *Chem. Eng. J.*, **2010**, *159*, 236-241.

89. L. Chen, G. Behlau, Y. Gogotsi and M. J. McNallan, *Ceram. Eng. Sci. Proc.*, **2003**, *24*, 57-62.

90. Z. G. Cambaz, G. N. Yushin, Y. Gogotsi, K. L. Vyshnyakova and L. N. Pereselentseva, *J. Am. Ceram. Soc.*, **2006**, 89, 509-514.

91. R. Dash, J. Chmiola, G. Yushin, Y. Gogotsi, G. Laudisio, J. Singer, J. Fischer and S. Kucheyev, *Carbon*, **2006**, *44*, 2489-2497.

92. S. Osswald, J. Chmiola and Y. Gogotsi, *Carbon*, **2012**, *50*, 4880-4886.

93. G. N. Yushin, E. N. Hoffman, A. Nikitin, H. Ye, M. W. Barsoum and Y. Gogotsi, *Carbon*, **2005**, *43*, 2075-2082.

94. C. Portet, D. Kazachkin, S. Osswald, Y. Gogotsi and E. Borguet, *Thermochim. Acta*, **2010**, *497*, 137-142.

95. E. N. Hoffman, G. Yushin, T. El-Raghy, Y. Gogotsi and M. W. Barsoum, *Microporous Mesoporous Mater.*, **2008**, *112*, 526-532.

96. J. Leis, A. Perkson, M. Arulepp, M. Kaarik and G. Svensson, *Carbon*, **2001**, *39*, 2043-2048.

97. A. Janes, T. Thomberg and E. Lust, *Carbon*, **2007**, *45*, 2717-2722.

98. S. Urbonaite, J. M. Juarez-Galan, J. Leis, F. Rodriguez-Reinoso and G. Svensson, *Microporous Mesoporous Mater.*, **2008**, *113*, 14-21.

99. R. K. Dash, A. Nikitin and Y. Gogotsi, *Microporous Mesoporous Mater.*, **2004**, *72*, 203-208.

100. J. Leis, M. Arulepp, A. Kuura, M. Laett and E. Lust, *Carbon*, **2006**, *44*, 2122-2129.

101. M. Schmirler, T. Knorr, T. Fey, A. Lynen, P. Greil and B. J. M. Etzold, *Carbon*, **2011**, *49*, 4359-4367.

102. S.-H. Yeon, S. Osswald, Y. Gogotsi, J. P. Singer, J. M. Simmons, J. E. Fischer, M. A. Lillo-Rodenas and A. Linares-Solano, *J. Power Sources*, **2009**, *191*, 560-567.

103. M. Sevilla and R. Mokaya, *J. Mater. Chem.*, **2011**, *21*, 4727-4732.

104. M. Schmirler, F. Glenk and B. J. M. Etzold, *Carbon*, **2011**, *49*, 3679-3686.

105. M. Kormann and N. Popovska, *Microporous Mesoporous Mater.*, **2010**, *130*, 167-173.

106. M. Sevilla, R. Foulston and R. Mokaya, *Energy Environ. Sci.*, **2010**, *3*, 223-227.

107. A.-H. Lu and F. Schüth, *Adv. Mater.*, **2006**, *18*, 1793-1805.

108. P. Krawiec, C. Schrage, E. Kockrick and S. Kaskel, *Chem. Mater.*, **2008**, *20*, 5421-5433.

109. C. Hoffmann, T. Biemelt, A. Seifert, K. Pinkert, T. Gemming, S. Spange and S. Kaskel, *J. Mater. Chem.*, **2012**, *22*, 24841-24847.

110. S. Bernard and P. Miele, *New J. Chem.*, **2014**, *38*, 1923-1931.

111. P. Krawiec, D. Geiger and S. Kaskel, *Chem. Commun.*, **2006**, 2469-2470.

112. M. Kotani, K. Nishiyabu, S. Matsuzaki and S. Tanaka, *J. Ceram. Soc. Jpn.*, **2011**, *119*, 563-569.

113. A. Cruz-Espinoza, V. Ibarra-Galvan, A. Lopez-Valdivieso and J. Gonzalez-Gonzalez, *J. Colloid Interface Sci.*, **2012**, *374*, 321-324.

114. P. Adelhelm, K. Cabrera and B. M. Smarsly, *Sci. Technol. Adv. Mater.*, **2012**, *13*, 015010/1-015010/8.

115. D. Zhao, J. Feng, Q. Huo, N. Melosh, G. H. Frederickson, B. F. Chmelka and G. D. Stucky, *Science*, **1998**, *279*, 548-552.

116. F. Kleitz, S. H. Choi and R. Ryoo, *Chem. Commun.*, **2003**, 2136-2137.

117. P. Krawiec, E. Kockrick, L. Borchardt, D. Geiger, A. Corma and S. Kaskel, *J. Phys. Chem. C*, **2009**, *113*, 7755-7761.

118. M. Oschatz, E. Kockrick, M. Rose, L. Borchardt, N. Klein, I. Senkovska, T. Freudenberg, Y. Korenblit, G. Yushin and S. Kaskel, *Carbon*, **2010**, *48*, 3987-3992.

119. V. Shilapuram, N. Ozalp, M. Oschatz, L. Borchardt and S. Kaskel, *Carbon*, **2014**, *67*, 377-389.

120. M. Oschatz, L. Borchardt, S. Rico-Frances, F. Rodriguez-Reinoso, S. Kaskel and J. Silvestre-Albero, *Langmuir*, **2013**, *29*, 8133-8139.

121. T. Yu, Y. Deng, L. Wang, R. Liu, L. Zhang, B. Tu and D. Zhao, *Adv. Mater.*, **2007**, *19*, 2301-2306.

122. C. T. Kresge, M. E. Leonowicz, W. J. Roth, J. C. Vartuli and J. S. Beck, *Nature*, **1992**, *359*, 710-712.

123. D. Zhao and Y. Wan, *Stud. Surf. Sci. Catal.*, **2007**, *168*, 241-300.

124. L. Borchardt, M. Oschatz, M. Lohe, V. Presser, Y. Gogotsi and S. Kaskel, *Carbon*, **2012**, *50*, 3987-3994.

125. H.-J. Liu, J. Wang, C.-X. Wang and Y.-Y. Xia, *Adv. Energy Mater.*, **2011**, *1*, 1101-1108.

126. E. Kockrick, P. Krawiec, U. Petasch, H.-P. Martin, M. Herrmann and S. Kaskel, *Chem. Mater.*, **2008**, *20*, 77-83.

127. J. Henle, P. Simon, A. Frenzel, S. Scholz and S. Kaskel, *Chem. Mater.*, **2007**, *19*, 366-373.

128. E. Kockrick, L. Borchardt, C. Schrage, C. Gaudillere, C. Ziegler, T. Freudenberg, D. Farrusseng, A. Eychmüller and S. Kaskel, *Chem. Mater.*, **2011**, *23*, 57-66.

129. I. Pulko and P. Krajnc, *Macromol. Rapid Commun.*, **2012**, *33*, 1731-1746.

130. M. G. Schwab, I. Senkovska, M. Rose, N. Klein, M. Koch, J. Pahnke, G. Jonschker, B. Schmitz, M. Hirscher and S. Kaskel, *Soft Matter.*, **2009**, *5*, 1055-1059.

131. R. Frind, M. Oschatz and S. Kaskel, *J. Mater. Chem.*, **2011**, *21*, 11936-11940.

132. L. Borchardt, M. Oschatz, R. Frind, E. Kockrick, M. R. Lohe, C. P. Hauser, C. K. Weiss, K. Landfester, B. Buechner and S. Kaskel, *Beilstein J. Nanotechnol.*, **2011**, *2*, 638-644.

133. K. Landfester, *Angew. Chem. Int. Ed.*, **2009**, *48*, 4488-4507.

134. K. Landfester, N. Bechthold, F. Tiarks and M. Antonietti, *Macromolecules*, **1999**, *32*, 5222-5228.

135. G. D. Soraru, F. Dalcanale, R. Campostrini, A. Gaston, Y. Blum, S. Carturan and P. R. Aravind, *J. Mater. Chem.*, **2012**, *22*, 7676-7680.

136. E. Zera, R. Campostrini, P. R. Aravind, Y. Blum and G. D. Soraru, *Adv. Eng. Mater.*, **2014**, *16*, 814-819.

137. P. Simon and Y. Gogotsi, *Nat. Mater.*, **2008**, *7*, 845-854.

138. P. G. Bruce, S. A. Freunberger, L. J. Hardwick and J.-M. Tarascon, *Nat. Mater.*, **2012**, *11*, 19-29.

139. J. B. Goodenough, *Energy Environ. Sci.*, **2014**, *7*, 14-18.

140. J. R. Akridge, Y. V. Mikhaylik and N. White, *Solid State Ionics*, **2004**, *175*, 243-245.

141. F. Beguin, E. Frackowiak (Eds.), *Supercapacitors: Materials, Systems, and Applications*, Wiley-VCH, **2013**.

142. F. Beguin, V. Presser, A. Balducci and E. Frackowiak, *Adv. Mater.*, **2014**, *26*, 2219-2251.

143. F.-Y. Cheng, J. Liang, Z.-L. Tao and J. Chen, *Adv. Mater.*, **2011**, *23*, 1695-1715.

144. E. Frackowiak, Q. Abbas and F. Beguin, *J. Energy Chem.*, **2013**, *22*, 226-240.

145. W. Gu and G. Yushin, *Wiley Interdiscip. Rev.: Energy Environ.*, **2014**, *3*, 424-473.

146. S. Boukhalfa, K. Evanoff and G. Yushin, *Energy Environ. Sci.*, **2012**, *5,* 6872-6879.

147. K. Pinkert, L. Giebeler, M. Herklotz, S. Oswald, J. Thomas, A. Meier, L. Borchardt, S. Kaskel, H. Ehrenberg and J. Eckert, *J. Mater. Chem. A*, **2013**, *1*, 4904-4910.

148. Y. Zhu, S. Murali, M. D. Stoller, K. J. Ganesh, W. Cai, P. J. Ferreira, A. Pirkle, R. M. Wallace, K. A. Cychosz, M. Thommes, D. Su, E. A. Stach and R. S. Ruoff, *Science*, **2011**, *332*, 1537-1541.

149. L. Zhao, L.-Z. Fan, M.-Q. Zhou, H. Guan, S. Qiao, M. Antonietti and M.-M. Titirici, *Adv. Mater.*, **2010**, *22*, 5202-5206.

150. A. Balducci, R. Dugas, P. L. Taberna, P. Simon, D. Plee, M. Mastragostino and S. Passerini, *J. Power Sources*, **2007**, *165*, 922-927.

151. R. Lin, P.-L. Taberna, S. Fantini, V. Presser, C. R. Perez, F. Malbosc, N. L. Rupesinghe, K. B. K. Teo, Y. Gogotsi and P. Simon, *J. Phys. Chem. Lett.*, **2011**, *2*, 2396-2401.

152. J. A. Fernandez, M. Arulepp, J. Leis, F. Stoeckli and T. A. Centeno, *Electrochim. Acta*, **2008**, *53*, 7111-7116.

153. C. Portet, M. A. Lillo-Rodenas, A. Linares-Solano and Y. Gogotsi, *Phys. Chem. Chem. Phys.*, **2009**, *11*, 4943-4945.

154. C. Largeot, C. Portet, J. Chmiola, P.-L. Taberna, Y. Gogotsi and P. Simon, *J. Am. Chem. Soc.*, **2008**, *130*, 2730-2731.

155. C. Largeot, P. L. Taberna, Y. Gogotsi and P. Simon, *Electrochem. Solid State Lett.*, **2011**, *14*, A174-A176.

156. Y. Korenblit, M. Rose, E. Kockrick, L. Borchardt, A. Kvit, S. Kaskel and G. Yushin, *ACS Nano*, **2010**, *4*, 1337-1344.

157. M. Rose, Y. Korenblit, E. Kockrick, L. Borchardt, M. Oschatz, S. Kaskel and G. Yushin, *Small*, **2011**, *7*, 1108-1117.

158. K. Pinkert, M. Oschatz, L. Borchardt, M. Klose, M. Zier, W. Nickel, L. Giebeler, S. Oswald, S. Kaskel and J. Eckert, *ACS Appl. Mater. Interfaces*, **2014**, *6*, 2922-2928.

159. J. Chmiola, C. Largeot, P.-L. Taberna, P. Simon and Y. Gogotsi, *Angew. Chem. Int. Ed.*, **2008**, *47*, 3392-3395.

160. E. Raymundo-Pinero, K. Kierzek, J. Machnikowski and F. Beguin, *Carbon*, **2006**, *44*, 2498-2507.

161. T. M. Arruda, M. Heon, V. Presser, P. C. Hillesheim, S. Dai, Y. Gogotsi, S. V. Kalinin and N. Balke, *Energy Environ. Sci.*, **2013**, *6*, 225-231.

162. M. M. Hantel, V. Presser, R. Koetz and Y. Gogotsi, *Electrochem. Commun.*, **2011**, *13*, 1221-1224.

163. A. C. Forse, J. M. Griffin, H. Wang, N. M. Trease, V. Presser, Y. Gogotsi, P. Simon and C. P. Grey, *Phys. Chem. Chem. Phys.*, **2013**, *15*, 7722-7730.

164. F. W. Richey, B. Dyatkin, Y. Gogotsi and Y. A. Elabd, *J. Am. Chem. Soc.*, **2013**, *135*, 12818-12826.

165. H. Wang, A. C. Forse, J. M. Griffin, N. M. Trease, L. Trognko, P.-L. Taberna, P. Simon and C. P. Grey, *J. Am. Chem. Soc.*, **2013**, *135*, 18968-18980.

166. H. Wang, T. K. J. Koster, N. M. Trease, J. Segalini, P.-L. Taberna, P. Simon, Y. Gogotsi and C. P. Grey, *J. Am. Chem. Soc.*, **2011**, *133*, 19270-19273.

167. M. D. Levi, G. Salitra, N. Levy, D. Aurbach and J. Maier, *Nat. Mater.*, **2009**, *8*, 872-875.

168. M. D. Levi, S. Sigalov, G. Salitra, R. Elazari and D. Aurbach, *J. Phys. Chem. Lett.*, **2011**, *2*, 120-124.

169. S. Boukhalfa, L. He, Y. B. Melnichenko and G. Yushin, *Angew. Chem., Int. Ed.*, **2013**, *52*, 4618-4622.

170. G. Feng, S. Li, V. Presser and P. T. Cummings, *J. Phys. Chem. Lett.*, **2013**, *4*, 3367-3376.

171. S. Kondrat, C. R. Perez, V. Presser, Y. Gogotsi and A. A. Kornyshev, *Energy Environ. Sci.*, **2012**, *5*, 6474-6479.

172. N.-S. Choi, Z. Chen, S. A. Freunberger, X. Ji, Y.-K. Sun, K. Amine, G. Yushin, L. F. Nazar, J. Cho and P. G. Bruce, *Angew. Chem. Int. Ed.*, **2012**, *51*, 9994-10024.

173. Y.-X. Yin, S. Xin, Y.-G. Guo and L.-J. Wan, *Angew. Chem. Int. Ed.*, **2013**, *52*, 13186-13200.

174. G. Xu, B. Ding, J. Pan, P. Nie, L. Shen and X. Zhang, *J. Mater. Chem. A*, **2014**, *2*, 12662-12676.

175. X. Ji and L. F. Nazar, *J. Mater. Chem.*, **2010**, *20*, 9821-9826.

176. J. T. Lee, Y. Zhao, H. Kim, W. I. Cho and G. Yushin, *J. Power Sources*, **2014,** *248*, 752-761.

177. X. Li, Y. Cao, W. Qi, L. V. Saraf, J. Xiao, Z. Nie, J. Mietek, J.-G. Zhang, B. Schwenzer and J. Liu, *J. Mater. Chem.*, **2011**, *21*, 16603-16610.

178. G. Zhou, D.-W. Wang, F. Li, P.-X. Hou, L. Yin, C. Liu, G. Q. Lu, I. R. Gentle and H.-M. Cheng, *Energy Environ. Sci.*, **2012**, *5*, 8901-8906.

179. C. Liang, N. J. Dudney and J. Y. Howe, *Chem. Mater.*, **2009**, *21*, 4724-4730.

180. X. Ji, K. T. Lee and L. F. Nazar, *Nat. Mater.*, **2009**, *8*, 500-506.

181. J. Schuster, G. He, B. Mandlmeier, T. Yim, K. T. Lee, T. Bein and L. F. Nazar, *Angew. Chem. Int. Ed.*, **2012**, *51*, 3591-3595.

182. N. Jayaprakash, J. Shen, S. S. Moganty, A. Corona and L. A. Archer, *Angew. Chem. Int. Ed.*, **2011**, *50*, 5904-5908.

183. S. Xin, L. Gu, N.-H. Zhao, Y.-X. Yin, L.-J. Zhou, Y.-G. Guo and L.-J. Wan, *J. Am. Chem. Soc.*, **2012**, *134*, 18510-18513.

184. J. M. D. Tascon (Ed.), *Novel Carbon Adsorbents*, Elsevier, **2012**.

185. Y. Gogotsi, R. K. Dash, G. Yushin, T. Yildirim, G. Laudisio and J. E. Fischer, *J. Am. Chem. Soc.*, **2005**, *127*, 16006-16007.

186. R. E. Morris and P. S. Wheatley, *Angew. Chem. Int. Ed.*, **2008**, *47*, 4966-4981.

187. N. Klein, A. Henschel and S. Kaskel, *Microporous Mesoporous Mater.*, **2010**, *129*, 238-242.

188. C. Vakifahmetoglu, V. Presser, S.-H. Yeon, P. Colombo and Y. Gogotsi, *Microporous Mesoporous Mater.*, **2011**, *144*, 105-112.

189. M. Thommes, *Chem. Eng. Technol.*, **2010**, *82*, 1059-1073.

190. K. S. W. Sing, D. H. Everett, R. A. W. Haul, L. Moscou, R. A. Pierotti, J. Rouquerol and T. Siemieniewska, *Pure Appl. Chem.*, **1985**, *57*, 603-619.

191. J. Silvestre-Albero, A. Silvestre-Albero, F. Rodriguez-Reinoso and M. Thommes, *Carbon*, **2012**, *50*, 3128-3133.

192. A. Silvestre-Albero, M. Goncalves, T. Itoh, K. Kaneko, M. Endo, M. Thommes, F. Rodriguez-Reinoso and J. Silvestre-Albero, *Carbon*, **2012**, *50*, 66-72.

193. C. J. Rasmussen, A. Vishnyakov, M. Thommes, B. M. Smarsly, F. Kleitz and A. V. Neimark, *Langmuir*, **2010**, *26*, 10147-10157.

194. E. P. Barrett, L. G. Joyner and P. P. Halenda, *J. Am. Chem. Soc.*, **1951**, *73*, 373-380.

195. G. Horvath and K. Kawazoe, *J. Chem. Eng. Jpn.*, **1983**, *16*, 470-475.

196. M. Thommes, *Ser. Chem. Eng.*, **2004**, *4*, 317-364.

197. J. P. Olivier, *J. Porous Mater.*, **1995**, *2*, 9-17.

198. A. V. Neimark, Y. Lin, P. I. Ravikovitch and M. Thommes, *Carbon*, **2009**, *47*, 1617-1628.

199. G. Y. Gor, M. Thommes, K. A. Cychosz and A. V. Neimark, *Carbon*, **2012**, *50*, 1583-1590.

200. I. Langmuir, *J. Am. Chem. Soc.*, **1916**, *38*, 2221-2295.

201. S. Brunauer, P. H. Emmett and E. Teller, *J. Am. Chem. Soc.*, **1938**, *60*, 309-319.

202. J. H. de Boer, B. C. Lippens, B. G. Linsen, J. C. P. Broekhoff, A. van den Heuvel and T. J. Osinga, *J. Colloid Interface Sci.*, **1966**, *21*, 405-414.

203. P. Wollmann, M. Leistner, W. Graehlert, O. Throl, F. Dreisbach and S. Kaskel, *Microporous Mesoporous Mater.*, **2012**, *149*, 86-94.

204. P. Wollmann, M. Leistner, U. Stoeck, R. Gruenker, K. Gedrich, N. Klein, O. Throl, W. Graehlert, I. Senkovska, F. Dreisbach and S. Kaskel, *Chem. Commun.*, **2011**, *47*, 5151-5153.

205. M. Leistner, W. Graehlert and S. Kaskel, *Chem. Eng. Technol.*, **2013**, *85*, 747-752.

206. H. Giesche, *Mercury porosimetry*, in: *Handbook of Porous Solids*, Wiley-VCH, **2002**, 309-351.

207. L. Madler, H. K. Kammler, R. Mueller and S. E. Pratsinis, *J. Aerosol Sci.*, **2001**, *33*, 369-389.

208. I. Senkovska and S. Kaskel, *Microporous Mesoporous Mater.*, **2008**, *112*, 108-115.

209. B. M. Fung, A. K. Khitrin and K. Ermolaev, *J. Magn. Reson.*, **2000**, *142*, 97-101.

210. G. Metz, X. Wu and S. O. Smith, *J. Magn. Reson., Ser. A*, **1994**, *110*, 219-227.

211. H. C. Hoffmann, B. Assfour, F. Epperlein, N. Klein, S. Paasch, I. Senkovska, S. Kaskel, G. Seifert and E. Brunner, *J. Am. Chem. Soc.*, **2011**, *133*, 8681-8690.

212. M. Oschatz, L. Borchardt, M. Thommes, K. A. Cychosz, I. Senkovska, N. Klein, R. Frind, M. Leistner, V. Presser, Y. Gogotsi and S. Kaskel, *Angew. Chem. Int. Ed.*, **2012**, *51*, 7577-7580.

213. M. Oschatz, L. Borchardt, I. Senkovska, N. Klein, M. Leistner and S. Kaskel, *Carbon*, **2013**, *56*, 139-145.

214. K. Faber, F. Badaczewski, M. Oschatz, G. Mondin, W. Nickel, S. Kaskel and B. M. Smarsly, *J. Phys. Chem. C*, **2014**, *118*, 15705-15715.

215. V. Presser, C. R. Dennison, J. Campos, K. W. Knehr, E. C. Kumbur and Y. Gogotsi, *Adv. Energy Mater.*, **2012**, *2*, 895-902.

216. W. Nickel, M. Oschatz, M. von der Lehr, M. Leistner, G.-P. Hao, P. Adelhelm, P. Müller, B. M. Smarsly and S. Kaskel, *J. Mater. Chem. A*, **2014**, *2*, 12703-12707.

217. P. Schmidt-Winkel, W. W. Lukens, Jr., D. Zhao, P. Yang, B. F. Chmelka and G. D. Stucky, *J. Am. Chem. Soc.*, **1999**, *121*, 254-255.

218. J. Yan, A. Wang and D.-P. Kim, *J. Phys. Chem. B*, **2006**, *110*, 5429-5433.

219. Y. V. Mikhaylik and J. R. Akridge, *J. Electrochem. Soc.*, **2004**, *151*, A1969-A1976.

220. S.-R. Chen, Y.-P. Zhai, G.-L. Xu, Y.-X. Jiang, D.-Y. Zhao, J.-T. Li, L. Huang and S.-G. Sun, *Electrochim. Acta*, **2011**, *56*, 9549-9555.

221. T. Hara, S. Mascotto, C. Weidmann and B. M. Smarsly, *J. Chromatogr. A*, **2011**, *1218*, 3624-3635.

222. M. Oschatz, W. Nickel, M. Thommes, K. A. Cychosz, M. Leistner, M. Adam, G. Mondin, P. Strubel, L. Borchardt and S. Kaskel, *J. Mater. Chem. A*, **2014**, *2*, 18472-18479.

223. P. J. Reucroft and D. Rivin, *Thermochim. Acta*, **1999**, *328*, 19-24.

224. M. Oschatz, J. T. Lee, H. Kim, W. Nickel, L. Borchardt, W. I. Cho, C. Ziegler, S. Kaskel and G. Yushin, *J. Mater. Chem. A*, **2014**, *2*, 17649-17654.

225. P. Simon and Y. Gogotsi, *Acc. Chem. Res.*, **2013**, *46*, 1094-1103.

226. L. Borchardt, M. Oschatz, S. Paasch, S. Kaskel and E. Brunner, *Phys. Chem. Chem. Phys.*, **2013**, *15*, 15177-15184.

227. T. Ito and J. Fraissard, *J. Proc. Int. Conf. Zeolites 5th*, **1980**, 510-515.

228. K. V. Romanenko, J.-B. d'Espinose de la Caillerie, J. Fraissard, T. V. Reshetenko and O. B. Lapina, *Microporous Mesoporous Mater.*, **2005**, *81*, 41-48.

229. K. V. Romanenko, X. Py, J.-B. D'Espinose de Lacaillerie, O. B. Lapina and J. Fraissard, *J. Phys. Chem. B*, **2006**, *110*, 3055-3060.

230. M. Oschatz, H. C. Hoffmann, J. Pallmann, J. Schaber, L. Borchardt, W. Nickel, I. Senkovska, S. Rico-Frances, J. Silvestre-Albero, S. Kaskel and E. Brunner, *Chem. Mater.*, **2014**, *26*, 3280-3288.

231. J. Demarquay and J. Fraissard, *Chem. Phys. Lett.*, **1987**, *136*, 314-318.

232. A. Silvestre-Albero, E. O. Jardim, E. Bruijn, V. Meynen, P. Cool, A. Sepulveda-Escribano, J. Silvestre-Albero and F. Rodriguez-Reinoso, *Langmuir*, **2009**, *25*, 939-943.

233. W. Kroll, *Titanium*, US2205854, **1940**.

234. M. Oschatz, S. Boukhalfa, W. Nickel, J. T. Lee, S. Klosz, L. Borchardt, A. Eychmüller, G. Yushin and S. Kaskel, *J. Mater. Chem. A*, **2014**, *2*, 5131-5139.

235. M. Oschatz, S. Thieme, L. Borchardt, M. R. Lohe, T. Biemelt, J. Brueckner, H. Althues and S. Kaskel, *Chem. Commun.*, **2013**, *49*, 5832-5834.

236. L. Wei, M. Sevilla, A. B. Fuertes, R. Mokaya and G. Yushin, *Adv. Funct. Mater.*, **2012**, *22*, 827-834.
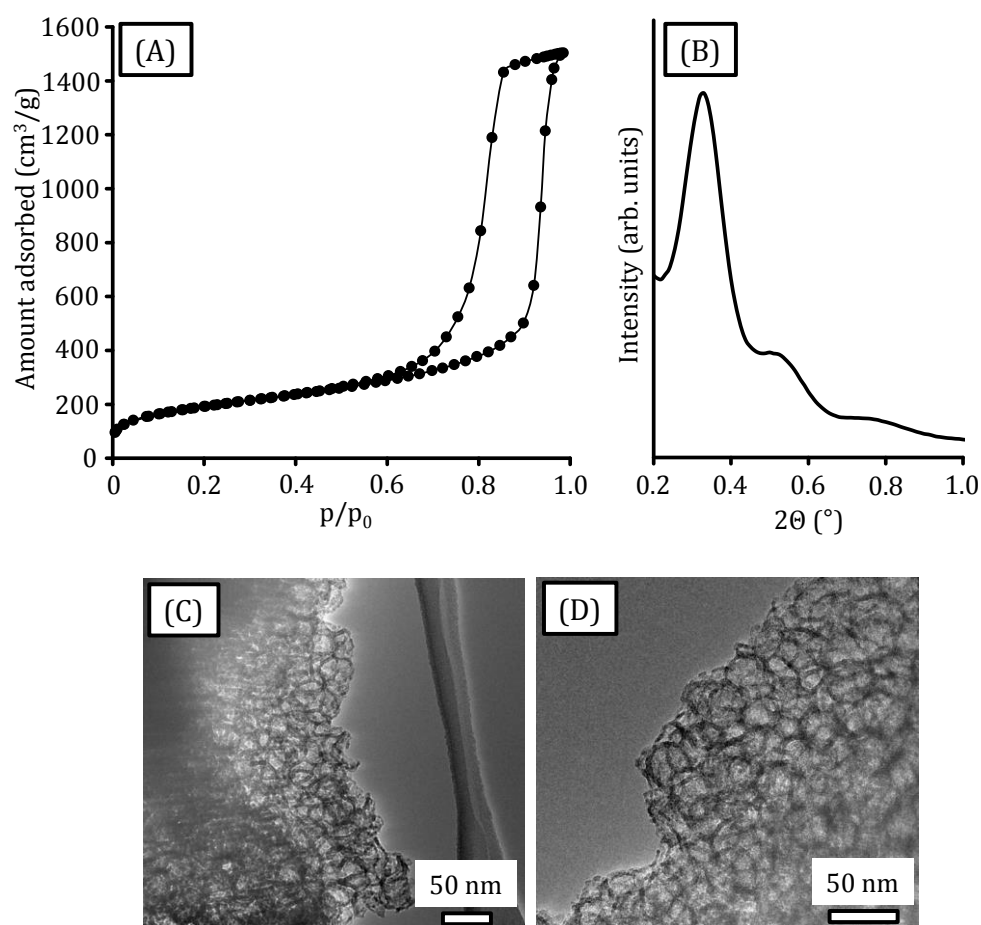
8. Appendix

8.1 List of Abbreviations

AC   Activated Carbon

BET   Brunauer-Emmett-Teller

C-D   Charge-Discharge

CDC   Carbide-Derived Carbon

CMC   Critical Micelle Concentration

CMK   Carbon Mesostructured by KAIST

CV   Cyclic Voltammetry

EDLC   Electrochemical Double-Layer Capacitor

EFC   Electrochemical Flow Capacitor

EIS   Electrochemical Impedance Spectroscopy

ESR   Equivalent Series Resistance

FT   Fourier Transform

FWHM   Full-Width at Half Maximum

HIPE   High Internal Phase Emulsion

IL   Ionic Liquid

IR   Infrared

IUPAC   International Union of Pure and Applied Chemistry

KIT   Korean Institute of Science and Technology

LIB   Lithium-Ion Battery

MAS   Magic Angle Spinning

MCF   Mesocellular SiO_2 Foam

n. s.   not specified

NLDFT   Non-Local Density Functional Theory

NMR   Nuclear Magnetic Resonance

NPs   Nanoparticles

OM   Ordered Mesoporous

OMC   Ordered Mesoporous Carbon

OMS   Ordered Mesoporous Silica

p/p_0 Relative Pressure

p-DVB   *para*-Divinylbenzene

PCS   Polycarbosilane

|	
PDI	Polydispersity Index
PSD	Pore Size Distribution
QSDFT	Quenched Solid Density Functional Theory
RT	Room Temperature
SBA	Santa Barbara Amorphous
SDA	Structure-Directing Agent
SEM	Scanning Electron Microscopy
SSA	Specific Surface Area
TEM	Transmission Electron Microscopy
V_{Micro}	Micropore Volume
$V_{Micro+Meso}$	Micro- and mesopore Volume
XRD	X-ray Diffraction

8.2 Supplementary Data

Appendix 1. *Nitrogen physisorption (-196°C) isotherm (A), small-angle XRD pattern (B) as well as TEM (C and D) micrographs of the mesocellular SiO$_2$ template used for the synthesis of CDC-MFs.*
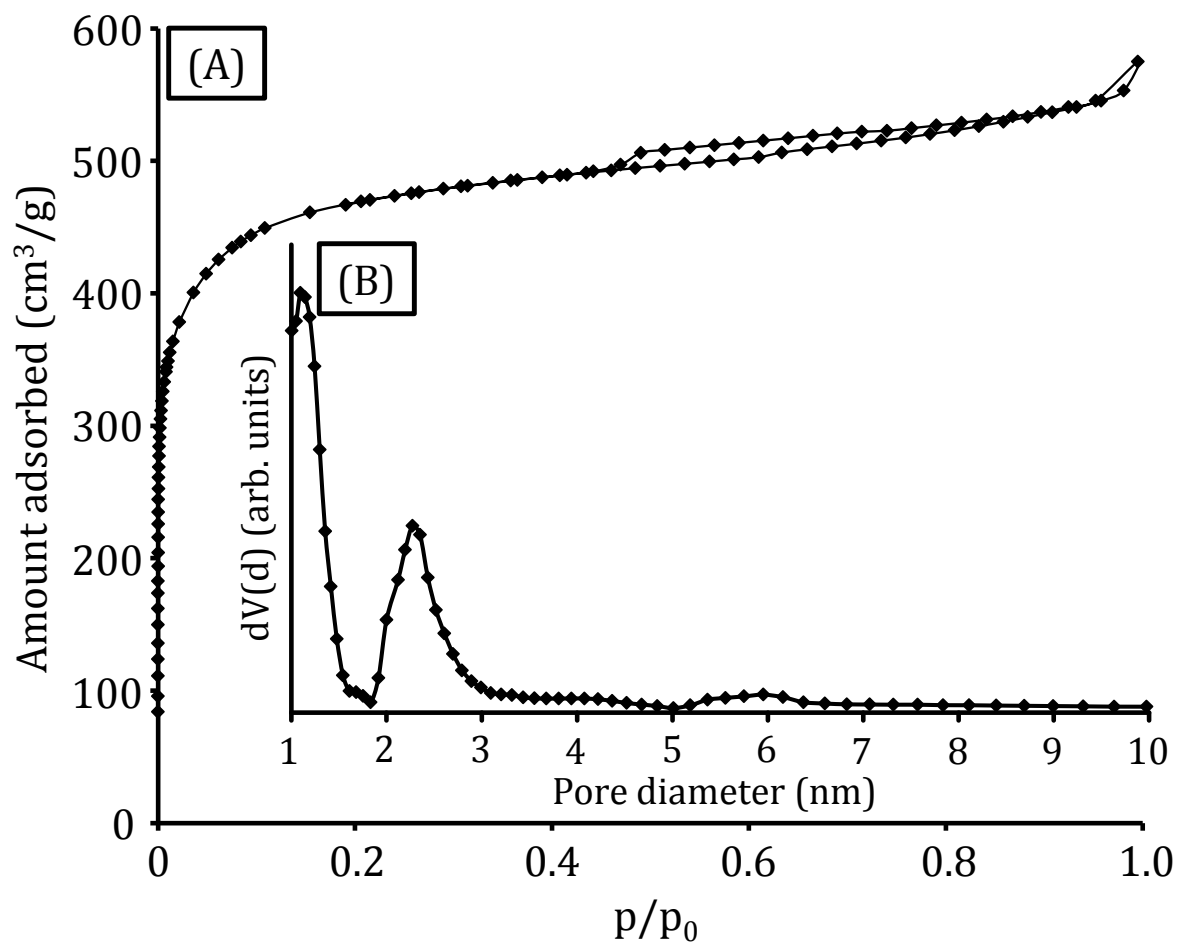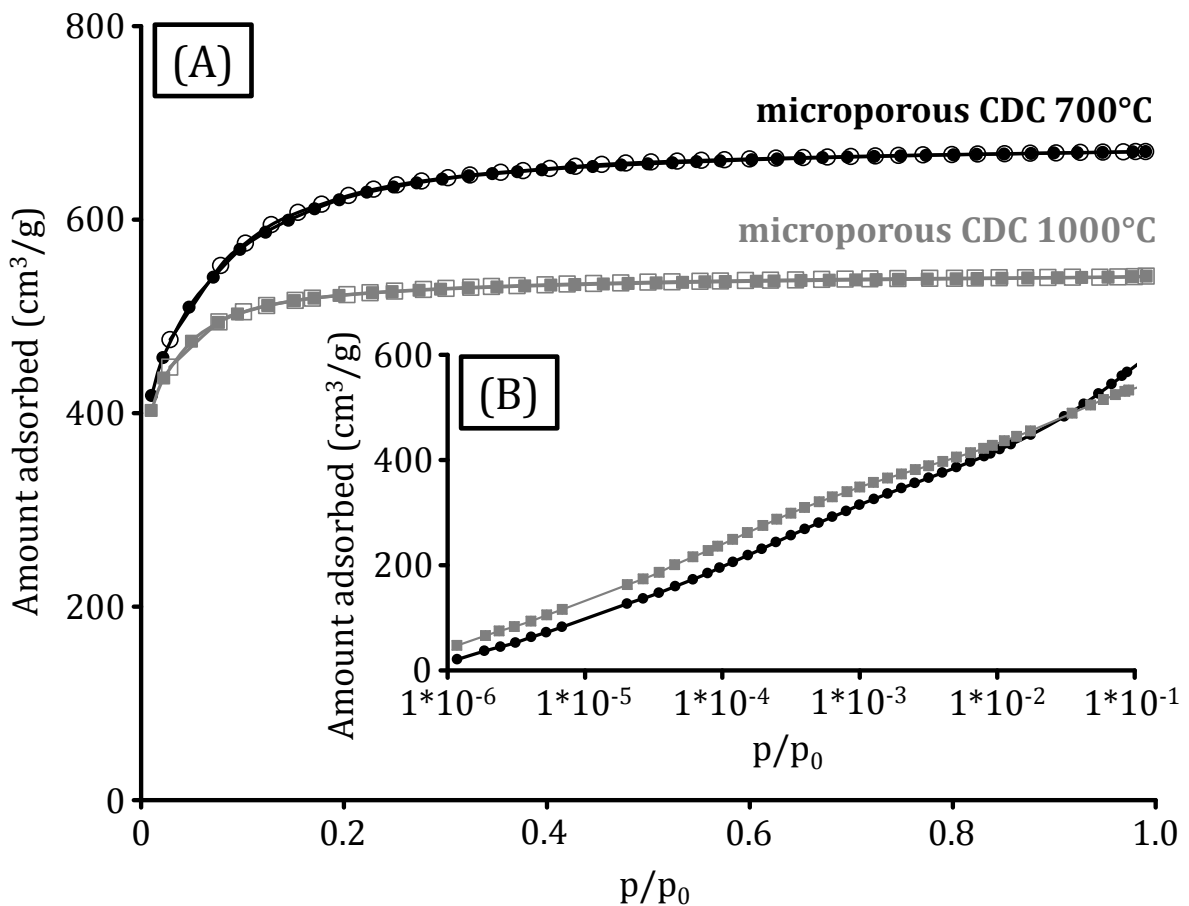
Appendix 2. *Nitrogen physisorption (-196°C) isotherm (A) and corresponding QSDFT (nitrogen on carbon with slit/cylindrical pores at -196°C, adsorption branch kernel) pore size distributions (B) of YP-50F.*
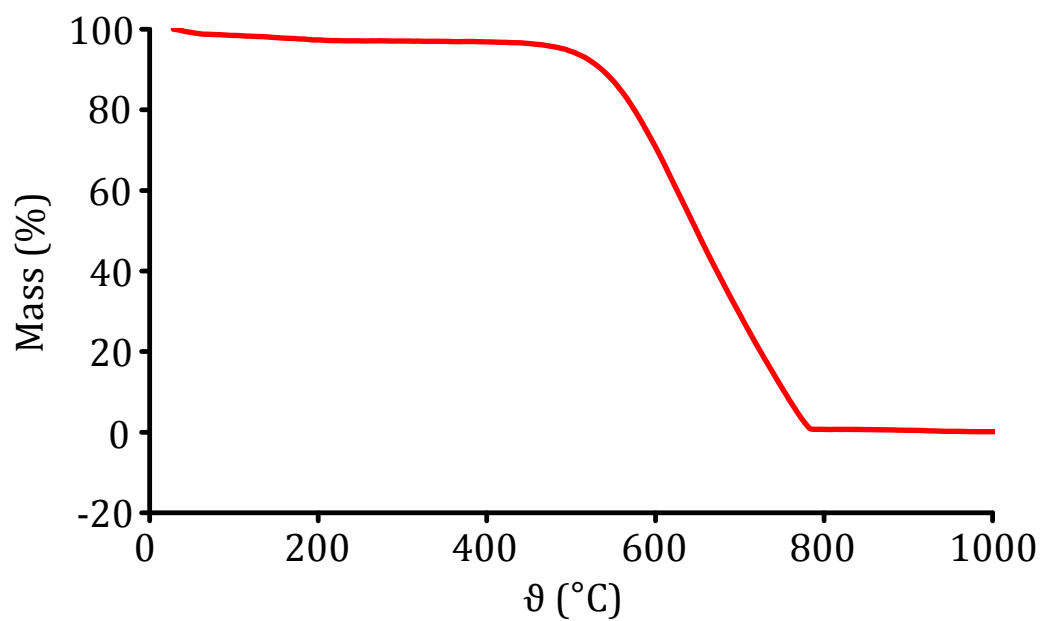
Appendix 3. *Thermogravimetrical analysis under air atmosphere of the CDC monoliths with a heating rate of 5 K/min.*
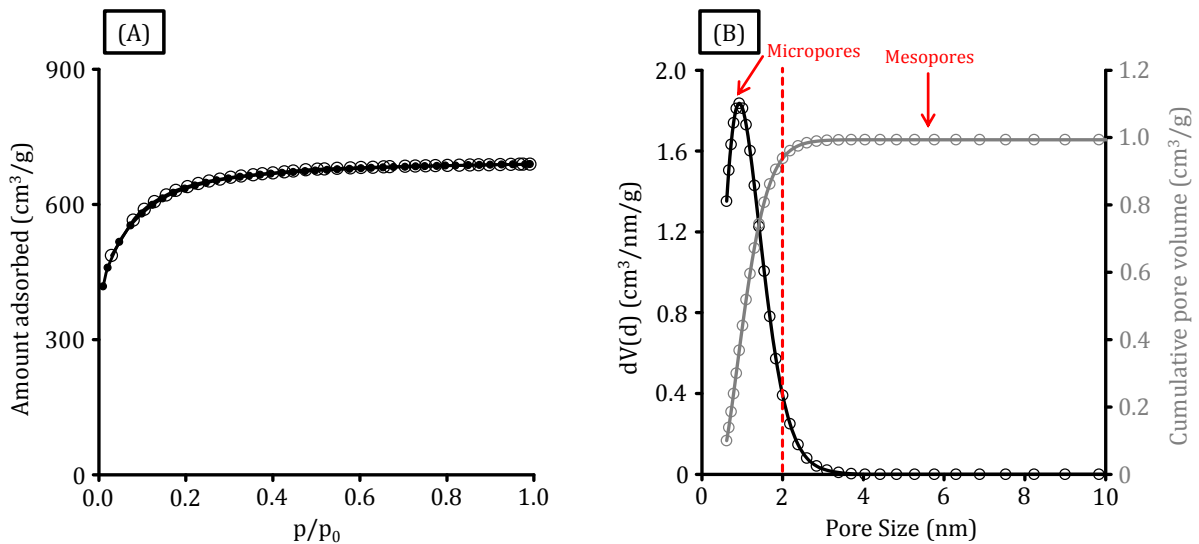
Appendix 4. *Nitrogen physisorption (-196°C) isotherm (A) and corresponding QSDFT (nitrogen on carbon with slit pores at-196°C, equilibrium branch kernel) pore size distributions (B) of the microporous CDC reference material.*
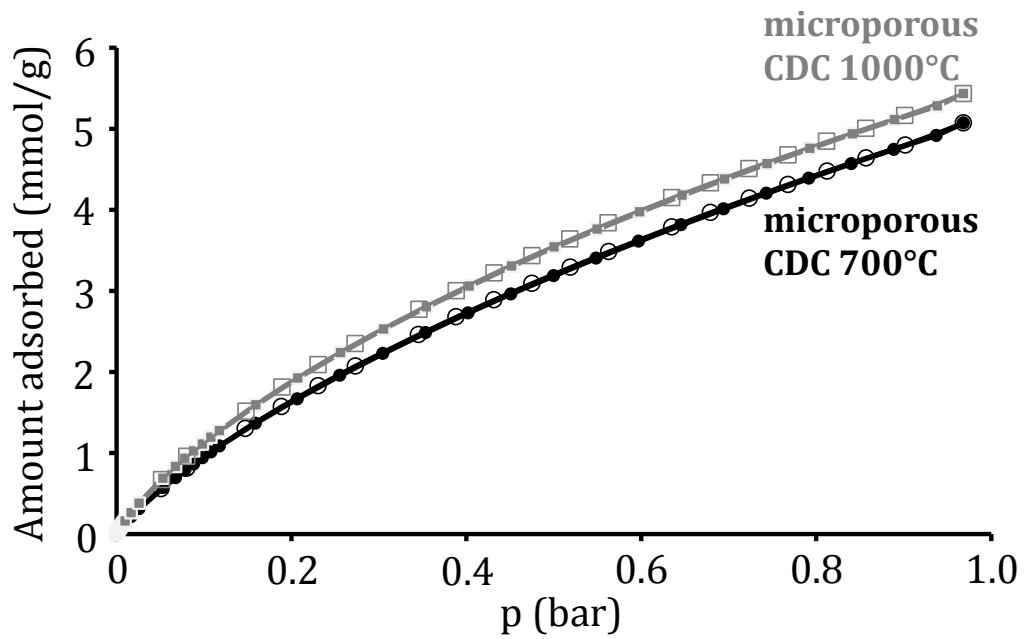

Appendix 5. *Linear (A) and semi-logarithmic (B, low pressure region) plots of nitrogen physisorption isotherms (-196°C) of the microporous CDC reference material prepared at 700°C (black) or 1000°C (grey).*

Appendix 6. *Carbon dioxide physisorption isotherms (0°C) of the microporous CDC reference material prepared at 700°C (black) or 1000°C (grey).*
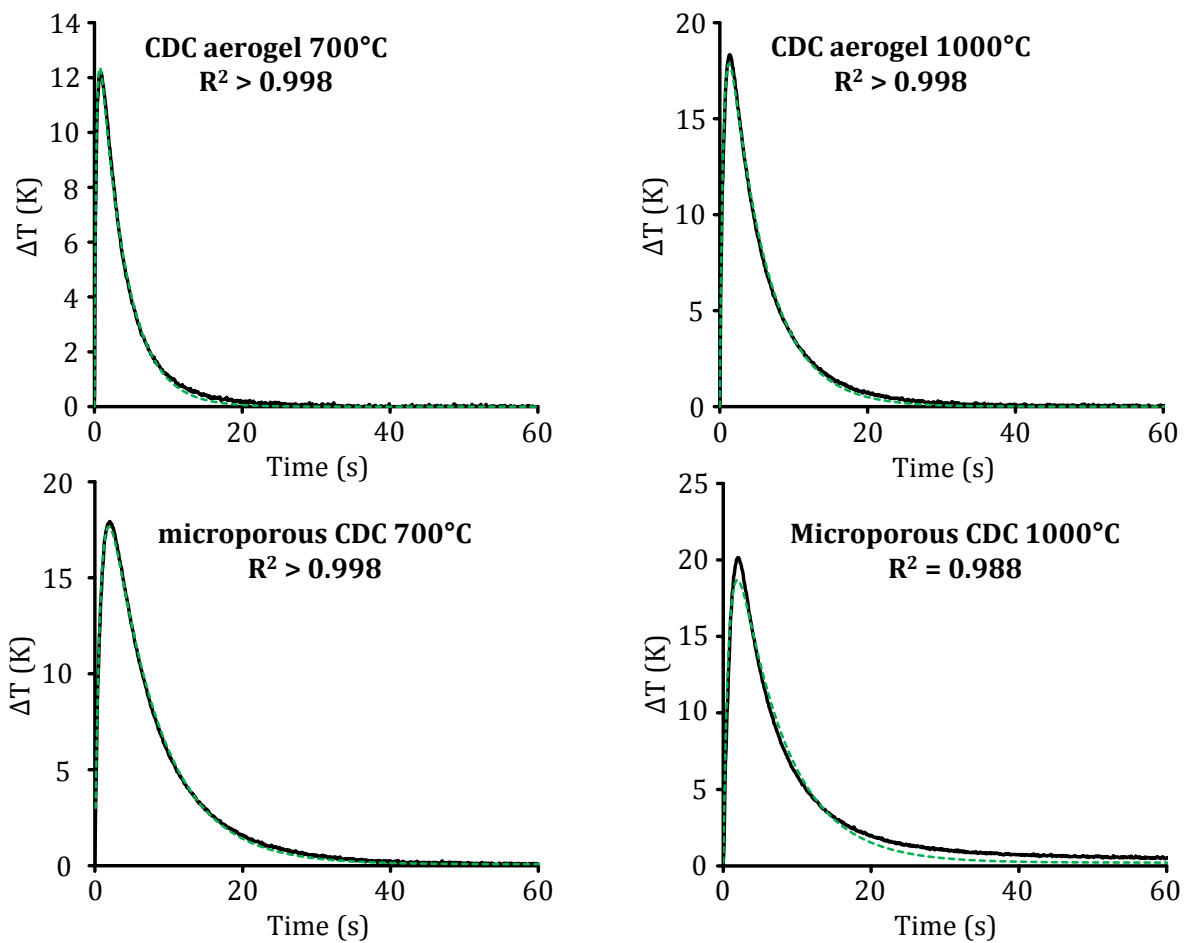
Appendix 7. *Fitting curves (dotted green lines) of the single peak thermal response function (Equation 24) to the measured data (straight black lines).*
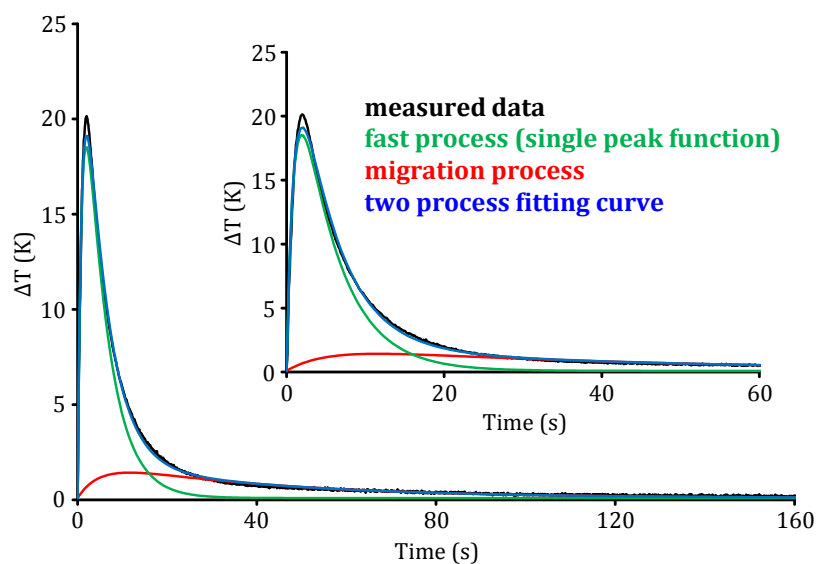
Appendix 8. *Fitting curve (blue) of the double-peak (green and red line) thermal response function (Equation 25) to the measured data (straight black line) for the microporous CDC reference prepared at 1000°C.*
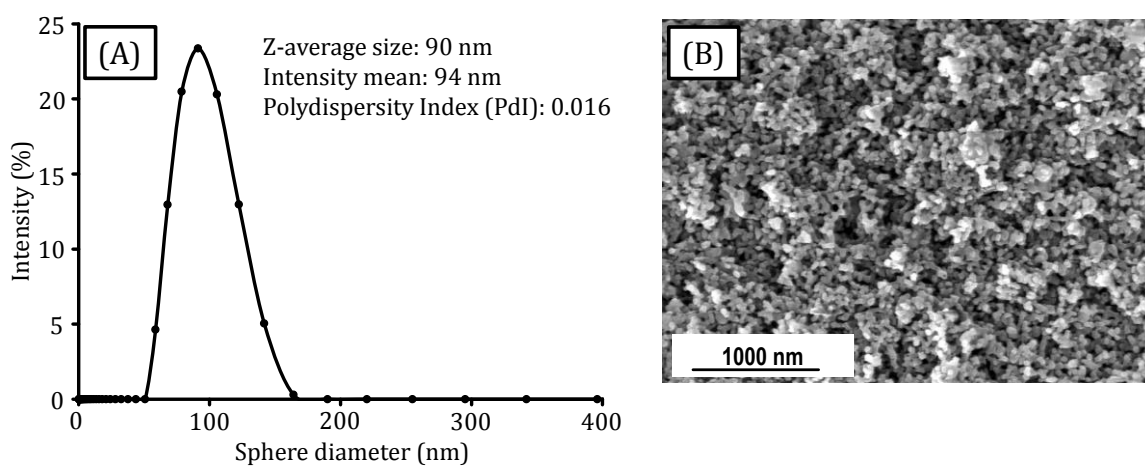
Appendix 9. *Dynamic light scattering measurement of PMMA template particles dispersed in water (A) and SEM micrograph of dried PMMA template particles (B).*
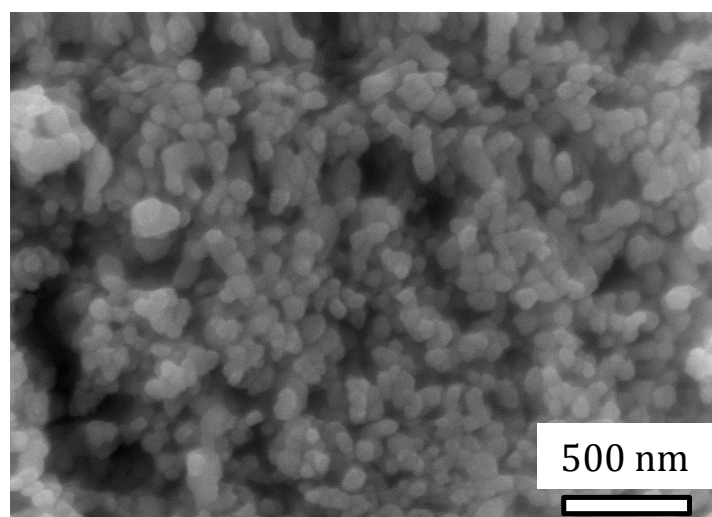
Appendix 10. *SEM micrograph of Degussa P25 particles.*

List of Publications of M. Sc. Martin Oschatz

Peer-Reviewed Journal Publications

1.) M. Oschatz, E. Kockrick, M. Rose, L. Borchardt, N. Klein, I. Senkovska, T. Freudenberg, Y. Korenblit, G. Yushin, S. Kaskel: „A cubic ordered, mesoporous carbide-derived carbon for gas and energy storage applications" *Carbon* **2010**, *48*, 3987-3992.

2.) M. Rose, Y. Korenblit, E. Kockrick, L. Borchardt, M. Oschatz, S. Kaskel, G. Yushin: „Hierarchical micro- and mesoporous carbide-derived carbon as a high-performance electrode material in supercapacitors" *Small* **2011**, *8*, 1108-1117.

3.) R. Frind, M. Oschatz, S. Kaskel: „Polymerization of polycarbosilanes in high internal phase emulsions for the synthesis of macroporous silicon carbide catalysts (polyHIPE-SiC)" *J. Mater. Chem.* **2011**, *21*, 11936-11940.

4.) L. Borchardt, M. Oschatz, R. Frind, E. Kockrick, M. R. Lohe, C. P. Hauser, C. K. Weiss, K. Landfester, B. Büchner, S. Kaskel: „Ceria/silicon carbide core-shell materials prepared by miniemulsion technique" *Beilstein J. Nanotechnol.* **2011**, *2*, 638-644.

5.) L. Borchardt, M. Oschatz, M. Lohe, V. Presser, Y. Gogotsi, S. Kaskel: „Ordered mesoporous carbide-derived carbons prepared by soft templating" *Carbon* **2012**, *50*, 3987-3994.

6.) M. Oschatz, L. Borchardt, M. Thommes, K. A. Cychosz, I. Senkovska, N. Klein, R. Frind, M. Leistner, V. Presser, Y. Gogotsi, S. Kaskel: „Carbide-derived carbon monoliths with hierarchical pore architectures" *Angew. Chem. Int. Ed.* **2012**, *51*, 7577-7580.

7.) J. Wang, M. Oschatz, T. Biemelt, L. Borchardt, I. Senkovska, M. R. Lohe, S. Kaskel: „Synthesis, characterization, and hydrogen storage capacites of hierarchical porous carbide derived carbon monolith " *J. Mater. Chem.* **2012**, *41*, 23893-23899.

8.) J. Wang, M. Oschatz, T. Biemelt, M. R. Lohe, L. Borchardt, S. Kaskel: „Preparation of cubic ordered mesoporous Silicon carbide conoliths by pressure-assisted Precramic polymer nanocasting" *Microporous Mesoporous Mater.* **2012**, *168*, 142-147.

9.) J. Wang, A. Heerwig, M. R. Lohe, M. Oschatz, L. Borchardt, S. Kaskel: „Fungi-based porous carbons for CO_2 adsorption and separation" *J. Mater. Chem.* **2012**, *22*, 13911-13913.

10.) L. Borchardt, C. Hoffmann, M. Oschatz, L. Mammitzsch, U. Petasch, M. Herrmann, S. Kaskel: „Preparation and application of cellular and nanoporous carbides" *Chem. Soc. Rev.* **2012**, *41*, 5053-5067.

11.) L. Borchardt, F. Hasche, M. R. Lohe, M. Oschatz, F. Schmidt, E. Kockrick, C. Ziegler, T. Lescouet, A. Bachmatiuk, B. Büchner, D. Farrusseng, P. Strasser, S. Kaskel: „Transition metal loaded silicon carbide-derived carbons with enhanced catalytic properties" *Carbon* **2012**, *50*, 1861-1870.

12.) M. Oschatz, L. Borchardt, I. Senkovska, N. Klein, M. Leistner, S. Kaskel: „Carbon dioxide activated carbide-derived carbon monoliths as high performance adsorbents" *Carbon* **2013**, *56*, 139-145.

13.) M. Oschatz, L. Borchardt, S. Rico-Francés, F. Rodríguez-Reinoso, S. Kaskel, J. Silvestre-Albero: „Textural characterization of micro- and mesoporous carbons using combined gas adsorption and n-nonane preadsorption" *Langmuir* **2013**, *29*, 8133-8139.

14.) S. Thieme, J. Brückner, I. Bauer, M. Oschatz, L. Borchardt, H. Althues, S. Kaskel: „High capacity micro-mesoporous carbon–sulfur nanocomposite cathodes with enhanced cycling stability prepared by a solvent-free procedure" *J. Mater. Chem. A* **2013**, *1*, 9225-9234.

15.) M. Oschatz, S. Thieme, L. Borchardt, M. R. Lohe, T. Biemelt, J. Brückner, H. Althues, S. Kaskel: „A new route for the preparation of mesoporous carbon materials with high performance in lithium–sulphur battery cathodes" *Chem. Commun.* **2013**, *49*, 5832-5834.

16.) J. Wang, I. Senkovska, M. Oschatz, M. R. Lohe, L. Borchardt, A. Heerwig, Q. Liu, S. Kaskel: „Imine-linked polymer-derived nitrogen-doped microporous carbons with excellent CO_2 capture properties" *ACS Appl. Mater. Interfaces* **2013**, *5*, 3160-3167.

17.) J. T. Lee, Y. Zhao, S. Thieme, H. Kim, M. Oschatz, L. Borchardt, A. Magasinski, W. I. Cho, S. Kaskel, G. Yushin: „Sulfur-infiltrated micro- and mesoporous silicon carbide-derived carbon cathode for high-performance lithium sulfur batteries" *Adv. Mater.* **2013**, *25*, 4573-4579.

18.) J. Wang, I. Senkovska, M. Oschatz, M. R. Lohe, L. Borchardt, A. Heerwig, Q. Liu, S. Kaskel: „Highly porous nitrogen-doped polyimine-based carbons with adjustable microstructures for CO_2 capture" *J. Mater. Chem. A* **2013**, *1*, 10951-10961.

19.) L. Borchardt, M. Oschatz, S. Paasch, S. Kaskel, E. Brunner: „Interaction of electrolyte molecules with carbon materials of well-defined porosity: characterization by solid-state NMR spectroscopy" *Phys. Chem. Chem. Phys.* **2013**, *15*, 15177-15184.

20.) J. R. Martin, L. Borchardt, M. Oschatz, G. Mondin, S. Kaskel: „Titanium Carbide and Carbide-Derived Carbon Composite Nanofibers by Electrospinning of Ti-Resin Precursor" *Chem. Ing. Tech.* **2013**, *85*, 1742-1748.

21.) H. Kim, J. T. Lee, D. Lee, M. Oschatz, W. Cho, S. Kaskel, G. Yushin: „Enhancing performance of Li–S cells using a Li–Al alloy anode coating" *Electrochem. Commun.* **2013**, *36*, 38-41.

22.) S. Porada, L. Borchardt, M. Oschatz, M. Bryjak, J. S. Atchison, K. J. Keesman, S. Kaskel, P. M. Biesheuvel, V. Presser: „Direct prediction of the desalination performance of porous carbon electrodes for capacitive deionization" *Energy Environ. Sci.* **2013**, *6*, 3700-3712.

23.) V. Shilapuram, N. Ozalp, M. Oschatz, L. Borchardt, S. Kaskel: „Hydrogen production from catalytic decomposition of methane over ordered mesoporous carbons (CMK-3) and carbide-derived carbon (DUT-19)" *Carbon* **2014**, *67*, 377-389.

24.) V. Shilapuram, N. Ozalp, M. Oschatz, L. Borchardt, S. Kaskel, R. Lachance: „Thermogravimetric Analysis of Activated Carbons, Ordered Mesoporous Carbide-Derived Carbons, and Their Deactivation Kinetics of Catalytic Methane Decomposition" *Ind. Eng. Chem. Res.* **2014**, *53*, 1741-1753.

25.) M. Oschatz, S. Boukhalfa, W. Nickel, J. T. Lee, S. Klosz, L. Borchardt, A. Eychmüller, G. Yushin, S. Kaskel: „Kroll-carbons based on silica and alumina templates as high-rate electrode material in electrochemical double-layer capacitors" *J. Mater. Chem. A* **2014**, *2*, 5131-5139.

26.) K. Pinkert, M. Oschatz, L. Borchardt, M. Klose, M. Zier, W. Nickel, L. Giebeler, S. Oswald, S. Kaskel, J. Eckert: „Role of Surface Functional Groups in Ordered Mesoporous

Carbide-Derived Carbon/Ionic Liquid Electrolyte Double-Layer Capacitor Interfaces"
ACS Appl. Mater. Interfaces **2014**, *6*, 2913-2919.

27.)   L. Borchardt, M. Oschatz, S. Graetz, M. R. Lohe, M. H. Rümmeli, S. Kaskel: „A Hard-Templating Route towards Ordered Mesoporous Tungsten Carbide and Carbide-Derived Carbons" *Microporous Mesoporous Mater.* **2014**, *186*, 163-167.

28.)   A. Meier, M. Weinberger, K. Pinkert, M. Oschatz, S. Paasch, L. Giebeler, H. Althues, E. Brunner, J. Eckert, S. Kaskel: „Silicon oxycarbide-derived carbons from a polyphenylsilsequioxane precursor for supercapacitor applications" *Microporous Mesoporous Mater.* **2014**, *188*, 140-148.

29.)   M. Oschatz, L. Borchardt, K. Pinkert, S. Thieme, M. R. Lohe, C. Hoffmann, M. Benusch, F. M. Wisser, C. Ziegler, L. Giebeler, M. H. Rümmeli, J. Eckert, A. Eychmüller, S. Kaskel: „Hierarchical carbide-derived carbon foams with advanced mesostructure as versatile electrochemical energy storage material" *Adv. Energy Mater.* **2014**, *4*, 1300645/1-1300645/9.

30.)   M. Oschatz, H. C. Hoffmann, J. Pallmann, J. Schaber, L. Borchardt, W. Nickel, I. Senkovska, S. Rico-Francés, J. Silvestre-Albero, S. Kaskel, E. Brunner: „Structural Characterization of Micro- and Mesoporous Carbon Materials Using In Situ High Pressure 129Xe NMR Spectroscopy" *Chem. Mater.* **2014**, *26*, 3280-3288.

31.)   K. Faber, F. Badaczewski, M. Oschatz, G. Mondin, W. Nickel, S. Kaskel, B. M. Smarsly: „In-Depth Investigation of the Carbon Microstructure of Silicon Carbide-Derived Carbons by Wide-Angle X-Ray Scattering" *J. Phys. Chem. C* **2014**, *118*, 15705-15715.

32.)   G.-P. Hao, F. Hippauf, M. Oschatz, F. Wisser, J. Deng, A. Leifert, W. Nickel, N. Mohamed Noriega, Z. Zheng, S Kaskel: „Stretchable and Transparent Conductive Hybrid Hydrogels for Flexible Supercapacitors" *ACS Nano* **2014**, *8*, 7138-7146.

33.)   W. Nickel, M. Oschatz, M. von der Lehr, M. Leistner, G.-P. Hao, P. Adelhelm, P. Müller, B. M. Smarsly, S. Kaskel: „Direct Synthesis of Carbide-Derived Carbon Monoliths with Hierarchical Pore Design by Hard-Templating", *J. Mater. Chem. A* **2014**, *2*, 12703-12707.

34.)   L. Borchardt, M. Oschatz, S. Kaskel: „Tailoring porosity in carbon materials for supercapacitor applications" *Mater. Horiz.* **2014**, *1*, 157-168.

35.)   G.-P. Hao, M. Oschatz, W. Nickel, M. Adam, S. Kaskel: „Design of Functional Nanostructured Carbons for Advanced Heterogeneous Catalysts: A Review" *Curr. Org. Chem.* **2014**, *18*, 1262-1279.

36.)   M. Oschatz, J. T. Lee, H. Kim, W. Nickel, L. Borchardt, W. I. Cho, C. Ziegler, S. Kaskel, G. Yushin: „Micro- and Mesoporous Carbide-Derived Carbon Prepared by a Sacrificial Template Method in High Performance Lithium Sulfur Battery Cathodes" *J. Mater. Chem. A* **2014**, *2*, 17649-17654.

37.)   M. Oschatz, W. Nickel, M. Thommes, K. A. Cychosz, M. Leistner, M. Adam, G. Mondin, P. Strubel, L. Borchardt, S. Kaskel: „Evolution of Porosity in Carbide-Derived Carbon Aerogels", *J. Mater. Chem. A* **2014**, *2*, 18472-18479.

38.)   J. T. Lee, H. Kim, M. Oschatz, D.-C. Lee, F. Wu, H.-T. Lin, B. Zdyrko, W. I. Cho, S. Kaskel, G. Yushin: „ Micro-and Mesoporous Carbide-Derived Carbon-Selenium Cathode for High Performance Lithium Selenium Battery" *Adv. Energy Mater.* **2014**, accepted, DOI: 10.1002/aenm.201400981.

39.)   C. Zhu, D. Wen, M. Oschatz, M. Holzschuh, W. Liu, A.-K. Herrmann, F. Simon, S. Kaskel, A. Eychmüller: „Kinetically controlled synthesis of PdNi bimetallic porous nanostructures with enhanced electrocatalytic activity" *Small* **2014**, accepted, DOI: 10.1002/smll.201401432.

40.)   C. Hoffmann, S. Thieme, J. Brückner, M. Oschatz, T. Biemelt, G. Mondin, H. Althues, S. Kaskel: „Nanocasting Hierarchical Carbide-Derived Carbons in Nano-structured Opal Assemblies for High Performance Cathodes in Lithium-Sulfur Batteries", *ACS Nano* **2014**, accepted, DOI: 10.1021/nn503394u.

41.)   H. Kim, F. Wu, J. T. Lee, N. Nitta, H.-T. Lin, M. Oschatz, W.-I. Cho, S. Kaskel, O. Borodin, G. Yushin: „ In-Situ Formation of Protective Coatings on Sulfur Cathodes in Lithium Batteries with LiFSI-based Organic Electrolytes" *Adv. Energy Mater.* **2014**, accepted, DOI: 10.1002/aenm.201401792.

42.)   P. Strubel, S. Thieme, T. Biemelt, A. Helmer, M. Oschatz, J. Brückner, H. Althues, S. Kaskel, „ ZnO hard templating for synthesis of hierarchical porous carbons with tailored

porosity and high performance in lithium-sulfur battery", *Adv. Funct. Mater.* **2014**, accepted, DOI: 10.1002/adfm.201402768.

43.) M. Adam, M. Oschatz, W. Nickel, S. Kaskel: „Preparation of hierarchical porous biomorphic carbide-derived carbon by polycarbosilane impregnation of wood", *Microporous Mesoporous Mater.* **2014**, submitted.

44.) C. Zhu, S. Leubner, D. Wen, M. Oschatz, S. Kaskel, A. Eychmüller: „Nickel cobalt oxide hollow nanosponges as advanced electrocatalysts for oxygen evolution reaction" *Small* **2014**, submitted.

Book Contribution

M. Oschatz, L. Borchardt, G.-P. Hao, S. Kaskel: „ Nanoporous Carbide-Derived Carbons as Electrode Materials in Electrochemical Double-Layer Capacitors" in *Nanocarbons for Advanced Energy Storage*, Wiley-VCH (Weinheim, Germany), **2014**, in print.

Conference Proceedings

S. Kaskel, L. Borchardt, M. Oschatz: "Ordered mesoporous silicon carbide and carbide-derived carbon materials" in *Abstracts of Papers, 243rd ACS National Meeting & Exposition*, San Diego, CA, United States (March 25-29) **2012**.

Patents

M. Oschatz, L. Borchardt, S. Kaskel: „Process for producing porous carbon using inorganic nanoparticles as template" *PCT Int. Appl.* **2014**, WO 2014019880 A1 20140206.

Conference Contributions

Oral Presentations as Presenting Author

20.-23.05.2012	10th International Symposium on Ceramic Materials and Components for Energy and Environmental Applications (CMCEE), Dresden, Germany Title: „New strategies towards carbide and carbon materials with hierarchical porosities - synthesis and applications" M. Oschatz, L. Borchardt, S. Kaskel

12.-16.05.2013	2nd International Conference on Materials for Energy (EnMat), Karlsruhe, Germany Title: „Hierarchical CDCs as Gas Storage and Electrode Materials" M. Oschatz, L. Borchardt, S. Kaskel
14.-19.07.2013	Annual World Conference on Carbon, Rio de Janeiro, Brazil Title: „Structural Varieties of Polymer-Based Carbide-Derived Carbons" M. Oschatz, L. Borchardt, M. Adam, K. Pinkert, S. Thieme, S. Kaskel
01.-05.04.2014 (on invitation)	Sino-German Symposium on „π-Conjugated Nanomaterials for Catalysis and Clean Energy Applications", Berlin, Germany Title: "Energy Storage in Carbon Materials with Hierarchical Pore Architecture" M. Oschatz, S. Kaskel
11.-14.05.2014	10th International Symposium on the Characterization of Porous Solids (COPS-X), Granada, Spain Title: „Adsorption Phenomena in Hierarchical Porous Carbon Materials" M. Oschatz, W. Nickel, M. Adam, S. Kaskel
22.-24.10.2014	Cellular Materials (CellMat 2014), Dresden, Germany Title: „Carbide-Derived Carbon (CDC) Materials with Cellular Pore Structures for Gas Filtration and Electrochemical Energy Storage" M. Oschatz, W. Nickel, S. Kaskel

Poster Presentations as Presenting Author

02.-04.03.2011	23th German Zeolithe Conference, Nürnberg, Germany Title: „DUT-19: A cubic ordered mesoporous "carbide-derived carbon" prepared via KIT-6 exotemplating" M. Oschatz, L. Borchardt, M. Rose, N. Klein, I. Senkovska, E. Kockrick, S. Kaskel
05.-08.06.2011	9th International Symposium on the Characterisation of Porous Solids (COPS-IX), Dresden, Germany Title: „Ordered mesoporous carbide-derived carbon (OM-CDC) and CDC-Nanofibres" L. Borchardt, M. Oschatz, M. Rose, I. Senkovska, E. Kockrick, P. Krawiec, Y. Korenblit, G. Yushin, S. Kaskel

07.-09.03.2012	24th German Zeolithe Conference, Magdeburg, Germany Title: „Macroporous silicon carbide monoliths produced by a PolyHIPE approach-synthesis, structure and catalytic applications" M. Oschatz, L. Borchardt, C. Hoffmann, S. Kaskel
20.-23.05.2012	10th International Symposium on Ceramic Materials and Components for Energy and Environmental Applications (CMCEE), Dresden, Germany Title: „Macroporous silicon carbide monoliths produced by a PolyHIPE approach-synthesis, structure and catalytic applications" M. Oschatz, L. Borchardt, S. Kaskel
12.-13.06.2012	Nanofair 2012-9th International Nanotechnology Symposium, Dresden, Germany Title: „Polycarbosilane-based porous silicon(oxy)carbide ceramics with controllable mesostructure" M. Oschatz, L. Borchardt, S. Kaskel
17.-22.06.2012	Annual World Conference on Carbon 2012, Krakow, Poland Title: „Carbide-derived carbon monoliths with open macropores" M. Oschatz, L. Borchardt, S. Kaskel
06.-08.03.2013	25th German Zeolithe Conference, Hamburg, Germany Title: „Carbide-Derived Carbon Monoliths with open Macropores" M. Oschatz, L. Borchardt, S. Kaskel
14.-19.07.2013	Annual World Conference on Carbon 2013, Rio de Janeiro, Brazil Title: „Carbide-Derived Carbon Aerogels with Ultrahigh Porosity prepared from Polycarbosilane Precursors" M. Oschatz, L. Borchardt, W. Nickel, S. Kaskel
06.-07.11.2013	2nd Workshop "Lithium-Sulfur-Batteries", Fraunhofer IWS, Dresden, Germany Title: „Carbon materials with hierarchical pore architectures as cathode component in lithium-sulfur batteries" M. Oschatz, S. Thieme, W. Nickel, L. Borchardt, H. Althues, S. Kaskel
11.-14.05.2014 (2 Posters)	10th International Symposium on the Characterization of Porous Solids (COPS-X), Granada, Spain

Title 1: „Pore Structure Optimization in Carbide-Derived Carbon Aerogels"
M. Oschatz, W. Nickel, S. Kaskel
Title 2: „Solid-State NMR Studies on Adsorption of Electrolyte Ions in Carbon Materials with well-defined Porosity"
M. Oschatz, L. Borchardt, S. Paasch, E. Brunner, S. Kaskel

01.-03.07.2014	Nanofair 2014-10th International Nanotechnology Symposium, Dresden, Germany Title: „Carbon Materials with Hierarchical Pore Structure as Versatile Electrode materials in Lithium-Sulphur Batteries and EDLCs" M. Oschatz, W. Nickel, S. Thieme, S. Kaskel
12.-13.11.2014	3rd Workshop "Lithium-Sulfur-Batteries", Fraunhofer IWS, Dresden, Germany Title: „Carbide-derived carbon materials with hierarchical pore structure as cathode component in lithium-sulfur batteries" M. Oschatz, S. Thieme, C. Hoffmann, W. Nickel, J. T. Lee, H. Althues, G. Yushin, S. Kaskel

Hiermit versichere ich, dass ich die vorliegende Arbeit ohne unzulässige Hilfe Dritter und ohne Benutzung anderer als der angegebenen Hilfsmittel angefertigt habe; die aus fremden Quellen direkt oder indirekt übernommenen Gedanken sind als solche kenntlich gemacht. Die Arbeit wurde bisher weder im Inland noch im Ausland in gleicher oder ähnlicher Form einer anderen Prüfungsbehörde vorgelegt.

Die vorliegende Arbeit wurde am Institut für Anorganische Chemie der Technischen Universität Dresden im Zeitraum von Oktober 2011 bis Oktober 2014 unter wissenschaftlicher Betreuung von Herrn Prof. Dr. S. Kaskel angefertigt.

Es haben bisher keine früheren erfolglosen Promotionsverfahren stattgefunden.

Hiermit erkenne ich die Promotionsordnung der Fakultät Mathematik und Naturwissenschaften der Technischen Universität Dresden vom 23. Februar 2011 an.

Dresden, 8.12.2014   Martin Oschatz